Recombination of charge carriers in dislocation-free silicon containing growth microdefects of various types

L. A. Kazakevich

A. N. Sevchenko Scientific Research Institute of Applied Physics Problems, 220064 Minsk, Belarus

P. F. Lugakov

Belorussian Agrarian Technical State University, 220608 Minsk, Belarus

(Submitted June 2, 1997; accepted for publication June 7, 1997)
Fiz. Tekh. Poluprovodn. **32**, 129–131 (February 1998)

The temperature and injection dependence of the charge-carrier lifetime in dislocation-free n-Si is analyzed, making it possible to characterize the recombination activity of various types of microdefects. The parameters of the primary recombination centers with A- and B-type microdefects have been found. © *1998 American Institute of Physics.*
[S1063-7826(98)00102-1]

The main structural growth defects in dislocation-free silicon single crystals are microdefects whose type is determined by the conditions of growth, primarily the growth rate V and the cooling regime (axial temperature gradient G).[1] Depending on the ratio V/G, microdefects of A, B, C, or D type can arise in the bulk of the crystal.[2] The use of selective etching, x-ray topography, and also electron-microscopy has made it possible to obtain information about the macroscopic distribution of such defects in crystal boules, as well as their size, structure, and nature.[2–4] However, results of studies of the electrical properties of microdefects have been few and to a significant degree contradictory,[5,6] while in fact practically nothing is known about the recombination activity of the various types of microdefects. To fill this latter gap is the aim of the present work.

Dislocation-free single crystals of n-type silicon with resistivity $\rho = 20-100\ \Omega\cdot$cm were investigated, where these crystals were obtained by crucible-less zone melting in vacuum or in an argon atmosphere with variable growth rate V from 1 to 6 mm/min and containing by virtue of this microdefects of types A, B, or D. The presence of microdefects and their type were monitored with the help of metallographic methods. Three groups of samples were prepared from parts of a boule grown in vacuum at different rates. The first group consisted of crystals containing primarily type-A microdefects (slow rate of growth), the second—types A and B, and the third—type D. The fourth group consisted of silicon crystals grown in an argon atmosphere, in which selective etching did not reveal any known microdefects (''defect-free'' samples). Using the stationary photoconductivity method, the photomagnetoelectric effect, and modulation of the conductivity at a point contact, we measured the temperature ($T_m = 80-400$ K) and injection $[\Delta n/n_0 = (1\times10^{-3})-(1\times10^{0})]$ dependence of the lifetime (τ) of the nonequilibrium majority and minority charge carriers (CC). Before making the measurements, the samples were subjected to special processing (heating to around 1000 K in an oxidizing medium for roughly 10 min with subsequent cooling at a rate of 0.2–0.3 K/s), as a result of which a thin thermal oxide layer was created on the surface, having built-in positive charge,[7] which eliminated surface recombination of charge carriers.

Curves *1–4* in Fig. 1 plot the dependence of the lifetime τ of the minority charge carriers on the inverse temperature (a) and their injection level (b) in the investigated materials (the numbers of the curves and the groups of crystals coincide). Also shown (curve *5*) is the temperature dependence of τ of the majority charge carriers (electrons), which in the low-temperature region ($T_m < 250$ K) has essentially the same character for all four groups of crystals. The observed increase of the lifetime τ of the majority charge carriers as the temperature is lowered is evidence of the presence in all the investigated materials of sticking centers for holes of identical nature.

We note some peculiarities of the temperature and injection curves of the lifetime τ of the minority charge carriers. First, for the crystals of the first and second groups the curves of the increasing dependence of the charge-carrier lifetime τ on temperature, have characteristic segments of activational variation. Second, in these same materials a stronger injection dependence of τ is observed (in comparison with samples from the third and fourth groups). Finally, in the crystals of the third and fourth groups τ varies monotonically with temperature while in the investigated interval of injection levels the charge-carrier lifetime remains practically constant.

These dependences of the charge-carrier lifetime τ on the temperature and injection level were analyzed within the framework of the Hall–Shockley–Read model.[8,9] For crystals containing microdefects of A or A and B type, it gives the following results. The variation of the lifetime τ of the minority charge carriers with temperature for $T_m < 200$ K is due to the temperature dependence of the capture cross section σ_p of the holes, which has the form $\sigma_p \sim \exp \varepsilon_p/kT$, where $\varepsilon_p = 0.065$ eV and $\varepsilon_p = 0.045$ eV for the first and second groups, respectively. Further increase of τ ($T_m > 250$ K)

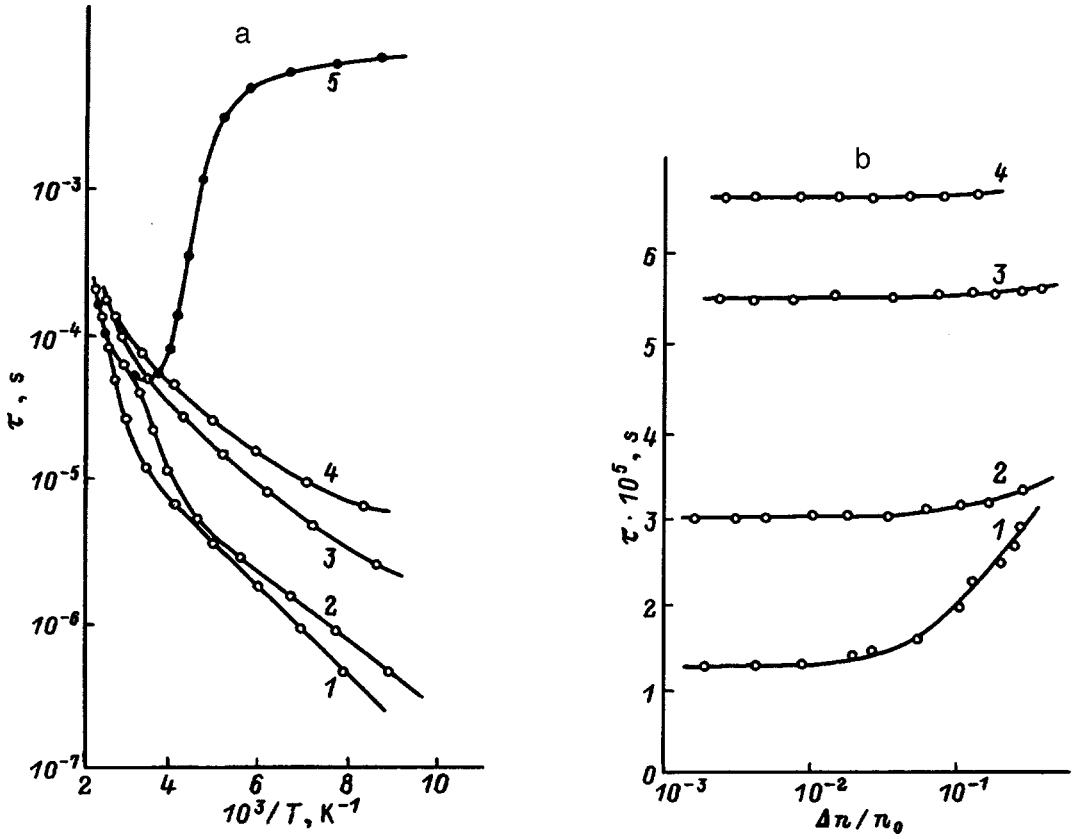

FIG. 1. Temperature (a) and injection (b) dependences of the lifetime of the minority (*1–4*) and majority (*5*) charge carriers in crystals of the first (*1*), second (*2*), third (*3*), and fourth (*4*) group.

is associated mainly with variation of the degree of filling of the levels of the recombination centers. As calculations have shown, in crystals with *A*-type microdefects recombination of charge carriers goes through the level with energy position $\Delta E_{r1}=0.41$ eV, while in crystals with microdefects of types *A* and *B* two energy levels in the temperature dependence of τ—$\Delta E_{r1}=0.41$ eV and $\Delta E_{r2}=0.30$ eV—are distinctly observed. Therefore we may assume that the first of these is associated with microdefects of type *A*, and the second, with microdefects of type *B*.

Taking into account the position of the Fermi level ($E_c-0.37$ eV and $E_c-0.25$ eV) at the temperatures corresponding to the transitions from the temperature dependences of σ_p to the activation-like dependence of τ ($10^3/T_m=3.1$ and $10^3/T_m=4.4$), we may assume that in the investigated crystals the energy levels of the primary recombination centers are located in the lower half of the band gap, i.e., $\Delta E_{r1}=E_v+0.41$ eV and $\Delta E_{r2}=E_v+0.30$ eV. From the injection dependences of the lifetime τ of the minority charge carriers measured at $T_m=300$ K, we determined the ratios of the hole and electron capture cross sections. It turns out that $\sigma_p/\sigma_n=4.5$ for the samples of group 1, while $\sigma_p/\sigma_n=4.0$ for those of group 2. The ratio of the capture cross sections of the minority charge carriers ($\sigma_p>\sigma_n$), and also the nature of the temperature dependence of the hole capture cross sections ($\sigma_p\sim\exp \varepsilon_p/kT$) allows one to conclude that in crystals containing microdefects of type *A* or types *A* and *B*, nonequilibrium charge carriers recombine through centers negatively charged relative to the captured holes, i.e., they correspond to acceptor energy levels in the lower half of the band gap.

Microdefects of *A*-type, as is well known,[2,4] are dislocation loops of interstitial type, the presence on which of dangling bonds and the capture to them of charge carriers define the recombination activity of microdefects of *A*-type. According to our estimates, which allow for the degree of filling of the dangling bonds ~ 0.01 characteristic of dislocations,[10] the concentration of the charge-carrier capture centers associated with type-*A* microdefects does not exceed $10^{10}-10^{11}$ cm^{-3}. Thus, the values of the defect concentrations have hardly any effect on the degree of compensation of the material, but have a marked effect on recombination processes.

Associated with microdefects of *B* type are clusters of interstitial atoms or microparticles of a new phase composed of atoms of residual impurities.[2,3] The presence of such defects in the bulk of the crystal leads to the appearance of deformation stress fields, under the action of which an atmosphere of impurities or complexes consisting of primary recombination centers in the material is formed near the microdefects.

As for the third and fourth groups of crystals, they are characterized by monotonic variation of τ with temperature and their very weak injection dependence cannot be described within the framework of Hall–Shockley–Read recombination statistics.[8,9] Therefore we can assume that the lifetime of the charge carriers in these crystals is limited by their diffusion to the walls with a high local recombination

rate.[11] In crystals of the third group, microdefects of D-type can enter in the role of such sinks, while in crystals of the fourth group (''defect-free'' silicon) shallow inclusions not revealed by selective etching may enter in this role.[12,13] The presence of potential barriers surrounding the charge-carrier sinks, whose heights decrease with increase of the temperature, is the cause of the monotonic temperature dependence of τ as a result of variation of the diffusion coefficient of the charge carriers to growth defects with temperature. For $T_m = 300$ K the potential barriers disappear and τ is practically independent of the charge-carrier injection level, as is observed in experiment.

Thus, the above experimental results and their analysis allow us to come to the following conclusions about the recombination activity of the various types of microdefects in dislocation-free n-silicon. We have found that in samples with microdefects of types A and B, charge-carrier recombination takes place on centers introducing acceptor energy levels $E_v + 0.41$ eV and $E_v + 0.30$ eV in the lower half of the band gap of silicon, with asymmetry of their capture cross sections $\sigma_p/\sigma_n = 4.5$ and $\sigma_p/\sigma_n = 4.0$, respectively. In the crystals of the third and fourth groups the charge carriers recombine primarily on centers in an impurity or impurity-defect atmosphere near microdefects of D type or shallow inclusions of interstitial type not revealed by selective etching.

[1] V. V. Voronkov, J. Cryst. Growth **59**, 625 (1982).
[2] K. V. Ravi, *Imperfections and Impurities in Semiconducting Silicon* (Wiley, New York, 1981).
[3] A. A. Sitnikova, L. M. Sorokin, I. E. Talanin, K. L. Malyshev, É. G. Sheĭkhet, and É. S. Fal'kevich, Fiz. Tverd. Tela **28**, 1829 (1986) [Sov. Phys. Solid State **28**, 1015 (1986)].
[4] H. Foll and B. O. Kolbesen, Appl. Phys. **8**, 319 (1975).
[5] V. G. Mokerov, S. M. Nikiforova-Denisova, E. N. Ovcharenko, V. P. Panasyuk, V. I. Smirnov, Yu. A. Timoshenko, and I. P. Chernov, Mikroelektronika **15**, 36 (1986).
[6] A. F. Muratov, *Nuclear-Physics Methods of Control of Semiconductor Materials and Metals* [in Russian] (Tashkent, 1984), p. 115.
[7] N. V. Rumak, *The System Silicon–Silicon Dioxide in MOS Structures* [in Russian] (Minsk, 1986).
[8] R. N. Hall, Phys. Rev. **87**, 387 (1952).
[9] W. Shockley and W. Read, Phys. Rev. **87**, 835 (1952).
[10] H. F. Matare, *Defect Electronics in Semiconductors* (Wiley, New York, 1971).
[11] S. R. Dhariwal and D. R. Mehrotra, Solid State Commun. **67**, 1007 (1988).
[12] C. Junichi, in *Defects and Properties of Semiconductors: Def. Eng. Symp. Qual. Semicond* (Tokyo, 1987), p. 143.
[13] I. I. Kolkovskii, P. F. Lugakov, and V. V. Shusha, Phys. Status Solidi A **127**, 103 (1991).

Translated by Paul F. Schippnick

Radiation defect formation in Ge-doped silicon as a result of low-temperature irradiation

L. I. Khirunenko, V. I. Shakhovtsov, and V. V. Shumov

Institute of Physics of the National Academy of Sciences of the Ukraine, 252650 Kiev, Ukraine
(Submitted May 26, 1997; accepted for publication June 9, 1997)
Fiz. Tekh. Poluprovodn. **32**, 132–134 (February 1998)

An investigation of the influence of germanium doping ($\leqslant 1$ at. %) on the formation efficiency of the main secondary radiation defects in silicon under low-temperature ($T \leqslant 90$ K) electron irradiation has been carried out. The significant decrease of the formation efficiency of A and V_2 centers in Si⟨Ge⟩ is explained by assuming that the germanium atoms are indirect recombination centers of primary radiation defects (V and I) in Si⟨Ge⟩. © *1998 American Institute of Physics.* [S1063-7826(98)00202-6]

The high probability of interaction of germanium atoms with vacancies (V) in silicon, and also additional internal elastic stresses arising due to the difference in the covalent radii of the Si and Ge atoms lower the formation efficiency of the main secondary radiation defects (RD) in crystals irradiated at room temperature.[1–3] It is of great interest to investigate the defect formation in samples of Si⟨Ge⟩ irradiated at temperatures $T \leqslant 200$ K, where the nascent GeV centers are thermally stable and their influence on the formation of secondary radiation defects should be substantial.

In this paper we report the results of an experimental study of the radiation defect formation in Si⟨Ge⟩ single crystals irradiated at temperatures $T \leqslant 90$ K. We used Czochralski grown samples of n-type silicon, undoped and Ge-doped with concentrations 5×10^{18}–2×10^{20} cm^{-3} and resistivity $\rho \approx 25\ \Omega\cdot$cm. The oxygen concentration in the samples varied in the limits $(7-8)\times10^{17}$ cm^{-3}; the oxygen concentration did not exceed $(1-2)\times10^{16}$ cm^{-3}. Irradiation was carried out on a linear accelerator by 3.5-MeV electrons with a dose of 5×10^{17}–1.2×10^{18} cm^{-2} at $T \leqslant 90$ K.

Figure 1 shows comparative infrared absorption spectra of Si and Si⟨Ge⟩ in the region of the V_2 and A-center bands immediately after irradiation. As can be seen, doping of silicon by germanium leads to a significant lowering of the formation efficiency of the A centers and a moderate lowering of the formation efficiency of the divacancies; i.e., most of the irradiation-generated divacancies are captured to the GeV centers.

Isochronous annealing of the investigated samples (with duration $\Delta t = 15$ min) shows that raising the temperature to $T \approx 200$–280 K, at which dissociation of the GeV centers takes place, leads to a significant increase in the intensity of the absorption band of the A centers in Si⟨Ge⟩ crystals. In this case some increase in the intensity of the absorption band of the divacancies is also observed (Fig. 1). Thus, the main part of the formation of the A centers in Si⟨Ge⟩ occurs not immediately after irradiation, but after annealing of the GeV centers, when the liberated vacancies interact with the atoms of interstitial oxygen. In this case, apparently, some of the vacancies interact with each other, forming secondary divacancies, which leads to an increase in the intensity of the absorption band of the divacancies.

The circumstance that the concentrations of the A centers and divacancies in Si⟨Ge⟩ (both immediately after irradiation and after annealing of the GeV centers) are significantly less than in Si is worthy of note. This circumstance makes it possible, as in Ref. 3, to assume that the Ge atoms under our experimental conditions are centers of indirect recombination of primary radiation defects.

Based on this assumption, the processes of formation of secondary radiation defects can be described with the help of a system of quasimechanical equations.

The main processes under conditions of low-temperature electron (e^-) irradiation of Si⟨Ge⟩ are

$$\{\text{a}\}\ e^- \rightarrow I, V, V_2, \quad \{\text{b}\}\ \text{Ge}+V \rightarrow \text{Ge}V,$$
$$\{\text{c}\}\ \text{Ge}V + I \rightarrow \text{Ge}, \quad \{\text{d}\}\ V+V \rightarrow V_2,$$
$$\{\text{e}\}\ V_2 + I \rightarrow V, \quad \{\text{f}\}\ V+\text{O} \rightarrow A,$$
$$\{\text{g}\}\ A + I \rightarrow \text{O}, \quad \{\text{h}\}\ V_2 + I \rightarrow V_2 I,$$

where {a} describes processes of formation of primary V, V_2, and interstitial atoms I; {b}–{h} describe the formation of secondary radiation defects.

Taking the above processes into account, we can write the system of quasichemical equations in the form

$$\frac{dN_I}{dt} = \lambda_1 + 2\lambda_2 - \chi_{gI} N_g N_I - \chi_{AI} N_A N_I - \chi_{V_2 I} N_{V_2} N_I - \frac{N_I}{\tau_I},$$

$$\frac{dN_V}{dt} = \lambda_1 - \chi_{\text{Ge}V} N_{\text{Ge}} N_V - \chi_{V\text{O}} N_{\text{O}} N_V - 2\chi_{VV} N_V^2 + \chi^*_{V_2 I} N_{V_2} N_I,$$

$$\frac{dN_g}{dt} = \chi_{\text{Ge}V} N_{\text{Ge}} N_V - \chi_{gI} N_g N_I;$$

$$\frac{dN_A}{dt} = \chi_{V\text{O}} N_{\text{O}} N_V - \chi_{AI} N_A N_I,$$

$$\frac{dN_{V_2}}{dt} = \lambda_2 + \chi_{VV} N_V^2 - \chi_{V_2 I} N_{V_2} N_I. \qquad (1)$$

Here N_I, N_V, N_{V_2}, and N_A are the concentrations of the defects I, V, V_2, and A; N_g is the concentration of the GeV

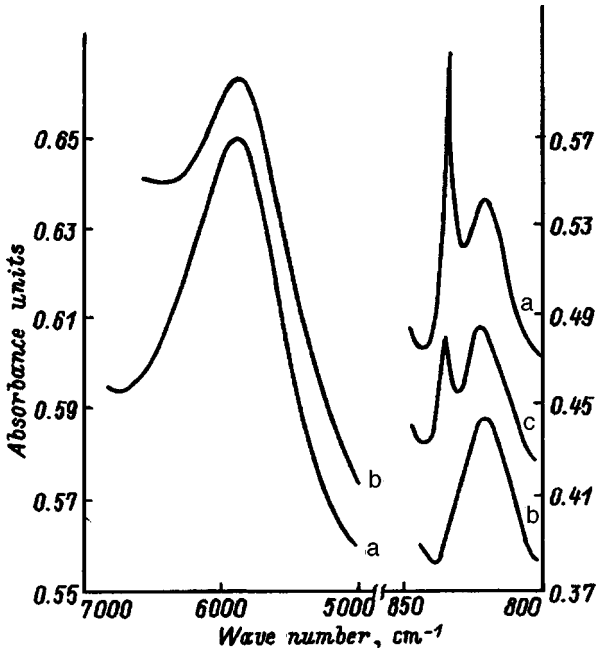

FIG. 1. Infrared absorption spectra in the region of the V_2 center and A center for Si (a) and Si⟨Ge⟩ (b,c) ($N_{Ge}\approx 2\times 10^{20}$ cm^{-3}), irradiated by electrons at $T\leqslant 90$ K. a,b—after irradiation; c—after annealing at $T=300$ K.

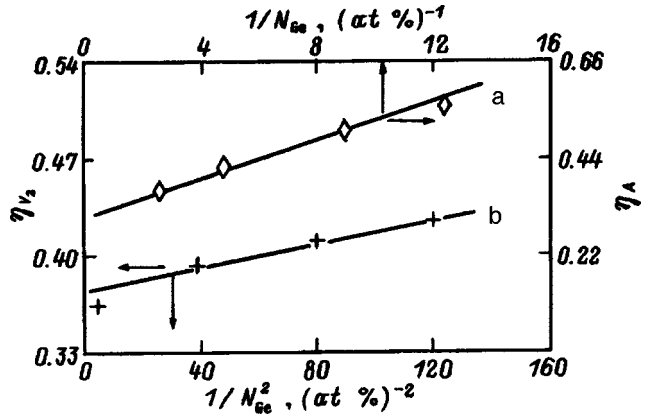

FIG. 2. Formation efficiency (η) of the A centers (a) and V_2 centers (b) in ⟨Ge⟩ plotted as a function of germanium concentration after electron irradiation at $T\leqslant 90$ K.

centers; χ_{ij} is the probability for the interaction of the i- and j-type centers; τ_I is the mean lifetime of the interstitial atoms relative to the remaining sinks, which are ignored in system (1); λ_1 is the rate of formation of Frenkel' pairs; and λ_2 is the rate of formation of primary divacancies.

Note that under low-temperature irradiation of Si and Si⟨Ge⟩ both reoriented (V_2) and unreoriented (V_2I) divacancies (whose infrared absorption bands coincide) are efficiently formed. The equation for the V_2 centers describes the variation of their total concentration (the probability $\chi^*_{V_2I}$ corresponds to process {e}, and the probability χ_{V_2I} corresponds to the sum of processes {e} and {h}).

The assumption advanced above about the germanium atoms as centers of indirect recombination of primary radiation defects allows us to make the following additional assumptions:

$$\chi_{GeV}N_{Ge}N_V \gg 2\chi_{VV}N_V^2, \quad \lambda_1 \gg \chi^*_{V_2I}N_{V_2}N_I. \tag{2}$$

Invoking the quasistationary assumption ($dN_I/dt=dN_V/dt=dN_g/dt=dN_A/dt=0$) and assumptions (2), we obtain the following expressions for the equilibrium concentrations of the secondary radiation defects under conditions of low-temperature ($T\leqslant 90$ K) irradiation:

$$N_g \approx \frac{\lambda_1}{2\lambda_2\tau_I\chi_{gI}}\frac{\chi_{GeV}N_{Ge}}{\chi_{GeV}N_{Ge}+\chi_{VO}N_O}, \tag{3}$$

$$N_A \approx \frac{\lambda_1}{2\lambda_2\tau_I\chi_{AI}}\frac{\chi_{VO}N_O}{\chi_{GeV}N_{Ge}+\chi_{VO}N_O}, \tag{4}$$

$$N_{V_2} \approx \frac{1}{2\tau_I\chi_{V_2I}}\left\{1+\frac{\chi_{VV}}{\lambda_2}\frac{\lambda_1^2}{(\chi_{GeV}N_{Ge}+\chi_{VO}N_O)^2}\right\}. \tag{5}$$

To elucidate the dependence of the efficiencies (η) of secondary radiation defect formation in Si⟨Ge⟩ on the germanium concentration, it is necessary to compare the corresponding quantities in Si and Si⟨Ge⟩. Let $\eta_{V_2}=N_{V_2}(N_{Ge})/N_{V_2}(0)$ be the relative formation efficiency of the divacancies in Si⟨Ge⟩ (the ratio of divacancy concentrations in Si⟨Ge⟩ and Si at temperatures $T\leqslant 90$ K). Using Eq. (5) and assuming that the reaction probabilities χ_{ij} between the i and j centers, and also the rates of primary radiation defect generation λ_1 and λ_2, are identical in Si and Si⟨Ge⟩, we can write the relative efficiency of divacancy formation in Si⟨Ge⟩ in the form

$$\eta_{V_2} \approx \left(1+\frac{\chi_{VV}}{\lambda_2}\frac{\lambda_1^2}{\chi_{VO}^2N_O^2}\right)^{-1} + \left(1+\frac{\chi_{VV}}{\lambda_2}\frac{\lambda_1^2}{(\chi_{GeV}N_{Ge}+\chi_{VO}N_O)^2}\right). \tag{6}$$

To write the analogous expression for the A centers, we must take into account the fact that the concentration of the A centers for $T\leqslant 90$ K is insignificant and that the process of their formation is completed at $T\geqslant 280$ K. The concentration of the A centers at temperatures $T\geqslant 280$ K is equal to the sum of the concentration of the A centers formed at $T\leqslant 90$ K and the concentration of the A centers formed during annealing of the GeV centers ($T\geqslant 250$ K). Since the main sink for vacancies during annealing of the GeV centers is oxygen, we can represent the concentration of the A centers formed during annealing of the GeV centers in the form

$$N_A=\beta\cdot N_g, \tag{7}$$

where β is a proportionality factor ($\beta\leqslant 1$) which allows for capture of vacancies by other sinks besides oxygen atoms during annealing of GeV centers, and N_g is given by expression (3). Thus, the quantity $\eta_A=N_A(N_{Ge})/N_A(0)$, the relative formation efficiency of the A centers in Si⟨Ge⟩ at $T\geqslant 280$ K, can be represented by the expression

$$\eta_A \approx \beta\frac{\chi_{AI}}{\chi_{gI}}+\left(1-\beta\frac{\chi_{AI}}{\chi_{gI}}\right)\frac{\chi_{VO}N_O}{\chi_{GeV}N_{Ge}+\chi_{VO}N_O}. \tag{8}$$

Analysis of expressions (6) and (8) shows that the relative formation efficiency of the A and V_2 centers in Si⟨Ge⟩ decreases with growth of the germanium concentration: $\eta_A \propto 1/N_{\mathrm{Ge}}$ and $\eta_{V_2} \propto 1/N_{\mathrm{Ge}}^2$ for $\chi_{\mathrm{Ge}V} N_{\mathrm{Ge}} \gg \chi_{V\mathrm{O}} N_{\mathrm{O}}$.

Figure 2 compares the experimental and theoretical dependences of the relative formation efficiency of the main secondary radiation defects in Si⟨Ge⟩. As can be seen from the figure, the experimental dependences of the relative formation efficiencies of the A centers and divacancies on the germanium concentration demonstrate satisfactory agreement with the corresponding theoretical dependences under the assumption that the germanium atoms are centers of indirect recombination of primary radiation defects.

[1] A. A. Bugaĭ, V. M. Maksimenko, B. M. Turovskiĭ, L. I. Khirunenko, V. I. Shakhovtsov, and N. I. Gorbacheva, Fiz. Tekh. Poluprovodn. **18**, 2020 (1984) [Sov. Phys. Semicond. **18**, 1260 (1984)].
[2] I. G. Atabaev, M. S. Saidov, L. I. Khirunenko, V. I. Shakhovtsov, V. K. Shinkarenko, L. I. Shpinar, and A. Yusupov, Fiz. Tekh. Poluprovodn. **21**, 570 (1987) [Sov. Phys. Semicond. **21**, 350 (1987)].
[3] L. I. Khirunenko, V. I. Shakhovtsov, V. K. Shinkarenko, L. I. Shpinar, and I. I. Yakovlets, Fiz. Tekh. Poluprovodn. **21**, 562 (1987) [Sov. Phys. Semicond. **21**, 345 (1987)].

Translated by Paul F. Schippnick

Diffusion doping of undoped hydrogenated amorphous silicon with tin

G. S. Kulikov and K. Kh. Khodzhaev

A. F. Ioffe Physicotechnical Institute, Russian Academy of Sciences, 194021 St. Petersburg, Russia
(Submitted June 14, 1997; accepted for publication July 15, 1997)
Fiz. Tekh. Poluprovodn. **32**, 135–136 (February 1998)

The solubility of tin in undoped, hydrogenated, amorphous silicon is determined by diffusion-doping films of this material with the radioactive isotope ^{119m}Sn. The temperature dependence of the tin solubility is described by the relation $S[\mathrm{cm}^{-3}]=4\times10^{22}\exp(-0.46/kT[\mathrm{eV}])$. © *1998 American Institute of Physics.* [S1063-7826(98)00302-0]

Kodzhaev *et al.*[1] used the method of diffusion doping to determine the tin solubility in films of amorphous hydrated silicon (*a*-Si:H) doped with phosphorus during growth. In the present work we use this same method to determine the tin solubility in undoped films of *a*-Si:H.

The technology of film preparation and the diffusion process was the same as that described in Refs. 1–3. The films were grown on silicon substrates by decomposition of monosilane in a rf glow-discharge plasma. The film thickness was ~0.6 μm, and the oxygen content of the films was 13 at. %. A layer of the radioactive isotope ^{119m}Sn sputtered in vacuum on the film surface served as the tin source. The diffusion doping time was varied from 20 min to 20 h, and the temperature, from 350 to 500 °C. The tin concentration profiles were determined by layer-by-layer radioactive analysis.[1–3] As in the doped films, they consisted of three segments (Fig. 1): skin layer region, a bulk region, and a transitional region (at the film–substrate boundary). In the skin layer and transitional region the concentration was found to rise toward the boundary of the film due to the decreased oxygen content in these regions;[4] in the bulk region the tin is distributed uniformly. We took the concentration level in the region of uniform distribution as the solubility.

As follows from the results shown in Fig. 2, the tin solubility grows as the temperature is raised and its temperature dependence is given by

$$S[\mathrm{cm}^{-3}]=4\times10^{22}\exp(-0.46/kT[\mathrm{eV}]).$$

Comparison of these results with the data of Ref. 1 shows that phosphorus doping lowers the solubility of tin in *a*-Si:H. This effect, in our view, is attributable to the fact that phosphorus atoms, by attaching themselves to the dangling bonds in the amorphous network, reduce the number of sites the tin atoms can occupy. For the same reason, phosphorus doping also lowers the tin diffusion rate in *a*-Si:H films.[3]

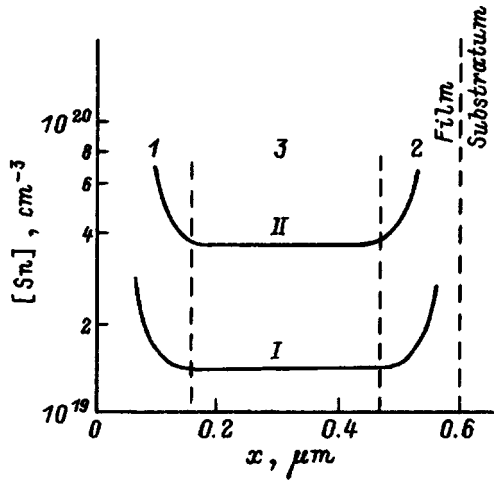

FIG. 1. Typical tin concentration profiles in diffusion-doped *a*-Si:H films in the depth *x*. *1*—near-surface region, *2*—transitional, *3*—bulk. Diffusion temperature *T*, °C: *I*—400, *II*—500; t_1: *I*—90, *II*—20.

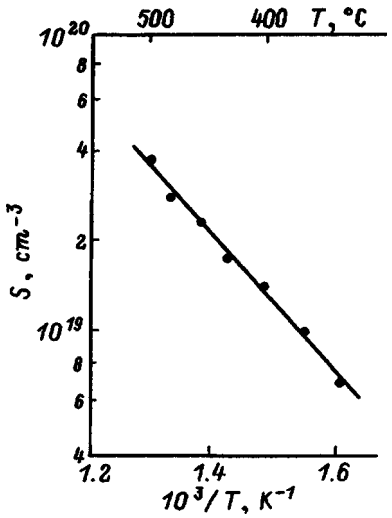

FIG. 2. Temperature dependence of the tin solubility in undoped *a*-Si:H films.

[1] K. Kh. Khodzhaev, K. P. Abdurakhmanov, Yu. Ya. Amirov, G. S. Kulikov, E. I. Terukov, and D. P. Utkin-Édin, Fiz. Tekh. Poluprovodn. **19**, 2219 (1985) [Sov. Phys. Semicond. **19**, 1369 (1985)].
[2] K. Kh. Khodzhaev, K. P. Abdurakhmanov, Yu. Ya. Amirov, V. A. Didik, G. S. Kulikov, E. I. Terukov, and D. P. Utkin-Édin, Fiz. Tekh. Poluprovodn. **19**, 1182 (1985) [Sov. Phys. Semicond. **19**, 725 (1985)].
[3] G. S. Kulikov and K. Kh. Khodzhaev, Fiz. Tekh. Poluprovodn. **29**, 961 (1995) [Semiconductors **29**, 498 (1995)].
[4] V. Kh. Kudoyarova, G. S. Kulikov, and K. Kh. Khodzhaev, *Proceedings of the Fifth International School on Condensed Matter Physics ''Disordered Systems and New Materials''*, Varna, Bulgaria, September 19–27, 1988 (World Scientific, Singapore, 1988), p. 640.

Translated by Paul F. Schippnick

Ultrashallow p^+-n junctions in silicon (100): electron-beam diagnostics of the surface zone

A. N. Andronov and S. V. Robozerov

St. Petersburg State Technical University, 195251 St. Petersburg, Russia

N. T. Bagraev and L. E. Klyachkin

A. F. Ioffe Physicotechnical Institute, Russian Academy of Sciences, 194021 St. Petersburg, Russia
(Submitted February 19, 1997; accepted for publication April 22, 1997)
Fiz. Tekh. Poluprovodn. **32**, 137–144 (February 1998)

Ultrashallow p^+-n junctions formed in silicon (100) under nonequilibrium impurity diffusion conditions are analyzed by electron-beam diagnostics of the surface zone using a probe of low- to medium-energy electrons. The energy dependence of the radiation conductivity is investigated, along with its distribution over the area of the p^+-n junction. This procedure can be used to determine the depth distribution (in the crystal) of the probability of separation of electron-hole pairs by the field of the p-n junction; the experimental results show that this distribution differs according to whether the kick-out mechanism or the dissociative vacancy mechanism of impurity diffusion is predominant as the basis of formation of the ultrashallow p^+-n junctions. Also reported here for the first time are the results of investigations of the distribution of secondary point centers formed near the boundary of the ultrashallow diffusion profile, which exert a major influence on the transport of nonequilibrium carriers. The data obtained in the study demonstrate the possibility of improving the efficiency of photodetectors, α-particle detectors, and solar batteries constructed on the basis of ultrashallow $p-n$ junctions. © *1998 American Institute of Physics.* [S1063-7826(98)00201-4]

1. INTRODUCTION

Recently it has been shown experimentally that ultrashallow (to 10 nm) doping profiles with a sharp boundary can be obtained in silicon single crystals by in-plane diffusion technology making use of the entrainment of impurity levels by excess fluxes of vacancies or native interstitial atoms generated by a silicon-oxide interface.[1–4] The doping level and the spatial distribution of the injected impurity in such profiles depend on which nonequilibrium diffusion mechanism—kick-out or the dissociative vacancy mechanism[4–6]—is predominant, and they are determined primarily by the diffusion temperature and the thickness of the initial oxide.[3] Here we discuss the results of an experimental study of the influence of these factors on the properties of the resulting structures in the example of surface quantum-well p^+-n junctions in silicon (100). Our choice of working method is to probe the surface zone by low- to medium-energy electrons[7] as a means of determining the depth distribution (in the crystal) of the probability of separation of electron-hole pairs by the field of the p^+-n junction.

2. PREPARATION OF ULTRATHIN p^+-n JUNCTIONS IN SILICON

The basic materials used in preparing the p^+-n junctions were single-crystalline n-type silicon (100) wafers of thickness 350 μm with resistivities of 1.0 $\Omega\cdot$cm, 5.0 $\Omega\cdot$cm, 20 $\Omega\cdot$cm, or 500 $\Omega\cdot$cm. In the initial stage of the process both sides of the wafer were oxidized in dry oxygen at 1150 °C. Windows of a desired geometry were then exposed in the oxide layer on the working side by photolithography, and p^+-n junctions were formed in the windows by the diffusion of boron from the gaseous phase after short time intervals (4 min). The diffusion temperature was varied during the investigations (800 °C, 900 °C, and 1100 °C), and so was the thickness of the surface oxide, in such a way as to facilitate simulation of the conditions of the kick-out[3,5,6] and dissociative vacancy[3,5] impurity diffusion mechanisms, which were induced by excess fluxes of native interstitial atoms and vacancies, respectively. The generation of primary defects responsible for the entrainment and drag of diffusing impurity atoms was maintained at a high level during diffusion by saturating the boron-containing gaseous phase with additional dry oxygen and chlorides. The technological cycle was terminated with the formation of ohmic contacts around the perimeter of the windows and on the opposite face of the wafer. The doping profiles were measured by secondary-ion mass spectrometry (SIMS).[3,8]

3. ELECTRON-BEAM DIAGNOSTICS OF THE SURFACE LAYERS OF SILICON SINGLE CRYSTALS

To compare the properties of the surface zones of different samples, we measured the radiation conductivity excited in this zone by a focused electron beam, varying its energy E_p in the interval from 0.1 keV to 3.0 keV so as to smoothly vary the probing depth from 2 nm to 250 nm (Ref. 7). To separate the induced current from the dark current, we performed these measurements with sinusoidal modulation of the primary electron flux at a frequency of 1 kHz. Control tests using direct current confirmed that a steady-state radiation conductivity γ is well established at such frequencies. The computer-controlled electron beam scanned the target surface, permitting the radiation conductivity coefficient γ to

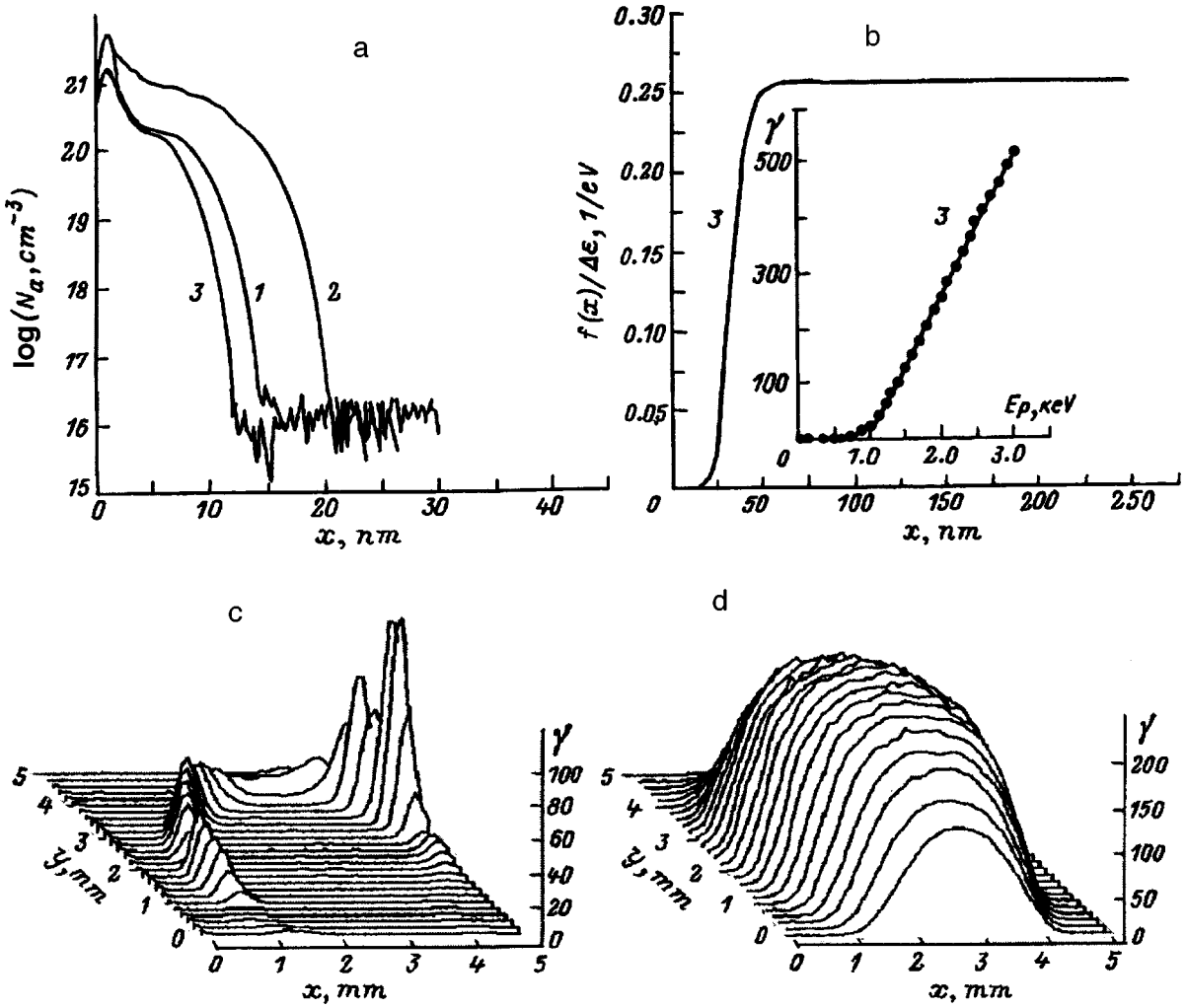

FIG. 1. Depth (x) distributions of the boron concentration N_a (a) and the collection function $f(x)$ (b) in structures prepared at $T_{\text{diff}}=800\,^{\circ}\text{C}$, and examples of distributions of the radiation conductivity coefficient γ at $E_p=1800$ eV over the surface of the same structures (c, d, respectively). Inset (b): one of the experimental $\gamma(E_p)$ curves. *1)* $d_{\text{SiO}_2}/d_0=0.31$; *2)* 1.0; *3)* 1.28; c) 0.31; d) 1.28. Substrate resistivity: *1)* 20.0 $\Omega\cdot$cm; *2)* 1.0 $\Omega\cdot$cm; *3)* 500 $\Omega\cdot$cm.

be measured at uniformly spaced points, so that images of this surface could be obtained in excited electrons at various energies E_p. In the case of area-inhomogeneous samples the set of raster images enabled us to pick out a working zone on the sample surface and to plot the experimental $\gamma(E_p)$ curve for it. This curve, which is related to the spectral characteristic of the photoconductivity in a reverse-biased $p-n$ junction,[9] can be described by the integral equation

$$\gamma(E_p)=\int_0^{\infty}\frac{g(E_p,x)}{\Delta\varepsilon}f(x)dx, \tag{1}$$

where $g(E_p,x)$ is the one-dimensional distribution function of the specific energy losses by primary electrons with respect to the depth x in the silicon, $\Delta\varepsilon$ is the average energy spent in the formation of one electron-hole pair, and $f(x)$ is the carrier collection function of the $p-n$ junction[7,9]; this represents the fraction of electron-hole pairs, excited at a given depth x, that are separated by the field and contribute to the current in the external circuit.

Figure 1b shows an example of the $\gamma(E_p)$ curve for one of the samples (see inset) and the form of the carrier collection function reconstructed on the basis of this curve. The collection function, which is global parameter of the $p-n$ junction by definition and which completely determines its response to external ionizing radiation, depends on the conditions of transport and recombination of the excited carriers. In our case nonequilibrium carriers are generated for the most part directly in the charge zone of the $p-n$ junction. The behavior of $f(x)$ in this zone reflects the probability of the separation of electron-hole pairs by the field of the $p-n$ junction. This probability is determined primarily by the nonequilibrium carrier lifetime and the distribution of the electric field.

4. CHARACTERISTICS OF THE ULTRASHALLOW DIFFUSION PROFILES OF BORON IN SINGLE-CRYSTALLINE *n*-TYPE SILICON (100)

Figures 1–3 show the main results for samples formed at various diffusion temperatures T_{diff} and thicknesses of the oxide layer (d_{SiO_2}). At $T_{\text{diff}}=800\,^{\circ}\text{C}$ diffusion takes place primarily by the dissociative vacancy mechanism, whereby boron atoms are entrained by excess fluxes of vacancies. When diffusion takes place at $T_{\text{diff}}=1100\,^{\circ}\text{C}$, the kick-out

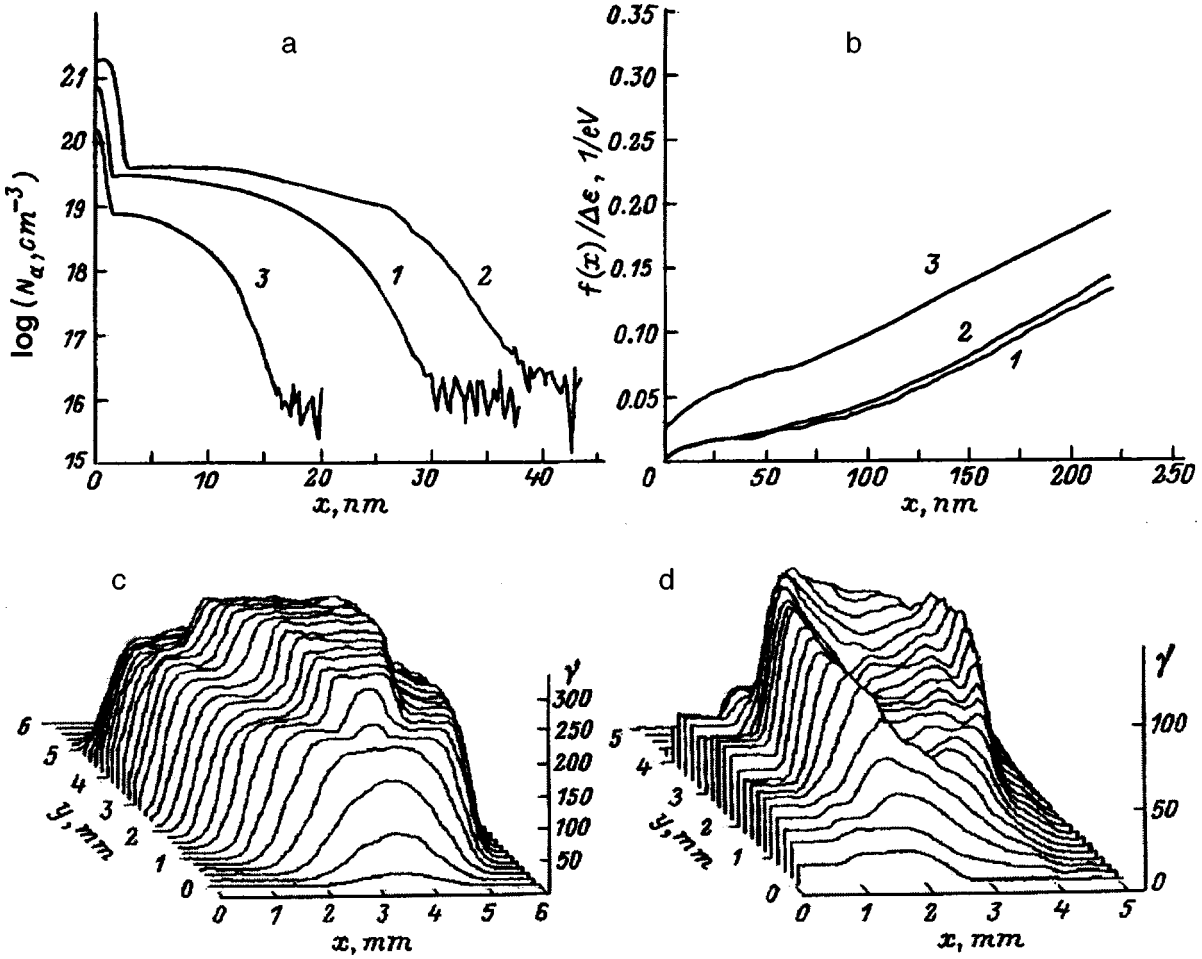

FIG. 2. Profiles of the boron concentration N_a (a) and the collection function $f(x)$ (b) in the case $T_{\text{diff}}=1100$ °C; c, d) raster images of the surfaces of samples prepared at this temperature in excited electrons at $E_p=1400$ eV. *1)* $d_{\text{SiO}_2}/d_0=0.31$; *2)* 1.0; *3)* 1.28; c) 1.28; d) 0.31. Substrate resistivity: *1)* 500 Ω·cm; *2)* 5.0 Ω·cm; *3)* 500 Ω·cm.

mechanism plays the dominant role. In this case impurity atoms diffuse by virtue of strong exchange interaction with native interstitial silicon atoms. Finally, at intermediate temperatures ($T_{\text{diff}}=900$ °C) both diffusion mechanisms contribute about equally, where the rate of movement of the diffusion front becomes a minimum under such parity conditions. It is evident from the figures that the effects of entrainment of impurity atoms by excess fluxes of native defects, given short diffusion times, causes the shape of the profile to depart substantially from that observed in classical diffusion. Moreover, in every case the diffusion rate depends very strongly on the thickness of the SiO_2 oxide layer previously deposited on the working and opposite (backside) faces of the silicon wafer, because this thickness determines which is the dominant type of excess defects. For sufficiently small values of d_{SiO_2} a predominant generation of interstitial atoms is stimulated at the Si/SiO_2 interface, whereas for large thicknesses mainly vacancies are generated.[1–4] In the figure captions the thicknesses of the oxide layer are given in relative units obtained by normalization to the thickness d_0 at which a change takes place in the type of native defects generated by the oxide surface. If $d_{\text{SiO}_2}/d_0=1$, the backside of the silicon substrate essentially has no influence on the diffusion process at any temperature, because it is a center of annihilation of vacancies and interstitial atoms generated in equal measure on its surface.

Doping with prevalence of the dissociative vacancy diffusion mechanism (Fig. 1) facilitates the penetration of boron to the lattice sites and can yield the highest impurity concentration inside the diffusion profile.[3,5,10] If the thickness of the predeposited oxide is greater than d_0 and if vacancy generation prevails at the Si/SiO_2 interface, the temperature and the oxide thickness are both favorable to the propagation of diffusion, and the $p-n$ junction is formed uniformly over the entire area of the exposed window (Fig. 1d). The diffusion rate in this case is determined by the drag effect of the oncoming flux of vacancies from the opposite side of the silicon wafer. As a result, the vacancy concentration gradient from the working side of the wafer becomes minimal, and the depth of the diffusion profile does not exceed 15 nm (Fig. 1a, profile *3*). Moreover, the interaction of the opposing fluxes results in the rapid formation of divacancies and more complex vacancy clusters,[11–13] which automatically lowers the concentration of solitary vacancies and, accordingly, is manifested in a reduction of the boron concentration inside the diffusion profile (Fig. 1a, profile *3*). The vacancy clusters

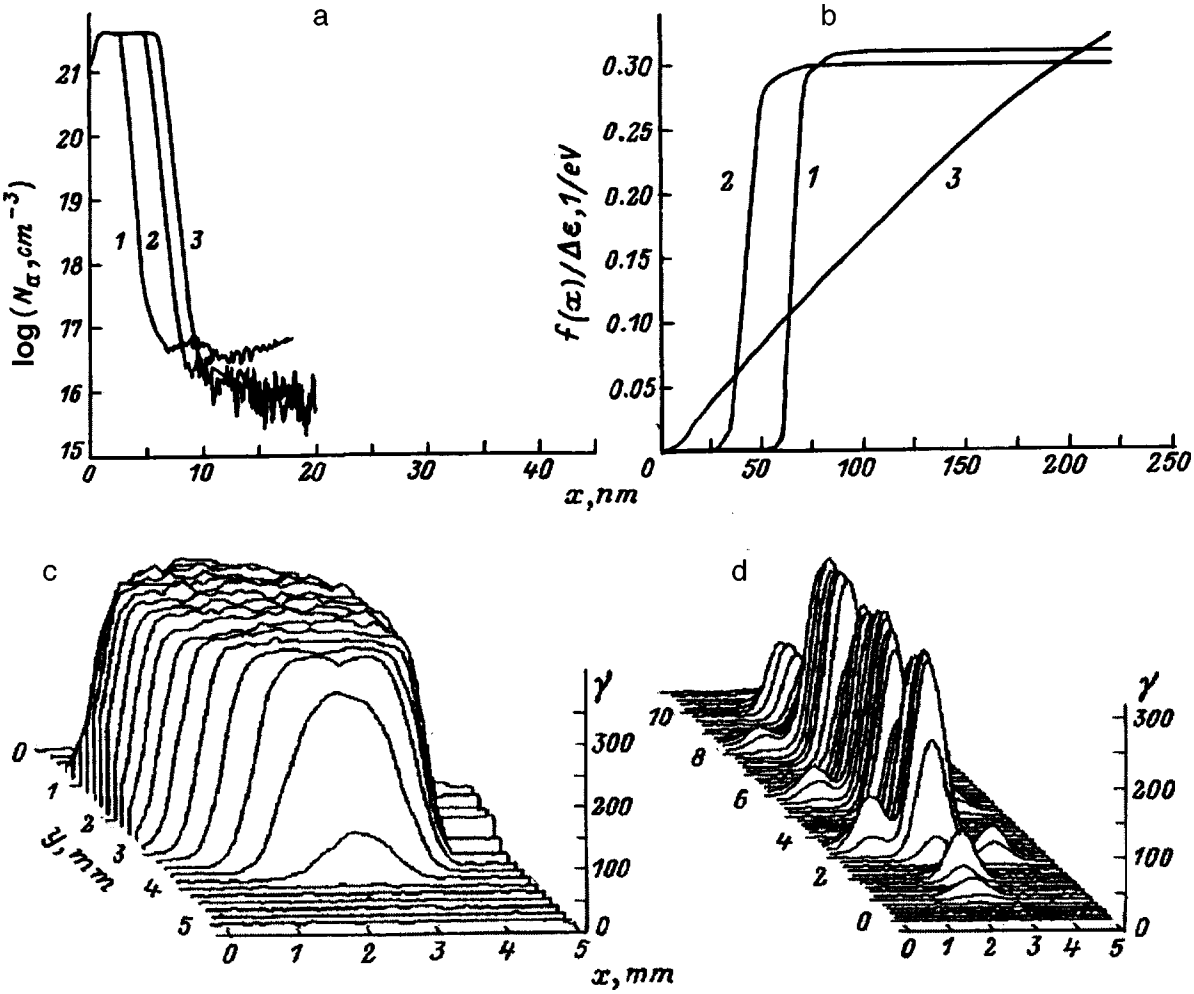

FIG. 3. Profiles of the boron concentration N_a (a) and the collection function $f(x)$ (b) in structures prepared at $T_{\text{diff}}=900$ °C; (c, d) raster images of the surfaces of the same samples in excited electrons at $E_p=1600$ eV; in case (d) the sample has the standard Hall effect geometry. *1*) $d_{\text{SiO}_2}/d_0=0.31$; *2*) 1.0; *3*) 1.28; c) 1.0; d) 1.28. Substrate resistivity: *1*) 500 Ω·cm; *2*) 1.0 Ω·cm; *3*) 20.0 Ω·cm.

stabilize near the boundary of the diffusion profile during the rapid cooldown of the p^+-n junctions from 800 °C to room temperature. The latter event is also conducive to the rapid departure of equilibrium interstitial silicon atoms from the region of the diffusion window as a result of the onset of low-temperature gettering conditions due to the generation of excess vacancies.[14,15] All these factors impart a characteristic step profile to the collection function $f(x)$ calculated from the experimental $\gamma(E_p)$ curve for such structures (Fig. 1b), confirming the existence in the surface zone of a ''dead layer'' extending as deep as 25 nm, in which excited electron-hole pairs do not participate in the generation of the radiation conduction current, either on account of the extremely short lifetime or because of a potential barrier due to vacancy defects.[7]

For a thin initial oxide layer at the same temperature the conditions for diffusion become unfavorable, because excess fluxes of interstitial atoms drastically reduce the steady-state vacancy concentration near the diffusion front. Consequently, even comparatively slight fluctuations of this concentration induced by various random factors can significantly affect the course of diffusion. In particular, for an exposed window of sufficiently large area the differences in the conditions of generation and annihilation of excess native defects generally produces an appreciable difference between the concentration profiles recorded at the center of the window and near its edge. As an example, Figure 1a shows one such profile (profile *1*) obtained in the immediate vicinity of the boundary of the window. The high boron content confirms the fact that, despite the significantly lower vacancy concentration than in the preceding case, diffusion is still driven by the dissociative vacancy mechanism, and its rate is even somewhat higher than for a thick oxide layer. The latter consideration is more likely attributable to the fact that the oncoming flux of vacancies from the opposite face exerts more drag on the diffusion flow than such a flux of interstitial atoms, since the (100) direction in silicon is the one most favorable to vacancy motion, whereas for native interstitial atoms this role is taken by (111) (Refs. 5 and 16).

The electron-beam scanning of such structures has shown that over the entire energy range from 0.1 keV to 3.5 keV the excited conduction current occurs only around the perimeter of the window, exhibiting an extremely nonuniform spatial distribution (Fig. 1c). In this light, there is little reason to enter into a detailed discussion of the experimental $\gamma(E_p)$ curves for different parts of the sample, rather

it will suffice to consider only the main qualitative conclusions of the reported measurements. First and foremost, in contrast with the preceding case, an energy threshold for the onset of radiation conduction is not detected anywhere on the part of the surface where it is observed; i.e., the above-mentioned ''dead layer'' does not exist. In addition, at high energies the values of the coefficient γ for any part of the surface is significantly lower than for a thick-oxide sample, and everywhere on the central part of the sample the radiation conductivity coefficient remains equal to zero, even when the probing depth is increased to 250 nm. All this indicates a high concentration of residual defects, but they do not accumulate near the sharp boundary of the diffusion profile as in the case of vacancy clusters and are instead distributed over a large depth. The nature and spatial distribution of such defects are dictated by the fact that under conditions favoring the predominant degeneration of interstitial atoms at the Si/SiO_2 interface, the low-temperature gettering processes proceed extremely slowly and, at the same time, there is a very high probability of formation of stable clusters, or so-called reconstructed interstices,[11,13] which differ from amphoteric vacancy complexes in that they are double donors and exert a much stronger influence on the lifetime of nonequilibrium carriers. The highest concentration of these ''killer'' defects, which severely lower the nonequilibrium carrier concentration, is formed in the region of the exposed diffusion window, where the diffusion conditions are rendered least favorable by strong suppression of the flux of vacancies generated by the silicon/oxides interface around the perimeter of the window. The role of the thin, backside, oxide layer, which generates native interstitial atoms that penetrate the region of the working surface at the center of the diffusion window, is strengthened in this case. The given process is responsible for the formation of the above-described double donors, which has the twofold effect of shortening the nonequilibrium carrier lifetime and heavily compensating the doping acceptor impurity with the accompanying emergence of semiinsulating *i*-layers in the center of the diffusion window.

In many respects, similar behavior is exhibited by samples prepared at $T_{\text{diff}}=800\ ^\circ\text{C}$ with medium thicknesses of the initial oxide ($d_{SiO_2}=d_0$). SIMS analysis data (Fig. 1a, profile *2*) show that diffusion is driven by the vacancy mechanism in this case and, as should be expected, the deepest doping profile of the dopant for the given temperature is formed without the drag exerted by oncoming fluxes of defects from one direction. The raster patterns of the distribution of the excited conductivity over the area of these structures have the same character as in the preceding case (Fig. 1c) and can be explained from the same principles, the only difference being that the role of the backside in the formation of ''killer'' defects is now diminished. The main causes of the observed strong inhomogeneity are, as before, the rapid formation of stable defects on the basis of reconstructed native interstices and the insufficient concentration of vacancies, whose spatial distribution is subjected to the influence of various random factors and is minimized at the center of the diffusion window as its dimensions increase.

We now turn to the results obtained for samples prepared at high temperature (Fig. 2). It is evident from the concentration profiles in Fig. 2a that the average dopant concentrations in them are an order of magnitude lower than for structures with vacancy-type impurity diffusion (Fig. 1a). The behavior of the depth of the profile as a function of the oxide thickness is identical at high and low temperatures, and its causes have already been discussed. All other conditions being equal, the depth of the high-temperature diffusion profiles is naturally greater than at low temperatures, but the change of diffusion mechanism makes the difference between them less than might be expected.

The rate of movement of the diffusion front under the kick-out mechanism is determined by the diffusion coefficient, which depends on the temperature and the concentration gradient of excess interstitial atoms at the working surface and also on the total number density of such atoms.[3] When oxide is present on both sides of the wafer, the most favorable conditions for kick-out diffusion are encountered when the SiO_2 thicknesses are small (high concentrations) and medium (maximum gradient). Electron-beam probing of the structures prepared under such conditions has shown (Figs. 1 and 2b, curves *1* and *2*) that the form of the collection function, which reflects the depth distribution of electrically active defects, is very close for the two cases in question. As in the low-temperature case, such structures are characterized by the absence of a dead layer and comparatively low values of the collection function, even at the maximum probing depth. This result is a consequence of the formation of gettering microdefects during oxidation, since the interface between the thin oxide layer and silicon is a source of native interstitial atoms, whose clusters represent powerful centers for the trapping of native point defects in all subsequent heat treatments.[14,17] The form of the distribution of gettering microdefects in the bulk changes according to whether only the working face or both faces of the wafer are oxidized.[14] In every case, nonetheless, these microdefects vigorously trap native interstitial atoms during impurity diffusion, thereby preventing their accumulation near the boundary of the diffusion profile and, hence, the formation of a dead layer.

Raster patterns of the distribution of the excited conductivity over the area of such structures, obtained for various energies of the primary beam, can be used to estimate the distribution of these defects in the transverse direction as well. Figure 2d shows an example of such an image for a sample with $d_{SiO_2}/d_0=0.31$, obtained at a primary electron energy $E_p=1400$ eV. The reduction of the radiation conductivity toward the center is typical of such samples and is attributable to the fact that the generation of interstices capable of driving the nonequilibrium diffusion of boron takes place mainly at the boundary of the exposed window. Despite the greatly accelerated penetration of the pair {boron atom-interstice} into the crystal at high temperature, the lower mobility of the native interstitial atom in the crystallographic (100) direction relative to vacancies makes it impossible for a uniform diffusion front to be established over the entire area of the $p-n$ junction during the short diffusion time.

The situation changes when the $p-n$ junction is formed

at high temperature with an initially thick oxide layer. In this case the temperature imparts an interstitial character to the diffusion process, and the generation of vacancies is prevalent at the Si/SiO_2 interface. The excess vacancy fluxes lower the density of native interstitial atoms in the surface zone and, as a result, decrease the rate of formation of the unwanted defects responsible for shortening the nonequilibrium carrier lifetime.[4,14] This process increases the collection function considerably, but does not radically alter its depth distribution (Fig. 2b). A graphic illustration of the combined action of vacancies and interstices in this case is the change in the form of the raster images of the surface of the structure (Fig. 2c). The uniform suppression of the excited conduction current near the boundary of the exposed window is attributable to the rapid annihilation of vacancies continuously generated by the boundary and of native interstitial atoms, which further slows diffusion. The dimensions of the indicated region depends on the average vacancy diffusion length, which is much shorter at $T_{\text{diff}}=1110\,^{\circ}\text{C}$ than at low temperatures, in particular, because of the change in the charge state of the vacancies.[3,5,6]

A special case is the formation of $p-n$ junctions under conditions close to parity of the kick-out and dissociative vacancy diffusion mechanisms (Fig. 3), when the dopant can be entrained with equal probability by excess fluxes of vacancies and interstitial atoms. The competition between these processes decreases the total diffusion, so that for any oxide thickness the resulting, very shallow (to 10 nm) diffusion profiles have a sharp boundary and a high doping level (Fig. 3a), which is maintained by the involvement of the vacancy mechanism. Moreover, in the course of diffusion at a reduced rate there is time for steady-state conditions to be established over the entire area of the resulting $p-n$ junction, even at a low concentration of nonequilibrium vacancies. This situation makes it possible to obtain structures with a surface distribution of properties that is uniform and independent of the shape of the window. As an example, Figs. 3c and 3d show raster images of samples prepared with various oxide thicknesses and window geometries.

The results of electron-beam probing of the structures prepared at this temperature (Fig. 3b) show that the differences in the thicknesses of the predeposited oxide layer are manifested primarily in the spatial distribution of residual defects in the surface zone. If the generation of excess vacancies is predominant in diffusion on the oxidized surface, the collection function increases monotonically from zero at the surface itself to values close to unity at a depth of 250 nm (Fig. 3b, curve *3*). A comparison with data obtained for samples with the same oxide at different temperatures (Figs. 1b and 2b) indicates that the concentration of secondary vacancy defects near the boundary of the diffusion profile decreases as the temperature is raised, but these defects are distributed over an ever-greater depth as a result of the trapping of vacancies by gettering microdefects. This phenomenon reflects the influence of temperature on gettering and cluster-forming processes in the presence of excess vacancy fluxes.[10–12,14,15]

In the opposite case of samples having a thin, preliminary deposited oxide layer ($d_{SiO_2}/d_0=0.31$) at the same temperature (900 °C) the diffusion flux of boron impurity atoms is preceded by a slowly moving front of excess point defects dominated by interstitial atoms. The interaction of these defects leads to the formation of numerous stable clusters consisting of interconnected reconstructable interstices and very small vacancy clusters,[11,12,15] which are ''frozen into'' a surface layer having a fairly sharp boundary upon termination of the diffusion process. This behavior is indicated by the previously discussed stepped character of the collection function (Fig. 3b, curve *1*). The shallowest diffusion profile can be obtained under the given conditions (Fig. 3a), but the defect-induced dead layer has the maximum thickness in this case (~ 60 nm). Essentially all the nonequilibrium carriers excited within the boundaries of this layer participate in the induced current (Fig. 3b), indicating that the bulk interior is effectively purged of buried point defects localized near gettering microdefects.

Similar processes also take place at this temperature during nonequilibrium diffusion in samples with an intermediate oxide thickness, except that now the flux of point defects near the working surface contains approximately the same number of interstitial atoms and vacancies. As a result of their particle recombination, the rate of formation of residual defects is greatly reduced, significantly decreasing the thickness of the dead layer (Fig. 3b, curve *2*). Here the values of the collection function in the bulk are somewhat lower than in the preceding case, owing to the additional trapping of native interstitial atoms and vacancies by getters, and the interstitial atom lifetime is shortened as a result. However, these differences are slight. Consequently, this technological regime is the one that will ensure the highest efficiency of crystal photodetectors, α-particle detectors, and solar batteries constructed from such structures.[4]

5. CONCLUSIONS

In summary, our study has enabled us to further identify the mechanisms of nonequilibrium boron diffusion in silicon (100) during the generation of native interstitial atoms and vacancies at the silicon/oxides interface and also to determine the influence of these mechanisms on the formation near the boundary of a $p-n$ junction of secondary point centers, which significantly influence interstitial atom transport processes.

This work has received partial support from the Soros International Science Foundation (Project NTX300 for 1995) and the State Committee of the Russian Federation on Higher Education (Grant 5-88 for Research in Electronics and Radio Engineering in 1996).

[1] N. T. Bagraev, L. E. Klyachkin, and V. L. Sukhanov, Pis'ma Zh. Tekh. Fiz. **17**(2), 42 (1991) [Sov. Tech. Phys. Lett. **17**, 55 (1991)].
[2] N. T. Bagraev, L. E. Klyachkin, and V. L. Sukhanov, Semicond. Sci. Technol. **6**, 577 (1991).
[3] N. T. Bagraev, L. E. Klyachkin, and V. L. Sukhanov, Defect Diffus. Forum **103–105**, 192 (1993).
[4] N. T. Bagraev, L. E. Klyachkin, A. M. Malyarenko, and V. L. Sukhanov, Solid-State Electron. **34**, 1149 (1991).
[5] W. Frank, U. Gösele, H. Mehrer, and A. Seeger, *Diffusion in Crystalline Solids* (Academic Press, New York, 1984), p. 63.
[6] R. B. Fair, Diffus. Defect Data **37**, 1 (1984).

[7] A. N. Andronov, N. T. Bagraev, L. E. Klyachkin, S. V. Robozerov, and N. S. Faradzhev, Fiz. Tekh. Poluprovodn. **28**, 2049 (1994) [Semiconductors **28**, 1128 (1994)].
[8] N. T. Bagraev, L. E. Klyachkin, and E. I. Chaĭkina, JETP Lett. **58**, 598 (1993).
[9] E. N. Pyatyshev and D. V. Kuzichev, Izmer. Tekh. **9**, 3 (1991).
[10] E. Antoncik, J. Electrochem. Soc. **141**, 3593 (1994).
[11] N. T. Bagraev, I. S. Polovtsev, and K. Schmalz, Phys. Status Solidi A **113**, 233 (1989).
[12] K. Schmalz, F.-G. Kirscht, H. Klose, H. Richter, and K. Tittelbach-Helmrich, Phys. Status Solidi A **100**, 567 (1987).
[13] N. T. Bagraev, S. N. Gorin, V. V. Vysotskaya, and Yu. A. Sidorov, J. Phys. (France) **1**, 733 (1990).
[14] N. T. Bagraev, L. E. Klyachkin, A. M. Malyarenko, I. S. Polovtsev, and V. L. Sukhanov, Fiz. Tekh. Poluprovodn. **24**, 1557 (1990) [Sov. Phys. Semicond. **24**, 973 (1990)].
[15] R. M. Amal'skaya, N. T. Bagraev, L. E. Klyachkin, and V. L. Sukhanov, Fiz. Tekh. Poluprovodn. **26**, 1004 (1992) [Sov. Phys. Semicond. **26**, 562 (1992)].
[16] S. Mizho and H. Higuchi, Jpn. J. Appl. Phys. **20**, 739 (1981).
[17] W. K. Tice and T. Y. Tan, Appl. Phys. Lett. **28**, 564 (1976).

Translated by James S. Wood

Exciton characteristics of intercalated $TlGaSe_2$ single crystal

S. N. Mustafaeva, E. M. Kerimova, and N. Z. Gasanov

Institute of Physics, Academy of Sciences of Azerbaijan, 370143 Baku, Azerbaijan
(Submitted May 12, 1996; accepted for publication June 3, 1997)
Fiz. Tekh. Poluprovodn. **32**, 145–147 (February 1998)

It is shown that lithium-ion intercalation of $TlGaSe_2$ single crystal leads to a shift of the exciton peak associated with the direct edge toward longer wavelengths ($\Delta E = 15$ meV at 5 K). As a result, the temperature shift of the exciton peak in $TlGaSe_2$ ($\partial E^{ex}/\partial T$) decreases more than twofold in absolute value to -1.1×10^{-4} eV/K at $20 \lesssim T \lesssim 105$ K and -0.25×10^{-4} eV/K at $5 \lesssim T \lesssim 20$ K. Lithium-ion (Li^+) intercalation of $TlGaSe_2$ has almost no effect on the energy position of the exciton associated with indirect transitions. © *1998 American Institute of Physics.* [S1063-7826(98)00502-X]

One of the advantages of layered semiconductors is the possibility of their intercalation by various ions, atoms, and molecules, which leads to changes in the interlayer interaction and the degree of anisotropy of the properties of these semiconductors, and allows one to control their physical properties.[1]

The aim of the present paper is to examine the influence of lithium-ion intercalation on the exciton characteristics in layered single crystals of $TlGaSe_2$.

$TlGaSe_2$ single crystals were grown by the vertical Bridgman method.[1,2] The characteristics of the crystals prepared in this way were found to be in good agreement with the data in the literature.[3,4] The $TlGaSe_2$ crystals were bright-red in color and easily cleaved into wafers (thin plates) of varying thickness. The $TlGaSe_2$ single-crystal wafers were intercalated using the pulling electric field method.[5] This method has been successfully used to intercalate layered single crystals of GaSe with ions of various metals (Li, K, Na).[5,6] Using radioisotope analysis, we determined that the ions of these metals are well implanted in the spaces between the layers. $TlGaSe_2$ single crystals are ternary analogs of GaSe, and their intercalation was realized in an analogous way. As the intercalant we chose lithium ions (Li^+), which makes it possible to achieve efficient intercalation without damaging the $TlGaSe_2$ single crystal, because of the rather small ionic radius ($r = 0.68$ Å) of the lithium ion. A single crystal of $TlGaSe_2$ in the form of a rectangular parallelepiped, with a metallic (indium) electrode mounted on top, was placed in a glass cell with the intercalant (a 0.5-molar aqueous solution of LiCl) in such a way that the lower face of the $TlGaSe_2$ crystal, perpendicular to the layers, made contact with the surface of the LiCl solution. The cell contained a graphite electrode located under the lower face of the single-crystal sample. A constant voltage was applied to this system: minus—to the indium electrode soldered to the entire upper surface of the sample perpendicular to the layers, and plus—to the graphite electrode. In this setup the electric field was directed along the layers of the $TlGaSe_2$ crystal. Application of the electric field caused lithium ions from the LiCl solution to enter the interlayer spaces of the $TlGaSe_2$ single crystals. This arrangement generated a flow of electric current through the system ⟨graphite electrode/aqueous LiCl solution+$TlGaSe_2$ single crystal/metallic electrode⟩. The optimal intercalation regime was provided by current densities j and intercalation times t, for which the degree of intercalation jt was 15–20 C/cm^2 (Ref. 1). Results of a combined study of the electrical, photoelectric, and x-ray dosimetric characteristics of lithium-intercalated single crystals of $TlGaSe_2$ indicated[1] that intercalation increases the degree of anisotropy of the electrical, photoelectrical, and x-ray conductivity, and that this in turn is due to a change in the interlayer interaction brought about by the presence of lithium ions between the layers.

Studies of the exciton spectra of $TlGaSe_2$ samples were performed on a special setup for combined studies of the optical and photoelectric spectra of semiconducting crystals by modulation spectroscopy. The setup is based on the universal spectral calculational complex KSVU-6M, which makes it possible to automate the recording and mathematical processing of the spectra. A wide temperature range of the measurements was achieved with the help of an optical helium cryostat of the type UTREKS with a temperature stabilization system (the stabilization accuracy was 0.02 K). Optical measurements were performed in the temperature range 5–120 K.

We distinguished both a high- and a low-energy exciton band in the absorption spectra of $TlGaSe_2$ single crystals. The high-energy absorption peak is due to an exciton associated with the direct band gap, and the low-energy peak is due to an exciton associated with the indirect band gap.

Figure 1 plots absorption spectra of $TlGaSe_2\langle Li^+\rangle$ single crystal at different temperatures. In these spectra the light was directed perpendicular to the cleavage plane of the single crystal; the thickness of the $TlGaSe_2\langle Li^+\rangle$ sample was $L = 18$ μm. At all temperatures the high-energy exciton absorption band, whose maximum shifts toward higher energies as the temperature is lowered from 105 to 10 K, is clearly visible.

Curve *2* in Fig. 2 plots the temperature dependence of the position of the maximum of the high-energy exciton ab-

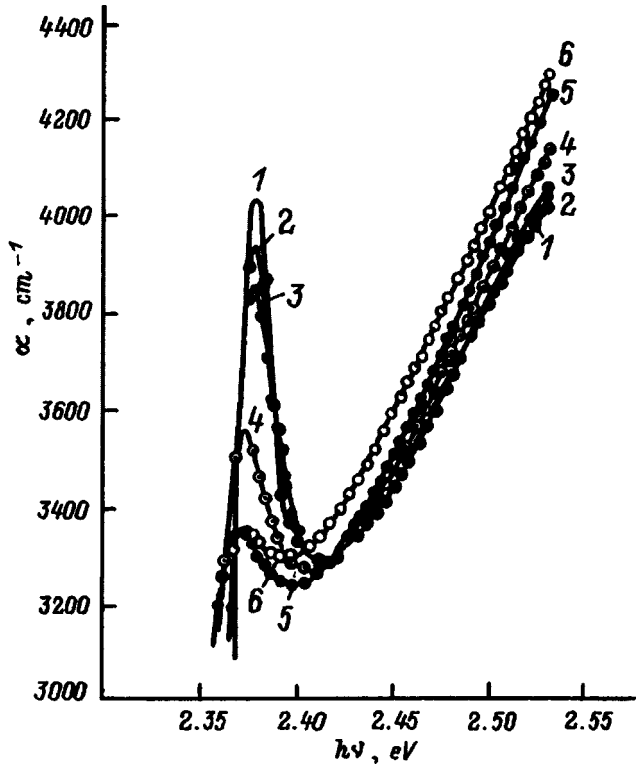

FIG. 1. Absorption coefficient α spectra in $TlGaSe_2\langle Li^+\rangle$ single crystal at various temperatures T, K: *1*—10, *2*—35, *3*—45, *4*—75, *5*—95, *6*—105. $L=18$ μm.

sorption band in the spectrum of a single crystal of $TlGaSe_2\langle Li^+\rangle$. For comparison, curve *1* plots the corresponding temperature dependence for a single crystal of nonintercalated $TlGaSe_2$ of the same thickness $L=18$ μm. Note that the high-energy exciton in the absorption spectra of $TlGaSe_2$ single crystals appears in the temperature range 5–90 K, while in single crystals of $TlGaSe_2\langle Li^+\rangle$ it is seen in a wider temperature range from 5 to 110 K. The energy position of the ground state of the direct exciton in $TlGaSe_2$ shifts from 2.3820 to 2.3937 eV as the temperature is lowered from 90 to 10 K. The temperature shift of the high-energy exciton peak in $TlGaSe_2$ is $\partial E^{ex}/\partial T=-2\times10^{-4}$ eV/K in the temperature interval $20\leqslant T\leqslant 90$ K and -0.5×10^{-4} eV/K in the temperature interval $5\leqslant T\leqslant 20$ K. As a result of intercalation, the temperature shift of this exciton peak decreases almost twofold in absolute value to $\partial E^{ex}/\partial T=-1.1\times10^{-4}$ eV/K in the temperature interval $20\leqslant T\leqslant 105$ K and -0.25×10^{-4} eV/K in the temperature interval $5\leqslant T\leqslant 20$ K.

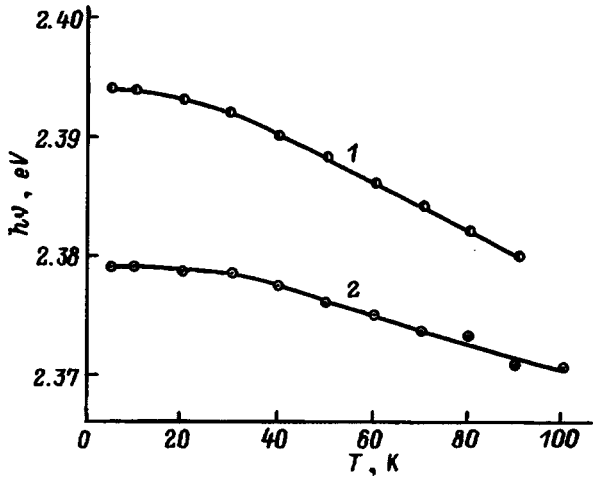

FIG. 2. Temperature dependence of the energy position of the maximum of the high-energy exciton absorption band in $TlGaSe_2$ single crystal before (*1*) and after (*2*) intercalation with Li^+ ions. $L=18$ μm.

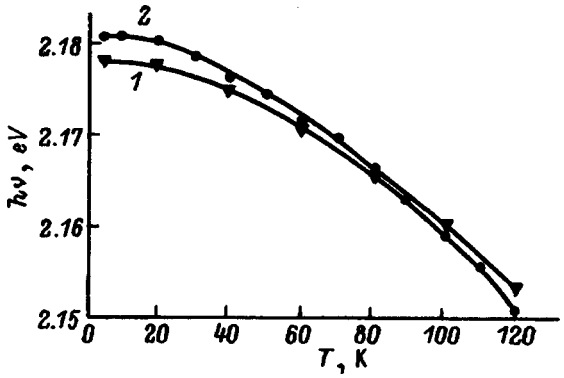

FIG. 3. Temperature dependence of the energy position of the low-temperature exciton peak for a non-intercalated (*1*) and an intercalated (with Li^+ ions) single crystal of $TlGaSe_2$ (*2*). $L=100$ μm.

The above experimental results show that Li^+ ion intercalation of $TlGaSe_2$ single crystals shifts the energy position of the exciton absorption peak associated with the direct edge toward longer wavelengths (e.g., at 5 K the shift is $\Delta E=15$ meV). The energy position of the exciton associated with the indirect edge in the absorption spectrum of $TlGaSe_2$ did not undergo any substantial changes as a result of intercalation. Figure 3 plots the temperature dependence of the energy position of the low-energy exciton peak for non-intercalated (curve *1*) lithium-intercalated (curve *2*) single crystals of $TlGaSe_2$, 100 μm in thickness. It can be seen that in a $TlGaSe_2$ single crystal the band with which the high-energy exciton is associated is more sensitive to changes in the interlayer interaction than the band with which the low-energy exciton is associated.

Thus we may conclude that lithium-ion intercalation of $TlGaSe_2$ single crystals leads to a change in its exciton characteristics—the energy position of the exciton absorption peak, which is associated with the direct edge, and its temperature shift, i.e., it makes it possible to control the optical parameters of $TlGaSe_2$ single crystals.

We are deeply grateful to Prof. F. M. Gashimzade for a discussion of the results of this work and for valuable advice.

[1] S. N. Mustafaeva, Neorg. Mater. **30**, 1033 (1994).
[2] S. N. Mustafaeva, S. D. Mamedbeĭli, and I. A. Mamedbeĭli, Neorg. Mater. **30**, 626 (1994).
[3] T. J. Isaacs and J. D. Feichther, J. Solid State Chem. **14**, 260 (1975).
[4] D. Müller and H. Hahn, Z. Anorg. Allg. Chem. **438**, 258 (1978).
[5] I. I. Grigochak, Z. D. Kovalyuk, and S. P. Yurtsenyuk, Neorg. Mater. **17**, 412 (1981).
[6] S. D. Kovalyuk, A. I. Seredyuk, and K. D. Tovstyuk, Ukr. Fiz. Zh. **27**, 1516 (1982).

Translated by Paul F. Schippnick

Deformation potentials of the $\Gamma(000)$ band extrema in $CdGa_2S_4$

T. G. Kerimova, Sh. S. Mamedov, and I. A. Mamedova

Institute of Physics, Academy of Sciences of Azerbaijan, 370143 Baku, Azerbaijan
(Submitted February 3, 1997; accepted for publication June 7, 1997)
Fiz. Tekh. Poluprovodn. **32**, 148–150 (February 1998)

For the ternary compound $CdGa_2S_4$ the values of the contributions to the temperature coefficient of the absorption edge due to lattice dilatation $(dE/dT)_L$ and the electron–phonon interaction $(dE/dT)_{\text{eph}}$ are found. The deformation potentials of the bottom of the conduction band (12.3 eV) and top of the valence band (-10.9 eV) are calculated. © *1998 American Institute of Physics.* [S1063-7826(98)00602-4]

The semiconductor compounds II-III-VI that crystallize in the space group S_4^2 have been investigated only relatively recently. The most studied among them are $CdGa_2S_4$ and $CdGa_2Se$. For these compounds a band structure has been constructed explaining the polarization dependence of the optical spectra in the region of the intrinsic absorption edge.[1] The valence band of $CdGa_2S_4$ at the $\Gamma(000)$ point consists of two subbands $(\Gamma_3+\Gamma_4)^v$ and Γ_2^v, split by the crystal field while the bottom of the conduction band is formed by the state Γ_1^c in an electric field $\mathbf{E}\|\mathbf{c}$, where $\mathbf{c}$ is the direction of the tetragonal axis.

In addition, studies of the energy spectrum of semiconductors subjected to external perturbations (temperature, pressure, etc.) give additional information about the energy spectrum. Thus, studies of the intrinsic absorption edge at various temperatures of $CdGa_2S_4$ crystals subjected to uniaxial pressure[2,3] yielded very interesting results. The pressure dependences are identical in magnitude and opposite in sign ($dE/dP=\pm 8.6\times 10^{-9}$ eV/Pa) for application of pressure parallel and perpendicular to the tetragonal $\mathbf{c}$ axis.[2] The intrinsic absorption edge is shifted according to a linear law. In the interval 105–300 K $(dE/dB)^{\perp}=-5.3\times 10^{-4}$ eV/K (for $\mathbf{E}\perp\mathbf{c}$) and $(dE/dT)^{\|}=-5.1\times 10^{-4}$ eV/K (for $\mathbf{E}\|\mathbf{c}$). In the temperature interval 80–100 K the temperature shift coefficients take positive values.[3]

In general, two factors contribute to the temperature shift of the intrinsic absorption edge: the electron–phonon interaction $(dE/dT)_{\text{eph}}$ and the lattice deformation $(dE/dT)_L$ (Ref. 4). The part describing the electron–phonon interaction has the form

$$\left(\frac{dE}{dT}\right)_{\text{eph}}=\frac{8}{9\pi}\left(\frac{3}{4\pi}\right)^{1/3}(k_B\Omega^{2/3}/\hbar Mv^2)(m_hc_h^2+m_ec_e^2) \tag{1}$$

and the part describing lattice dilatation has the form

$$\left(\frac{dE}{dT}\right)_L=2\alpha_L(c_e+c_h). \tag{2}$$

In expressions (1) and (2) $M=18.87\times 10^{-22}$ g and $\Omega=3.34\times 10^{-22}$ cm^{-3} are the mass and volume of the unit cell, respectively, v is the sound velocity in the material, equal to $(k_B\theta_D/\hbar)(\Omega_1/6\pi^2)^{1/3}$, and θ_D is the Debye temperature, which is equal to 173 K (Ref. 5). The volume per atom is $\Omega_1=2.246\times 10^{-23}$ cm^{-3}. From known values of θ_D and Ω we calculated the sound velocity $v=1.6\times 10^5$ cm/s; α_L is the linear lattice dilatation coefficient, m_e and m_h are the effective masses of the bottom of the conduction band and the top of the valence band, and c_e and c_h are the deformation potentials of the bottom of the conduction band and the top of the valence band, respectively. Solving the system of equations (1) and (2) for known values of $(dE/dT)_{\text{eph}}$ and $(dE/dT)_L$, we can estimate the deformation potentials of the band extrema in $CdGa_2S_4$.

The temperature shift coefficient $(dE/dT)_L$ of the intrinsic absorption edge is related to the baric coefficient dE/dP as follows:

$$\left(\frac{dE}{dT}\right)_L=-3\,\frac{\alpha_L}{k}\,\frac{dE}{dP}, \tag{3}$$

where k is the compressibility. To estimate $\alpha_L=(2\alpha_a+\alpha_c)/3$ we took the values of the dilatation coefficients $\alpha_a=7.5\times 10^{-6}$ K^{-1} and $\alpha_c=8.5\times 10^{-6}$ K^{-1} from Ref. 6.

Unfortunately, the value of the compressibility of $CdGa_2S_4$ is not given in the literature. Therefore, we chose this parameter by analyzing the values of the compressibility for ternary compounds. From the data in Table I it can be seen that the compressibility for ternary compounds varies in the limits $(1.5-3.3)\times 10^{-11}$ Pa^{-1}. Therefore, we chose the compressibility for $CdGa_2S_4$ to be equal to 2×10^{-11} Pa^{-1}. The pressure coefficient $dE/dP=8.6\times 10^{-6}$ eV/Pa was taken from Ref. 2. For the lattice deformation we obtained the value $(dE/dT)_L=1.01\times 10^{-2}$ eV/K. Subtracting from the total shift of the absorption edge the fraction associated with lattice dilatation, we determined the contribution associated with the electron–phonon interaction $(dE/dT)_{\text{eph}}=-106.3\times 10^{-4}$ eV/K. Substituting the values for $(dE/dT)_L$ and $(dE/dT)_{\text{eph}}$ into expressions (1) and (2) and solving this system of equations, we obtain estimates for the deformation potentials of the bottom of the conduction band and the top of the valence band. For the effective mass of the electrons of the bottom of the conduction band Γ_1^c and of the top of the valence band Γ_2^v we used the values[9]

$$m_l^*=(m_e^{\perp})^{2/3}(m_l^{\|})^{1/3}=0.203m_0,$$

$$m_h^*=(m_h^{\perp})^{2/3}(m_h^{\|})^{1/3}=0.664m_0,$$

TABLE I.

Compound	Coefficient of compressibility k, 10^{-11} Pa^{-1}	Reference
$CuInSe_2$	2.3	Ref. 7
$CdGeAs_2$	1.43	Ref. 8
$AgGaS_2$	1.51	Ref. 8
$HgIn_2Te_4$	3.33	Ref. 8

where $m_l^{\perp}=0.198m_0$, $m_l^{\parallel}=0.214m_0$, $m_h^{\parallel}=0.381m_0$, and $m_h^{\perp}=0.77m_0$.

Solving the system of equations (1) and (2) for the deformation potentials, we obtain the values $c_l=351$ eV and $c_h=319$ eV for $\mathbf{P}\perp\mathbf{c}$, but for $\mathbf{P}\parallel\mathbf{c}$ this system of equations does not have a solution. It should be noted that for the deformation potentials of the band extrema we obtained very exaggerated values, in contrast to the isoelectronic analogs $CuInSe_2$ ($c_e=9.48$ eV, $c_n=7.78$ eV) and $AgInTe_2$ ($c_e=-11.08$ eV, $c_n=8.82$ eV).[10] This apparently stems from the fact that the pressure coefficients for the isotropic point for $\mathbf{P}\parallel\mathbf{c}$ and $\mathbf{P}\perp\mathbf{c}$ have large values.[2] They differ by almost two orders of magnitude from the pressure coefficients of the isoelectronic analogs and do not describe a shift of the intrinsic absorption edge with pressure since the isotropic point for $\lambda=4900$ Å (2.53 eV) is located in a longer-wavelength region of the spectrum than the optical transitions A', B',C' (equal to 2.95, 3.23, 3.34 eV at $T=300$ K, respectively).[1]

Since the isoelectronic analog of $CdGa_2S_4$ is $ZnGeP_2$, we can assume that the pressure coefficients of their band extrema are similar. Using the values of the pressure coefficients[11] $dE/dP=-1.91\times10^{-11}$ eV/Pa for the A' transitions, $dE/dP=-1.87\times10^{-11}$ eV/Pa for the B' transitions, and $dE/dP=-1.87\times10^{-11}$ eV/Pa for the C' transitions, we obtain for the temperature shift of the edge associated with lattice dilatation the value $(dE/dT)_L=2.44\times10^{-4}$ eV/K, and for the edge associated with the electron–phonon interaction $(dE/dT)=-5.34\times10^{-4}$ eV/K. Solution of the system of equations (1) and (2) gives for the deformation potentials the values $c_l=12.3$ eV, $c_h=-10.9$ eV and $c_l=-10.2$ eV, $c_h=11.6$ eV. Since the condition $|c_l|>|c_h|$ must be satisfied,[7] we chose the first pair of values. Because of the absence of data for the effective masses in the $(\Gamma_3+\Gamma_4)^v$ states, the calculated deformation potentials pertain to the Γ_2^v and Γ_1^c states of the top of the valence band and the bottom of the conduction band, respectively.

Using the values of the deformation potentials, let us attempt to determine how the band extrema shift when pressure is applied parallel and perpendicular to the tetragonal **c** axis. According to Ref. 2, application of pressure parallel to the **c** axis ($\mathbf{P}\parallel\mathbf{c}$) increases, the tetragonal compression, equal to $2-c/a$, which leads to an increase in the crystal-field splitting. The width of the band gap also increases at the same time.[2] It is well known that when the deformation potentials of the states of the bottom of the conduction band and the top of the valence band have different signs, the bands shift in the same direction.[7] To increase the width of the band gap, the band extrema must shift upward (Fig. 1a). Due to the absence of values for the effective masses for the valence-band states $(\Gamma_3+\Gamma_4)^v$ we were not able to estimate the value of the deformation potential for this band. However, analyzing the behavior of the band extrema under pressure, it is possible to estimate the value of the deformation potential for $(\Gamma_3+\Gamma_4)^v$. Since the crystal-field splitting increases when pressure is applied parallel to the **c** axis, this is possible only if the deformation potential of the $(\Gamma_3+\Gamma_4)^v$ state is larger than that of the Γ_2 state of the valence band (Fig. 1a).

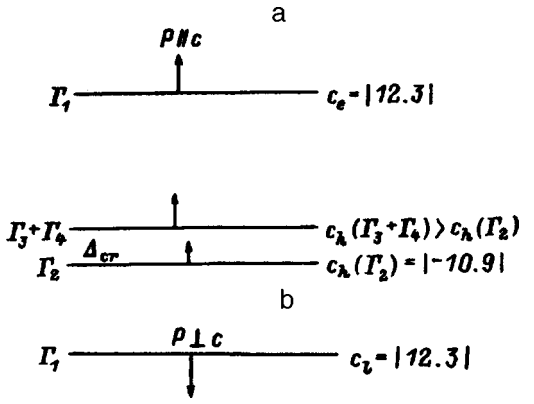

FIG. 1. Movement of bands in $CdGa_2S_4$ subjected to uniaxial pressure: a—$\mathbf{P}\parallel\mathbf{c}$, b—$\mathbf{P}\perp\mathbf{c}$.

When pressure is applied perpendicular to the **c** axis ($\mathbf{P}\perp\mathbf{c}$), the crystal-field splitting decreases since the tetragonal compression $2-c/a$ decreases. In this case the width of the band gap also decreases. This is possible if the band extrema shift downward (Fig. 1b).

In recent years band-edge deformation potentials in semiconductors have also been determined from the temperature dependence of the shift of the intrinsic absorption edge according to the technique of Manoogian and Leclerc.[12] According to Ref. 12, the temperature dependence of the absorption edge shift in semiconductors is described by the expression

$$E(0)-E(T)=UT^x+V\varphi[\coth(\varphi/2T)-1], \tag{4}$$

where U, V, φ, and x are parameters which are independent of temperature. In this expression the quantity U describes lattice dilatation, V is the electron–phonon interaction, and φ is a parameter having the dimensions of temperature. Since two factors contribute to the temperature shift of the absorption edge (lattice dilatation and the electron–phonon interaction), in the Manoogian–Leclerc technique the part describing the electron–phonon interaction can be represented in the form

$$\left(\frac{dE}{dT}\right)_{\text{eph}}=-\frac{V\varphi^2}{2T^2}\,\text{csch}^2\left(\frac{\varphi}{2T}\right), \tag{5}$$

and the part describing lattice dilatation can be represented in the form

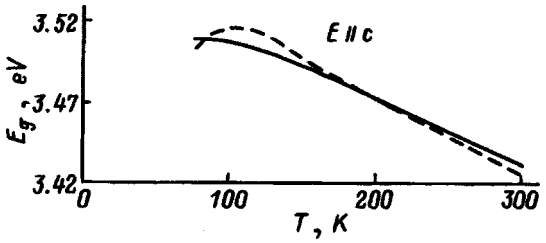

FIG. 2. Temperature dependence of the absorption edge shift in $CdGa_2S_4$. Dashed curve—experiment,[3] solid curve—calculated by the method of Ref. 12; parameters: $U=-2.44\times10^{-5}$ eV/K, $V=2.7\times10^{-4}$ eV/K, $\varphi=360$ K, $E(0)=3.51$ eV.

$$\left(\frac{dE}{dT}\right)_L = -xUT^{x-1}. \tag{6}$$

Assuming that $\varphi/2T<\pi$ (this condition is satisfied for a number of semiconductors[10,12,13]) and expanding $\mathrm{csch}(\varphi/2T)$ in a series about $x=1$, we obtain $dE/dT=-(U+2V)$. Since the shift due to the lattice deformation is $(dE/dT)_L=-U=-2.44\times10^{-5}$ eV/K for $x=1$, we obtain for V the value 2.7×10^{-4} eV/K. Substituting these parameters in Eq. (4) and varying E_0 and φ, we fit Eq. (4) by the least squares method to the experimental dependence $E_g=f(T)$ (Fig. 2). The accuracy of the fit is roughly 0.2%. This indicates that the deformation potentials calculated above describe the temperature dependence of the absorption edge shift in $CdGa_2S_4$.

We are grateful to Prof. F. M. Gashimzade for helpful advice in the course of discussion of the results of this work.

[1] T. G. Kerimova, Author's Abstract of Doctoral Dissertation [in Russian] (Baku, 1986).
[2] L. M. Suslikov, Z. P. Gad'mashi, D. Shch. Kovach, and V. Yu. Slivka, Fiz. Tekh. Poluprovodn. **16**, 143 (1982) [Sov. Phys. Semicond. **16**, 86 (1982)].
[3] T. G. Kerimova, Sh. S. Mamedov, and I. A. Mamedova, Neorg. Mater. **29**, No. 7 (1993).
[4] N. I. Fan, Phys. Rev. **82**, 900 (1951).
[5] M. A. Aldzhanov, D. A. Guseinov, and R. K. Veliev, Phys. Status Solidi A **86**, K19 (1984).
[6] P. I. Babyuk, V. F. Donu, V. F. Zhitar', and G. F. Mocharnyuk, Izv. Akad. Nauk MSSR, Ser. Fiz. Tekh. Mat. Nauk, No. 2, 72 (1981).
[7] C. Rincon, J. Phys. Chem. Solids **49**, 391 (1988).
[8] Tu. Hailing, G. A. Saunders, W. A. Lambson, and R. S. Fegolson, J. Phys. C: Solid State Phys. **15**, 1399 (1982).
[9] V. J. Chizikov, V. L. Panyutin, B. E. Ponedelnikov, and A. E. Rosenson, J. Physique **42**, 1003 (1981).
[10] M. Quintero, R. Towar, C. Bellabarba, and J. C. Woolley, Phys. Status Solidi B **162**, 517 (1990).
[11] M. Cubo, S. Shirakava, and J. Naudi, Phys. Lett. **90A**, 97 (1982).
[12] A. Manoogian and A. Leclerc, Phys. Status Solidi B **92**, K23 (1979).
[13] M. Quintero, B. D. Marks, and J. C. Woolley, J. Appl. Phys. **66**, 2402 (1989).

Translated by Paul F. Schippnick

Optical spectra of microcrystals of the layered semiconductor PbI_2 grown in glass matrices

A. S. Ablitsova, V. F. Agekyan, and A. Yu. Serov

Scientific-Research Institute of Physics, St. Petersburg State University, 198904 St. Petersburg, Russia
(Submitted May 29, 1997; accepted for publication June 7, 1997)
Fiz. Tekh. Poluprovodn. **32**, 151–154 (February 1998)

The transmittance, luminescence, and Raman spectra in PbI_2 microcrystals of $2H$ polytype, grown in the voids of alkali-borosilicate glasses (void dimensions 4–30 nm), are investigated. Depending on the conditions of growth, the exciton states of the microcrystalline systems were found to shift toward higher energies by 35–60 meV relative to the free exciton energy in bulk single crystals as a result of the quantum-well effect. The resonant Raman spectra of PbI_2 microcrystals exhibit not only the conventional Raman component A_{1g}, but also components associated with the appearance of the E_u and A_{2u} optical phonons and the two-phonon processes. [S1063-7826(98)00702-9]

Semiconducting microcrystals have been the object of intense study for a decade already. The motivation for this interest is the size-related properties of these structures and the possibility of their practical application.

The most widely employed method of growing microcrystalline structures is by imbedding the semiconductor in an insulating matrix such as some polymer or glass or other system. Recently the ion exchange method was used to obtain PbI_2 microcrystals in a polymer matrix, allowing their optical and magneto-optical properties to be studied.[1,2]

EXPERIMENTAL PROCEDURE

In the present work we have examined PbI_2 microcrystals grown in the voids of a glassy matrix. Microporous alkali-borosilicate glasses with void dimensions in the range 25–30 nm (type 1), 14–20 nm (type 2), and 4–10 nm (type 3) serve as the matrix for the PbI_2 microcrystals. According to the data in the literature,[3] in the glasses we studied the void volume can reach 20–30% of the total volume of the matrix. We used two techniques to imbed the semiconductor in the glassy matrix: sublimation in vacuum and precipitation from solution.

To obtain samples by sublimation, the porous glass was first annealed in air at $T=200$ °C. Then the matrix, together with powdered lead iodide, was placed in a quartz cell, which was sealed off and evacuated. The sublimation process lasted from 2 to 8 h at 290 °C; the cell was then slowly cooled. The optical density of the samples was regulated by the amount of material placed in the cell and by the temperature.

To obtain samples by precipitation from solution, the porous glass was submerged in a saturated aqueous solution of PbI_2 at 100 °C, then taken out of the solution and cooled. The solubility of lead iodide increases sevenfold in the temperature range from 20 to 100 °C, approaching 0.4 g per 100 g water at 100 °C. Because of this procedure, microcrystals were formed inside the voids upon cooling the sample. The samples were then dehydrated. When necessary, the optical density of the samples was increased by repeating the above procedure.

We investigated the transmission, luminescence, and Raman spectra of the synthesized samples. For the measurements we used an experimental setup based on a DFS-24 diffraction spectrometer with reciprocal linear dispersion 0.5 nm/mm. The Raman spectra were obtained in 180° geometry. To excite scattering and luminescence, we used the 488-nm (2.54-eV) and 476.5-nm (2.6-eV) lines of an LG-502 argon-ion laser.

RESULTS AND DISCUSSION

In the transmission spectra of porous glasses with PbI_2 grown by sublimation, we were not able to observe the exciton spectrum. This is possible because highly strained microcrystals are formed on the surface of the voids during growth at lower vapor density. The electric fields caused by these strains destroy the free exciton. As a result, a structureless edge is observed in the transmission spectrum.

In the low-temperature ($T=77$ K) transmission spectra of the porous glasses of the above-indicated three types, containing PbI_2 microcrystals precipitated from solution, peculiarities associated with the appearance of a free exciton are observed (Fig. 1). The longest-wavelength exciton peak with energy position of the maximum $E_{ex}=2.505$ eV was observed in a type-1 matrix. Comparison with the reflection spectra of PbI_2 bulk single crystals grown from the same solution allows us to conclude that comparatively large PbI_2 crystals are formed in the type-1 matrix. The exciton energy in these crystals coincides with the exciton energy in a PbI_2 bulk single crystal of $2H$ polytype.

In the microcrystals grown in the type-2 matrix the exciton band is significantly broadened in comparison with the previous case and shifted toward shorter wavelengths relative to the position of the exciton in bulk crystals.

In type-3 matrices we were able to obtain the largest shift of the exciton peak toward shorter wavelengths. In these samples the exciton half-width was less than in the of type-2 matrices, but greater than in those of type 1.

Of greatest interest are the microcrystals grown in type-3 matrices. The magnitude of the exciton short-wavelength shift in type-3 matrices depends on the concentration of the

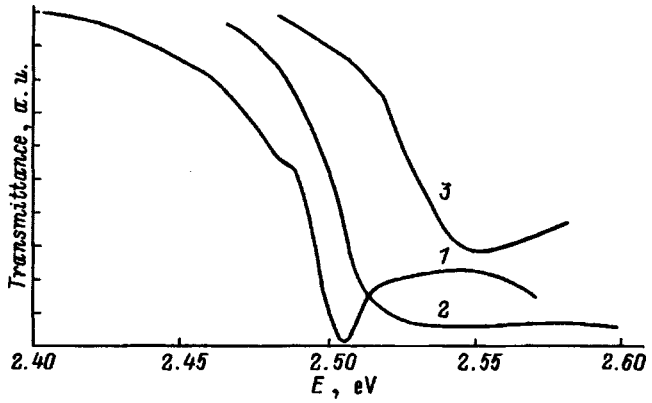

FIG. 1. Transmission spectra of PbI_2 microcrystals grown in the voids of three types of glassy matrices. Void dimensions 25–30 (*1*), 14–20 (*2*), 4–10 nm (*3*). $T=77$ K.

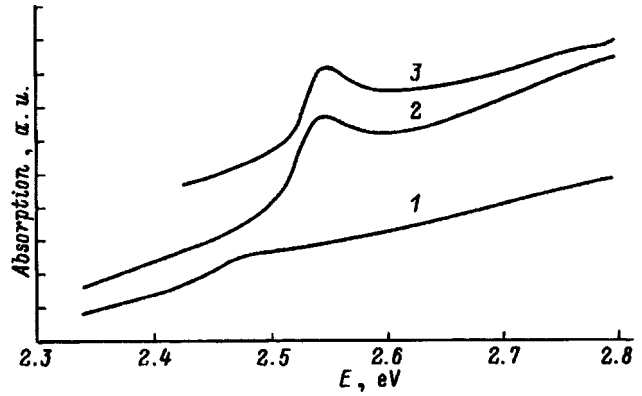

FIG. 3. Absorption spectra of PbI_2 microcrystals at various temperatures, grown in the voids of glassy type-3 matrices. $T=300$ (*1*), 77 (*2*), 4 K (*3*).

solution in which the microcrystals were grown. Figure 2 shows transmission spectra obtained at 77 K in microcrystalline samples. Depending on the conditions of synthesis in type-3 matrices, we were able to obtain an exciton structure shifted relative to the exciton in the bulk-crystal spectrum by 35 to 60 meV.

When the temperature is raised to room temperature, the exciton minima shift toward lower energies by 0.08 eV. When the samples were cooled from 77 to 4.2 K, neither a noticeable shift nor any narrowing of the exciton peaks was observed (Fig. 3). Obviously, the half-width of the exciton minimum in this temperature interval is associated with the size dispersion of the microcrystals; i.e., it is determined by inhomogeneous broadening.

In the luminescence spectra of the as-grown samples we observed a band whose maximum coincides with the minimum of the transmission spectrum, which allows us to identify it as the emission of a free exciton. The free-exciton luminescence intensity fell rapidly during the course of the experiment. Apparently, optical excitation of the lead iodide microcrystals initiates the formation on their surface of defects that localize the excitons. In samples stored for several hours in air the free-exciton emission is also completely degraded, and in the luminescence spectra at 77 K we observed a band which shifted in various samples toward longer wavelengths by 15–25 meV relative to the free exciton energy.

As the temperature is lowered from 77 to 4.2 K, the luminescence band of the localized exciton is shifted toward still lower energies and becomes highly asymmetric (Fig. 4). Aging of the samples is most likely a function of changes in the surface properties of the microcrystals; i.e., a potential well which localizes the excitons is formed on the surface. These changes are accelerated by photophysical and photochemical processes.

The spread in the exciton energies in PbI_2 microcrystals imbedded in type-3 matrices depends on the quantum-well effect. Estimates show that as a result of its low solubility, less than ten molecules of PbI_2 are dissolved per void in voids with linear dimension 10 nm at 100 °C. This allows us to draw the following conclusions about the formation mechanism of the microcrystals:

—active diffusion of PbI_2 takes place during the growth process;

—the number of crystallization centers is small.

Attention is drawn to the fact that repeating the microcrystal growth cycle in the same matrix does not shift the position of the exciton minimum—it only increases the optical density of the sample. Thus, during the growth process either the crystals do not grow in size or the increase in size

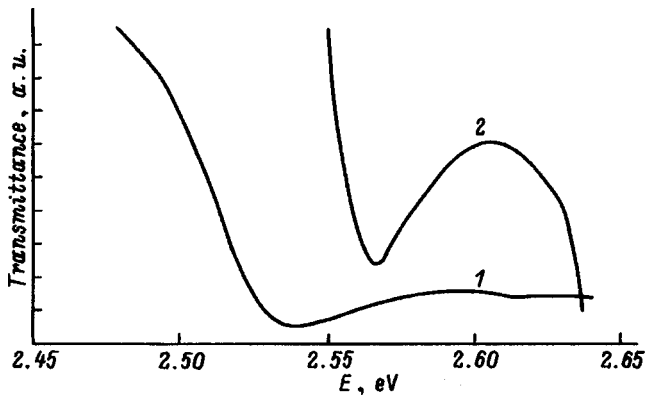

FIG. 2. Transmission spectra of PbI_2 microcrystals ($T=77$ K), grown in the voids of glassy type-3 matrices under various conditions (in case *1* the solution temperature was higher).

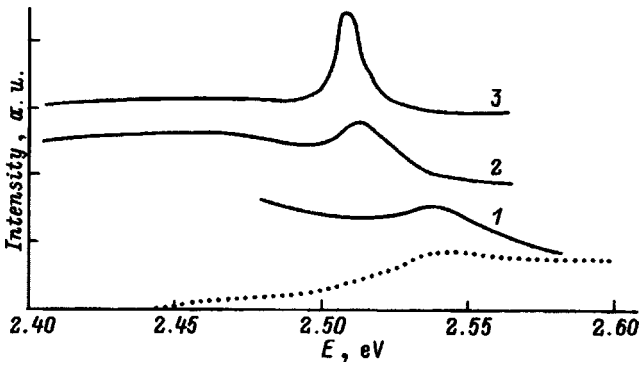

FIG. 4. Exciton luminescence spectra and absorption spectrum of PbI_2 microcrystals grown in the voids of a glassy type-3 matrix: *1*—luminescence of an as-grown sample at $T=77$ K; *2* and *3*—luminescence of a relaxed sample at $T=77$ and 4 K; the dotted curve represents the absorption spectrum at $T=77$ K.

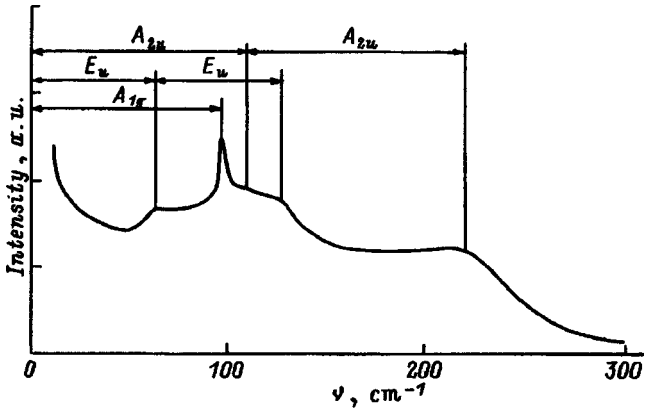

FIG. 5. Resonant Raman scattering spectrum in PbI_2 microcrystals grown in the voids of a type-3 matrix. The energy of the 2.54-eV exciting line coincides with the exciton energy. Frequencies of the A_{1g}, A_{2u} (LO), and E_u (TO) phonons are shown. $T=77$ K.

does not have a substantial effect on the exciton spectra. In layered crystals the growth rate for the direction in the plane of the layer differs markedly from that perpendicular to it. In view of this circumstance, it is natural to assume that the thickness of the crystals growing in the voids is significantly less than their dimensions in the layer plane; i.e., thin islet-films are formed. In this case the quantum-well shift depends mainly on the thickness of the crystal, and the limitation of the area of the films by the void dimensions has a diminished effect on the energy shift of the excitons. Such a conclusion is supported by the particular features of the Raman spectra in the structures which we have grown. The phonon energies coincides with the phonon energies of PbI_2 bulk crystals of $2H$ polytype.

Under specially chosen conditions of synthesis we grew samples in which the energy of the exciton transition is 2.54 eV, i.e., it coincides with the energy of one of the argon-ion laser lines. Such conditions give rise to the excitation of Raman scattering (Fig. 5), which clearly reveals the vibrational structure characteristic of the $2H$ polytype.

A narrow line is observed in the Raman spectrum, which is offset from the exciting line by 98 cm^{-1} and which corresponds to the totally symmetric vibration A_{1g} (Ref. 4). Other features of the Raman spectrum, absent in the nonresonance spectra, belong to the polar vibrations E_u and A_{2u}. The significant broadening of the structure, which is associated with polar phonons, is governed by the decay and strong angular dispersion of the energy of the polar phonons.

It is well known that the E_u and A_{2u} phonons are polarized parallel and perpendicular to the hexagonal Z axis, respectively,[4] and for an arbitrary direction a mixed wave propagates in the crystal.[5] For this wave the dielectric constant at frequency ω is given by the following expression (if the condition $\omega \gg \omega_{1t}$ is satisfied and if the attenuation and spatial dispersion are disregarded):

$$\varepsilon_0(\omega)=\left[\frac{\cos^2\psi}{\varepsilon_{0\perp}\left[1+\dfrac{\omega_{lt\perp}}{\omega_{0\perp}-\omega}\right]}+\frac{\sin^2\psi}{\varepsilon_{0\parallel}\left[1+\dfrac{\omega_{lt\parallel}}{\omega_{0\parallel}-\omega}\right]}\right]^{-1}.$$

Here ψ is the angle between the Z axis and the direction of propagation of the phonon, $\omega_{lt\perp}$ and $\omega_{lt\parallel}$ are the values of the longitudinal-transverse splitting of the A_{2u} and E_u phonons, respectively, $\varepsilon_{0\perp}$ and $\varepsilon_{0\parallel}$ are the phonon dielectric constants, and ω is the current frequency.

As the angle ψ varies from 0° to 90°, the poles of ε_0 (the transverse frequencies of the mixed wave) shift from $\omega_{t\parallel}$ to $\omega_{r\perp}$ and from ω_l to $\omega_{l\parallel}$. Thus, regions should appear in the Raman spectrum of the reoriented system of microcrystals from $\omega_{t\parallel}$ (59 cm^{-1}) to $\omega_{t\perp}$ (88 cm^{-1}) and from $\omega_{l\perp}$ (97 cm^{-1}) to $\omega_{l\parallel}$ (112 cm^{-1}) when the density of states is taken into account.

It is clear from Fig. 5 that the features in the experimental first-order Raman spectrum are found in precisely these energy intervals and that the polar phonons also show up in the second-order Raman spectrum.

The Raman spectrum of microcrystals grown in a type-2 matrix is similar to the one described above, but has lower intensity. We were not able to record the resonant Raman spectrum for excitation by the 2.54-eV line in a type-1 matrix.

Since according to our thinking microcrystalline films grow in the voids, it is natural to estimate their thickness using the model of a two-dimensional quantum well with infinite barriers. It is well known[6] that in this case the quantum-size shift of the exciton level (without allowing for changes in the binding energy) is given by

$$\Delta E=\frac{h^2n^2}{2\mu L^2}, \tag{1}$$

where μ is the reduced mass of the carriers, L is the thickness of the quantum well, h is Planck's constant, and n is the principal quantum number.

In the case of PbI_2 the estimate of the energy shift is complicated by the scatter in the available data on the effective hole and electron masses.[7–9] The calculations are therefore assumed to be rough estimates. After analyzing the available data we come to the conclusion that the most reliable values of the effective hole and electron masses for the direction parallel to the Z axis are $m_h=1.1m_0$ and $m_e=1.25m_0$.

In this case the experimental values of the quantum-size shifts allow us to conclude that the thickness of the lead iodide crystals is 4–6 monolayers (see Table I).

Thus, the application of spectroscopic methods makes it possible to determine the dimensions of lead iodide crystals grown in a porous glassy matrix by precipitation from an aqueous solution.

TABLE I. Relation between the thickness L of a microcrystalline PbI_2 film and the quantum-well shift of the exciton maximum ΔE according to Eq. (1) for $m_h=1.1m_0$ and $m_e=1.25m_0$.

L, nm	Number of PbI_2 layers	ΔE, meV
2.1	3	123
2.8	3	69
3.5	5	44
4.2	6	31
4.9	7	23

[1] T. Goto, S. Saito, and M. Tanaka, Solid State Commun. **80**, 331 (1991).
[2] T. Goto, H. Tanaka, Meng-Yan Shen, S. Sasaki, and N. Miura, Solid State Commun. **97**, 587 (1996).
[3] *Two-Phase Glasses and Their Applications* [in Russian], edited by B. G. Varshal (Leningrad, 1991), p. 276.
[4] A. Grisel and P. Schmid, Phys. Status Solidi B **78**, 587 (1976).
[5] V. V. Katal'nikov and O. S. Rudenko, Fiz. Tverd. Tela **11**, 3343 (1975) [Sov. Phys. Solid State **17**, 2190 (1975)].
[6] G. Bastard, *Wave Mechanics Applied to Semiconductor Heterostructures* (Paris, Les Editions de Physique, 1988), p. 4.
[7] P. B. Bloch, J. W. Hodby, T. E. Jenkins, D. W. Stacey, G. Lang, F. Levy, and C. Schwab, J. Phys. C: Solid State Phys. **11**, 4997 (1978).
[8] M. S. Brodin and I. V. Blonskiĭ, *Exciton Processes in Layered Crystals* [in Russian] (Kiev, Naukova Dumka, 1986), p. 103.
[9] S. G. Elkomoss and J. Biellmann, Phys. Rev. B **29**, 4697 (1984).

Translated by Paul F. Schippnick

Excited states of chalcogen ions in germanium

A. Yu. Ushakov, R. M. Shterengas, L. M. Shterengas, and N. B. Radchuk

St. Petersburg State Technical University, 195251 St. Petersburg, Russia
(Submitted July 26, 1997; accepted for publication July 31, 1997)
Fiz. Tekh. Poluprovodn. **32**, 155–158 (February 1998)

The energy spectra of chalcogen impurities in germanium are studied by photoconductivity, optical absorption, and photoluminescence. The previously found excited states of these impurities are identified. The observed excited states of tellurium (Te^+) and selenium (Se^+) ions are shown to be associated with the Γ and L points of the germanium Brillouin zone, respectively.
 [S1063-7826(98)00802-3]

Chalcogens, which have two more valence electrons than the atoms of the main lattice, behave in germanium as deep, doubly charged, donor substitution impurities,[1] which create two levels in the band gap corresponding to the neutral state and singly positively charged state of the chalcogen atom. Studies on the energy spectrum of chalcogens in germanium are few in number.[2–6] Most of the attention in the literature is given to the ground states of these impurities. Less studied are their excited states, a study of which would be of unquestioned interest, since in contrast to the deep ground states the effective mass approximation applies to them. Only the results of Grimmeiss *et al.*,[5,6] who observed excited states of neutral atoms of sulfur, selenium, and tellurium in germanium, are known. For singly positively charged atoms, those researchers[5] present data only for the selenium ion. However, in their own words identification of the states was hindered by the poor resolution of the structure in the spectrum. We have detected for the first time excited states of ions of sulfur, selenium, and tellurium in germanium in studies employing optical and photoelectric methods.[7,8] In later studies, by examining samples with different degrees of compensation we confirmed that the observed resonance peaks in the spectra are associated with transitions to the excited states of the tellurium ion,[9] and sulfur and selenium ions,[10] and also refined the energy spectra of the impurity states created in germanium by chalcogens. We also detected photoluminescence with participation of selenium and tellurium ions.[11] In the present paper we identify the excited states of selenium and tellurium, justify associating the excited states of these impurities with various points of the germanium Brillouin zone, and propose an explanation for the substantially different contribution to the photoconductivity spectra of selenium and tellurium impurities allowing for all of the results obtained.

Samples for study were prepared by recrystallization in evacuated cells in a gradient furnace with subsequent rapid quenching to prevent the liberation of the chalcogen in the form of electrically inactive complexes. To control the charge state of the doubly charged chalcogen donor impurities, as the starting material we used germanium with p-type conductivity, doped with the shallow acceptor impurity, gallium, in different concentrations from 7×10^{13} to 2×10^{15} cm^{-3}. The electrical parameters of the samples were monitored by the Hall effect. Optical and photoelectric measurements in the energy range 240–500 meV were performed on a spectrometer with a grating of 200 rulings/mm. For the lower-energy region we used a grating of 50 lines/mm. Most of the measurements were performed at temperatures near 54 and 77 K. Photoluminescence was excited by a pulsed xenon lamp.

Our photoelectric and optical measurements[7,9] show that the energy gaps between the donor levels created by tellurium in the germanium band gap and by the bottom of the conduction band are 95 and 280 meV for the tellurium atom (Te^0) and tellurium ion (Te^+), respectively, which agrees with the known data of other authors.[2,5] In addition, in a certain interval of values of the degree of compensation k ($k=N_{Ga}/N_{ch}$, where N_{Ga} is the gallium concentration and N_{ch} is the chalcogen concentration), against the background of the ordinary impurity photoconductivity we detected the maximum of the photoelectric effect at 375 meV. Figure 1 shows the photoconductivity spectrum of a Ge:Te sample with degree of compensation $k\simeq1$ at 77 K. The narrow peak width, of the order of kT at half-maximum, indicates that this feature in the spectrum is due to transitions to the excited state. What is unusual about the observed results is that the transition to the excited state is observed against the background of the continuous spectrum, i.e., it takes place at energies greater than the depth of the impurity state (280 meV), whereas conventional excited states are localized in the region of lower energies.

To analyze the nature of the observed feature, we investigated a number of samples with different charge states of tellurium at different temperatures.[9] The temperature was lowered by outpumping nitrogen vapor. The resulting temperature drop was accompanied by a growth of the amplitude and narrowing of the peak, and also by its shift toward higher energies, which corresponds to a negative temperature coefficient of variation of the width of the germanium band gap. At liquid-nitrogen temperature, the level corresponding to neutral tellurium Te^0 (with ionization energy 95 eV) is ionized, and photoconductivity begins at 280 meV. As the temperature is lowered below 77 K in samples with low compensation ($k<0.1$), the upper level fills up and the photoelectric effect begins at 95 meV. For $k=2$ the peak is absent at all temperatures and photoconductivity begins at 450 meV, which corresponds to transitions from the valence band to the tellurium ion level (Te^+). The relative magnitude of the peak turns out to be maximum for $k\simeq1$ and exceeds the background level by roughly an order of magni-

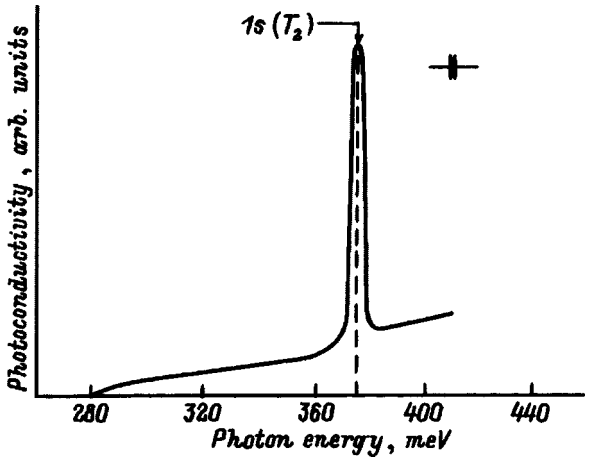

FIG. 1. Photoconductivity spectrum of Ge:Te at 77 K, $k \simeq 1$.

tude. Thus, the amplitude of the peak is proportional to the number of tellurium ions, which is determined by the degree of compensation and by change in the temperature.

The optical absorption spectra are similar to the spectral dependences of the photoconductivity and have their maximum at the same energy 375 meV. The absorption cross section in the region of the maximum, calculated from the spectrum, grows by an order of magnitude and reaches a value of $\sim 10^{-15}$ cm^2. The maximum value of the absorption coefficient was observed in samples with $k \simeq 1$. All of these data, taken together, allow us to assign the observed feature in the photoconductivity spectrum to transitions to the excited state of the tellurium ions.

Figure 2 shows an energy diagram of states of tellurium in germanium. Numerical values are shown for liquid-nitrogen temperature. Since Te creates deep energy levels in Ge, the tellurium electrons are strongly spatially localized. The great depth of both ground states of tellurium in germanium implies strong localization of the impurity electrons in **r**-space and, correspondingly, an indeterminacy in the wave vector, which is reflected in the figure by the dashed lines within the limits of the entire Brillouin zone of germanium. The measured values of the ionization energy of Te^+ and the energy of the transition to the excited state Te^{*+} correspond to a level lying against the background of the conduction band above the absolute minimum located at the L point and 38-meV below the extremum at the Γ point. It is reasonable to assume that in the excited state the electron of the tellurium ion is associated with the Γ extremum. Electrons from the excited state undergo a transition, as they emit a series of phonons, to the absolute minimum of the conduction band and contribute to the photocurrent. Since the absorption coefficient for transitions to the excited state exceed the value for the ''background'' impurity absorption by an order of magnitude, the contribution of this process to the photoconductivity can be very large. As a result, transition to the excited state leads to an abrupt growth of the photoelectric effect and a peak appears on the photoconductivity curve.

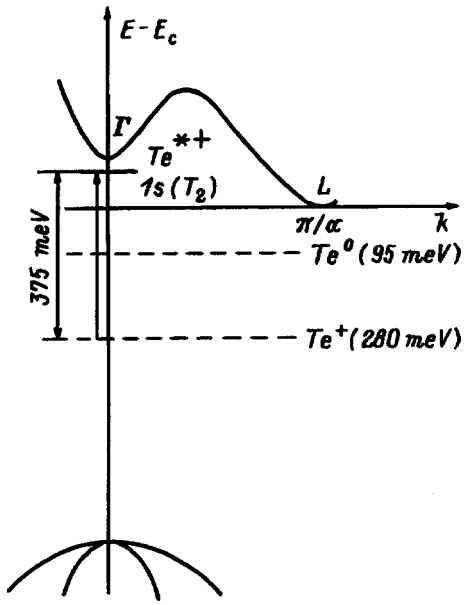

FIG. 2. Energy level diagram of tellurium impurity states in germanium at 77 K. The arrow indicates the transition of an electron of a tellurium ion to an excited state.

To identify the excited state, the value of the binding energy found experimentally was compared with the results of a theoretical calculation[12] performed in the effective mass approximation for the actual band structure of germanium. Best agreement with the results of Ref. 12 is noted for the $1s$ state. In Refs. 6 and 13 it was found that the binding energy of the $1s$ state calculated in the effective mass approximation corresponds in the case of deep impurities in Si and Ge to the triply degenerate state $1s(T_2)$, formed as a result of splitting of the sextuply (for Si) and quadruply (for Ge) degenerate ground state as a result of the valley–orbit interaction. In germanium the $1s$ state splits into the $1s(A_1)$ and $1s(T_2)$ states,[14] where A_1 and T_2 are the irreducible representations of the tetrahedral group T_d, to which the germanium lattice belongs. The deepest state, the true ground state, turns out in this case to be the nondegenerate $1s(A_1)$ state. Transitions between the s states are forbidden by the selection rules in the dipole approximation. However, arguments presented in Refs. 6 and 13 suggest that for deep impurities with strongly spatially localized orbitals the requirements of the selection rules in the dipole approximation are less rigid, and that the symmetry, which resolves optical transitions of the type $ns(A_1) \rightarrow ns(T_2)$, is the basic consideration.

The study of Se impurity gave substantially different results. Figure 3 shows a typical spectral dependence of the photoconductivity of Ge:Se at 77 K for the degree of compensation $k \simeq 0.5$. In the energy region 350–370 meV we observed an abrupt drop of the photocurrent against the background of the ordinary impurity photoelectric effect. In this region we notice three partially overlapping spectral lines with a width of the order of kT at the energies 353, 362, and 368 meV, which are associated with transitions to excited states. The feature in the spectrum is observed in the narrow interval of values of the compensation and is most strongly manifested for the degree of compensation $k \simeq 0.5$, i.e., when atoms (Se^0) and ions (Se^+) of the selenium impurity are present in the material at the same time. Lowering the temperature to 54 K causes only a narrowing and a shift of the lines proportional to kT. Thus, Se and Te impurities

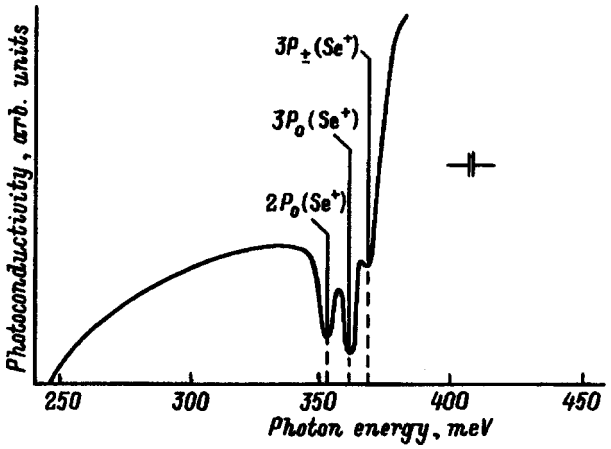

FIG. 3. Photoconductivity spectrum of Ge:Se at 77 K, $k \simeq 0.5$.

give a substantially different contribution to the photoconductivity. The feature associated with the transition of the tellurium ion to the excited state is observed against the background of the photoconductivity due to transitions from the Te^+ level. In the case of selenium the features are observed against the background of the transitions of electrons from the neutral selenium atom Se^0 and, additionally, they give a negative contribution to the photocurrent.

In the Ge:Se absorption spectra we detected maxima at the same energies. The absorption cross section relative to the impurity ''background'' grows by an order of magnitude. The absorption coefficient in this region reaches its maximum value for the degree of compensation $k \simeq 1$.

The above results, taken together, indicate that the observed excited states belong to the selenium ion Se^+.

The energy spectrum of the selenium impurity in germanium, in accordance with our results, is shown in Fig. 4. The excited states of the selenium ion Se^+ are situated under the

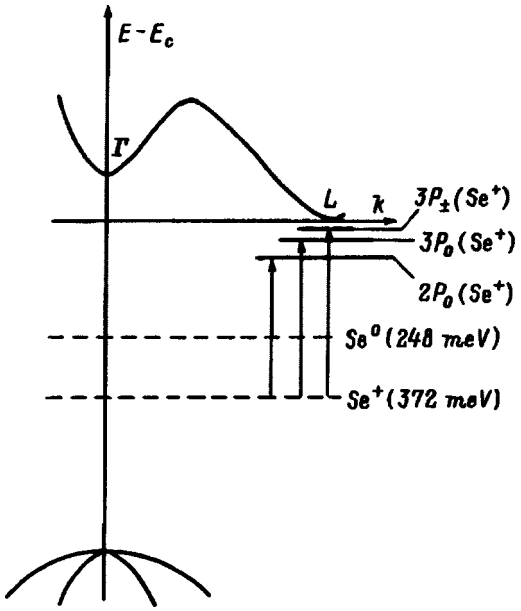

FIG. 4. Energy level diagram of selenium impurity states in germanium at 77 K. The arrows indicate transitions of electrons of the selenium ion to excited states.

absolute minimum of the conduction band of Ge at the L point with gaps 4, 10, and 19 meV. The negative contribution to the photoconductivity of the transitions of selenium ions to the excited states is connected with the fact that due to the order-of-magnitude greater cross section such transitions compete effectively with the impurity photoconductivity associated with transitions from the level of the selenium atom Se^0. The energy gap between the excited states and the germanium conduction band, as follows from our data, is not large, and the fact that at liquid-nitrogen temperature the electrons are not thermally dumped into the band is evidence of the short lifetime of excited states. As a result, excitation of an electron is accompanied by a lowering of the photoelectric effect.

To identify the states, we compared the energy values obtained by us with the theoretical results of Ref. 12. The small value of the energy gaps between the excited states and the germanium conduction band allows us to use the effective mass approximation. Our results are in good agreement with the results of Ref. 12 for the $2P_0$, $3P_0$, and $3P_{\pm}$ states.

To determine the possible connection of the observed spectral features with the complexes, we examined some samples with mixed tellurium and selenium doping in different ratios with the same degree of compensation, $k \simeq 0.8$, at which the features in germanium with tellurium impurity (Ge:Te) and with selenium impurity (Ge:Se) are manifested.[8] Mixed doping led to a simple summation of contributions from the two impurities without the formation of qualitatively new details. The relative magnitude of the contributions of the elements of the spectra characteristic of each of the impurities is proportional to the percent content of the components. Thus, the transitions we observed to the excited states are associated with the individual chalcogens and in the growth technology which we used and which is based on introducing the impurity during recrystallization of germanium with subsequent rapid quenching, chalcogen vapor probably does not form.

With the aim of obtaining additional information, we undertook a study of photoluminescence.[11] For this experiment we took samples of Ge:Te and Ge:Se with degree of compensation $k \simeq 1$, which corresponds to the highest concentration of chalcogen ions. The spectral dependences so obtained turned out to be similar to the absorption spectra, but the lines were shifted toward lower energies by roughly 5 meV for Te^+ and by roughly 37 meV for Se^+. In the case of selenium the observed Stokes shift can be explained by the participation in the transitions to the ground state of the optical intervalley Γ_0 phonon, which in germanium has the energy 37.7 meV. Grimmeiss *et al.*[5] mention the large probability for the participation of this phonon in the optical transitions of atoms and ions of selenium in germanium. This result also explains the negative contribution of the excited states of the selenium ion Se^+ to the photoconductivity. An electron transitions to an intermediate state with the emission of an optical phonon during a time of the order of 10^{-11} s, and the probability of thermal dumping of the electron into the germanium conduction band at liquid-nitrogen temperature turns out to be already vanishingly small. Thus, photo

transitions accompanying excitation of selenium ions are excluded.

The difference in the energy spectra of the chalcogen impurities in germanium, which also showed up in a study of photoluminescence, correlates with ordinal number of the chalcogen in the periodic table. Selenium, which has the same number of electron shells as germanium, in contrast to the heavier tellurium, forms a substantially different energy spectrum of excited states. Note that the energy spectrum of excited states of the sulfur ion[10] is almost identical to the spectrum of the selenium ion. The difference in the behavior of the lighter sulfur and selenium impurities and that of the heavier tellurium impurity can be explained by a spatial displacement relative to the unit cell upon the transition to the excited state of the selenium and sulfur ions, while the tellurium ion, with a larger ionic radius, remains at the center of the cell.

[1] S. Pantelides, *Deep Centers in Semiconductors* (New York, 1986), Ch. 1, p. 186.
[2] W. W. Tyler, J. Phys. Chem. Solids **8**, 59 (1959).
[3] S. J. Pearton, Solid-State Electron. **25**, 499 (1981).
[4] S. J. Pearton, Austral. J. Phys. **35**, 53 (1982).
[5] H. G. Grimmeiss, L. Montelius, and K. Larsson, Phys. Rev. B **37**, 6916 (1988).
[6] H. G. Grimmeiss, K. Larsson, and L. Montelius, Solid State Commun. **54**, 863 (1985).
[7] N. B. Radchuk and A. Yu. Ushakov, Fiz. Tekh. Poluprovodn. **16**, 1855 (1982) [Sov. Phys. Semicond. **16**, 1192 (1982)].
[8] N. B. Radchuk and A. Yu. Ushakov, Fiz. Tekh. Poluprovodn. **19**, 749 (1985) [Sov. Phys. Semicond. **19**, 462 (1985)].
[9] N. B. Radchuk, A. Yu. Ushakov, and R. M. Shterengas, Fiz. Tekh. Poluprovodn. **29**, 483 (1995) [Semiconductors **29**, 250 (1995)].
[10] N. B. Radchuk and R. M. Shterengas, Fiz. Tekh. Poluprovodn. **29**, 754 (1995) [Semiconductors **29**, 392 (1995)].
[11] A. Yu. Ushakov and R. M. Shterengas, Pis'ma Zh. Tekh. Fiz. **21**, 92 (1995) [Tech. Phys. Lett. **21**, 42 (1995)].
[12] R. A. Faulkner, Phys. Rev. **184**, 713 (1969).
[13] H. G. Grimmeiss, E. Janzen, and K. Larsson, Phys. Rev. B **25**, 2627 (1982).
[14] J. H. Reuszer and P. Fisher, Phys. Rev. **135**, A1125 (1964).

Translated by Paul F. Schippnick

Self-compensation in CdTe⟨Cl⟩ in the presence of phase equilibrium of the system crystal-cadmium (tellurium) vapor

O. A. Matveev and A. I. Terent'ev

A. F. Ioffe Physicotechnical Institute, Russian Academy of Sciences, 194021 St. Petersburg, Russia
(Submitted April 14, 1997; accepted for publication April 16, 1997)
Fiz. Tekh. Poluprovodn. **32**, 159–163 (February 1998)

The self-compensation of charged point defects in CdTe⟨Cl⟩ is investigated down to the lower limit of free-carrier densities (n_i, p_i) over the entire range of vapor pressures P_{Cd} and P_{Te} in equilibrium of the crystal-gas phases during annealing. Under conditions where P_{Te2} is controlled during annealing of the crystal, the electron density n is observed to increase from 10^7 cm^{-3} to 10^{14} cm^{-3} as P_{Te} increases from P_{min} to CdTe⟨Te⟩ saturation. This result is attributed to the formation of a Te_{Cd} antistructural defect. The appearance of Te_{Cd} in the crystal lowers the concentration of cadmium vacancies to the point that the mechanism of exact self-compensation of CdTe⟨Cl⟩ is disrupted, and low-resistivity n-type crystals are obtained. The data obtained on the concentration $p(n)$ as a function of P_{Te2} is used to plot the total $n-n_i-p_i$ dependence with the variation of $P_{Cd}-P_{Te2}$, reflecting the state of point defects in CdTe⟨Te⟩. The procedure for annealing crystals in two-phase crystal-gas equilibrium is used to reversibly induce n_i-p_i inversion of the electrical conductivity of the crystal. © *1998 American Institute of Physics.* [S1063-7826(98)00701-7]

Calcium telluride is a binary compound with two volatile components. The vapor pressure of cadmium (P_{Cd}) [or tellurium (P_{Te})] is the state parameter that determines at a given temperature of the CdTe crystal (t_{cr}) its composition when enriched with cadmium (or tellurium) over and above the congruent sublimation composition (P_{min}) (Fig. 1).

It is a well-known fact that self-compensation of the electrical conductivity, i.e., a drop in the number of conduction electrons as a result of their trapping by native point defects formed in the crystal, is observed in CdTe⟨Cl⟩ (Refs. 1 and 2). Practically speaking, self-compensation occurs with fairly high accuracy in thermodynamic equilibrium of the crystal with the gaseous phase.[2,3]

We have previously[4] described in detail a procedure for annealing CdTe⟨Cl⟩ in application to the investigation of the self-compensation effect. It essentially entails the following. In the first stage of annealing the crystals are held at a high temperature $t_{cr} \geqslant 700$ °C to bring the crystal phase (CdTe) and the gaseous phase (Cd, Te) into the equilibrium state. Depending on t_{cr}, the vapor pressure P_{Cd} (P_{Te}), and the chlorine concentration (N_{Cl}), the appropriate numbers of native point defects are formed: cadmium and tellurium vacancies (N_{VCd}, N_{VTe}) and interstitial atoms (N_{Cdi}, N_{Tei}). The formation of associates of native point defects with Cl_{Te} is not very probable at these values of t_{cr} (Ref. 5).

In the second stage of annealing, where the crystal is slowly cooled down to room temperature and the pressure P_{Cd} (P_{Te}) is controlled, the association of charged native point defects with Cl_{Te} takes place. In this case not only is the self-compensated state of the crystal preserved,[2] but ''self-purification'' of the crystal occurs simultaneously.[6] Self-compensation leads to low conductivity ($\sim 10^{-9}\Omega^{-1}\cdot$cm^{-1}) and low values of n and p ($\sim n_i$), while self-purification increases the mobilities and lifetimes of free charge carriers.

The samples to be annealed were prepared from a CdTe⟨Cl⟩ single crystal cut from the middle of the crystal ingot. The concentration $N_{Cl}=2\times10^{18}$ cm^{-3} is determined by the relative weight of $CdCl_2$ introduced into the melt during growth of the ingot. The crystals used in the study were p-type with $p=(1-5)\times10^8$ cm^{-3} and $\mu \cong 40$ cm^2/(V·s).

It is advisable to investigate self-compensation of the conductivity of such semiinsulating crystals approximately in the vicinity of conduction inversion, which takes place near P_{min}, when $P_{Cd} \approx P_{Te}(P_{Te2}^{1/2})$. In this case it is required to establish sample annealing conditions not only to prevent even the slightest sublimation of the crystal, but also to assume that the composition of the sample will be determined by the specified vapor pressure of one volatile component and will not fluctuate as a result of the second volatile component that escapes from it into the cell.

All these requirements can be met by annealing in Te_2 or Cd vapor in the equipment shown schematically in Fig. 2. The samples are placed in zone 1, a filler in zone 2, and tellurium (cadmium) in zone 3 of the evacuated cell (10^{-4} Pa). The filler was prepared by crushing out small crystals from the same ingot as the samples to be annealed. The large surface area of the many small filler crystals suppresses mass transfer of the sample from the gaseous state, preventing sublimation of the sample. However, since the vapor pressure of one of the volatile components, say P_{Te2}, in the cell does not, strictly speaking, safeguard the investigated sample against losses of the other volatile component (Cd), the filler must be maintained at a temperature 5 °C lower than the sample so as not to alter the initial state of the sample. In this case the volume of the gaseous phase is filled with both volatile components as a result of the filler and the tellurium (cadmium) in zone 3, thereby protecting the sample from unmanageable fluctuations.

The correctness of the adopted annealing regime is well supported by results from anneals in cadmium (tellurium) vapor at various sample and filler temperatures. No sublima-

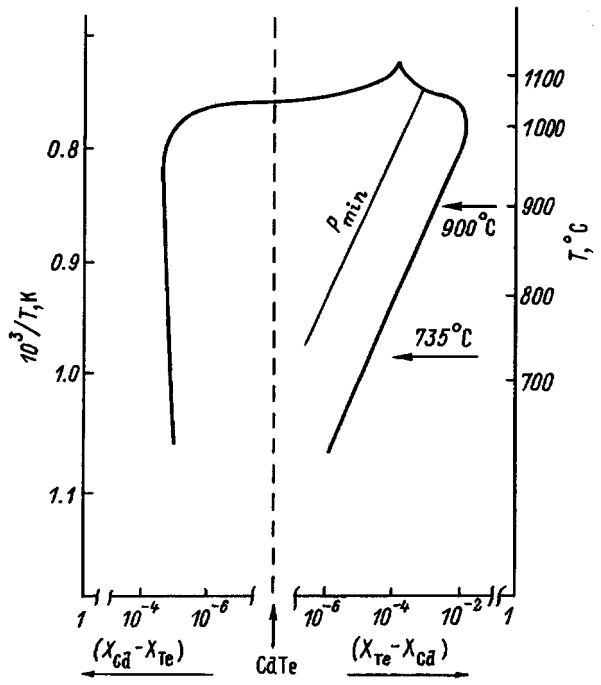

FIG. 1. Region of existence of solid CdTe on the Cd–Te state diagram ($T-X$ coordinates).

tion of the samples was observed. However, for anneals in cadmium vapor the samples retained n-type conductivity over the entire range of P_{Cd}. Inversion to p-type was not observed, even for low P_{Cd}. This fact has been demonstrated previously[4] (Fig. 3), probably on account of losses of tellurium escaping from the sample into the gaseous phase during the cooldown stage. Similar results have been obtained in annealing in Te vapor in the present study (Fig. 3b).

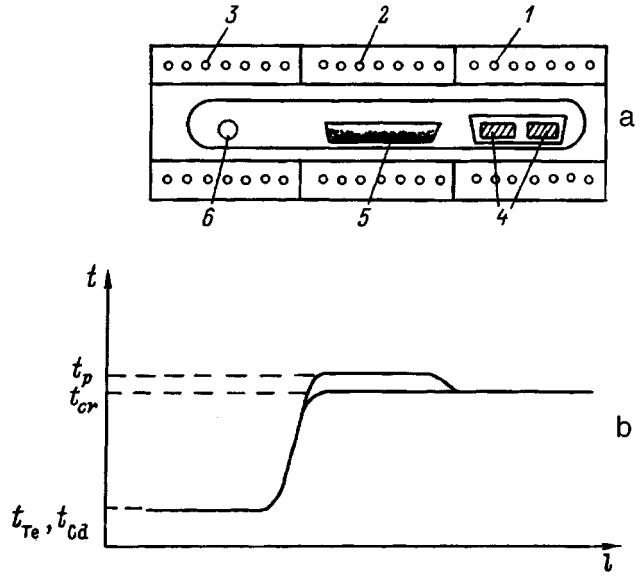

FIG. 2. a) Diagram of the crystal annealing equipment: *1*) sample annealing zone; *2*) filler zone of the oven; *3*) cold zone, specifying P_{Te2} (P_{Cd}); *4*) annealed crystals; *5*) filler; *6*) tellurium (cadmium). b) Temperature distribution in the system along the length of the furnace during annealing of the crystals.

The results of our investigation of equilibrium between the crystal phase CdTe⟨Cl⟩ and the vapor phase Te_2 are given below. The region controlled by the Te_2 pressure is interesting in that $N_{V\mathrm{Cd}}$, which is known to play a decisive role in the self-compensation process, must increase in this case.

The anneals were carried out at temperatures $t_{\mathrm{cr}}=735$ °C and 900 °C. The anneal temperatures at which self-compensation was investigated in CdTe⟨Cl⟩ with P_{Cd2} controlled were limited above ($t_{\mathrm{cr}}\leqslant 900$ °C) by the observed deformation of the sample due to CdTe sublimation. The choice of lower limit of the anneal temperatures $t_{\mathrm{cr}}\sim 735$ °C was dictated by considerations of the duration of the diffusion processes, which determine the crystal composition corresponding to the given P_{Te2}. The anneal time at t_{cr} was ≈ 24 h.

The free-carrier density as a function of P_{Te2}, obtained from measurements of the Hall coefficient for the annealed crystals, is shown in Fig. 3. Sublimation of the sample takes place at low pressures $P_{\mathrm{Te2}}\sim P_{\mathrm{min}}$, corresponding to the region $P_{\mathrm{Te}}<10^{-3}$ Pa in Fig. 3. It is evident from Fig. 3 that the samples acquired both p-type and n-type conductivity after annealing. For all anneal temperatures t_{cr} there are three well-discerned intervals: the first with a low and approximately constant concentration $n(p)\sim(10^7-10^9)$ cm^{-3} at low vapor pressures P_{Te2}, the second with a high value of $n\sim 10^{14}$ cm^{-3} at high pressures P_{Te2}, and the third a transition zone between these intervals. The first interval corresponds to a very precise self-compensated state of donor and acceptor defects of the crystal lattice ($\mathrm{Cl}_{\mathrm{Te}}^{+}$ and V_{Cd}^{-2}). The energy level of V_{Cd}^{-2} in the band gap is $E_v+0.83$ eV (Ref. 7). The second interval corresponds to a donor-controlled conductivity mechanism.

Two curves for the anneal conditions $t_p=t_{\mathrm{cr}}$ and $t_p=t_{\mathrm{cr}}+5$ °C are plotted in Fig. 3b in the interval of the self-compensated state of donor and acceptor point defects. Curve *1*, corresponding to the first condition, is lower on the concentration axis and characterizes samples having minimum n-type conductivity. Curve *2* characterizes predominantly p-type samples. The greater vulnerability to losses of cadmium atoms into the gaseous phase during annealing in the first case produces a higher content of V_{Cd}^{-2}. The deep energy level of this defect lies above the middle of the band gap in CdTe and explains the lower curve. In samples ''protected'' by the filler during annealing the p-type conductivity is attributable to the formation of $[V_{\mathrm{Cd}}\mathrm{Cl}]^{-}$ complexes, whose energy level is situated in the lower half of the band gap.

We now discuss the results shown in Fig. 3 in the region of low $P_{\mathrm{Te2}}\sim P_{\mathrm{min}}$. Samples annealed at $t_{\mathrm{cr}}=735$ °C exhibit only n-type conductivity (Fig. 3a). At this temperature the solubility of V_{Cd} is small in comparison with the concentration of $\mathrm{Cl}_{\mathrm{Te}}^{+}$ in the crystal (see Fig. 1). In keeping with the self-compensation process,[2] a charged V_{Cd}^{-2} center is formed, creating a deep level in the band gap and dictating a small value of n. The value of n is lowest here in comparison with the value measured for crystals annealed at higher temperatures t_{cr}. As t_{cr} is raised, following the P_{min} line (see Fig. 1), a high concentration of acceptor native point defects (V_{Cd}) is obtained in the crystal (Fig. 3b). Samples annealed at

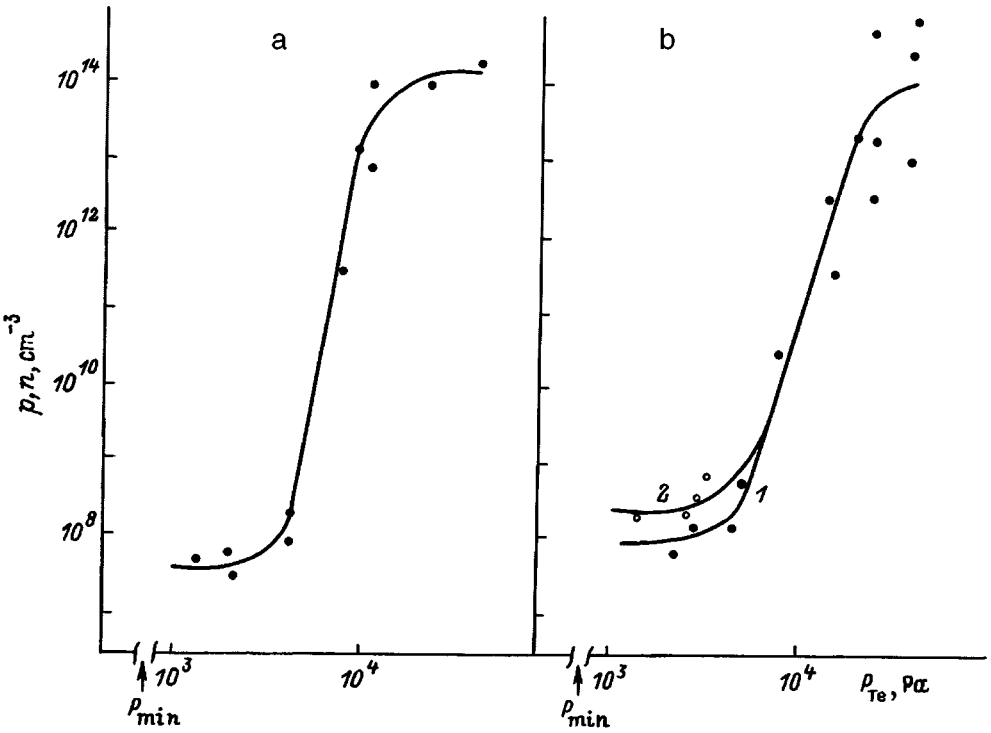

FIG. 3. Free-carrier density in the crystal versus P_{Te2}. a) $t_{\mathrm{cr}}=735$ °C; b) 900 °C; *1*) $t_p=t_{\mathrm{cr}}$; *2*) $t_p=t_{\mathrm{cr}}+5$ °C. The dark symbols correspond to n, and the light symbols to p.

$t_{\mathrm{cr}}=900$ °C for $P_{\mathrm{Te2}}\sim P_{\min}$ have p-type conductivity at low pressures, which goes over to n-type conductivity as the pressure increases (Fig. 3b, curve *2*), and then the conductivity, still n-type, rises abruptly. This transition to n-type conductivity with a sharp increase in the density of electrons as P_{Te2} increases cannot be explained by the native point defects customarily invoked in the self-compensation mechanism.

The results pertaining to the transition to n-type conductivity with a sharp increase in the electron density as P_{Te2} increases can be explained by analyzing the participation of an antistructural defect, in this case the donor $\mathrm{Te}_{\mathrm{Cd}}^{+2}$, in thermodynamic equilibrium. The formation of antistructural defects can be portrayed as the transition of Te atoms from lattice sites or interstitial Te_i to V_{Cd} sites, whose concentration increases with P_{Te2}:

$$V_{\mathrm{Cd}}+\mathrm{Te}_i=\mathrm{Te}_{\mathrm{Cd}}. \qquad (1)$$

A calculation of the enthalpy of formation of $\mathrm{Te}_{\mathrm{Cd}}$ for the conditions of saturation of CdTe with tellurium gives $\Delta H(\mathrm{Te}_{\mathrm{Cd}})=3.76$ eV (Ref. 8), which is lower than the enthalpy of formation $\Delta H(V_{\mathrm{Cd}})=4.75$ eV (Ref. 8). These values differ considerably from the previously published results $\Delta H(\mathrm{Te}_{\mathrm{Cd}})=5.56$ eV and $\Delta H(V_{\mathrm{Cd}})=2.5$ eV (Refs. 9 and 10). The data of Ref. 8 lead to the conclusion that the equilibrium (1) shifts toward the formation of an antistructural defect. However, the domination of the latter cannot account for n increasing to $\sim 10^{14}$ cm^{-3} in the crystal as P_{Te2} increases, because the level of the $\mathrm{Te}_{\mathrm{Cd}}^{+2}$ center is below $E_c=0.6$ eV in the band gap of cadmium telluride.[8] The concentration $n\sim 10^{14}$ cm^{-3} can be obtained in the crystal by virtue of a decrease in the total quantity of V_{Cd} due to the shift of the equilibrium (1) to the right. The equilibrium of self-compensation $N_{\mathrm{Cl}}^{+}=(1/2)N_{V\mathrm{Cd}}^{-2}$ is violated in this case. The remaining uncompensated $\mathrm{Cl}_{\mathrm{Te}}^{+}$ donor ($E_c-0.01$ eV, Ref. 11) is then the center responsible for n-type conductivity with such a high carrier density.

A calculation in Ref. 8 shows that compensation can take place not only at high temperatures of the thermodynamic equilibrium state, but also when the crystal is cooled, owing to a local energy gain when it becomes impossible for a diffusion sink of native point defects to evolve. The Te_i content is known to become large, $\geqslant 10^{16}$ cm^{-3}, at high temperatures.[12] Residing in a tetrahedral interstice, Te_i exhibits high external relaxation and becomes readily attracted to regions where lattice stresses (generated during cooldown) can be relieved, i.e., to regions of high V_{Cd} concentration, in which the relaxation and movement of neighboring atoms take place.[13] This process is conducive to the creation of a $\mathrm{Te}_{\mathrm{Cd}}$ antistructural defect, where the concentration of the center can be quite high ($\geqslant N_{\mathrm{Te}i}$), and the distribution in the crystal is very nonuniform, forming n-type and p-type regions with compensated conductivity.

A generalized dependence of the variation of the carrier density on P_{Cd} and P_{Te} can be plotted on the basis of the results from the annealing of CdTe⟨Cl⟩ crystals in tellurium vapor (data of our study) and in cadmium vapor (data of our earlier work[4]). It is evident (Fig. 4) that for $P_{\mathrm{Cd}}\sim 10^4$ Pa the crystal has n-type conductivity with $n\approx 10^{14}$ cm^{-3}, which is determined by shallow $\mathrm{Cl}_{\mathrm{Te}}^{+}$ donors uncompensated by V_{Cd}^{-2}, owing to their low density at high values of P_{Cd}. As P_{Cd} is lowered, the concentration of V_{Cd}^{-2} increases, enhancing the degree of self-compensation, whereupon the electron density drops to $\sim 10^7$ cm^{-3}, and then the inversion of p-type con-

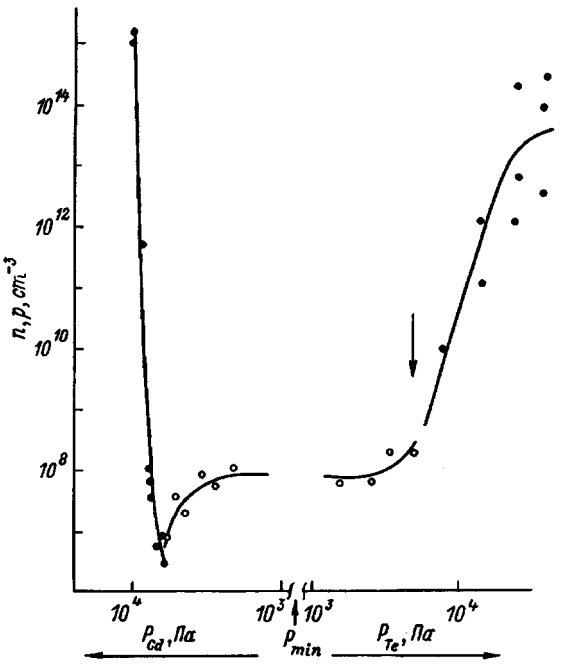

FIG. 4. Free-carrier density in a crystal versus P_{Cd} and P_{Te2} at t_{cr}=900 °C. The dark symbols correspond to n, and the light symbols to p.

ductivity sets in. With a further reduction in P_{Cd}, the hole density increases slightly to $\sim 10^8$ cm^{-3} and then, even as P_{Te2} increases, continues to also increase slightly to $\sim 10^9$ cm^{-3}. In this region of low pressures P_{Cd} and P_{Te} the hole conductivity is determined by the deep V_{Cd}^{-2} acceptor, whose concentration increases with P_{Te2}. Then, in the vicinity of pressures $P_{\mathrm{Te}} \sim 5 \times 10^3$ Pa (indicated by the arrow in Fig. 4), the conductivity of the crystal again changes sign to n-type, and the electron density climbs abruptly to $\sim 10^{14}$ cm^{-3}. This unexpected inversion of the conductivity and its sharp rise are attributable (as for large P_{Cd}) to shallow $\mathrm{Cl}_{\mathrm{Te}}^{+}$ donors, which can emerge only as a result of a decrease in the concentration of V_{Cd}^{-2}. For a high pressure P_{Te} the only way such a decrease can take place is by the formation of a $\mathrm{Te}_{\mathrm{Cd}}^{+2}$ antistructural defect. Indeed, as P_{Te2} increases, more and more V_{Cd}^{-2} and Te_i are encountered, where, as mentioned above, it is energetically favorable for the latter to take the place of V_{Cd}^{-2} and to disrupt the self-compensation process. It is evident, therefore, that self-compensation is more or less complete and leads to the formation of semiinsulating p-type and n-type crystals at pressures $P_{\mathrm{Cd}}, P_{\mathrm{Te}} < 10^4$ Pa, whereas at high pressures P_{Cd} and P_{Te} self-compensation is disrupted, and low-resistivity n-type crystals are obtained.

[1] F. A. Kröger and J. Vink, Phys. Status Solidi **3**, 310 (1956).
[2] G. Mandel, Phys. Rev. A **134**, 1073 (1964).
[3] F. A. Kröger, *The Chemistry of Imperfect Crystals* (North-Holland, Amsterdam; Wiley, New York, 1964).
[4] O. A. Matveev and A. I. Terent'ev, Fiz. Tekh. Poluprovodn. **27**, 1894 (1993) [Semiconductors **27**, 1043 (1993)].
[5] R. O. Bell, F. V. Wald, C. Canaly, F. Nava, and G. Ottaviani, IEEE Trans. Nucl. Sci. **NS-21**, 331 (1974).
[6] O. A. Matveev, E. N. Arkad'eva, and L. N. Goncharov, Dokl. Akad. Nauk SSSR **221**, 325 (1975) [Sov. Phys. Dokl. **20**, 147 (1975)].
[7] E. N. Arkadyeva and O. A. Matveev, Rev. Phys. Appl. **12**, 239 (1977).
[8] M. A. Berding, M. Van Schilfgaarde, A. T. Paxton, and A. Sher, J. Vac. Sci. Technol. A **8**, 1103 (1990).
[9] J. A. Van Vechten, J. Electrochem. Soc. **122**, 423 (1975).
[10] V. N. Martynov and S. P. Kobeleva, Kristallografiya **28**, 394 (1983) [Sov. Phys. Crystallogr. **28**, 232 (1983)].
[11] D. Nobel, Philips Res. Rep. **14**, 361 (1959).
[12] S. S. Chern and F. A. Kröger, J. Solid State Chem. **14**, 44 (1975).
[13] J. T. Schick and C. G. Morgan-Pond, J. Vac. Sci. Technol. A **8**, 1108 (1990).

Translated by James S. Wood

Negative dynamic differential conductivity at the cyclotron frequency in $Ga_{1-x}Al_xAs$ under conditions of ballistic intervalley electron transfer

G. É. Dzamukashvili, Z. S. Kachlishvili, and N. K. Metreveli

Tbilisi State University, 380028 Tbilisi, Georgia
(Submitted May 20, 1996; accepted for publication May 22, 1997)
Fiz. Tekh. Poluprovodn. **32**, 164–170 (February 1998)

It is theoretically shown that under certain conditions a cyclotron resonance maser can be fabricated based on n-$Ga_{1-x}Al_xAs$-type materials. Low temperatures and strong crossed fields ($\mathbf{E}\perp\mathbf{H}$) are considered. In these fields the electrons in the lower (light) valley of the conduction band dynamically (ballistically) transit the band up to the onset energy of intervalley scattering ε_0. Studies were carried out on solid solutions with composition $0<x<0.39$ ($\varepsilon_0=(2-17)\hbar\omega^*$, where $\hbar\omega^*$ is the intervalley phonon energy). The magnitudes of the **E** and **H** fields were varied within the limits $E=5-20$ kV/cm and $H=6-40$ kOe. This produced a smooth change in the transit conditions in the passive region ($\varepsilon<\varepsilon_0$), which makes it possible to obtain the desired frequency dependence of the differential conductivity (DC), $\sigma(\omega)$. As our studies show, previously unknown, interesting peculiarities of the hot electron system appear under these conditions. © *1998 American Institute of Physics.* [S1063-7826(98)00901-6]

1. The idea of building a semiconductor maser at the cyclotron resonance (CR) has been around for a long time.[1–3] Andronov and Kozlov[4] noted the possibility of negative differential conductivity (NDC) of hot electrons under conditions of cyclotron resonance and their scattering by optical phonons under conditions that had been considered in Ref. 5. This possibility was discussed in detail in Ref. 6 on the basis of a Monte Carlo calculation, where it was shown that in pure p-type Ge and n-type GaAs materials negative differential conductivity at the cyclotron resonance is manifested at $\omega>10^{12}$ Hz and higher.

In the indicated works, strong inelastic scattering of the current carriers enters only at energies above some threshold energy ε_0, while for $\varepsilon<\varepsilon_0$ (the passive region) scattering is weak and the carriers move almost freely under the action of the electromagnetic fields. The energy ε_0 here is the energy of the optical phonon $\varepsilon_0=\hbar\omega_0$. Under such conditions, as is well known, the distribution of hot carriers is strongly anisotropic.

The authors of Ref. 6 also noted the possibility of the realization of negative differential conductivity in a strong electric field in n-GaAs under conditions of intense exchange of electrons between the light and heavy valleys. The possibility of the realization of this idea was also addressed in Refs. 7–9, in which the energy of the intervalley transitions (IVT) enters as the energy ε_0: $\varepsilon_0=\Delta\varepsilon+\hbar\omega^*$ ($\Delta\varepsilon$ is the energy gap between the light and heavy valleys, and $\hbar\omega^*$ is the intervalley phonon energy). It was shown that under conditions of the ballistic heating regime in a strong electric field **E** regions of dynamic NDC appear at frequencies in the submillimeter range. It was also shown, in particular, that by using the material n-$Ga_{1-x}Al_xAs$ and varying its composition it is possible to smoothly vary $\Delta\varepsilon$ and thereby, in contrast to the results of Refs. 4–6, vary the transit conditions, which in turn makes it possible to smoothly vary the NDC frequency by varying the electric field **E**. This can be used as a method for modifying the frequency dependence of the differential conductivity $\sigma(\omega)$.

In Refs. 7–9 the problem was considered in the absence of a magnetic field. Obviously, a study of the dynamics of the intervalley transitions in n-$Ga_{1-x}Al_xAs$ in the presence of a transverse magnetic field ($\mathbf{E}\perp\mathbf{H}$) with smooth variation of the region of dynamic heating within the limits of one to several multiples of $\hbar\omega^*$ would be of definite scientific and practical interest. Such a study could reveal the optimal size of the region of free motion of the electrons (and correspondingly the optimal composition of the ternary compound) and the optimal relationship between the **E** and **H** fields for realizing NDC at the cyclotron resonance with better parameters than are known at present under such conditions.[4–6] As far as we know, such studies have not yet been performed.

The present paper presents an analytic study of dynamic NDC in transverse electric and magnetic fields (where the latter is not a quantizing field) $\mathbf{E}\perp\mathbf{H}$ under conditions of dynamic intervalley transitions in n-$Ga_{1-x}Al_xAs$ over a wide range of variation of its composition $0<x<0.39$, where $\Delta\varepsilon$ varies in the limits $\Delta\varepsilon=(1-16)\hbar\omega^*$. The possibility of observing NDC at the cyclotron resonance in the submillimeter range under these conditions was noted in Ref. 10.

2. The calculations use the two-valley model of intervalley transport[7–9] under the assumption that scattering by phonons is absent in the lower valley. As is known, this assumption is valid in a strong enough electric field if the following condition is satisfied $\tau_E<\tau_{op}$, where τ_E and τ_{op} are the collision time of the Γ valley and the intravalley scattering time on the optical phonons, respectively. We assume that the lattice temperature is low ($k_0T\ll\hbar\omega^*$). In this case the electrons, which pass through the Γ valley without scattering, acquire the energy ε_0 and, after the emission of an intervalley phonon, transition into the X valley. In the X valleys the energy of the electrons ε^* is small due to their large effective mass, $\varepsilon^*\ll\hbar\omega^*$ (this condition also imposes

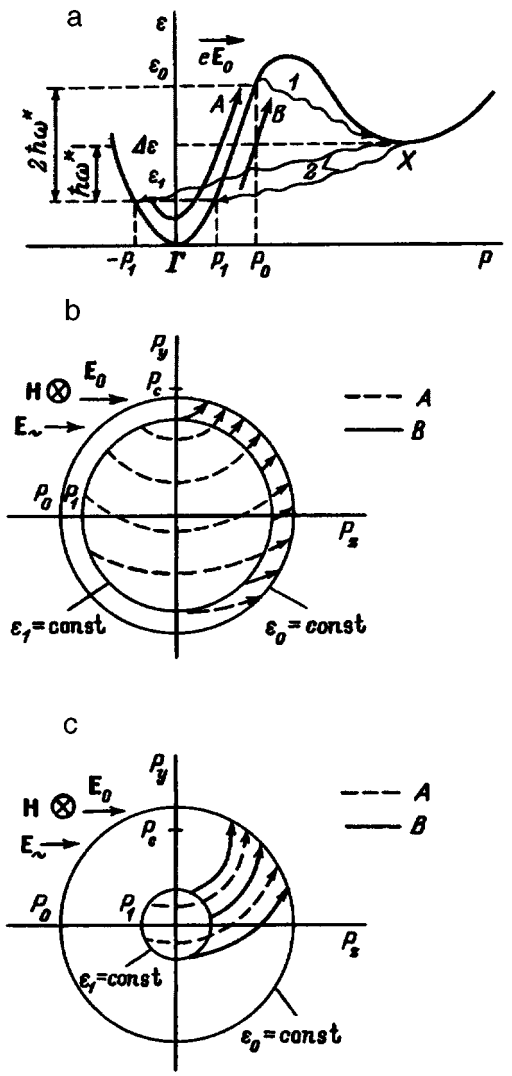

FIG. 1. Diagram of intervalley transitions (a) and their distribution in the momentum space of the Γ-valley for the case $\Delta\varepsilon \gg \hbar\omega^*$ (b) and $\Delta\varepsilon \approx \hbar\omega^*$ (c). The following transitions are indicated: *1*—$\Gamma \to X$, *2*—$X \to \Gamma$. In figures a and b the dashed lines with arrows represent the free motion of the *A* electrons and the solid lines with arrows denote the *B* electrons.

a limit on the maximum value of the applied electric field); therefore, after returning to the Γ valley they are concentrated near the isoenergy surface $\varepsilon_1 = \Delta\varepsilon - \hbar\omega^*$ (see Fig. 1), where they begin a new cycle of acceleration. Under such conditions, in materials of the type $Ga_{1-x}Al_xAs$ two types of electrons appear in the lower Γ valley (*A* and *B*) with different acceleration times (τ_E^A and τ_E^B) in the electric field[7–9]

$$\tau_E^A = \frac{P_0 + P_1}{eE_0}, \quad \tau_E^B = \frac{P_0 - P_1}{eE_0}, \tag{1}$$

where

$$P_{0,1} = \sqrt{2m_\Gamma^*(\Delta\varepsilon \pm \hbar\omega^*)},$$

m_Γ^* is the effective electron mass in the Γ valley, and E_0 is the magnitude of the constant electric field. The configuration of the fields is shown in Fig. 1. Calculations were carried out in the regime of prescribed field direction (closed Hall contacts), where the applied electric field plays the role of the heating field and the electrons move under the action of the magnetic field in cyclotron trajectories in momentum space, whose centers lie on the segment $(P_x, P_c, 0)$, $-P_1 < P_x < P_1$ ($P_c = c_0 m_\Gamma^* E_0 / H$, where c_0 is the speed of light). The radii of these trajectories increase with distance from the *yz* plane since the radii of the circles obtained by intersection of the spherical surfaces $\varepsilon_1 = \text{const}$ and $\varepsilon_0 = \text{const}$ with the plane $x = \text{const}$ vary correspondingly (they decrease). These radii are $P_1' = \sqrt{P_1^2 - P_x^2}$ and $P_0' = \sqrt{P_0^2 - P_x^2}$, respectively, and reach their maxima at $P_x = 0$ and their minima at $P_x = \pm P_1$. Hence it follows that the curvature of the cyclotron trajectories increases with decreasing, the smaller is P_x. In the case

$$P_c \geqslant (P_0 + P_1)/2 \equiv P_c^* \tag{2}$$

all trajectories are open (they intersect the surface $\varepsilon_0 = \text{const}$). Inequality (2) imposes a constraint on the magnitudes of the electric and magnetic fields

$$\frac{H}{E_0} \leqslant \frac{2c_0 m_\Gamma^*}{P_0 + P_1} = \frac{c_0 m_\Gamma^*}{P_c^*}. \tag{3}$$

If this condition is satisfied, not one electron will be held in a magnetic ''trap.''

3. The linearized kinetic equation (linearized Boltzmann equation) was solved for a small additional term added to the distribution function, $f_\sim = f_\sim^0 e^{i\omega t}$, which arises in a small-amplitude variable field $\mathbf{E}_\sim = \mathbf{E}_\sim^0 e^{i\omega t}$ ($\mathbf{E} = \mathbf{E}_0 + \mathbf{E}_\sim, \mathbf{E}_\sim^0 \ll \mathbf{E}_0$). For convenience, the equation is written in the coordinates $\{P_x, P_r, \varphi\}$, which are related to the phase coordinates $\{P_x, P_y, P_z\}$ by the equations $P_x = P_x$, $P_y = P_c + P_r \cos\varphi$, and $P_z = -P_r \sin\varphi$, where $P_r = [P_z^2 + (P_y - P_c)^2]^{1/2}$ and $\tan\varphi = P_z/(P_c - P_y)$. In fields with the configurations $\mathbf{E}_0 \| z$, $\mathbf{H} \| x$, $\mathbf{E}_\sim \| \mathbf{E}_0$ equations exist for the functions $f_\sim^A$ and $f_\sim^B$ corresponding to the two groups of electrons (*A* and *B*):

$$i\omega f_\sim^A + \omega_c \frac{\partial f_\sim^A}{\partial \varphi} = -eE_\sim^0 \frac{\partial f_0^A}{\partial P_z}\theta(\varphi - \varphi_1), \quad \varepsilon < \varepsilon_0;$$

$$i\omega f_\sim^B + \omega_c \frac{\partial f_\sim^B}{\partial \varphi} = -eE_\sim^0 \frac{\partial f_0^B}{\partial P_z}\theta(\varphi - \varphi_2), \quad \varepsilon < \varepsilon_0, \tag{4}$$

$$\theta(\zeta) = \begin{cases} 1, & \zeta \geqslant 0; \\ 0, & \zeta < 0; \end{cases} \tag{5}$$

$$\varphi_1 = \arccos\left(\frac{P_1^2 - P_x^2 - P_r^2 - P_c^2}{2P_c P_r}\right), \quad \varphi_2 = 2\pi - \varphi_1, \tag{6}$$

where $\omega_c = eH/m_\Gamma^* c_0$ is the cyclotron frequency, and f_0^A and f_0^B are the distribution functions in the Γ valley in constant crossed fields $\mathbf{E}_0 \perp \mathbf{H}$. They satisfy the kinetic equation in constant fields and the condition of conservation of the total number of electrons in both valleys:

$$\omega_c \frac{\partial f_0^A}{\partial \varphi} = \frac{N_X \nu_1}{2\pi P_1}\,\delta(P^2 - P_1^2)\,\theta(\varphi - \varphi_1), \quad \varepsilon < \varepsilon_0; \tag{7}$$

$$\omega_c \frac{\partial f_0^B}{\partial \varphi} = \frac{N_X \nu_1}{2\pi P_1}\,\delta(P^2 - P_1^2)\,\theta(\varphi - \varphi_2), \quad \varepsilon < \varepsilon_0; \tag{8}$$

$$\int (f_0^A + f_0^B) d^3P + N_X = N_0 = \text{const}, \tag{9}$$

where N_X is the electron concentration in the X valleys, $\nu_1 = D_{\Gamma X}^2 (m_\Gamma^*) \sqrt{\varepsilon_1}/\sqrt{2}\pi\hbar^3\rho\omega^*$ is the characteristic frequency of the transition $X \to \Gamma$, $D_{\Gamma X}$ is the coupling constant of the Γ and X valleys, and ρ is the density of the sample. Among the kinetic coefficients the characteristic frequency of the transition $\Gamma \to X$ (ν_0) is the largest parameter. It far exceeds ν_1: $\nu_0/\nu_1 = (m_X^*/m_\Gamma^*)^{3/2}(\varepsilon_0/\varepsilon_1)^{1/2} \gg 1$. Therefore, the number of electrons in the energy region $\varepsilon > \varepsilon_0$ is small and their contribution to the conductivity can be ignored.[9] The main processes determining the conductivity take place in the region $\varepsilon < \varepsilon_0$. Therefore, those terms which appear when $\varepsilon > \epsilon_0$ are absent in the equations. The Dirac δ-function appears on the right-hand side of Eqs. (7) and (8) because of the small width of the source in the Γ valley. The factor preceding the δ-function is associated with the normalization condition (9).

We do not go through the derivation of the solution of the system of differential equations (4)–(9) here, but merely note that the component of the differential conductivity tensor σ_{zz} is represented in the form of a sum of two terms corresponding to the two different groups of electrons:

$$\sigma_{zz} = \sigma^A + \sigma^B = \frac{1}{E_\sim^0}\frac{e}{m_\Gamma^*}\int\int\int (-P_r \sin\varphi) \times (f_\sim^A + f_\sim^B) P_r dP_r dP_x d\varphi, \tag{10}$$

$$\sigma^A = \sigma_0 \frac{a}{4\pi\alpha}\frac{1}{1-\Omega_c^2}\int\int_{\Sigma_A}\int \frac{\sin\varphi}{|\sin\varphi_1|} \times [(1+\Omega_c^2)\cos\varphi_1 \cos\Omega_c(\varphi-\varphi_1) - 2\Omega_c \sin\varphi_1 \sin\Omega_c(\varphi-\varphi_1) - 2\cos\varphi] dx dr d\varphi, \tag{11}$$

$$\sigma^B = \sigma_0 \frac{a}{4\pi\alpha}\frac{1}{1-\Omega_c^2}\int\int_{\Sigma_B}\int \frac{\sin\varphi}{|\sin\varphi_2|} \times [(1+\Omega_c^2)\cos\varphi_2 \cos\Omega_c(\varphi-\varphi_2) - 2\Omega_c \sin\varphi_2 \sin\Omega_c(\varphi-\varphi_2) - 2\cos\varphi] dx dr d\varphi, \tag{12}$$

$$\sigma_0 = \frac{e^2 N_X \nu_1}{m_\Gamma^* \nu_E^2},$$

where $a = P_c/P_0$, $\alpha = \sqrt{\varepsilon_1/\varepsilon_0}$, $\Omega_c = \omega/\omega_c$, $\nu_E = \tau_E^{-1} = eE_0/P_0$ is the transit frequency in the Γ valley, $x = P_x/P_0$, $r = P_r/P_0$, and $\Sigma_{A,B}$ are the regions of motion of the A and B electrons in momentum space. The integrals in Eqs. (10) and (11) were calculated numerically using the Monte Carlo technique.

4. The frequency dependences of the differential conductivity for different values of the initial parameters are shown in Fig. 2–5. These dependences are easily explained by taking into account the changes in the dynamics of heating of the electrons brought about by changes in $\Delta\varepsilon$, $\mathbf{E}_0$, and $\mathbf{H}$. These quantities uniquely determine the relationships between τ_E^A, τ_E^B, ν_E, and ω_c. To these parameters we add one more, ω, the frequency of the external variable electric field, applied as a small perturbation of the strongly nonequilibrium system of electrons. By varying $\Delta\varepsilon$ we can take into account all the particular features of the band structure: the effective masses of the electrons in the different valleys, the coupling constants between the valleys, the energy of the intervalley phonons, the density of the sample, and so on, which are uniquely determined by the composition of the solution.[11]

4.1. Small $\Delta\varepsilon$. For $\Delta\varepsilon = (1-3)\hbar\omega^*$ (corresponding to composition of the solid solution $0.34 < x < 0.39$) the radius of the surface $\varepsilon_1 = \text{const}$ is small (the difference between P_1 and P_0 is large), and the two different groups of electrons have similar heating times (for heating by the electric field) ($\tau_E^A \approx \tau_E^B$). Here, because of the smallness of P_1 there is no noticeable difference between the transit times within one of the groups of electrons. In this case, by the so-called process of intervalley streaming,[8] as the electrons heat up, their trajectories form a narrow beam in momentum space which is preserved along the cyclotron trajectories (Fig. 1c). Under these conditions the magnetic fields satisfying condition (3) are entirely sufficient for the appearance of a resonance in $\sigma(\omega)$. The resonance appears near the cyclotron frequency $\omega \approx \omega_c$. If we consider the field region in which all the trajectories are open, it turns out that the most pronounced resonance is set up at $\omega_c = \omega_c^*$ (Fig. 2a), where

$$\omega_c^* = eH^*/m_\Gamma^* c_0 = eE_0/P_c^* = 2eE_0/(P_0+P_1). \tag{13}$$

From conditions (3) and (13) we find the optimal relationship between the magnitudes of the electric and magnetic fields (between E_0^* and H^*), for which the width of the resonance line is maximum

$$H^*/E_0^* = 2c_0 m_\Gamma^*/(P_0+P_1). \tag{14}$$

For small $\Delta\varepsilon$ the existence in the system of a well-defined transit time has the result that a decrease in the ratio H/E_0 within certain limits (when P_c becomes larger than P_c^*) does not suppress the resonance (Fig. 2b). For $\Delta\varepsilon = \hbar\omega^*$ the range of variation of P_c in which resonance is observed is quite wide: $0.55P_0 < P_c < 0.7P_0$. For $E_0 = 10$ kV/cm it corresponds to the region of magnetic fields 29 kOe$< H <$37.5 kOe. The width of this region varies in proportion to E_0. Here we may note that the position of the point P_c in momentum space uniquely defines the relation between the characteristic transit time in the Γ valley and the cyclotron frequency $\nu_E/\omega_c = P_c/P_0$.

4.2. Intermediate and large $\Delta\varepsilon$. For $\Delta\varepsilon = (3-8)\hbar\omega^* \times (0.2 < x < 0.34)$, P_1 and P_0 converge and a difference appears between the transit times inside one group of electrons as well as between τ_E^A and τ_E^B. In the system a distinct heating time is no longer present, and therefore at $\omega_c = \omega_c^*$ the resonance peak is narrow in comparison with the case $\Delta\varepsilon \approx \hbar\omega^*$ (Figs. 3 and 4). The shift of P_c toward larger values suppresses the resonance. The suppression is that efficiency increases with increasing value of $\Delta\varepsilon$.

In the case of the band structure of GaAs ($\Delta\varepsilon = 16\hbar\omega^*$), where the difference between P_1 and P_0 is limitingly small ($P_1/P_0 = 0.94$), τ_E^A and τ_E^B differ widely

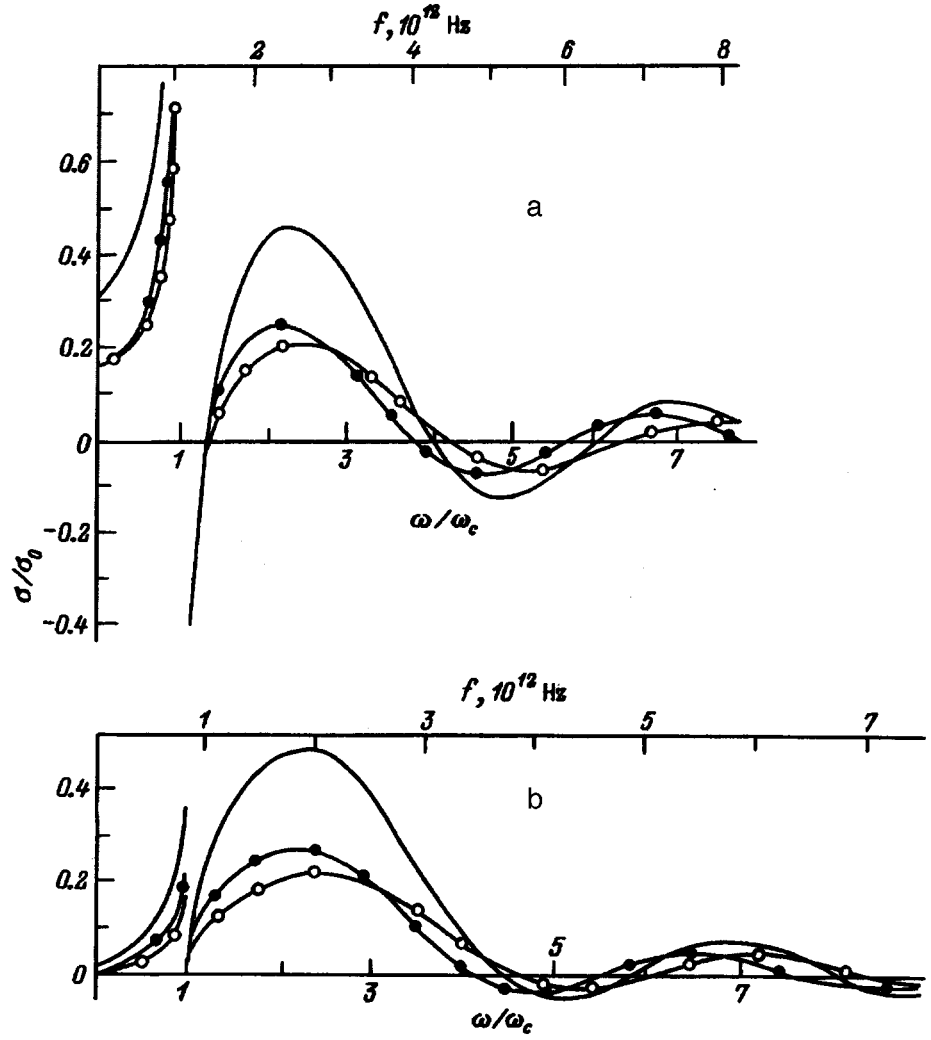

FIG. 2. Dependence of the differential conductivity in the Γ valley, σ, on the frequency of the external variable electric field, ω, for $\Delta\varepsilon = 1.02\hbar\omega^*(Ga_{0.61}Al_{0.39}As)$, $\sigma_0 = e^2 N_X \nu_1 / m_\Gamma^* \nu_E^2$. Calculation parameters: $E_0 = E_0^* = 10$ kV/cm; a—$H = H^* = 37.5$ kOe ($P_c = 0.55P_0$), $\omega_c = 6.67\times10^{12}$ s^{-1}; b—$H = 29.5$ kOe ($P_c = 0.7P_0$), $\omega_c = 5.24\times10^{12}$ s^{-1}. The solid curves with filled points plot the calculated conductivity of the *A* electrons, and the solid curves with empty points plot that of the *B* electrons; the solid lines without points correspond to the total conductivity.

($\tau_E^A/\tau_E^B \approx 32$), and the difference between the heating times of the different electrons inside group *A* is greater than 20%. On the other hand, the electrons in group *B* acquire almost identical transit times (Fig. 1b). This latter circumstance results in the appearance of a resonance in the differential conductivity of the *B* electrons only for $P_c = P_c^*$; however, this resonance can no longer ensure total dynamic negative differential conductivity since for $\omega = \omega_c$ the *A* electrons have positive differential conductivity, which exceeds the negative differential conductivity of the *B* electrons in absolute value (Fig. 5a). A small increase in P_c causes the disappearance of the resonance peak in $\sigma^B(\omega)$. In our opinion, this also ex-

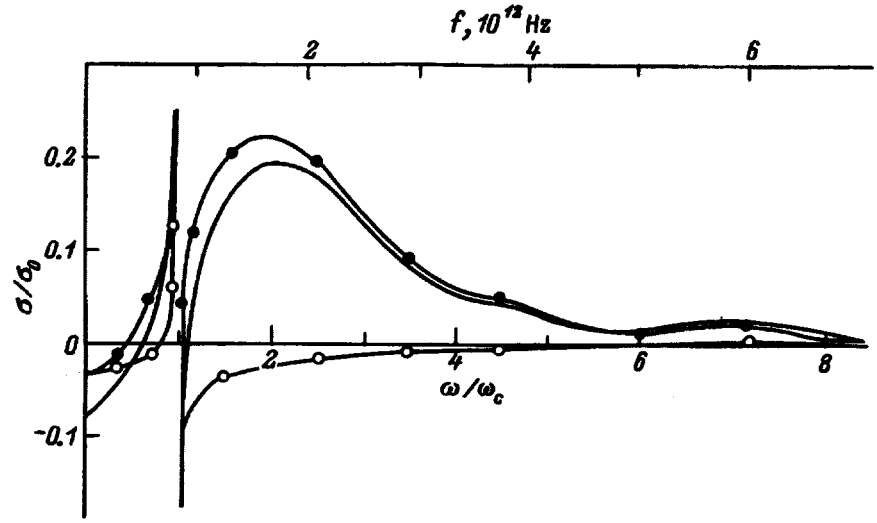

FIG. 3. Dependence of the differential conductivity in the Γ valley, σ, on the frequency of the external variable electric field, ω, for $\Delta\varepsilon = 4.5\hbar\omega^* \times (Ga_{0.7}Al_{0.3}As)$. Calculation parameters: $E_0 = E_0^* = 20$ kV/cm, $H = H^* = 27$ kOe ($P_c = 0.9P_0$), $\omega_c = 6.23\times10^{12}$ s^{-1}. The notation is the same as in Fig. 2.

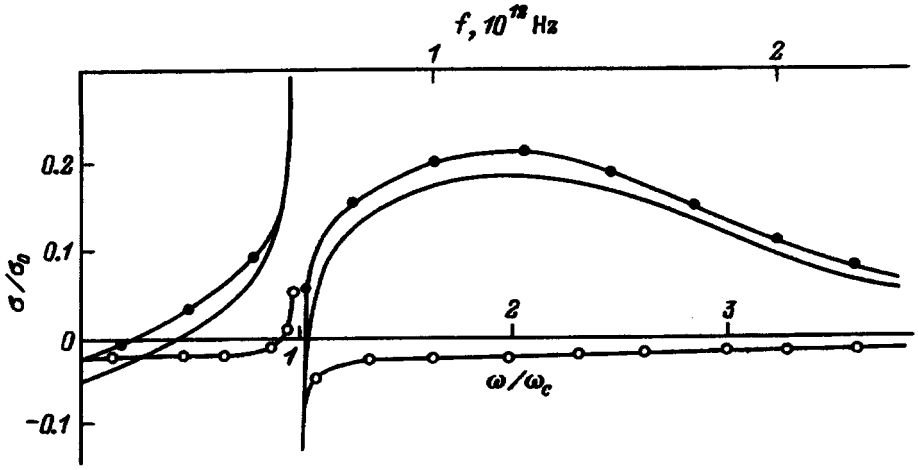

FIG. 4. Dependence of the differential conductivity in the Γ valley, σ, on the frequency of the external variable electric field, ω, for $\Delta\varepsilon = 10\hbar\omega^*(Ga_{0.84}Al_{0.16}As)$. Calculation parameters: $E_0 = E_0^* = 20$ kV/cm, $H = H^* = 18$ kOe, $\omega_c = 3.88\times 10^{12}$ s^{-1}. The notation is the same as in Fig. 2.

plains the fact that efforts to obtain negative differential conductivity at the cyclotron resonance in GaAs have been so far unsuccessful. Apparently, for such values of $\Delta\varepsilon$ the magnetic field must be increased to the point at which closed trajectories appear in the system.

Thus, when $\Delta\varepsilon \gg \hbar\omega^*$ and the condition (3) is satisfied, the resonance does not appear. However, at such values of $\Delta\varepsilon$, as in GaAs, there is a different mechanism for the appearance of dynamic negative differential conductivity, based on the wide difference between τ_E^A and τ_E^B. In the high-frequency region of NDC, the conductivity of the fast B electrons is greater in absolute value than the positive differential conductivity of the slow A electrons. As a result, in the frequency region $1/\tau_E^A \ll \omega_c < 1/\tau_E^B$ we have dynamic negative differential conductivity in a strong electric field.[7,8]

5. In the experimental detection of dynamic NDC the magnitude of the static NDC, which gives rise to the appearance of the low-frequency oscillations, plays no small role. In the case of negative differential conductivity at the cyclotron resonance,[4,6] static negative differential conductivity is

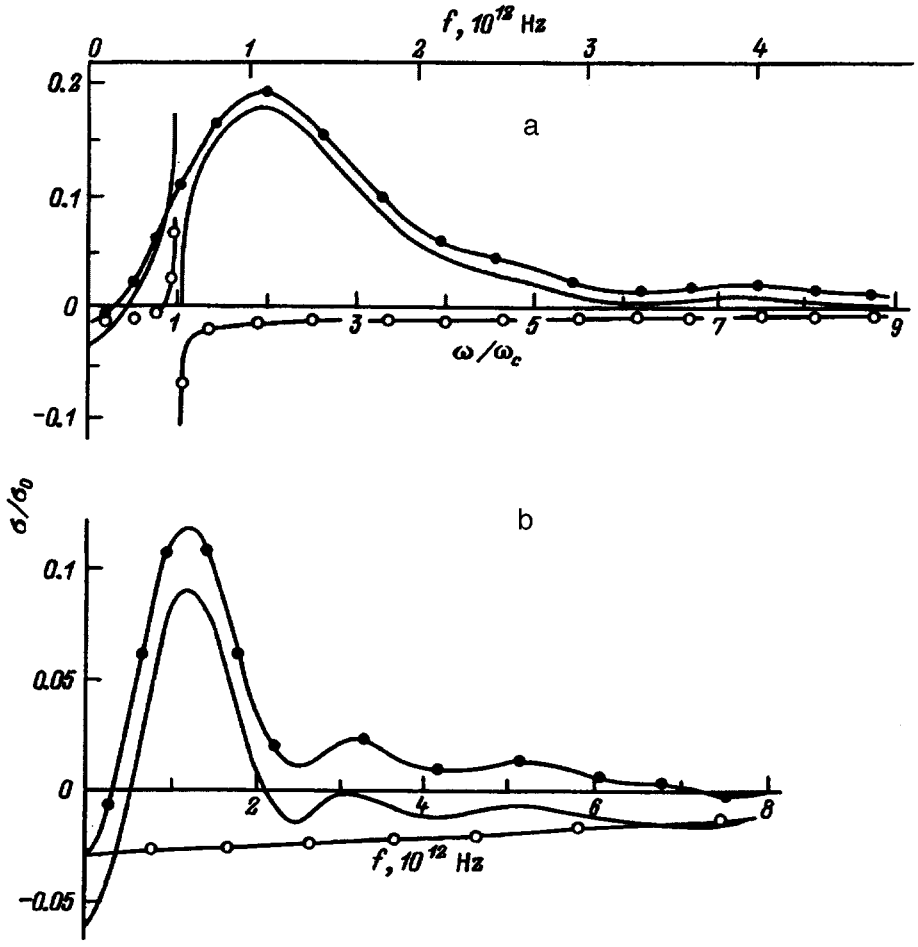

FIG. 5. Dependence of the differential conductivity in the Γ valley, σ, on the frequency of the external variable electric field, ω, for $\Delta\varepsilon = 16\hbar\omega^*$ (GaAs). Calculation parameters: $E_0 = E_0^* = 20$ kV/cm; a—$H = H^* = 13$ kOe ($P_c = 0.97P_0$), $\omega_c = 3.36\times 10^{12}$ s^{-1}; b—$H = 0$, calculation from Ref. 8. The notation is the same as in Fig. 2.

absent. This circumstance which eliminates the need for special measures to prevent low-frequency oscillations, which interfere with the detection of superhigh-frequency NDC. In the case of transit intervalley transitions in n-GaAs and n-$Ga_{1-x}Al_xAs$ (Refs. 6, 7–9) the static NDC dominates over the dynamic NDC. The appearance of static NDC is due to strong inversion of the electrons ($\partial f/\partial\varepsilon>0$) in an electric field.[8,12]

In Ref. 13 it was shown that energy inversion is reduced by switching on a transverse magnetic field. Such a reduction is that much more effective, the smaller is $\Delta\varepsilon$. Calculations of the current-voltage characteristics in n-$Ga_{1-x}Al_xAs$ in crossed fields $\mathbf{E}_0\perp\mathbf{H}$ show[14] that the magnitude of the static NDC also increases in absolute value with increase of the magnetic field and decrease of $\Delta\varepsilon$. For $\Delta\varepsilon\approx\hbar\omega^*$ the elimination of the static NDC is easily achieved. These results are in good agreement with the calculated dependences $\sigma=\sigma(\omega)$ shown in Figs. 2–5. The differential conductivity near zero frequency $\sigma(\omega\approx0)$ decreases in absolute value, with increasing magnetic field (for the same value of $\Delta\varepsilon$). For $\Delta\varepsilon\approx\hbar\omega^*$ in fields in which dynamic NDC is present, $\sigma(\omega=0)\gtrsim0$. This result is important since it is precisely at such values of $\Delta\varepsilon$ that the width of the resonance band is maximum (see Fig. 2a). As was shown above, the width of the cyclotron resonance line decreases with increase of H. For this reason, the cyclotron resonance at small $\Delta\varepsilon$ manifests its lowest sensitivity to external factors and inadequacies of the model.

The inadequacy of the model consists mainly in the fact that we do not consider the region $\varepsilon>\varepsilon_0$. Penetration of electrons into this region increases the heating time and introduces a positive contribution to the differential conductivity.[9] On the other hand, such penetration smears the distinct picture shown in Fig. 1c. The frequency of the $\Gamma-X$ transition (ν_0) plays an important role in the discussion of this problem and in the determination of the width of the region $\varepsilon>\varepsilon_0$. The coupling constant between the valleys $D_{\Gamma X}$ entering into ν_0 ($\nu_0\sim D_{\Gamma X}^2$), unfortunately, is not accurately known and serves in the calculations as a fitting parameter.[11] We hope that its value is sufficiently large, specifically that it is on the order of 10^9 eV/cm (Ref. 15). In such a case, the assumption that the region $\varepsilon>\varepsilon_0$ is narrow (and the results that follow from this assumption) is (are) valid, and the quantitative results presented here are reliable. In the opposite case, NDC still appears at the cyclotron resonance, but the results will then be of a qualitative character.

The assumption of dynamic heating is one of the main assumptions in our treatment. As was noted above, the electric fields in which dynamic NDC appears are entirely sufficient for such heating, especially for small $\Delta\varepsilon$, when the time it takes the electrons to accelerate to the energy ε_0 is too short—for $\Delta\varepsilon\approx\hbar\omega^*$ ($\varepsilon_0\approx2\hbar\omega^*$) and for $E_0=10$ kV/cm, $\tau_E\simeq3\times10^{-13}$ s.

In the case $\Delta\varepsilon\gg\hbar\omega^*$ τ_E is larger, and the assumption that $k_0T\ll\hbar\omega^*$ is a necessary condition for dynamic intervalley transitions. In the extreme case for $\Delta\varepsilon>10\hbar\omega^*$ (when the width of the cyclotron resonance line is small) the mechanism of dynamic NDC changes and appears to have a transit character.[8] Dynamic NDC, which was investigated in Refs. 7 and 8, appears on account of the fast B electrons. They transit the Γ valley in a dynamic fashion, even if we take intravalley scattering into account. Scattering of the A electrons, however, which gives a positive contribution to the total conductivity, will apparently decrease their conductivity.

A consideration of the finite magnitude of τ_{op} is important only in the case where closed cyclotron trajectories appear in crossed fields $\mathbf{E}_0\perp\mathbf{H}$. ''Escape'' of electrons from these trajectories is possible only for a finite value of τ_{op}. But, as has been shown, NDC at the cyclotron resonance appears even in the absence of closed trajectories. For this reason, the term cyclotron resonance must be understood here not in the ''classical'' sense.

In the case of large $\Delta\varepsilon$, when NDC at the cyclotron resonance is problematic, it appears necessary to increase the magnetic field to the point at which closed trajectories appear in addition to the open trajectories of types A and B. The conditions of transit of the electrons and their redistribution between these trajectories will be determined uniquely by the parameters $\Delta\varepsilon$, $\mathbf{H}$, $\mathbf{E}_0$, and τ_{op}. For the above-indicated reasons, $\Delta\varepsilon$ plays the most important role (since all the other band-structure parameters are bound up with it[11]). On the one hand, a simultaneous consideration of all these parameters would be complicated. On the other, it is obvious that new and interesting possibilities of ''control'' of the transit processes will appear and, accordingly, it will be possible to attain favorable conditions for NDC at the cyclotron resonance.

[1] B. Lax and J. G. Mavraides, Solid State Phys. **11**, 261 (1960).
[2] P. Wolff, Physics (Long Island City, NY) **1**, 147 (1964).
[3] A. S. Tager, Pis'ma Zh. Éksp. Teor. Fiz. **3**, 369 (1966) [Sov. Phys. JETP **3**, 239 (1966)].
[4] A. A. Andronov and V. A. Kozlov, JETP Lett. **17**, 87 (1973).
[5] I. I. Vosilius and I. B. Levinson, Zh. Éksp. Teor. Fiz. **50**, 1660 (1966) [Sov. Phys. JETP **23**, 1104 (1966)]; Zh. Éksp. Teor. Fiz. **52**, 1013 (1967) [Sov. Phys. JETP **25**, 672 (1967)].
[6] Ya. I. Al'ber, A. A. Andronov, V. A. Valov *et al.*, Zh. Éksp. Teor. Fiz. **72**, 1030 (1977) [Sov. Phys. JETP **45**, 539 (1977)].
[7] A. A. Andronov and G. E. Dzamukashvili, Solid State Commun. **55**, 915 (1985).
[8] A. A. Andronov and G. É. Dzamukashvili, Fiz. Tekh. Poluprovodn. **19**, 1810 (1985) [Sov. Phys. Semicond. **19**, 1111 (1985)].
[9] A. A. Andronov, G. É. Dzamukashvili, Z. C. Kachlishvili, and I. M. Nefedov, Fiz. Tekh. Poluprovodn. **21**, 1813 (1987) [Sov. Phys. Semicond. **21**, 1098 (1987)].
[10] G. É. Dzamukashvili, Z. C. Kachlishvili, N. K. Metreveli, Pis'ma Zh. Éksp. Teor. Fiz. **62**, 220 (1995) [JETP Lett. **62**, 234 (1995)].
[11] S. Adachi, J. Appl. Phys. **58**, R1 (1985).
[12] G. É. Dzamukashvili, Fiz. Tverd. Tela **32**, 676 (1990) [Sov. Phys. Solid State **32**, 398 (1990)].
[13] T. A. Golovko and G. É. Dzamukashvili, Soobshch. Akad. Nauk Gruzii **149**, 219 (1994).
[14] G. É. Dzamukashvili, Z. C. Kachlishvili, N. K. Metreveli, Soobshch. Akad. Nauk Gruzii (1996).
[15] A. K. Saxena and K. S. Gurumurthy, J. Phys. Chem. Solids **43**, 801 (1982).

Translated by Paul F. Schippnick

The effect of copper doping of *n*-ZnSe crystals on the structure of luminescence centers of long-wavelength luminescence

G. N. Ivanova, V. A. Kasiyan, D. D. Nedeoglo, and S. V. Oprya

Kishinev State University, 277009 Kishinev, Moldova
(Submitted October 17, 1995; accepted for publication June 9, 1997)
Fiz. Tekh. Poluprovodn. **32**, 171–177 (February 1998)

The photoluminescence and luminescence excitation spectra of copper-doped *n*-ZnSe crystals were investigated in the temperature range 77–400 K during diffusion of the copper into the crystal from the liquid, gas, and and solid phases. It is shown that the structure of the associative centers responsible for emission in the red and green regions of the spectrum depends on the method of copper doping. It is established that during the interphase interaction on the (ZnSe crystal)–(copper film) boundary, zinc atoms dissolve in the copper film and the copper atoms diffuse into the zinc selenide crystal. © *1998 American Institute of Physics.* [S1063-7826(98)01101-6]

INTRODUCTION

The participation of copper atoms in the formation of centers responsible for the luminescence of zinc selenide in the long-wavelength red and green regions of the spectrum was established in a number of studies.[1–4] At the same time, studies[5–9] that have shown that centers incorporating intrinsic and impurity defects (associated with copper) are responsible for the emission in this spectral region. Finally, according to the data of Refs. 10 and 11, copper can be present in ZnSe crystals in the form of an uncontrollable impurity and can, by interacting with the intrinsic defects, participate in the formation of red and green color centers. Thus, there is now a large number of models of red and green color centers in ZnSe crystals containing copper and intrinsic and impurity defects in various combinations.

The present study shows that the formation of red and green color centers of different structure is possible in *n*-ZnSe crystals, depending on the method of copper doping.

DOPING AND CONDITIONS OF EXPERIMENT

As our starting crystals we used highly resistive *n*-ZnSe single crystals grown from melt. The crystals were copper doped using one of three methods.

1. Thermal diffusion of copper from a Zn+Xat. % Cu melt. The copper content X was varied from 0.05% to 25%. The samples were then annealed at 950 °C for 100 h.

2. Annealing of the crystals in CuCl vapors at 500 °C. The anneal time varied from 5 to 75 h.

3. Thermal diffusion of copper from a thin metallic film deposited on the surface of the crystal. The copper film was sputtered onto the *n*-ZnSe surface for 1 min, after which the sample was annealed in vacuum at 700 °C. The annealing time was varied from 0.5 to 20 min. At the end of the doping process the thin copper film was removed from the crystal surface by chemical etching. All anneals were terminated by rapid cooling of the quartz cells holding the samples by immersing the it in a vessel of cold water.

Thus, copper diffusion into *n*-ZnSe crystals was realized from the liquid, vapor, and solid phases. Three series of samples were prepared in each of the last two cases. The starting crystals of the first series were pre-annealed in a Zn melt at 950 °C for 100 h. The second series of crystals were pre-annealed in vacuum in the same heat regime. The third series of crystals were copper-doped, without any pre-annealing.

Photoluminescence spectra and luminescence excitation spectra were recorded in the temperature interval from 77 to 400 K. Photoluminescence was excited by monochromatic light from a VSU-1 monochromator with a halogen lamp or by an LGI-21 laser with a wavelength of 337 nm. The photoluminescence and luminescence excitation spectra were investigated using an MDR-23 monochromator with linear dispersion 14 Å/mm in the wavelength region from 450 to 700 nm.

EXPERIMENTAL RESULTS AND DISCUSSION

A. Thermal diffusion of copper from a Zn+X at. % Cu *melt.* The photoluminescence spectrum at 77 K of the initial, unannealed *n*-ZnSe sample subtends the wide spectral region from 520 to 700 nm (Fig. 1, curve *1*). The main maximum is observed at 580 nm, and the long-wavelength limb has a dip at 617 nm. Annealing of the crystals in a pure zinc melt leads to a shift of the photoluminescence spectrum toward longer wavelengths, the main maximum turns out to be located at 600 nm, the dip is transformed into an independent photoluminescence band with a maximum at 630 nm. The addition of 0.1 at. % Cu to the zinc melt leads to pulling of the short-wavelength limb of the photoluminescence spectrum to 500 nm and the appearance at 530 nm of a new photoluminescence band (Fig. 1, curve *3*). Further increase of the copper content in the zinc melt leads to a narrowing of the red luminescence band, its localization at $\lambda = 640$ nm, and the more distinct manifestation of the green luminescence band at 530 nm, which becomes predominant in intensity in the photoluminescence spectra of *n*-ZnSe crystals annealed in zinc melts containing 0.6 at. % copper and higher (Fig. 1, curves *4–6*). Starting at a copper concentration of 5 at. %, the intensity of the green luminescence band also falls, i.e., on the whole, the radiative properties of the crystals deteriorate.

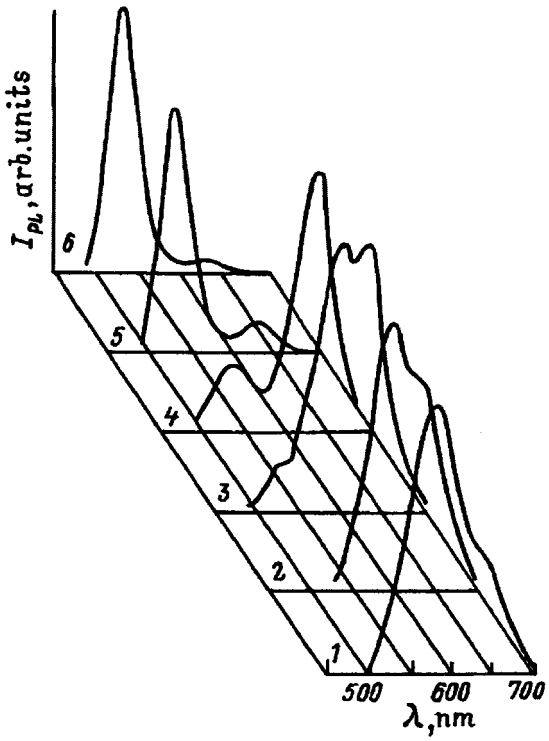

FIG. 1. Photoluminescence spectra of ZnSe crystals annealed in a $(100-X)$ at. % Zn$+X$ *at*. % Cu melt. $T=77$ K. $\lambda_{ex}=440$ nm. *1*—Photoluminescence spectrum of the initial, unannealed ZnSe. *2–6* correspond to X at. % Cu: 0, 0.1, 0.2, 0.6, 1.75.

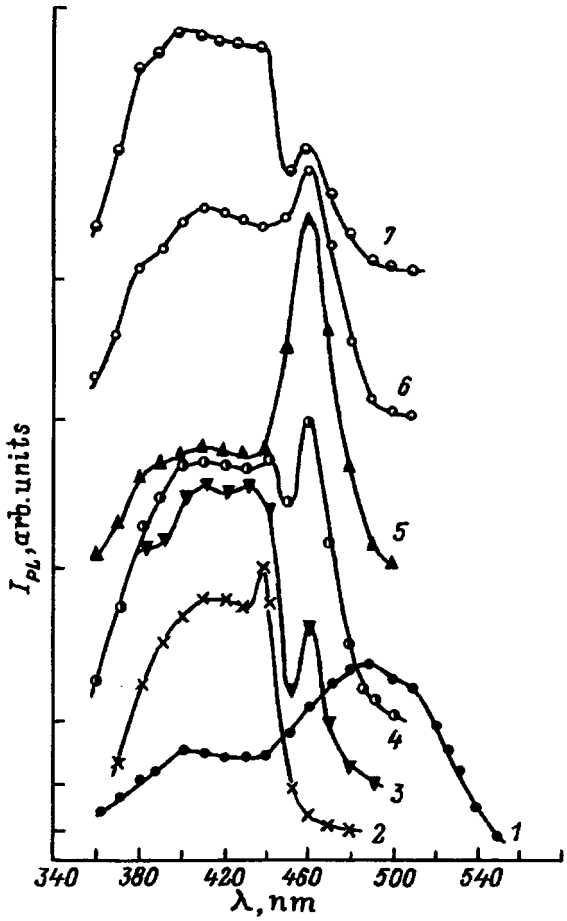

FIG. 2. Excitation spectra of the red (*1*) and green photoluminescence bands (*2–7*). $T=77$ K. X, at. % Cu: *1,2*—0.6, *3*—0.75, *4*—1.25, *5*—1.75, *6*—2, *7*—10.

The excitation spectra of the green (530 nm) and red (640 nm) luminescence bands of *n*-ZnSe:Zn:Cu crystals are shown in Fig. 2. It can be seen that at 77 K the luminescence in the red is excited mainly by light from the region near the fundamental absorption edge (the maximum of the luminescence excitation spectrum for different samples lies in the wavelength region from 480 to 490 nm) and partly by shorter-wavelength radiation ($\lambda_{max}\sim 400$ nm). This indicates that the photoluminescence band with maximum at 640 nm is not elementary since it is excited both by interband transitions and by electron transitions from shallow acceptor levels ($E_g-h\nu_{ex}=0.217-0.269$ eV) to the conduction band.

In crystals with low copper content, green luminescence is excited by light from the intrinsic absorption region (Fig. 2, curve *2*). The width of the band gap, determined from the spectral position of the abrupt long-wavelength edge of the luminescence excitation spectrum, turns out to be equal to 2.799–2.802 eV at 77 K. Increasing the copper content to 0.75 at. % leads to the appearance in the luminescence excitation spectrum in the impurity absorption region of a new, less intense peak with maximum at 460 nm (Fig. 2, curve *3*). With further increase in the copper content of the zinc melt, its position does not change, but its intensity grows together with the intensity of the green luminescence band. The decrease in the intensity of this peak at copper contents greater than 2 at. % correlates well with the decrease in the intensity of the green luminescence band in the photoluminescence spectrum with increase of the copper concentration in the investigated crystals. The dependence of the intensity of the 460-nm peak in the luminescence excitation spectrum on the copper content of the investigated crystals allows us to assume a connection between its nature and the presence of copper in them. The energy of the exciting optical transition, determined from the spectral position of this peak in the luminescence excitation spectrum, is 2.695 eV.

From our measurements of the temperature dependence of the photoluminescence spectra of the ZnSe:Zn:Cu crystal samples in the interval from 77 to 400 K we established that up to a temperature on the order of 120 K there is a constant quenching rate of the red and green luminescence bands. At higher temperatures abrupt quenching of the intensity of the green luminescence band is observed. At 150 K this band is completely quenched, while luminescence in the red is observed up to 400 K. The temperature dependence of the maximum intensities of the red and green luminescence bands in the coordinates $\ln I=f(10^3/T)$ has two well-expressed linear segments, regardless of the copper content—a low-temperature segment and a high-temperature segment. The activation energies, determined from the slopes of the low-temperature segments of these dependences for the red and green luminescence bands, are very close in value and lie in the interval 7–9 meV, while the high-temperature activation energies differ substantially and lie between 240 and 340 meV for the red luminescence band

and between 70 and 100 meV for the green luminescence band, depending on the copper content.

The presence of two slopes in the dependence $\ln I = f(10^3/T)$ and the substantially smaller (in comparison with Ref. 2) values of the activation energy determined from the high-temperature quenching of the intensity of the red and green luminescence bands allows us to assume, first, a donor–acceptor mechanism of radiative recombination and, second, a more complicated structure of the emission centers than in Ref. 2. The authors of Ref. 2 suggest that the red emission is due to radiative recombination of a free electron with a hole localized at a Cu_{Zn}^{+} acceptor located 0.72 eV above the top of the valence band, and that the green emission is due to recombination of a free electron with a hole at the Cu_{Zn}^{++} acceptor with a depth of 0.35 eV. Thomas *et al.*[12] proposed a model for the formation of complex associative emission centers in ZnS. According to this model, a simple green center Cu_{Zn}^{+} at a sufficiently high level of copper doping (>0.9 ppm) forms an associative acceptor blue center $(Cu_{Zn}^{+}-Cu_i^{+})$ with significantly shallower depth than a simple Cu_{Zn}^{+} center.

We are inclined to believe that in the examined ZnSe:Zn:Cu crystals the green emission is due to an electron transition from a shallow donor (possibly, V_{Se} with $E_D \sim 10$ meV or some other uncontrollable impurity) to an associative acceptor center $(Cu_{Zn}^{++}-Cu_i^{+})$, formed during copper doping of the crystals. Evidence for the participation of interstitial copper Cu_i^{+} in the formation of the acceptor complex is provided by the appearance and flare-up of the green emission band in the photoluminescence spectrum during prolonged (5–10 h) heating in vacuum at 413 K (Fig. 3). As a result of such heating, copper atoms leave their sites for interstitial positions.[13] This facilitates the more efficient formation of acceptor complexes $(Cu_{Zn}^{++}-Cu_i^{+})$ and the flaring-up of the green emission band.

Emission in the red, in our opinion, is due to radiative transitions of electrons from uncontrolled donors to associative acceptor centers of the type $(Cu_{Zn}^{+}-D_{Zn})$. The participation of Cu_{Zn}^{+} in the formation of the acceptor responsible for the red emission band can be justified as follows. We have found that an increase of the copper content in ZnSe:Zn:Cu samples causes an increase in the intensity of the green emission band which is accompanied by a decrease in the intensity of the red emission band (Fig. 1). On the other hand, the authors of Ref. 14 have convincingly shown that an increase in the copper concentration leads in a major way to growth of the concentration of acceptor centers at a depth of 0.35 eV, which, according to Ref. 2, can be identified as Cu_{Zn}^{++} centers, which are responsible for the green emission.[2] According to Ref. 14, the concentration of the centers with ionization energy 0.72 eV, which are identified as acceptor centers of the type Cu_{Zn}^{+}, and which are responsible for the red emission,[2] hardly varies as the copper content is increased. Their participation in the formation of the photoluminescence spectrum in this case is manifested more weakly in comparison with the Cu_{Zn}^{++} centers, which leads to a redistribution of intensity over the green and red emission bands. The substantially smaller (in comparison with Ref. 2) values of the thermal activation energy determined from the high-temperature quenching of the red emission band are evidence that the acceptors responsible for this emission band exist not in the form Cu_{Zn}^{+}, as in Ref. 2, but in the form of an associate of the type $(Cu_{Cu}^{+}-D_{Zn})$ (Ref. 15), whose activation energy is lower than the corresponding energy for the nonassociative acceptor Cu_{Zn}^{+}.

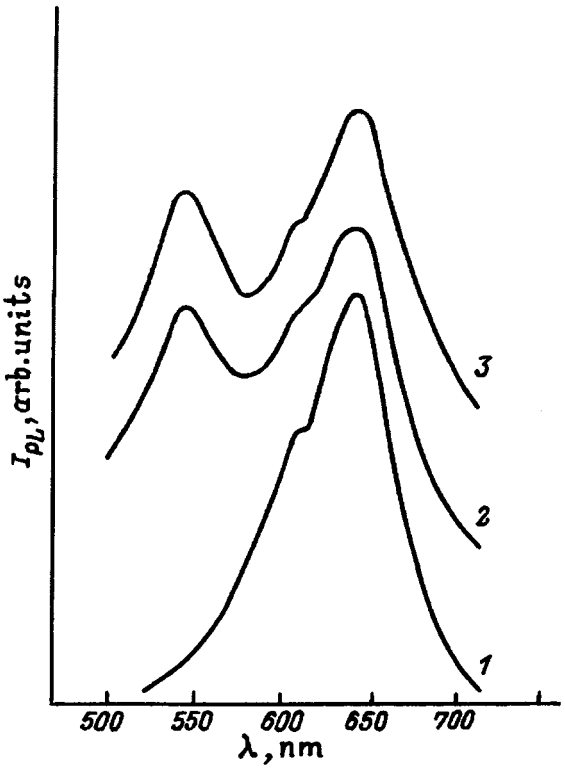

FIG. 3. Modification of the photoluminescence spectrum of ZnSe:Zn:Cu (0.05 at. % Cu) crystals after 5-hour (*2*) and 10-hour (*3*) heating in vacuum at $T = 413$ K. Curve *1* is the photoluminescence spectrum before heating.

B. Annealing in CuCl *vapors.* The simultaneous introduction into the *n*-ZnSe crystals during their heat treatment in CuCl vapors of an activator (Cu_{Zn}) and a co-activator (Cl_{Se}) in equivalent quantities has a marked effect on the structure of the long-wavelength luminescence spectrum. Figure 4 shows photoluminescence spectra of the three series of samples annealed in CuCl vapors for 5, 25, and 75 h. The most intense emission of the undoped *n*-ZnSe crystals obtained from melt is observed at 77 K at the band maxima at 630 and 557 nm (Fig. 4a, curve *1*). Annealing of the ZnSe crystals in CuCl vapors leads to a decrease in the intensity of all observed photoluminescence bands and to a transformation of the long-wavelength luminescence bands into two other bands located at 540 and 640 nm, respectively (Fig. 4a, curves *2–4*). The band at 540 nm flares up energetically with increase of the anneal time and becomes the dominant band in intensity for the 75-h anneal. The appearance in the photoluminescence spectra of the *n*-ZnSe crystals annealed in CuCl vapors of a green emission band at 540 nm and the decrease in the intensities of the *B* band [which is attributable to the $(V_{Zn}V_{Se})$ centers; Ref. 16] and the red emission band with shift of the latter to 640 nm may be linked with simultaneous diffusion of copper atoms and chlorine atoms into the crystals and the formation of defects of the types

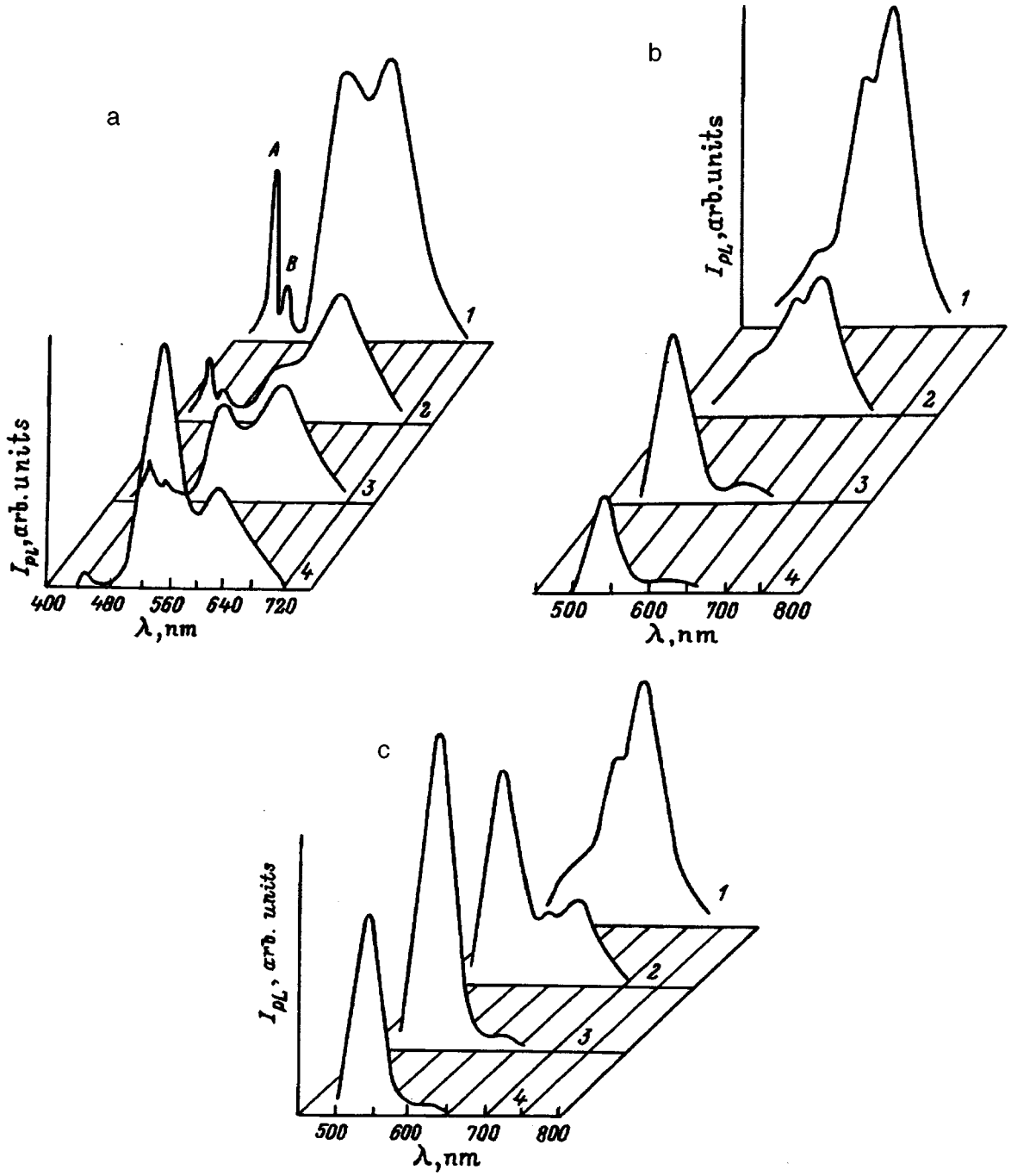

FIG. 4. Photoluminescence spectra of ZnSe (a), ZnSe:Zn (b), and ZnSe:vacuum (c) crystals annealed in CuCl vapor. $T=77$ K. $\lambda_{ex}=337$ nm. Anneal time in hours: *1*—0, *2*—5, *3*—25, *4*—75.

Cu_{Zn} and Cl_{Se}, which form new associative emission centers.

Since the concentration of the Cu_{Zn} and Cl_{Se} defects depends on the concentration of the intrinsic defects in the undoped *n*-ZnSe starting crystals, we pre-annealed the following series of samples in liquid zinc with the aim of reducing the concentration of V_{Zn} and uncontrolled shallow donors. The photoluminescence spectra of the *n*-ZnSe:Zn:CuCl crystals are shown in Fig. 4b. In contrast to the initial, unannealed *n*-ZnSe crystals, the photoluminescence spectrum of the *n*-ZnSe:Zn crystals consists of a wide band with two peaks at 600 and 640 nm and a weakly expressed band at 550 nm (Fig. 4b, curve *1*). Annealing in CuCl vapors for 5 h leads to a decrease in the intensity of all observed photoluminescence bands. The green emission band ($\lambda_{max}=50$ *nm*) in the photoluminescence spectrum flares up and becomes predominant in intensity after 25 h of annealing. Further increase in the anneal time leads to quenching of the intensity of all photoluminescence bands. Thus, pre-annealing in liquid zinc lowers the V_{Zn} concentration, limiting the possibility of introducing Cu atoms at the sites of the zinc sublattice. Annealing for 25 h leads to saturation of the filling of V_{Zn} sites by copper atoms and to a decrease in the intensity of the green emission band. The red emission band with maximum at 640 nm is almost com-

pletely quenched after 25 h of annealing of n-ZnSe:Zn:CuCl crystals, whereas it is present in the n-ZnSe:CuCl photoluminescence spectra even after a 75-h anneal in CuCl vapors.

Pre-annealing n-ZnSe crystals in vacuum leads to a growth in the V_{Zn} concentration.[17] Consequently, in n-ZnSe crystals annealed first in vacuum and then in CuCl vapors favorable conditions are created for the formation of Cu_{Zn} acceptors. The evolution of the photoluminescence spectra during an extended anneal of n-ZnSe crystals in vacuum and then in CuCl vapors is illustrated in Fig. 4c. As could be expected, in this case intense green emission (λ_{max}=540 nm) is observed already after 5 h of annealing in CuCl vapors and, in contrast to the previous series of samples, this photoluminescence band predominates for all anneal times. The intensity of the red emission bands at 600 and 640 nm decreases with increasing anneal time in CuCl vapors and almost completely quenches.

We believe that the acceptor responsible for the green emission band, as in the case of the crystals annealed in the Zn+Cu melt, is an associative complex of the type $(Cu_{Zn}^{++}-Cu_i^{+})$. At low temperatures ($T<120$ K) the electrons localized at the shallow donors (in the given case these can be defects of the type Cl_{Se}), recombine radiatively with holes localized at the associative acceptors $(Cu_{Zn}^{++}-Cu_i^{+})$. As the temperature is raised above 120 K, the shallow donors ionize and the free electrons recombine radiatively with the holes at the $(Cu_{Zn}^{++}-Cu_i^{+})$ centers.

The structure of the emission centers responsible for the red luminescence band in n-ZnSe crystals that were not annealed in CuCl vapors, and in crystals that were, appears to be different. In the n-ZnSe crystals that were not annealed in CuCl vapors, $(V_{Zn}^{++}-D_{Zn})$ donor–acceptor pairs are responsible for the red luminescence band. The thermal activation energy, determined from the high-temperature slope of the dependence $\ln I=f(10^3/T)$, turns out to be equal to 0.143 eV. Annealing of n-ZnSe crystals in CuCl vapors leads to the formation of the complex acceptor $(Cu_{Zn}^{+}-Cl_{Se})$. The red emission band in this case forms as a result of radiative transitions of electrons from the shallow donor onto the associative acceptor $(Cu_{Zn}^{+}-Cl_{Se})$. It was previously assumed[18] that the donor–acceptor associates $(Cu_{Zn}Cl_{Se})$ are responsible for the red emission band in ZnSe:Cu:Cl crystals.

C. Thermal diffusion of copper from a metallic film deposited on the surface of the crystal. Figure 5 shows photoluminescence spectra of the starting crystals of the three series of samples and of samples with different anneal times from the series of crystals annealed in vacuum after deposition on their surface of a thin copper film. The photoluminescence spectrum of the unannealed ZnSe starting crystal has a maximum at 635 nm and consists of two bands since its short-wavelength limb has a distinct dip in the region of 605 nm. Pre-annealing of the n-ZnSe starting crystal in liquid zinc at 950 °C for 100 h with the aim of reducing the number of V_{Zn} intrinsic defects leads to the disappearance of the dip on the short-wavelength slope of the emission band. The position of the maximum is shifted to 640 nm, and the half-width of the band, as in the previous case, is 250 meV. The band has an asymmetric shape. Annealing of the starting crystal in vacuum at 950 °C for 100 h leads to a narrowing of

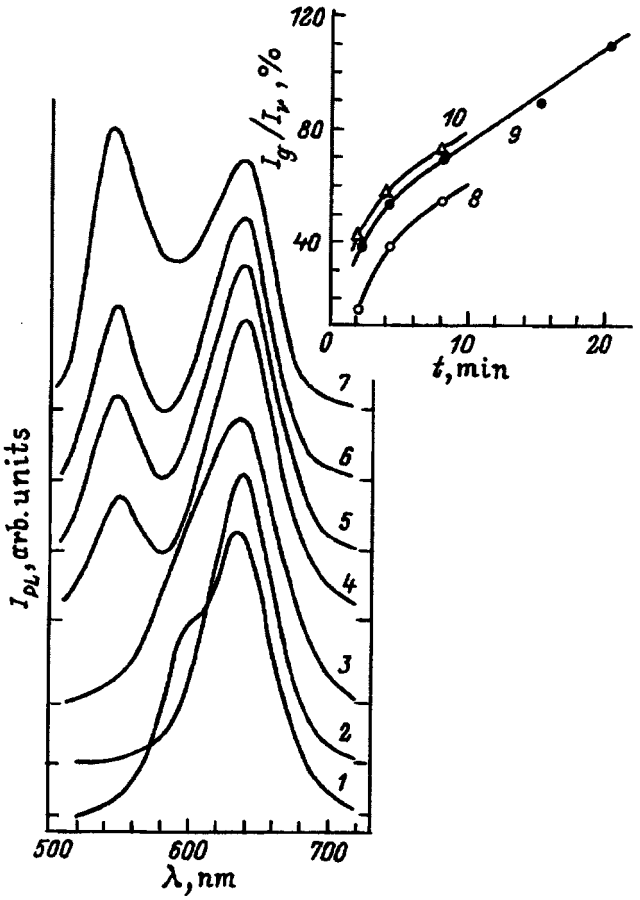

FIG. 5. Photoluminescence spectra of ZnSe (*1*), ZnSe:vacuum (*2*), and ZnSe:Zn (*3*) crystals, and crystals of ZnSe:Zn copper-doped from a metallic film (*4–7*). Anneal time of the copper film in minutes: *4*—2, *5*—4, *6*—8, *7*—20. λ_{ex}=460 nm. T=77 K. Inset plots the dependence of the ratio of intensities of the green and red emission bands for crystals of ZnSe:Cu (*8*), ZnSe:Zn:Cu (*9*), and ZnSe:vacuum:Cu (*10*) on the anneal time of the copper film.

the red emission band to 166 meV. The disappearance of the dip at 605 nm on the short-wavelength slope of the emission band of the n-ZnSe starting crystals after annealing in liquid zinc or in vacuum is a consequence of partial decay of the associative centers ($V_{Zn}V_{Se}$), which are responsible for the emission band located at 605 nm, as a result of the decrease in the number of V_{Zn} or V_{Se} intrinsic defects brought about by the corresponding heat treatments (anneals).

Regardless of the medium in which the n-ZnSe starting crystals are pre-annealed and, consequently, regardless of the concentration of the V_{Zn} and V_{Se} intrinsic defects and their relative numbers, subsequent annealing in vacuum of the crystals with a thin copper film deposited on their surfaces leads to the appearance in the photoluminescence spectrum at 77 K of a green emission band with maximum at 550 nm whose intensity increases with increasing anneal time, and the intensity of the red emission band with a maximum at 640 nm is essentially independent of the anneal time. It only slightly broadens with increase of the anneal time (Fig. 5, curves *4–6*). The ratio of the intensities of the green and red emission bands increases with increasing of the anneal time for all of the series of crystals (Fig. 5, inset).

Analyzing the structure of the emission centers in the n-ZnSe crystals copper-doped from a thin copper film deposited on the surface of the crystal, it is natural to assume that these centers include within themselves copper atoms which have diffused into the crystal from the film as well as intrinsic defects of the type V_{Zn} and V_{Se}, which arise as a result of the dissolution of Zn atoms in the copper film.[20] Evidence of the participation of copper in the formation of emission centers is provided by the appearance in the n-ZnSe:Cu photoluminescence spectra of a green emission band ($\lambda = 550$ nm), which according to numerous sources in the literature is identified with emission centers incorporating copper atoms in their makeup. It is characteristic that this emission band is absent in the photoluminescence spectra of the starting crystals.

An interesting peculiarity of the photoluminescence spectra of the investigated samples is the fact that the intensity of the red emission band ($\lambda_{max}=640$ nm) depends weakly on the anneal time (Fig. 5), while in the case of annealing of n-ZnSe crystals in a Zn+Cu melt or in CuCl vapors, along with growth of the intensity of the green emission band, the intensity of the red emission band is strongly quenched. This allows us to assume that the red emission band in this case is due to centers incorporating intrinsic defects. The red emission centers in this case can be associates of the type $V_{Zn}Zn_i$ proposed in Ref. 8. The maximum of the green emission band in the photoluminescence spectra of n-ZnSe crystals copper-doped from a deposited film is shifted toward longer wavelengths ($\lambda_{max}=550$ nm) in comparison with crystals copper-doped from a Zn+Cu melt or copper-doped in CuCl vapors ($\lambda_{max}=530$ nm). The authors of Ref. 15 propose a structure of the green emission center of n-ZnSe:Cu crystals ($\lambda_{max}=550$ nm) of the type ($Cu_{Zn}-Cu_{Zn}$). We allow for the possibility of the formation of such centers in our case, assuming that copper at the sites of the zinc sublattice is found in the doubly charged state (Cu_{Zn}^{++}). The depth of these centers, which is determined from the temperature quenching of the intensity of the green emission band, is 0.12–0.15 eV from the top of the valence band.

In summary, during the annealing of n-ZnSe crystals with a metallic copper film deposited on their surface dissolution of Zn atoms into the copper film and generation of V_{Zn} intrinsic defects take place along with generation of Cu_{Zn} impurity defects as a result of dissolution of copper into the zinc selenide crystal.

[1] M. K. Sheĭnkman and G. L. Belenkiĭ, Fiz. Tekh. Poluprovodn. **22**, 1635 (1988) [*sic*].
[2] G. B. Stringfellow and R. H. Bube, J. Appl. Phys. **39**, 3657 (1968).
[3] R. N. Bhargawa, J. Cryst. Growth **59**, 15 (1982).
[4] G. Jones and J. Woods, J. Lumin. **9**, 389 (1974).
[5] I. A. Mironov and L. Ya. Markovskiĭ, Fiz. Tekh. Poluprovodn. **6**, 2245 (1964).
[6] Yu. F. Vaksman, *Author's Abstract of Candidate's Dissertation* [in Russian] (Odessa, 1977).
[7] A. N. Georgobiani, E. Zade-Uly, I. D. Mullabaev, B. N. Levonovich, and N. V. Serdyuk, Brief Reports in Physics, Institute of Physics, Acad. of Sci. USSR, No. **2**, 55 (1984).
[8] V. D. Ryzhikov and N. P. Starzhinskiĭ, Ukr. Fiz. Zh. **33**, 818 (1988).
[9] O. V. Vakulenko, V. D. Ryzhikov, and B. M. Shutov, Zh. Prikl. Spektrosk. **49**, 440 (1988).
[10] V. M. Skobeeva, V. V. Serdyuk, L. N. Semenyuk, N. V. Malushin, Zh. Prikl. Spektrosk. **44**, 243 (1986).
[11] V. V. Serdyuk, V. M. Skobeeva, N. V. Malushin, Zh. Prikl. Spektrosk. **35**, 737 (1981).
[12] A. E. Thomas, G. J. Russell, and J. Woods, J. Phys. C: Solid State Phys. **17**, 6219 (1984).
[13] V. A. Kasiyan and D. D. Nedeoglo, and S. V. Oprea, Fiz. Tekh. Poluprovodn. **28**, 1734 (1994) [Semiconductors **28**, 963 (1994)].
[14] V. V. Borshch, P. E. Mozol', E. A. Sal'kov, I. I. Patskun, and I. V. Fekeshgazi, Fiz. Tekh. Poluprovodn. **16**, 1070 (1982) [Sov. Phys. Semicond. **16**, 684 (1982)].
[15] P. L. Kukk and N. V. Ryandur, Trudy Tallinn. Politekh. Instituta, No. 404, 139 (1976).
[16] A. N. Georgobiani, M. B. Kotlyarevskiĭ, A. A. Pegov, B. G. Chernyavskiĭ, Izv. Vuzov. Fizika **29**, 105 (1986).
[17] G. N. Ivanova, D. D. Nedeoglo, B. V. Novikov, and V. G. Tallalaev, Fiz. Tekh. Poluprovodn. **21**, 2693 (1987) [*sic*].
[18] P. Kukk, O. Palmre, and E. Mellikov, Phys. Status Solidi A **70**, 35 (1982).
[19] P. L. Kukk and O. Palmre, Izv. Akad. Nauk SSSR, Neorg. Mater. **16**, 1916 (1980).
[20] *Physics of II–VI Compounds* [in Russian], edited by A. N. Georgobiani and M. K. Sheĭnkman (Nauka, Moscow, 1986), p. 72.

Translated by Paul F. Schippnick

The structure of high-temperature blue luminescence centers in zinc selenide and mechanisms of this luminescence

G. N. Ivanova, V. A. Kasiyan, N. D. Nedeoglo, D. D. Nedeoglo, and A. V. Simashkevich

State University of Moldova, 277009 Kishinev, Moldova
(Submitted November 19, 1996; accepted for publication June 7, 1997)
Fiz. Tekh. Poluprovodn. **32**, 178–181 (February 1998)

The characteristic features of temperature quenching of the intensity of the edge luminescence bands of *n*-ZnSe crystals annealed in different media (vacuum, Zn, Se) are investigated a wide temperature range. A change in the mechanisms of high-temperature exciton luminescence in the short-wavelength region of the spectrum (443 nm) with increase in temperature of the crystal is observed. It is shown that the nature of temperature quenching of the long-wavelength edge luminescence band (458 nm) is evidence of dissociation of associative luminescence centers with increase in the sample temperature. © *1998 American Institute of Physics.* [S1063-7826(98)01201-0]

INTRODUCTION

The participation of excitons in the formation of the shortest-wavelength bands of the high-temperature edge luminescence of zinc selenide has been discussed within the context of studies of the electroluminescence,[1] cathodoluminescence,[2] and photoluminescence[3] of these crystals. It has been noted that at temperatures near liquid nitrogen the shortest-wavelength emission with energy 2.787 eV is due to recombination of free electrons.[3] As the temperature is increased, the role of the free electrons in the formation of the edge luminescence bands weakens and the defining mechanism becomes recombination of excitons bound to ionized shallow donors.[2] It has been suggested that the lower-energy blue emission band with maximum at 2.706 eV is due to recombination of a free electron with a hole at the acceptor.[3]

The characteristic features of the temperature quenching of these bands, which we have observed in the luminescence spectra of *n*-ZnSe crystals annealed in different media allow us to discuss with greater certainty the mechanisms of radiative recombination and the structure of the emission centers responsible for the observed high-temperature emission bands.

SAMPLE PREPARATION AND CONDITIONS OF THE EXPERIMENT

In the temperature interval from 82 to 400 K we have investigated the spectra of untreated high-ohmic *n*-ZnSe crystals obtained from melt, and also crystals annealed in vacuum and in zinc and selenium melts for 100 h at 950 °C. In the case of the selenium medium, the annealing temperature was varied from 400 to 900 °C with a 100 °C step. At the end of each anneal the samples were rapidly cooled to room temperature. Photoluminescence was excited by monochromatic light from a VSU-1 monochromator with a halogen lamp or by an LGI-21 laser with wavelength 337 nm. The photoluminescence spectra were examined with the help of an MDR-23 monochromator with a linear dispersion of 14 Å/mm over the wavelength interval from 430 to 500 nm.

EXPERIMENTAL RESULTS AND DISCUSSION

The effect of the medium and the annealing temperature of the *n*-ZnSe crystals on the photoluminescence spectra at 82 K is shown in Figs. 1a and 1b, respectively. It can be seen that regardless of the medium and the annealing temperature, two narrow blue emission bands are observed—the *A* band (443 nm, 2.799 eV) and the *B* band (458 nm, 2.707 eV). In the untreated crystal the *B* band has very low intensity. Annealing the crystals in liquid zinc quenches this band almost completely while annealing in vacuum, and even more so in liquid selenium, leads to a significant growth of the intensity of this photoluminescence band. It is interesting to note that annealing of crystals in vacuum is similar in its effect on the intensity of the *B* band to annealing in liquid selenium with somewhat lower efficiency. It can be assumed that during high-temperature annealing of ZnSe crystals in an evacuated cell, interstitial selenium atoms leave the crystal, creating a selenium vapor medium in the cell, and the crystal anneals in this selenium vapor. The shorter-wavelength *A* band has a narrow half-width ($\sim 4-5$ nm) and is located in the exciton emission region.

As the annealing temperature of the crystals in a selenium melt is increased from 400 to 950 °C, the intensity of the *B* band flares up, while the intensity of the *A* band decreases (Fig. 1b). The half-width and spectral absorption of the observed photoluminescence bands are independent of the annealing temperature.

Annealing of ZnSe crystals in a selenium melt at different temperatures does not alter the character of the temperature evolution of the photoluminescence spectra. Figure 2 shows the temperature evolution of the photoluminescence spectra of ZnSe crystals after annealing in a selenium melt at 500 °C (a) and 950 °C (b). It can be seen that increasing the temperature of the sample leads to a decrease in the intensity of the blue emission bands and causes them to shift into the long-wavelength region of the spectrum. The intensity of the *B* band quenches significantly faster than that of the *A* band.

The dependence of the intensity of the *A* emission band on the inverse temperature for ZnSe:Se crystals annealed at different temperatures is plotted in Fig. 3. On a semilog plot

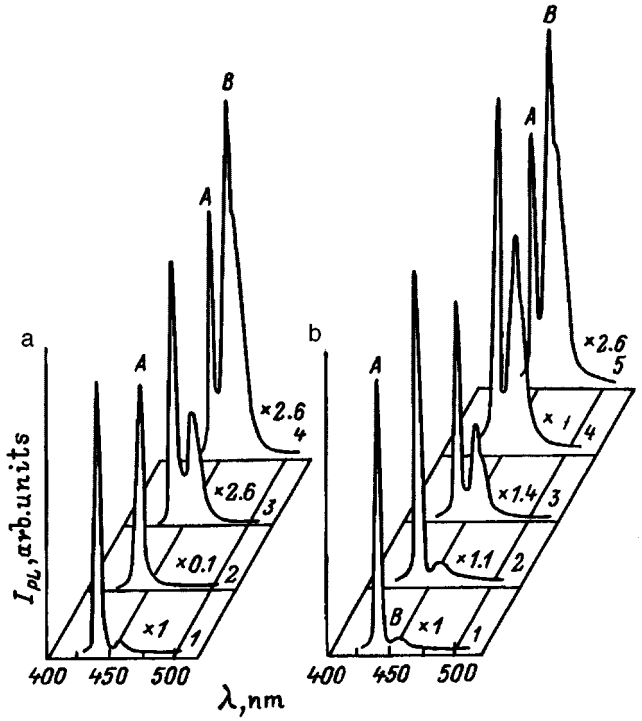

FIG. 1. Effect of the medium (a) and annealing temperature (b) of *n*-ZnSe crystals on the red luminescence spectra; $T=82$ K; *a*) *1*—initial crystal, *2*–*4*—crystal annealed in liquid zinc, in vacuum, and in liquid selenium; *b*) annealing temperature in liquid selenium T_a, °C: *1*—unannealed, *2*—400, *3*—700, *4*—800, *5*—950.

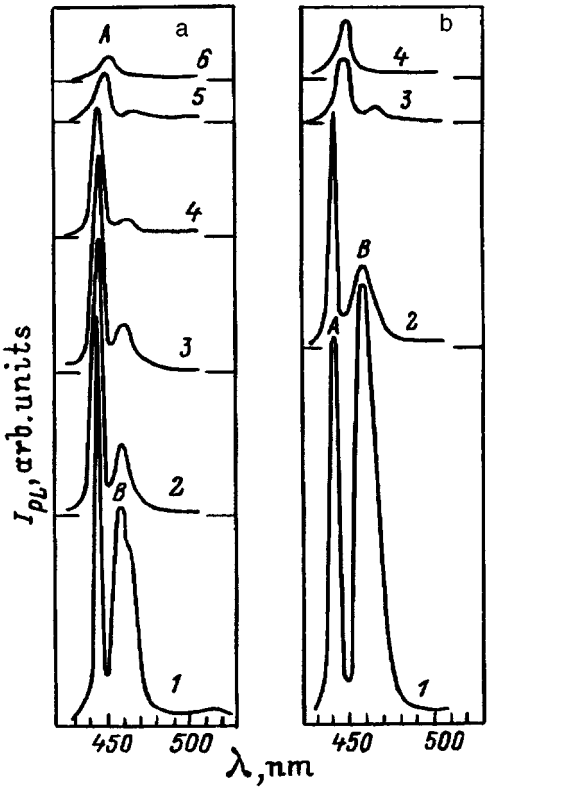

FIG. 2. Temperature evolution of the photoluminescence spectra of ZnSe crystals annealed in liquid selenium at 500 °C (a) and 950 °C (b). *T*, K: a) *1*—82, *2*—103, *3*—112, *4*—140, *5*—174, *6*—263; b) *1*—82, *2*—107, *3*—158, *4*—201.

these dependences consist of two straight lines with different slopes. The presence of two slopes usually indicates a donor–acceptor mechanism of radiative recombination. However, we have established that the energy position of the *A* band is independent of the excitation intensity over the entire temperature interval investigated, which eliminates the donor–acceptor mechanism.

It is evident from Fig. 3 that the activation energy of temperature quenching of luminescence at low temperatures ($T<120$–150 K) is 14–17 meV and varies only slightly as the annealing temperature is increased from 400 to 800 °C. Increasing the annealing temperature to 950 °C lowers this energy to 10 meV. In the high-temperature region the activation energy of temperature quenching of the luminescence also depends only weakly on the annealing temperature and is equal to 42–43 meV, falling to 35 meV at 950 °C. As the annealing temperature of the ZnSe:Se crystals is increased, the temperature of the break in the curves at the transition from low-temperature to high-temperature quenching, indicated by the arrows in Fig. 3, is observed to decrease.

We think that at low temperatures the *A* band is caused by annihilation of free electrons. This idea is based on the fact that, first, the difference between the width of the band gap ($E_g=2.812$ eV at 77 K, Ref. 1) and the energy at the maximum of the *A* band ($h\nu_{\max}=2.793$ eV) is 19 meV and, second, the energy of temperature quenching of this band in the low-temperature region is 14–17 meV. It is clear that both these values are near the binding energy of a free exciton, which takes values between 16 meV (Ref. 4) and 24 meV (Ref. 5). The excitonic nature of this band is also indicated by the fact that annealing ZnSe crystals in liquid zinc, which enhances the perfection of the crystalline lattice, strongly increases the intensity of the *A* band (Fig. 1a).

At temperatures above 150 K shallow donors in ZnSe are found in the ionized state, which favors the formation of excitons bound to these ionized donors. The activation energy of temperature quenching of the intensity of the *A* band in this temperature range is comprised of the ionization energy of the shallow donor impurity ($E_d\sim 20$ meV) and the binding energy of the exciton with the ionized donor [$E_b=E_g-h\nu_{\max}(A)\sim 23$–$25$ meV at 260 K], determined by comparing the dependences of the temperature shift of the maximum of this band and the width of the band gap. In ZnSe such shallow donors can be V_{Se} (14 meV), Al_{Zn} (19.5 meV), Ga_{Zn} (22 meV), and In_{Zn} (24 meV).[6]

The temperature at which the temperature quenching curve of the intensity of the *A* band changes slope (Fig. 3) corresponds to different contributions to the intensity of the given band from the two mechanisms of excitonic emission indicated above. The shift of this temperature toward lower values with increase of the annealing temperature is accompanied by a decrease in the intensity of the *A* band. This decrease in the intensity of the excitonic luminescence band is due to growth of the role of the recombination channel through bound excitons with increase of the annealing temperature. Since the concentration of shallow ionized donor impurities, including V_{Se} vacancies, decreases as the annealing temperature in liquid selenium is increased, due to filling

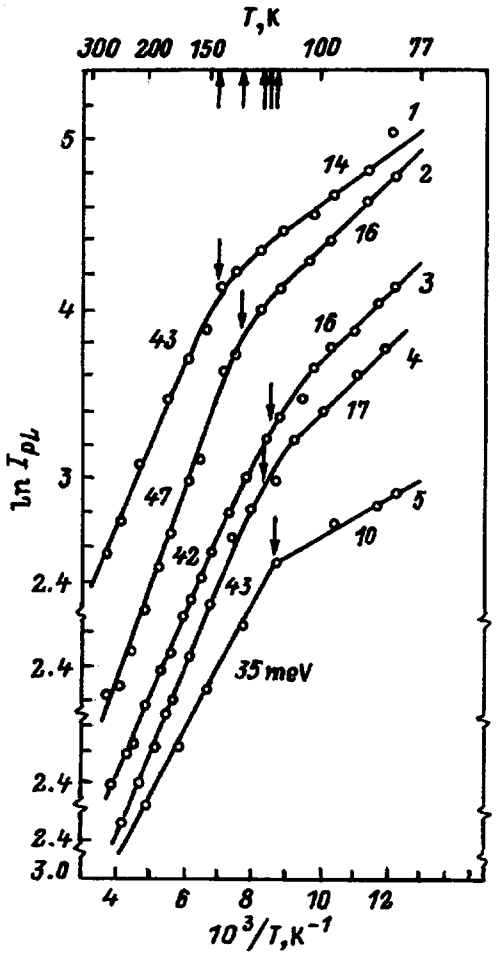

FIG. 3. Dependence of the intensity of the *A* luminescence band of ZnSe:Se crystals on the inverse temperature; T_a, °C: *1*—400, *2*—500, *3*—700, *4*—800, *5*—950.

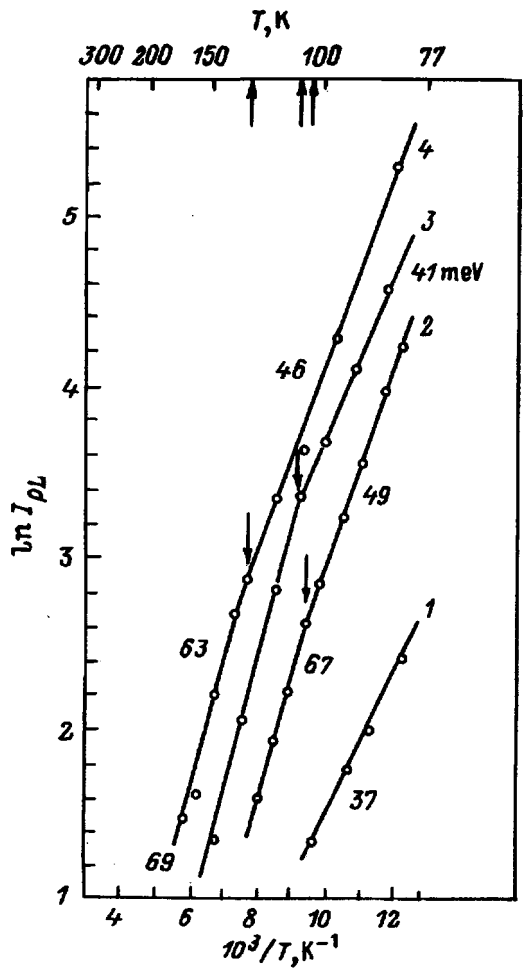

FIG. 4. Dependence of the intensity of the *B* luminescence band of ZnSe:Se crystals on the inverse temperature; T_a, °C: *1*—400, *2*—700, *3*—800, *4*—950.

of the selenium vacancies, the intensity of the emission caused by recombination of bound excitons decreases, leading to an overall lowering of the intensity of the *A* emission band. The predominant role of the V_{Se} vacancies as the defect that binds the excitons at high annealing temperatures of the ZnSe crystals is indicated by the decrease in the activation energy of high-temperature quenching of the *A* band observed in crystals annealed at 950 °C (Fig. 3).

The dependence of the intensity of the *B* emission band on the inverse temperature for different annealing temperatures of ZnSe crystals in liquid Se is plotted in Fig. 4. The absence of a shift of the maximum of this band as a function of the excitation intensity, as in the case of the *A* band, allows us to eliminate the donor–acceptor mechanism of formation of this photoluminescence band. The presence of two slopes on the temperature quenching curve of the intensity of the *B* band is evidence of a change in the structure of the emission center with growth of the temperature of the crystal accompanied by preservation of the mechanism of radiative recombination. We believe that recombination of a free electron with a hole localized on the associative center ($V_{Zn}D$) takes place at low temperatures. The incorporation of the intrinsic defect V_{Zn} in the makeup of the associate can be justified by the fact that annealing of ZnSe crystals in liquid Se, which lead to a growth of the V_{Zn} concentration, is accompanied by an abrupt growth in the intensity of the *B* band, especially at high annealing temperatures, when the rate of generation of defects of such type is high (Fig. 1b). The role of the donor in the associative center can be fulfilled by elements of groups III and VII (Al, Ga, In, Cl).

As the temperature of the crystal is increased above 100–120 K, thermal dissociation of the complex acceptor into the simple acceptor center V_{Zn} and a donor center occurs. The depth of the simple center V_{Zn} relative to the top of the valence band is greater than that of the associative center ($V_{Zn}D$), which leads to a greater activation energy of temperature quenching of the *B* band in the high-temperature region ($\sim$70 meV) (Fig. 4). The donors liberated after decay of the associative acceptors at temperatures above 100–150 K are found preferentially in the ionized state, which increases the probability of formation of excitons bound to the ionized donors and enhances the high-temperature recombination channel of the *A* band. This apparently promotes slower temperature quenching of the *A* band and its manifestation in the photoluminescence spectra of the investigated crystals all the way up to room temperature.

Figure 5 plots the intensity of the *B* band as a function of

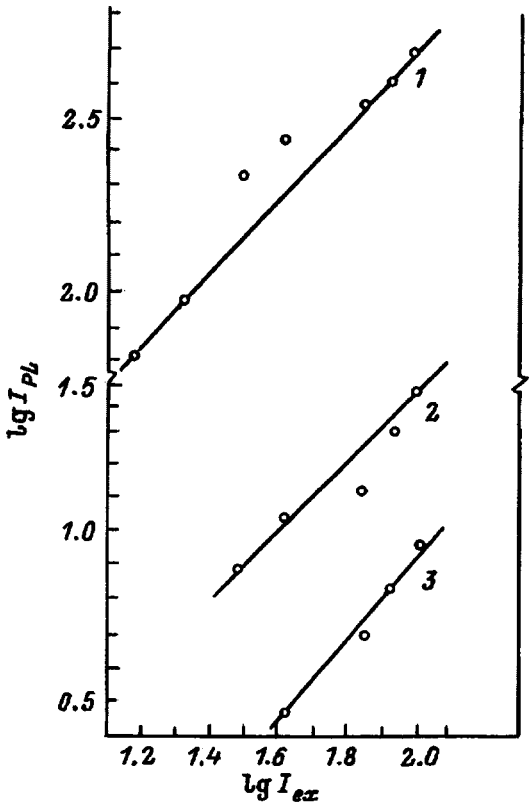

FIG. 5. Lux–brightness characteristic of the B luminescence band of a ZnSe:Se crystal; T_a=950 °C; T, K: *1*—82, *2*—126, *3*—166. α: *1*,*2*—1; *3*—1.2.

the excitation intensity—the so-called lux–brightness characteristics, which contain definite information about the mechanism of temperature quenching of this band. If the lux–brightness characteristic is linear, i.e., in the coordinates $\ln I_{PL}=f(\ln I_{ex})$ this dependence is a straight line with slope $\alpha=1$, then the internal quenching mechanism operates, whereas for $\alpha>1$ the external quenching mechanism is realized.[7] It is clear from Fig. 5 that the lux–brightness characteristics are nearly linear over a wide temperature interval and, consequently, it may be assumed that temperature quenching of the intensity of the *B* band is realized by the internal mechanism. This can apparently also explain the small values of the activation energy of temperature quenching of the intensity of the *B* band at both low and high temperatures. The values of the activation energy of temperature quenching obtained in this case are not equal to the depth of the associative acceptors ($V_{Zn}D$) or the simple acceptors V_{Zn}. By way of an example, the depth of the intrinsic defect V_{Zn} [$E_a(V_{Zn})\sim 0.6$ eV; Ref. 8] is an order of magnitude greater than the activation energy of thermal quenching of the intensity of the *B* band ($\sim 0.06-0.07$ eV), where this band is due, in our view, to emission centers of just this type in the high-temperature region.

[1] M. Yamoguchi and A. Yamomoto, Jpn. J. Appl. Phys. **16**, 77 (1977).
[2] V. S. Vavilov, Vu Zoan M'en, G. N. Ivanova, D. D. Nedeoglo, M. V. Chukichev, and A. V. Simashkevich, Fiz. Tverd. Tela **26**, 1457 (1984) [Sov. Phys. Solid State **26**, 883 (1984)].
[3] G. N. Ivanova, D. D. Nedeoglo, A. V. Simashkevich, and K. D. Sushkevich, Zh. Prikl. Spektrosk. **30**, 459 (1979).
[4] B. V. Novikov, G. Poppisher, and V. G. Talalaev, Fiz. Tverd. Tela **21**, 817 (1979) [Sov. Phys. Solid State **21**, 478 (1979)].
[5] T. Ido, M. Kato, and A. Yoshida, J. Phys. D **11**, 15 (1978).
[6] G. N. Ivanova, D. D. Nedeoglo, B. V. Novikov, and V. G. Talalaev, Fiz. Tverd. Tela **23**, 2693 (1981) [Sov. Phys. Solid State **23**, 1579 (1981)].
[7] I. B. Ermolovich, A. M. Pavelets, and L. N. Khanat, Zh. Prikl. Spektrosk. **31**, 446 (1986).
[8] J. Jacobs and H. Arnold, Krist. Tech. **10**, K71 (1975).

Translated by Paul F. Schippnick

Effect of heteroepitaxial surface passivation on the photosensitivity spectra and recombination parameters of GaAs layers

I. A. Karpovich and M. V. Stepikhova

N. I. Lobachevskiĭ Nizhniĭ Novgorod State University, 603600 Nizhniĭ Novgorod, Russia
(Submitted April 1, 1997; accepted for publication May 22, 1997)
Fiz. Tekh. Poluprovodn. **32**, 182–186 (February 1998)

The influence of heteroepitaxial passivation of the surfaces of GaAs layers by a deposition of thin layer of $In_{0.5}Ga_{0.5}P$ on the photomagnetic effect spectra, the barrier photoconductivity, and the capacitor photovoltage in GaAs is investigated. An increase in the surface recombination rate and the anomalous drift component of the photomagnetic effect with growth of the absorption coefficient in the region of strong absorption was observed. The influence of these effects on the photosensitivity spectra has been elucidated. The possibility of using photoelectric techniques to determine the recombination parameters of thin GaAs layers is demonstrated. © *1998 American Institute of Physics.* [S1063-7826(98)01302-7]

Difficulties arise in the determination of the recombination parameters of GaAs epitaxial layers by photoelectric methods, due to the strong influence of the surface on the photoelectric properties.[1] Thus, the presence of depleted layers and the associated barriers on the surface and on the inner boundary between the epitaxial layer and the semi-insulating substrate leads to the predominance of the barrier mechanism of photoconductivity (PC) in the layers under ordinary conditions (see, e.g., Ref. 2). In this situation the well-known methods of determining the lifetime of the majority carriers and the surface recombination rate (SRR) developed for bulk photoconductivity do not apply.[3,4] The determination of the lifetime of the minority carriers and the surface recombination rate from the photomagnetic effect (PME), as will be shown in this paper, requires an account of the spectral dependence of the surface recombination rate and the anomalous drift component in the photomagnetic effect, which are also associated with the presence of a surface barrier.

In this article we report the results of an experimental study of the effect that heteroepitaxial surface passivation of GaAs layers by deposition of a thin layer of InGaP (Ref. 5) has on the photomagnetic effect spectra, the photoconductivity spectra, and the capacitor photovoltage (CPV) in GaAs. The significant decrease in the surface recombination rate brought about by surface passivation substantially simplifies the problem of determining the recombination parameters in the layers and makes it possible to explain some features of the photoelectric sensitivity spectra.

EXPERIMENTAL TECHNIQUE

GaAs layers were grown on semi-insulating substrates with (100) orientation by gas-phase epitaxy from metallo-organic compounds (MOS-hydride epitaxy) at atmospheric pressure. The parameters of some of these samples are listed in Table I.

Heteroepitaxial passivation of the surface of the GaAs layers was effected by deposition of a lattice-matched layer of $In_{0.5}Ga_{0.5}P$ of thickness ~ 20 nm. In the presence of a cladding heterolayer the surface recombination rate is decreased by 1–2 orders of magnitude and the height of the surface barrier is lowered from ~ 0.6 to 0.3 eV (Ref. 5). In contrast to Ref. 5, passivation was effected not during growth but after exposure of the layers to air, which, as it turned out, did not degrade the passivation effect.

In our study of the photomagnetic effect, the measurements were performed in the open-circuit regime in a magnetic field with induction $B = 1.8$ T, and the short-circuit photocurrent I_{PM} was calculated from the photovoltage.

The photoconductivity in planar geometry was measured in modulated monochromatic and pulsed white light. In the second case the maximum intensity at the surface of the sample from the quantum efficiency corresponded to an intensity of $\sim 1\times 10^{18}\ \mathrm{cm^{-2}\cdot s^{-1}}$ of the strongly absorbed monochromatic radiation. Single light pulses of duration ~ 3 ms were obtained with the use of a flashlamp. The photocurrent pulse was recorded with the help of a recording oscilloscope.

The combined use of photoconductivity spectra and the capacitor photovoltage allowed us to estimate the contribution of each of the barriers to the barrier photoconductivity. For this purpose, we measured the capacitor photovoltage spectra separately on the surface barrier and the inner layer barrier (front-wall and rear-wall capacitor photovoltage, respectively) by the technique described in Ref. 6. All spectra were measured in the weak-signal, linear (in the illumination intensity) regime and were reduced to the same number of incident photons.

EXPERIMENTAL RESULTS AND DISCUSSION

1. The photomagnetic effect

The photomagnetic effect spectra in the investigated n- and p-type GaAs epitaxial layers with natural and etched surface are characterized by a significant drop in the photocurrent in the region of intrinsic absorption for photon ener-

TABLE I. Parameters of investigated GaAs layers.

Sample No.	d, μm	Type of conductivity	n_0, p_0, 10^{16} cm^{-3}	μ_n, μ_0, cm^2/(V·s)	L^*, L, μm	τ^*, τ, 10^{-8} s	s, 10^4 cm/s	Surface state
1	6.7	n	0.05	6700	1.1*	0.2*	5	Natural
					3.2	1.4	$\ll 1$	Passivated
2	2.5	n	12.0	3100	2.1*	0.6*	1.6	Natural
					3.5	1.4	$\ll 1$	Passivated
3	2.5	p	1.9	290	0.5*	3×10^{-3}*	—	Natural
4	3.0	p	6.6	290	0.8*	8×10^{-3}*	—	Natural

Note: The asterisk denotes the effective parameters, d is the layer thickness, $n_0(p_0)$ is the electron (hole) concentration, and $\mu_n(\mu_p)$ is the electron (hole) mobility.

gies $h\nu > E_g$, where E_g is the width of the band gap (Fig. 1, curves *3* and *5*). In GaAs single crystals, in contrast, the photocurrent was found to grow in this region,[7] where this growth, according to the diffusion theory of the photomagnetic effect,[8] is described by the factor $\alpha L/(1+\alpha L)$, where $\alpha(h\nu)$ is the absorption coefficient, and L is the diffusion length of the minority carriers. This made it possible to determine the diffusion length L from the dependence $1/I_{\mathrm{PM}} = f(1/\alpha)$, which in crystals with different conductivities varied randomly in the range 0.1–0.6 μm.

The decrease in I_{PM} for $\alpha w > 1$, where w is the thickness of the surface barrier, was predicted by the theory of the photomagnetic effect, which takes into account the inconstancy of the Fermi quasilevel for the minority carriers in the barrier region.[9] This decrease is due to an increase in the effective surface recombination rate s with increase of the absorption coefficient α from $\sim 1\times10^4$ to 5×10^4 cm^{-1} in the energy interval 1.45–2 eV. For sample 1 ($w \approx 1.2$ μm) this condition is satisfied quite well. Qualitatively, this explanation accords with the fact that the effect is diminished in the presence of illumination (curve *4*) and by increasing in the electron concentration n_0 (curve *3*), although for the heavily doped sample (sample 2, $w \approx 0.07$ μm) a larger shift of the maximum toward shorter wavelengths is expected.

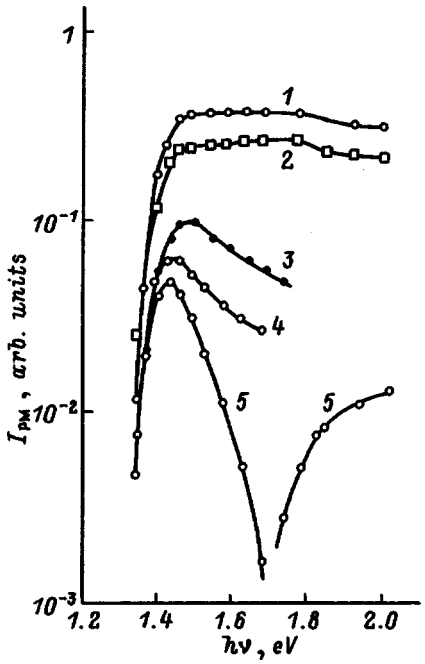

FIG. 1. Effect of surface passivation and doping level on the PME spectrum: *1,2*—passivated surface; *3,5*—unpassivated surface; *4*—unpassivated surface in the presence of illumination; *1,4,5*—sample 1; *2,3*—sample 2.

In view of the presence of a depleted layer and a high recombination rate on the GaAs surface, one should expect proof of a substantial role of the anomalous drift component in the photomagnetic effect, especially in epitaxial layers with low carrier concentration. Calculations based on the theory of the anomalous photomagnetic effect[9,10] show that for sample 1 for $s = 5\times10^4$ cm·s^{-1} (see Table I) the anomalous component lowers the current I_{PM} almost twofold at the edge of the absorption band. According to the theory, for constant surface recombination rate the relative contribution of the anomalous component should decrease with increasing absorption coefficient. In the investigated layers this decrease may be compensated for by an increase in the surface recombination rate with growth of α.

It follows from the theory that for $\alpha w > 1$ the resulting photomagnetic effect cannot be anomalous even for an infinite surface recombination rate. However, in contradiction to the existing theory, in sample 1 and other samples with $n_0 < 5\times10^{15}$ cm^{-3}, that is precisely what happens in this region when $h\nu > 1.7$ eV: The photomagnetic effect becomes anomalous (curve *5*). This result was confirmed by PME measurements with continuous illumination from a helium–neon laser ($h\nu = 1.96$ eV): the anomalous sign and linear dependence of I_{PM} on the illumination intensity were maintained up to intensities $\sim 10^{17}$ cm^{-2}·s^{-1}. In layers with $n_0 > 10^{16}$ cm^{-3} the photomagnetic effect did not change sign in the short-wavelength region. The theory of the anomalous photomagnetic effect apparently is in need of refinement in the spectral region $\alpha w > 1$.

As was previously reported,[5] heteroepitaxial surface passivation increases I_{PM} and completely eliminates the decrease of I_{PM} in the short-wavelength region (Fig. 1, curves *1* and *2*). Its effect on the photomagnetic effect is due mainly to the decrease in the surface recombination rate and not the barrier height, since the illumination lowering the barrier height from ~ 0.6 to ~ 0.2 eV has a relatively weak effect on the shape of the spectrum and the magnitude of I_{PM} (curve *4*). Evidence of a significant drop in the surface recombination rate is also provided by the gain in the edge photoluminescence of the layers: at 300 K in sample 1 it is increased by more than a hundredfold, and in sample 2 it is increased by a factor of 8. In layers with surface passivation it is possible in practice to ignore surface recombination and the as-

sociated anomalous component of the photomagnetic effect.

The diffusion component of the photomagnetic effect[4] can be written in the form

$$I_{\mathrm{PM}}=I_{\mathrm{PM}}^{0}F, \tag{1}$$

where

$$I_{\mathrm{PM}}^{0}=q(\mu_n+\mu_p)\beta(1-R)J_0BL\left(\frac{\alpha L}{1+\alpha L}\right) \tag{2}$$

is the photomagnetic current per unit width in a thick sample ($d\gg L,\alpha^{-1}$) for a small surface recombination rate ($s\ll D/L$), D is the diffusion coefficient of the minority carriers, μ_n and μ_p are the electron and hole mobilities, R is the reflection coefficient, β is the quantum yield, J_0 is the intensity of the incident radiation, and F is a known function which allow for surface recombination on both boundaries of the layer and for the size effects which are determined by the relative values of the lengths d, α^{-1}, and L.

In general, Eq. (1) contains three unknown recombination parameters: L, s, and s_d (s_d is the surface recombination rate on the dark side of the layer). The necessity of allowing for the spectral dependence $s(h\nu)$ and the anomalous drift component of the photomagnetic effect strongly complicates the problem of determining these parameters from the photomagnetic effect. However, the use of sufficiently thick layers with surface passivation radically eliminates all these difficulties since it makes it possible to use approximation (2) to determine L. For thick unpassivated layers, as a generalized characteristic of the recombination activity of the surface and the volume, we may introduce an effective diffusion length L^*, defining it from relation (2) for the maximum value of the photocurrent: $I_{\mathrm{PM}}(h\nu_m)$. If we can ignore the contribution of the anomalous component to the photomagnetic effect when $h\nu=h\nu_m$, then if L^* and L are known we can calculate the surface recombination rate $s(h\nu_m)$. Since in this case $F=(1+sL/D)^{-1}$ (Ref. 4), it can be shown that

$$s(h\nu_m)=\frac{D}{L}\left(\gamma\frac{\gamma+\alpha L}{1+\alpha L}-1\right), \tag{3}$$

where $\gamma=L/L^*>1$.

For n-type layers the parameter γ reaches values ~ 3 and decreases with increasing n_0 (see Table I). The hole diffusion length L_p in epitaxial layers is an order of magnitude greater than in single crystals,[7] which suggests their higher degree of structural perfection. In this light, a different form of the photomagnetic effect spectra of epitaxial layers and single crystals for $h\nu>E_g$ also makes sense. In the latter, due to their small value of L, surface recombination plays a relatively small role ($s<D/L$). The analogous inequality is also satisfied in layers with surface passivation, but since $\alpha L\gg 1$ for them when $h\nu>E_g$, according to relation (2), $I_{\mathrm{PM}}(h\nu)\simeq$const in this region. For p-type layers $L_n^*<L_p^*$. Since $D_n\simeq 20D_p$, we can conclude that the lifetime of the minority carriers in p-type layers is roughly two orders of magnitude shorter than in n-type layers.

The surface recombination rate $s(h\nu_m)$ determined from the photomagnetic effect depends weakly on n_0 (see Table I). This tendency, also confirmed for other layers, deviates from the dependence $s\sim n_0$ established in Ref. 11 on the basis of an analysis of the data in the literature. For sample 2 $s(h\nu_m)$ is almost two orders of magnitude less than the values $s\simeq 10^6$ cm·s^{-1}, which are determined from the cathodoconductivity[12] and cathodoluminescence[13] for similar values of n_0 and which are used in Ref. 11. For such a large value of the surface recombination rate, under our conditions the photomagnetic effect would be immeasurably small. One reason for the discrepancy between the surface-recombination-rate data may be the dependence of the surface recombination rate on the depth of excitation of the nonequilibrium carriers, which under conditions of photoexcitation is reflected in the spectral dependence of the surface recombination rate, and under conditions of electron excitation should lead to a dependence of the surface recombination rate on the electron energy.

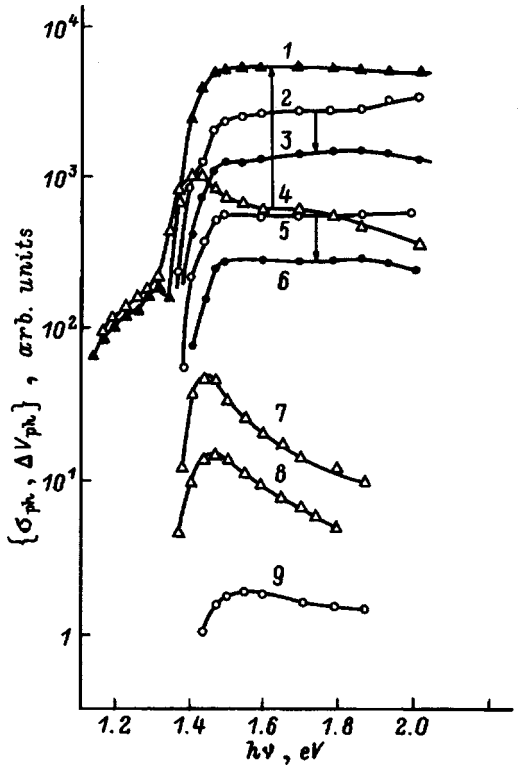

FIG. 2. Effect of surface passivation and illumination on the photoconductivity spectra σ_{ph} and capacitor photovoltage ΔV_{ph}. *1,4,8*—back-wall capacitor photovoltage; *2,3,9*—front-wall capacitor photovoltage; *5,6,7*—photoconductivity. Surface: *1,3,6*—passivated; *2,4,5*—unpassivated. Spectra *7–9* were taken in the presence of illumination. The arrows indicate the change in the photosensitivity as a consequence of surface passivation.

2. Photoconductivity and capacitor photovoltage

In contrast to the photomagnetic effect, on which illumination has only a weak effect, the photoconductivity and capacitor photovoltage in GaAs layers are very sensitive to illumination, as could be expected from their barrier nature.[2]

Without illumination, the photoconductivity spectrum σ_{ph} coincides in shape with the front-wall capacitor photovoltage spectrum ΔV_{ph} (Fig. 2, curves *2* and *5*) and differs noticeably from the rear-wall spectrum (curve *4*). The effect of a decrease in the photosensitivity for $h\nu>E_g$ is manifested in the latter, as in the photomagnetic effect spectrum,

and an impurity photosensitivity associated with absorption of the emission of the EL-2 centers in the substrate is observed. Obviously, under these conditions the barrier photoconductivity of the layers is determined by the surface barrier.

However, in white illumination with effective intensity $\sim 10^{17}$ cm$^{-2}\cdot$s^{-1}, as a result of a decrease in the height of both barriers, the photoconductivity and the capacitor photovoltage are decreased by 2–3 orders of magnitude (curves *7–9*) and the region of localization of barrier photoconductivity shifts since the photoconductivity spectrum now coincides with the spectrum of the rear-wall capacitor photovoltage (curves *7* and *8*), which also becomes significantly larger in magnitude than the front-wall photovoltage (curves *8* and *9*).

The spectral dependence of the rear-wall capacitor photovoltage for $h\nu > E_g$ directly reflects the spectral dependence of the surface recombination rate $s(h\nu)$. Since the inner boundary in n-type layers is a sink for holes, it is possible to replace it by a surface with large surface recombination rate $s_d \gg D/L$ when considering its effect on the hole distribution $\Delta p(x)$. An analysis of the hole distribution $\Delta p(x)$ shows[4] that in thick layers ($d \gg L$) for surface generation ($\alpha L \gg 1$) and $s \gg D/L$ (such conditions were realized in sample 1 without surface passivation) $\Delta p(d) \sim (D/ss_dL)\exp(-d/L)$. It is natural to assume that the weak-signal, rear-wall capacitor photovoltage $\Delta V_{\rm ph}(h\nu)$ is proportional to $\Delta p(d)$ and, consequently, inversely proportional to $s(h\nu)$ if $s_d(h\nu) = \text{const}$. From the spectra of this photovoltage (curves *4* and *8*) we can conclude that $s(h\nu)$ increases three- to fourfold in the interval $h\nu = 1.45$–2 eV. Note that the photomagnetic current in this spectral interval decreases significantly more rapidly and even changes sign (Fig. 1, curve *5*), which we attribute to an additional contribution to this falloff from the anomalous component of the photomagnetic effect.

In the case of bulk photoconductivity the decrease in the photosensitivity in the short-wavelength region can also take place for a constant surface recombination rate.[14] On this is based one method of determining it, which was also applied to GaAs layers.[1] However, in the case of barrier photoconductivity this effect has a different nature: it is controlled by the spectral dependence of the surface recombination rate itself, where the redistribution of the contribution to the photoconductivity from the surface barrier and the inner barrier upon illumination is of substantial importance. It is interesting that the spectral dependence of the surface recombination rate is not manifested in explicit form in the photosensitivity spectrum of the surface barrier in the photoconductivity and capacitor photovoltage, in contrast to the photomagnetic effect. This fact is tied to the barrier-trap nature of the surface photovoltage, in which an increase in the surface recombination rate can be compensated for by a corresponding change in the charge of the surface traps. Surface capture, as was shown in Ref. 1, can even lead to an increase in the photosensitivity in the short-wavelength region.

Surface passivation decreases the photoconductivity and front-wall capacitor photovoltage by roughly a factor of 2 (curves *3* and *6*) and significantly increases the back-wall capacitor photovoltage (curve *1*). As a result, the photosensitivity decrease at energies $h\nu > E_g$ ceases to show up in the back-wall spectrum, similar to the case for the spectrum of the photomagnetic effect. The decrease in the photosensitivity of the surface barrier upon passivation, as can be shown, does not contradict the decrease in the surface recombination rate, since the height of the surface barrier is also decreased by passivation, and the effect of the latter factor turns out to be predominant.

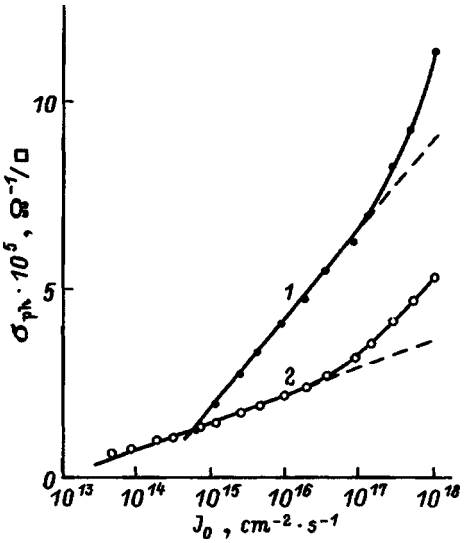

FIG. 3. Dependence of the photoconductivity $\sigma_{\rm ph}$ on pulsed illumination. Surface: *1*—passivated, *2*—unpassivated.

Only the decrease in the surface recombination rate evidently can have an effect on the photosensitivity of the inner barrier. Setting $s \ll D/L$ for the passivated surface and, as before, $s_d \ll D/L$, it can be shown that in this case $\Delta V_{\rm ph}(h\nu) \sim \Delta p(d) \sim (1/s_d)\exp(-d/L)$; i.e., it does not depend on s and, consequently, upon passivation the photosensitivity should increase by a factor of $K_p = sL/D$. Calculating from the tabulated data gives the result $K_p(h\nu_m) \simeq 2$ for sample 1. The experimental value is ~ 2.8 for curves *1* and *4*. For $h\nu = 2$ eV, driven by the growth in s K_p increases to 13. The photoconductivity at the surface barrier in the strong photovoltage signal regime is[2]

$$\sigma_{\rm ph}^b = \frac{\sigma_0 l_0 \Delta Y_{\rm ph}}{\sqrt{Y_0 - \Delta Y_{\rm ph} + 1} + \sqrt{Y_0 + 1}}, \tag{4}$$

where σ_0 is the conductivity of the quasineutral bulk of the sample, l_0 is the Debye screening length,

$$\Delta Y_{\rm ph} = \eta \ln(1 + CJ_0) \tag{5}$$

is the surface photovoltage in units of kT, Y_0 is the initial bending of the bands, $\eta \sim 1$ is a parameter that depends on the recombination properties of the barrier, and C is a constant. According to Eqs. (4) and (5), the dependence $\sigma_{\rm ph}^b(J_0)$ is nearly logarithmic. Such a dependence is observed in a wide intensity range of the pulsed illumination J_0 (Fig. 3). The slope of the straight line in Fig. 3 for the passivated surface is roughly three times larger than for the natural surface. This is explained by a decrease in Y_0 and an increase in the parameter η.

Because of the relatively weak dependence of the barrier photoconductivity on J_0 at high enough intensities, the bulk photoconductivity becomes commensurate with the barrier photoconductivity. This affects the deviation from a logarithmic dependence of curves *1* and *2* at high intensities. Analysis shows that the excess over the logarithmic component of the photoconductivity $\Delta\sigma_{\rm ph}$ is proportional to J_0^m with $m \simeq 1$ and 0.5 for the passivated surface and natural surface, respectively.

For total absorption of radiation in the layer the bulk photoconductivity reduced to the surface photoconductivity is (in units of $\Omega^{-1}/\square$)

$$\sigma_{\rm ph}^v = q\mu_n\tau_{\rm ph}(1-R)J_0, \tag{6}$$

where $\tau_{\rm ph}$ is the effective lifetime of the electrons in the layer. Since $\sigma_{\rm ph}^b \sim \sigma_0 l_0 \sim \sqrt{n_0}$, the condition $\sigma_{\rm ph}^v \simeq \sigma_{\rm ph}^b$ is more easily realized for small values of n_0. For $J_0 \simeq 10^{18}$ cm$^{-2}\cdot$s^{-1} we were able to distinguish the bulk component of the photoconductivity only in sample 1, which has a minimum concentration n_0. If we set $\Delta\sigma_{\rm ph} = \sigma_{\rm ph}^v$, then we have the estimate $\tau_n \simeq 3\times 10^{-8}$ s for the sample with surface passivation, in which $\tau_{\rm ph} = \tau_n$ and does not depend on J_0. For this same sample, from the photomagnetic effect we obtained the value $\tau_p = 1.4\times 10^{-8}$ s; i.e., the bulk lifetimes of the electrons and holes in *n*-type layers with surface passivation are roughly equal. Note that if we ignore the barrier nature of the photoconductivity and formally define τ_n from relation (6) in the region of linear dependence of the barrier photoconductivity on J_0 (for $J_0 < 10^{13}$ cm$^{-2}\cdot$s^{-1}), we obtain $\tau_n \sim 10^{-5}$ s. Such overestimates of τ_n were obtained in many earlier studies.[7,15]

CONCLUSIONS

These are the main conclusions of our study. In GaAs epitaxial layers with natural surfaces, in the strong absorption region ($h\nu > E_g$, $\alpha w > 1$) the surface recombination rate increases with growth of the absorption coefficient α and an anomalous sign of the photomagnetic effect is observed at low carrier concentrations. This latter result deviates from the prediction of the existing theory of the anomalous photomagnetic effect. Heteroepitaxial passivation of a GaAs surface under a layer of $In_{0.5}Ga_{0.5}P$ strongly reduces the surface recombination rate and eliminates the features in the PME, PC, and CPV spectra associated with these phenomena and also substantially facilitates the determination of the diffusion length and the surface recombination rate in the layers. No dependence of the surface recombination rate on the electron concentration in the interval $10^{15}-10^{17}$ cm^{-3} was detected for a natural surface.

[1] N. L. Dmitruk, V. L. Lyashenko, A. K. Tereshenko, and S. A. Spector, Phys. Status Solidi A **20**, 53 (1973).
[2] I. A. Karpovich, B. I. Bednyĭ, N. V. Baĭdus', S. M. Plankina, M. V. Stepikhova, and M. V. Shilova, Fiz. Tekh. Poluprovodn. **23**, 2164 (1989) [Sov. Phys. Semicond. **23**, 1340 (1989)].
[3] S. M. Ryvkin, *Photoelectric Phenomena in Semiconductors* [in Russian] (Fizmatgiz, Moscow, 1963).
[4] Yu. I. Ravich, *The Photomagnetic Effect in Semiconductors and Its Applications* [in Russian] (Sov. Radio, Moscow, 1967).
[5] I. A. Karpovich, B. I. Bednyĭ, N. V. Baĭdus', L. M. Batukova, B. N. Zvonkov, and M. V. Stepikhova, Fiz. Tekh. Poluprovodn. **27**, 1736 (1993) [Semiconductors **27**, 958 (1993)].
[6] I. A. Karpovich, V. Ya. Aleshkin, A. V. Anshon, N. V. Baĭdus', L. M. Batukova, B. N. Zvonkov, and S. M. Plankina, Fiz. Tekh. Poluprovodn. **26**, 1886 (1992) [Sov. Phys. Semicond. **26**, 1057 (1992)].
[7] V. G. Kustov and V. P. Orlov, Fiz. Tekh. Poluprovodn. **3**, 1728 (1968) [Sov. Phys. Semicond. **3**, 1457 (1970)].
[8] V. K. Subashiev, Fiz. Tverd. Tela **5**, 556 (1963) [Sov. Phys. Solid State **5**, 405 (1963)].
[9] V. A. Zuev, A. V. Sachenko, and N. B. Tolpygo, *Nonequilibrium Near-Surface Processes in Semiconductors and Semiconductor Devices* [in Russian] (Sov. Radio, Moscow, 1977).
[10] S. M. Gorodetskiĭ, N. S. Zhdanovich, and Yu. I. Ravich, Fiz. Tekh. Poluprovodn. **7**, 1270 (1973) [Sov. Phys. Semicond. **7**, 853 (1973)].
[11] D. E. Aspens, Surf. Sci. **132**, 406 (1983).
[12] L. Jastrzebski, J. Lagowski, and H. C. Gatos, Appl. Phys. Lett. **27**, 537 (1975).
[13] D. B. Wittry and D. F. Kyser, J. Phys. Soc. Jpn. **21**, 312 (1966).
[14] H. B. de Vore, Phys. Rev. **102**, 86 (1956).
[15] O. Madelung, *Physics of III–V Compounds* (Wiley, New York, 1964).

Translated by Paul F. Schippnick

Transient current in amorphous, porous semiconductor–crystalline semiconductor structures

L. P. Kazakova and E. A. Lebedev

A. F. Ioffe Physicotechnical Institute, Russian Academy of Sciences, 194021 St. Petersburg, Russia
(Submitted June 3, 1997; accepted for publication July 14, 1997)
Fiz. Tekh. Poluprovodn. **32**, 187–191 (February 1998)

The time-of-flight technique in the weak signal mode (i.e., under conditions of small charge drift in the sample) is used to study the transient photocurrent in amorphous (porous) semiconductor–crystalline semiconductor structures. Amorphous Se–As materials, porous Si, and crystalline Si and CdSe were incorporated in the structures. The carrier drift mobilities in the amorphous and porous layers of the structures were determined. The appearance of a cusp on the curves of the transient current is shown to be caused by acceleration of carriers passing through the interface between the amorphous (porous) layer and the crystal. It is established that the carrier acceleration influences the drift mobility and the dispersion parameters. © *1998 American Institute of Physics.* [S1063-7826(98)01402-1]

INTRODUCTION

Amorphous semiconductor–crystalline semiconductor structures are now used extensively in electronics. Television transmission tubes are based on them.[1,2] Similar structures are also utilized in memory elements and switches.[3] Porous silicon–crystalline silicon structures are promising for constructing radiation sources in the visible spectrum.[4,5] The porous silicon (por-Si) layers are deposited on a crystalline silicon (c-Si) surface in such a way that the (por-Si)–(c-Si) structure is a unit whole. Separation of the porous silicon layer from the crystalline surface requires additional technological operations in which it is possible to make use of the electrical properties of the layer.

In view of this circumstance, in the search for ways of enhancing the operating characteristics of devices, and also in the study of the process of charge carrier transport from the amorphous phase to the crystalline, it is necessary to study charge carrier transport in amorphous (porous) semiconductor–crystalline semiconductor structures. Since amorphous and porous materials possess high resistance, and since the charge carrier drift mobility in them is low, to study charge carrier transport in them we employed the time-of-flight measurement technique (TOF).[6]

The purpose of this study is to determine, by using the time-of-flight technique, the mobility in layers of amorphous and porous semiconductors that comprise these structures and to explain the effect of the boundary between the amorphous (porous) and crystalline semiconductors on the shape of the transient photocurrent and the main characteristics of charge carrier transport.

EXPERIMENTAL PROCEDURE

As the object of study we examined the structures (por-Si)–(c-Si), (a-As_2Se_3)–(c-Si), (a-As_2Se_3)–(c-CdSe), (a-$Se_{95}As_5$)–(c-CdSe), and (a-$Se_{95}As_5$)–(a-Se). The choice of amorphous semiconductors of the system Se–As was dictated by the fact that in these materials charge carrier transport has been examined rather broadly. The use of structures based on amorphous materials of the system Se–As makes it possible to compare the transport characteristics of the structure and of the monolayer.

Structures based on amorphous semiconductors were prepared in the following way. A layer of amorphous material was sputtered, using the thermal vacuum evaporation method, onto wafers of crystalline semiconductors (p-Si, n-CdSe) or onto a pre-sputtered layer of a-Se, for which a glass layer with a layer of aluminum or In_2O_3 deposited on it served as the substrate. This metallic layer or crystalline substrate was used as the lower electrode. A translucent aluminum film, vacuum-deposited on the amorphous layer, served as the upper electrode. The area of the upper electrodes was typically $3-7\ \mathrm{mm}^2$. The thickness of the layers was $0.2-1.5\ \mu$m.

To prepare a layer of porous silicon we used polished wafers of boron-doped crystalline p-type (100) Si with a resistivity of $4-5\ \Omega\cdot$cm. The thickness of the porous-silicon layers was $5-7\ \mu$m. The samples had the structure (por-Si)–(c-Si). A translucent chromium or aluminum electrode was vacuum-sputtered onto the porous-Si layer. The crystalline silicon wafer served as the second electrode. The resistivity of the samples was $10^9-10^{10}\ \Omega$.

The time-of-flight technique was employed under conditions of small charge drift, not affecting the electric field distribution (F).[6] The charge carrier drift mobility (μ) was found from the relation

$$\mu = L/t_T F, \tag{1}$$

where t_T is the transit time of the charge carriers through the layer, and L is the layer thickness. Nonequilibrium charge carrier injection into the sample was accomplished with the help of an LGI-21 nitrogen laser with wavelength $0.337\ \mu$m and pulse duration ~ 8 ns. Measurements were made during individual pulses. The time constant of the measuring circuit was significantly less than the transit time ($RC \ll t_T$).

The transit time was found from the transient photocurrent ($I(t)$) curves, whose shape depend on the nature of charge carrier transport in the material.[7–9] Under conditions of normal (Gaussian) transport there is a segment of weak

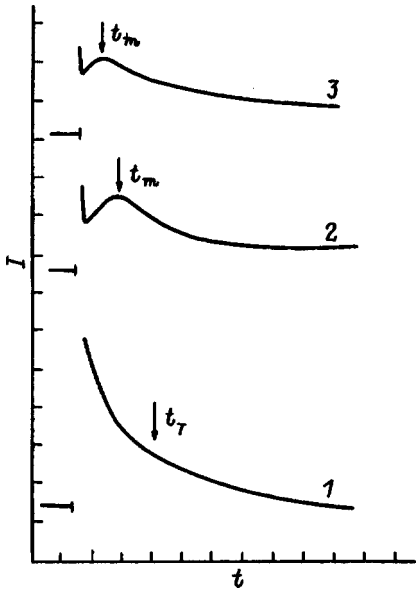

FIG. 1. Oscillograms of the transient photocurrent $I(t)$ corresponding to hole drift in an a-As_2Se_3 monolayer of thickness 1.3 μm (*1*) and in the structure (a-As_2Se_3)–(c-Si) (*2*,*3*). Voltage U, V: *1*,*3*—6; *2*—3. The scale on the t axis is 20 μs/div; on the I axis—0.1 (*1*,*3*), 0.05 (*2*) μA/div.

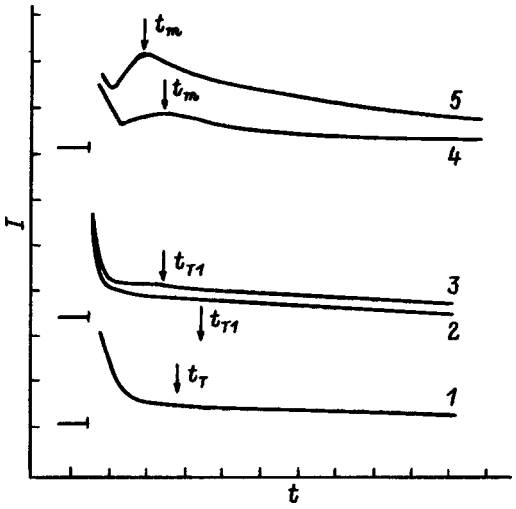

FIG. 2. Oscillograms of the transient photocurrent $I(t)$ corresponding to hole drift in an a-As_2Se_3 monolayer of thickness 0.24 μm (*1*) and in the structure (a-As_2Se_3)–(c-CdSe) (*2*–*5*). Voltage U, V: *1*,*3*—3; *2*—2; *4*—4; *5*—5. The scale on the t axis is 1 (*1*–*3*), 0.5 (*4*,*5*) μs/div; on the I axis—3 (*1*), 2 (*2*,*3*), 10 (*4*), 20 (*5*) μA/div.

time dependence of the current $I(t)$—a ''quasiplateau,'' followed by a rapid decay. The time of flight t_T is determined from the break in the current at the transition point from the first segment to the second.

Under conditions of dispersion transport, which is characteristic of amorphous semiconductors, the dependence $I(t)$ is a continuous decay which is described by different power laws before and after the transit $t=t_T$:[7,9]

$$I(t)\sim t^{-(1-\alpha_i)} \quad \text{for}$$

$$t<t_T \ \text{X} \ t\sim t^{-(1+\alpha_f)} \quad \text{for} \quad t>t_T, \tag{2}$$

where α_i and α_f are the dispersion parameters ($0<\alpha_i$, $\alpha_f<1$). The transit time in this case is determined from the break in the $I(t)$ curves when replotted on a log–log scale. A consequence of the nonequilibrium character of the process of dispersion transport is the presence of a drift mobility time dependence from which the dependence of the mobility on the thickness and the electric field intensity follows: $\mu\sim(F/L)^{(1/\alpha)-1}$, where α is a parameter characterizing the degree of dispersion of the transport process ($0<\alpha<1$). The higher the value of α, the smaller the degree of dispersion and the closer the transport is to Gaussian.

EXPERIMENTAL RESULTS AND DISCUSSION

Our studies showed that a characteristic feature of the transient photocurrents observed in amorphous (porous) layer–crystal structures is the presence of a maximum on the $I(t)$ curves at some time t_m (Figs. 1–4). In the graphs the time t_m is indicated by arrows. The time t_m varied in inverse proportion to the applied voltage (U). The transit time t_T behaves in the same way.

It should be noted that the shape of the $I(t)$ curves obtained on structures is similar to the shape that is characteristic of the space-charge bounded transient current. However, the magnitude of the photocurrent in the structures was significantly less (by 2–3 orders of magnitude) than should be observed under conditions of space-charge bounded transient current.[10] Additionally, the photocurrent varied in direct proportion to the injecting radiation intensity.

Thus, the shape of the photocurrent curves observed in the structures is not associated with the effect of space charge.

We compared the values of t_m and t_T obtained respectively in the structure and in its monolayer part at identical voltages. Figures 1, 2, and 5 show oscillograms of the transient currents observed in the a-As_2Se_3 and a-$Se_{95}As_5$ monolayers. From the figures it is clear that the shape of the $I(t)$ curves in a-As_2Se_3 (Figs. 1 and 2, curve *1*) is typical of dispersion transport, and in a-$Se_{95}As_5$ (Fig. 5, curves *1* and *2*) it is similar to that characteristic of normal (Gaussian) transport. The transit time in the a-As_2Se_3 layers was found by replotting the dependence $I(t)$ on a log–log scale (Fig. 6,

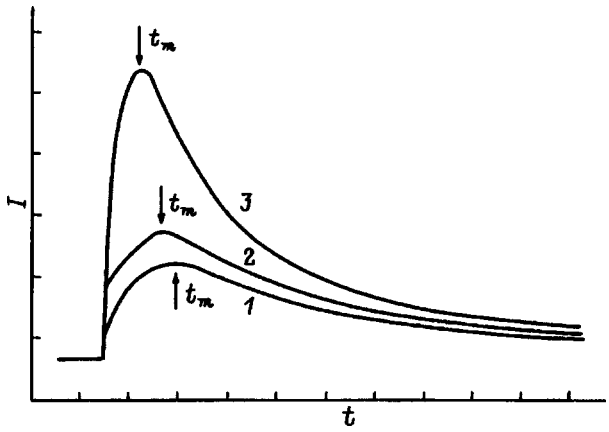

FIG. 3. Oscillograms of the transient photocurrent corresponding to hole drift in the structure (por-Si)–(c-Si). U, V: *1*—15, *2*—20, *3*—30. The scale on the t axis is 2 μs/div; on the I axis—0.3 μA/div.

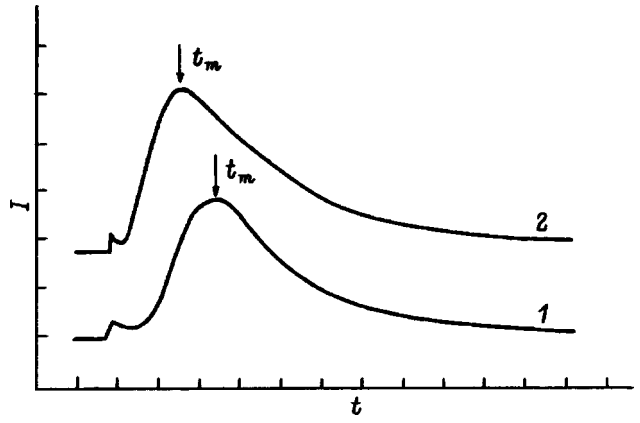

FIG. 4. Oscillograms of the transitory photocurrent corresponding to electron drift in the structure a-$Se_{95}As_5$ (1.1 μm)–c-CdSe (100 μm). U, V: *1*—6.4, *2*—12.8. The scale on the t axis is 10 μs/div; on the I axis—0.2 μA/div.

curve *1*), and in the a-$Se_{95}As_5$ layers directly from the oscillograms. The time of flight is indicated in the figures by an arrow. The drift mobility of the holes (μ_h) in a-As_2Se_3 and of the electrons (μ_e) in a-$Se_{95}As_5$ were $\sim 6\times10^{-5}$ and $\sim 8\times10^{-5}$ cm^2/(V·s), respectively.

Comparison of the values of t_m and t_T showed that they can differ substantially. Thus, in (a-As_2Se_3)–(c-Si) and (a-As_2Se_3)–(c-CdSe) structures $t_T \simeq (1.5-3)t_m$, while in the (a-$Se_{95}As_5$)–(c-CdSe) structure they are similar in value ($t_m \leq t_T$). Accordingly, a difference was obtained in the charge carrier drift mobilities determined from t_m and t_T according to Eq. (1).

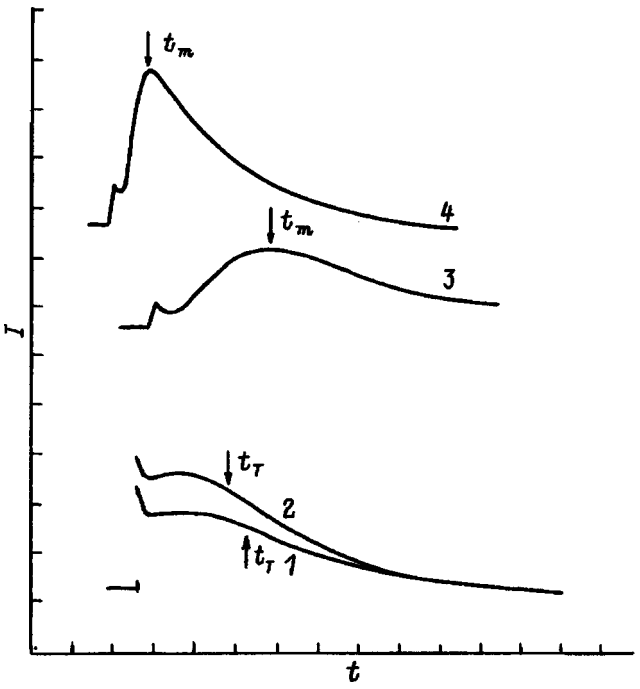

FIG. 5. Oscillograms of the transient photocurrent corresponding to electron drift in the a-$Se_{95}As_5$ monolayer of thickness 0.95 μm (*1,2*) and in the structure a-$Se_{95}As_5$ (0.95 μm)–a-Si (1.45 μm) (*3,4*). Voltage U, V: *1*—3.8; *2*—4.8, *3*—12.8, *4*—25.6. The scale on the t axis is 10 μs/div; on the I axis—0.2 (*1,2*), 0.1 (*3,4*) μA/div.

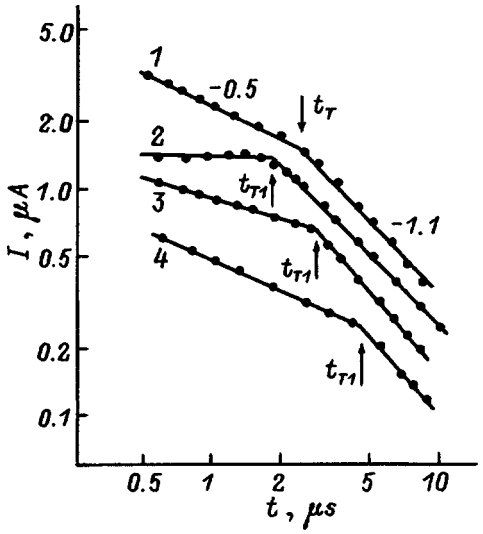

FIG. 6. Time dependence of the photocurrent in an a-As_2Se_3 monolayer of thickness 0.24 μm (*1*) and in the structure (a-As_2Se_3)–(c-CdSe) (*2–4*). Voltage U, V: *1,2*—3; *3*—2; *4*—1.5.

Our studies showed that the form of the transient photocurrent in amorphous (porous) semiconductor–crystalline semiconductor structures is analogous to that observed in the two-layer structure (a-$Se_{95}As_5$)–(a-Se) (Fig. 5). In such a structure the resistivities and dielectric constants of the first and second layers are similar; therefore the distribution of the electric field in such a structure should be roughly uniform. At the same time, the electron drift mobility in the a-$Se_{95}As_5$ layer is two orders of magnitude smaller than in a-Se, in which $\mu_e = 6\times10^{-3}$ cm^2/(V·s). In Ref. 11 it was shown that the appearance of a maximum on the $I(t)$ curves obtained in the (a-$Se_{95}As_5$)–(a-Se) structure is due to acceleration of the charge carriers as they pass from the first layer to the second. Since the charge carrier drift mobility in the amorphous (porous) layer is significantly less than in the crystal, the shape of the $T(t)$ curves obtained in amorphous (porous) semiconductor–crystalline semiconductor structures can also be explained in this way.

According to ideas developed in Refs. 11 and 12, the photocurrent in a two-layer structure consisting of layers with low and high charge carrier mobility in the presence of a transparent boundary between the layers has two components: $I(t)=I_1(t)+I_2(t)$, $I_1(t)=eq_1(t)\mu_1F/L$ and $I_2(t)=eq_2(t)\mu_2F/L$, where e is the charge of the electron, μ_1, μ_2, and $q_1(t)$, $q_2(t)$ are the mobility and number of charge carriers in the first and second layers of the structure, respectively, and L is the total thickness of the structure. For $q_2\mu_2 > q_1\mu_1$ the second term $I_2(t)$ dominates. In this term $q_2(t)\sim\int_{t_{T1}}^{t_{T1}+t_{T2}} P(L_1,t)\mu_1F\,dt$, where $P(L_1,t)$ is the density of delocalized charge carriers on the interlayer boundary, and t_{T1} and t_{T2} are the transit times of the charge carriers across the first and second layer, respectively. If t_{T2} is small enough that $P(L_1,t)$ can be assumed constant during this time, then $q_2\sim P(L_1,t)$ and, consequently, $I(t)\sim I_2(t)\sim P(L_1,t)$. Thus, the dependence $I(t)$ in this case reflects the time variation of the density of delocalized charge carriers on the boundary. The time t_m corresponds to

the maximum of $P(L_1,t)$. In Refs. 13 and 14 it was shown that t_m essentially coincides with the time of flight of the charge carriers across the layer with low mobility ($t_m \simeq t_T$) under conditions of normal (Gaussian) transport and can differ substantially from t_T under conditions of dispersion transport: $t_m/t_T \sim [(1/\sqrt{2})+(1/\alpha\sqrt{2})]^{-(1/\alpha)}$. The use of this formula yields the relation between t_m and t_T in (a-As_2Se_3)–(c-CdSe) and (a-As_2Se_3)–(c-Si) structures established experimentally for $\alpha = 0.7-0.8$. This result is in good agreement with the data obtained in Ref. 15 in a study of the dependence of the hole drift mobility in a-As_2Se_3 on the sample thickness and the electric field intensity, which yields the same values of the dispersion parameter α. The coincidence of the values of t_m and t_T obtained in (a-$Se_{95}As_5$)–(c-CdSe) and (a-$Se_{95}As_5$)–(a-Se) structures is evidence of the normal (Gaussian) nature of transport in a-$Se_{95}As_5$.

Thus, our analysis has shown that to explain the experimental data obtained in amorphous (porous) layer–crystal structures it is possible to invoke ideas about charge carrier transport in a two-layer structure consisting of materials with low and high charge carrier mobility. In this case the layer of amorphous (porous) material is the low-mobility layer and the thin, relatively high-resistance layer of crystalline semiconductor near the boundary with the amorphous material, to which part of the voltage is applied, serves as the high-mobility layer. The higher values of the drift mobility obtained in the a-$Se_{95}As_5$ layer [$\mu_e \simeq 8\times10^{-5}$ cm^2/(V·s)], in comparison with those found for this material from the value of t_m in the (a-$Se_{95}As_5$)–(c-CdSe) structure [$\mu_e \simeq 7\times10^{-5}$ cm^2/(V·s)] indicate a redistribution of the applied voltage in the structure. At the same time, the relatively small difference in these values indicates that the voltage drop in the crystal is not large.

From an analysis of the experimental data it follows that the following two cases are possible:

a) the charge carriers do not drift into the crystal, because of the barrier on the amorphous (porous) layer–crystal boundary;

b) the crystal plays the role of a low-resistance contact; in this case the transport characteristics obtained for the structure should not differ from those found for the layer.

The results we obtained for the structure (a-As_2Se_3)–(c-CdSe) in low electric fields are apparently due to the effect of a barrier on the amorphous (porous) layer–crystal boundary. Studies show that in the region of electric fields $F \lesssim 6\times10^4$ V/cm the dependence $I(t)$ in the structure (a-As_2Se_3)–(c-CdSe) (Fig. 2, curve *2* and Fig. 6, curve *4*) is a continuous time decay, analogous to that observed in the structure a-As_2Se_3 (Figs. 1, 2, 6, curves *1*). From this dependence we determined the values of the dispersion parameters according to expression (2): $\alpha_i = 0.5$ and $\alpha_f = 0.1$ (Fig. 6, curve *1*). As can be seen from Fig. 6 (curves *2–4*), the parameter α_i grows as the electric field is increased. In this case α_f remain virtually constant. Such behavior of the transient current can be explained by maintaining that holes do not drift into the crystal in weak electric fields due to the presence of a barrier on the amorphous layer–crystal boundary; therefore, the dependence $I(t)$ is the same as in the layer. As the electric field is increased, a growing number of the drifting charge carriers overcomes the barrier and winds up in the crystal. This leads to a growth of the parameter α_i.

The values of the hole drift mobilities in the a-As_2Se_3 layer (0.24 μm) and in the structure with a layer of this same material, which are determined from the $I(t)$ curves in weak electric fields, turned out to be nearly identical [$\mu_h \simeq 8\times10^{-5}$ cm^2/(V·s)]. However, they exceed the value $\mu_h \simeq 6\times10^{-5}$ cm^2/(V·s) obtained for the 1.3-μm-thick layer of a-As_2Se_3 used in the (a-As_2Se_3)–(c-Si) structure. This fact agrees with the dispersion nature of transport in a-As_2Se_3 and confirms the presence of a dependence of the drift mobility on sample thickness ($\mu \sim L^{-0.3}$), established earlier on thicker layers.[15]

It should be noted that the direct determination of the mobility in thin a-As_2Se_3 layers is hampered by breakdown phenomena. These difficulties were overcome by using a two-layer structure.

Our study of (por-Si)–(c-Si) structures has shown that for them, as for the (a-As_2Se_3)–(c-CdSe) structures considered above, two variants of the transport process are possible. Figure 3 shows oscillograms of the photocurrent, obtained in the (por-Si)–(c-Si) structure. The presence of a maximum on the $I(t)$ curves at $t = t_m$ indicates that in the given case the charge carriers drift out of the porous silicon layer into the crystalline silicon; i.e., the transport process in the sample can be treated as in a two-layer structure. At the same time, some data[16] indicate that in some samples the charge carriers do not drift out of the porous layer into the crystal. In this case the $I(t)$ curves consist of a continuous time decay, characteristic of dispersion transport. In this case the values of the parameter α_i grow as the electric field is increased. These data may be evidence of the presence of a barrier for holes on the porous silicon layer–crystal barrier.

Note that the drift mobilities obtained respectively from t_m and t_T were similar in both series of samples. This fact indicates the nearly normal nature of transport in por-Si with $\alpha \simeq 1$ and agrees with the weak electric-field dependence of the drift mobility established in Ref. 16.

CONCLUSIONS

We have thus demonstrated the possibility of effectively using the time-of-flight technique to determine the characteristics of transport in layers of high-resistance materials used in amorphous (porous) semiconductor–crystalline semiconductor structures. We have found the values of the hole drift mobility in porous silicon [$\mu_h = 6\times10^{-3}$ cm^2/(V·s)] and in a thin layer of a-As_2Se_3 [$\mu_h = 8\times10^{-5}$ cm^2/(V·s)] and of the electron drift mobility in a-$Se_{95}As_5$ [$\mu_e = 7\times10^{-5}$ cm^2/(V·s)].

The appearance of a maximum on the transient photocurrent curves in these structures is associated with acceleration of the charge carriers as they migrate from the amorphous (porous) layer into the crystal.

We have found that the acceleration of the charge carriers at the interlayer boundary in a two-layer structure does not significantly influence the magnitude of the drift mobility under normal transport conditions; however, it can lead to an

enhanced value of the mobility under conditions of dispersion transport. This effect also leads to an increase in the dispersion parameter α_i but has virtually no effect on the parameter α_f.

The data obtained in this study provide evidence of dispersion transport of holes in a-As_2Se_3, for which $\alpha = 0.7-0.8$, and normal Gaussian transport of electrons and holes in a-$Se_{95}As_5$ and porous silicon, respectively.

This work was carried out with the support of the Russian Fund for Fundamental Research (Grant No. 97-02-18079) and the Russian Ministry of Science program ''Physics of Solid-State Nanostructures'' (Project No. 97-1039).

E-mail: kazakova@ivom.ioffe.rssi.ru

[1] S. Fujiwara, H. Serizawa, O. Equchi, and M. Fukai, National Tech. Report **25**, 286 (1979).
[2] *Technik des Fernsehens*, edited by K. W. Bernath (Springer-Verlag, Berlin, Heidelberg-New York-Tokyo, 1986).
[3] A. Madan and M. P. Shaw, *The Physics and Applications of Amorphous Semiconductors* (Academic Press, Boston, 1988).
[4] L. T. Canham, Appl. Phys. Lett. **57**, 1046 (1990).
[5] N. Koshida and H. Koyama, Appl. Phys. Lett. **60**, 347 (1992).
[6] W. E. Spear, J. Non-Cryst. Solids **1**, 197 (1969).
[7] G. Pfister and H. Scher, Phys. Rev. B **15**, 2062 (1977).
[8] A. I. Rudenko and V. I. Arhipov, Philos. Mag. B **45**, 177 (1982).
[9] A. I. Rudenko and V. I. Arhipov, Philos. Mag. B **45**, 189 (1982).
[10] M. A. Lampert and P. Mark, *Current Injection in Solids* (Academic Press, New York, 1970)].
[11] É. A. Lebedev and L. N. Karpova, Fiz. Tekh. Poluprovodn. **15**, 2421 (1981) [Sov. Phys. Semicond. **15**, 1407 (1981)].
[12] S. Imamura, T. Kitamura, and N. Nakamura, Jpn. J. Appl. Phys. **23**, L537 (1984).
[13] V. I. Arkhipov, L. P. Kazakova, É. A. Lebedev, and A. I. Rudenko, Fiz. Tekh. Poluprovodn. **22**, 723 (1988) [Sov. Phys. Semicond. **22**, 449 (1988)].
[14] V. I. Arhipov, L. P. Kazakova, E. A. Lebedev, and A. I. Rudenko, Philos. Mag. B **66**, 443 (1992).
[15] L. P. Kazakova, B. T. Kolomiets, É. A. Lebedev, and S. A. Tauraĭtene, Fiz. Tekh. Poluprovodn. **21**, 274 (1987) [Sov. Phys. Semicond. **21**, 166 (1987)].
[16] É. A. Lebedev, G. Polisskiĭ, and V. Petrova-Kokh, Fiz. Tekh. Poluprovodn. **30**, 2108 (1996) [Semiconductors **30**, 1099 (1996).

Translated by Paul F. Schippnick

Current–voltage characteristics of Si:B blocked impurity–band structures under conditions of hopping-transport-limited photoresponse

B. A. Aronzon

Russian Scientific Center ''Kurchatov Institute,'' 123182 Moscow, Russia;
Scientific Center for Applied Problems of Electrodynamics, Russian Academy of Sciences, 127412 Moscow, Russia

D. Yu. Kovalev

Russian Scientific Center ''Kurchatov Institute,'' 123182 Moscow, Russia

A. M. Kozlov

Institute of Radio Engineering and Electronics, Russian Academy of Sciences, 141120 Fryazino, Russia

J. Leotin

Laboratoire de Physique des Solides, SNCMP-INSA Complexe Scientifique de Rangueil, 31077 Toulouse-Cedex, France

V. V. Ryl'kov

Scientific-Research Center for Applied Problems of Electrodynamics, Russian Academy of Sciences, 127412 Moscow, Russia; Institute of Radio Engineering and Electronics, Russian Academy of Sciences, 141120 Fryazino, Russia

(Submitted July 9, 1997; accepted for publication July 27, 1997)
Fiz. Tekh. Poluprovodn. **32**, 192–199 (February 1998)

The photoconductivity of Si:B blocked-impurity-band (BIB) structures with boron concentration in the active layer $\sim 10^{18}$ cm^{-3} has been studied. Measurements were performed in the temperature range 4.2–10 K at different intensities of the exciting radiation 10^{10}–10^{15} photons/cm$^2\cdot$s. Photoexcitation at 5.5 μm was realized using a semiconductor laser. At temperatures below 6 K and low bias voltages (<0.5 V) the current–voltage characteristics were found to have a threshold-like character. The threshold voltage rises as the temperature is lowered and the radiation intensity is increased. A model based on the Frenkel'–Poole effect in the impurity band has been developed. This model can be used to numerically describe the current-voltage characteristics with accuracy better than 5%. As a result, it is found that the photoconductivity rises and then reaches a plateau as the radiation intensity increases. Under these conditions, as under equilibrium conditions (in darkness), the hopping conductivity also depends exponentially on the electric field. This fact is explained in terms of the destruction by the electric field of $(A^+ - A^-)$ impurity complexes which appear under nonequilibrium conditions.
[S1063-7826(98)01502-6]

1. INTRODUCTION

Silicon structures with blocked impurity bands (BIB structures) are well known as photosensitive elements and are very promising in a matrix implementation for the construction of low-background infrared detectors, mainly for the reception and processing of optical signals for use in outer space.[1–3] A typical silicon-based BIB photodetector (Fig. 1a) consists of epitaxially grown layers: an active layer (of thickness 10–20 μm with doping level 10^{17}–10^{18} cm^{-3}) and a blocking layer (undoped silicon with thickness of a few microns), and also two n^+ or p^+ contacts, depending on the type of material. The high doping level of the active layer ensures high quantum efficiency for receivers with small dimensions; however, in the temperature region of impurity freeze-out the dark conductivity of the active layer can be substantial as a result of hopping transport of the charge carriers via the impurity band. The introduction of a blocking layer, on the one hand, increases the dark resistance of the structure and, on the other, leads for a certain polarity of the external electric field to the formation in the active layer of a space charge region (SCR) in which photocarrier recombination centers are absent.[3]

By virtue of the above-indicated circumstances, fundamental differences arise in the mechanisms of formation of a photoconductivity signal in BIB receivers and in ordinary photoconductors based on bulk silicon. Thus, for example, in BIB receivers under normal operating conditions a substantially higher level of electric fields is reached when impurity impact ionization processes, which lead to a multiple increase of the photoresponse, begin to play a decisive role.[3] Under these conditions one can also expect the manifestation of a number of other interesting field effects—so far virtually ignored—in BIB structures, as well as impurity photoconductors. These include, in particular, photofield impurity

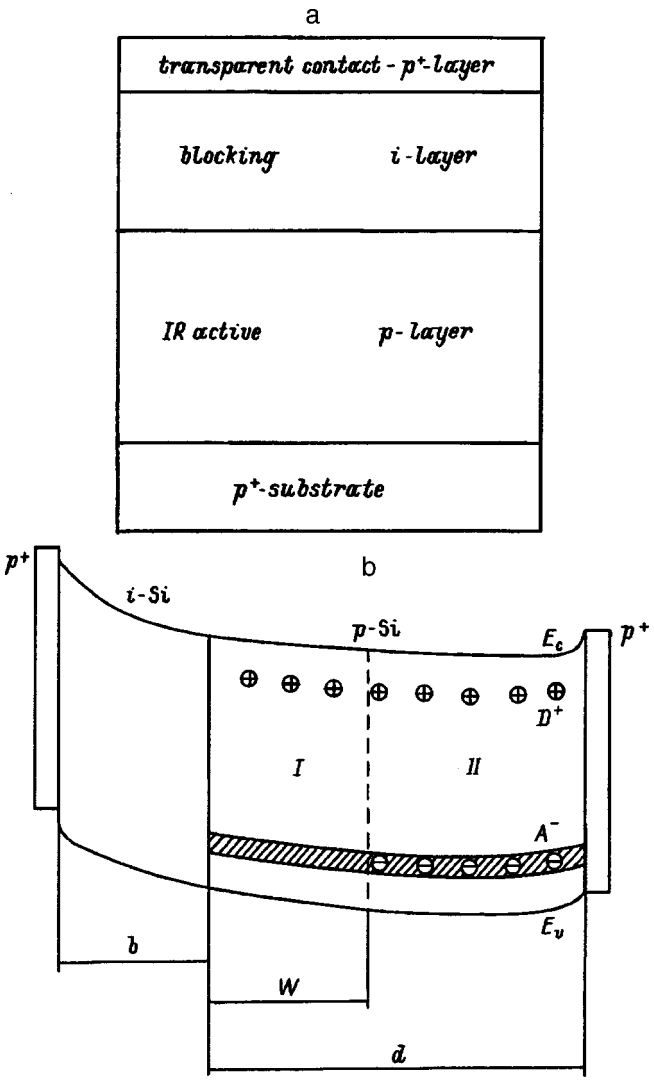

FIG. 1. a—Si:B based BIB-structure. b—band diagram of a Si:B based BIB-photodetector: b—width of the blocking layer, d—width of the active layer, W—width of the space charge region; E_c—bottom of the conduction band, E_v—top of the valence band; D^+—positively charged donors, A^-—negatively charged acceptors, p^+—ohmic contacts, I—space charge region, II—electrically neutral region.

ionization,[4] which may be responsible for the marked shift in the photoconductivity threshold of BIB structures toward the red[5] and the hopping-conductivity-limited photoresponse, which lead to saturation of the multiplication coefficient and a more uniform distribution of the electric field over the thickness of the structure.[6]

Using Si:B-based BIB structures with low concentrations of compensating centers in the active layer, $\leqslant 10^{13}$ cm^{-3}, we have investigated the transition to the impurity-band-limited photoresponse regime that takes place upon lowering the temperature and increasing the infrared photoexcitation intensity. We have found, in particular, that at such a transition the current–voltage characteristics of the structures acquire a threshold character, indicative of the substantial role of the field dependence of the impurity-band conductivity under nonequilibrium conditions, i.e., we have here a manifestation of the Frenkel'–Poole effect.[7]

2. EXPERIMENTAL PROCEDURE AND RESULTS

We examined Si:B-based BIB structures obtained by gas-phase epitaxy, with boron concentration in the active layer $N_a \simeq 10^{18}$ cm^{-3} (Ref. 5). The thicknesses of the blocking layer (b) and of the active layer (d) are 3 and 17 μm, respectively; the area of the structures is $S = 2 \times 2$ mm^2. The concentration of complexing donors $N_d \simeq 6 \times 10^{12}$ cm^{-3} in the samples was determined from measurements of the capacitor dark current for linearly varying bias voltage.[8] The structures together with the infrared source (a $Pb_{1-x}Sn_xSe$ semiconductor laser emitting at $\lambda = 5.5$ μm) were placed in a small cell,[9] which was immersed in a liquid-helium dewar. Such a setup allows one to measure the photoconductivity in a wide range of incident infrared photon fluxes from $<10^9$ to $\sim 10^{15}$ photon/cm$^2 \cdot$s (Ref. 9).

We analyzed the current–voltage characteristics for negative values of the potential V_b of the contact to the blocking layer, which corresponds to the operating regime of a p-type Si-based BIB photodetector. The band diagram of the structure in an external electric field, which explains the principle of operation of the photodetector, is shown in Fig. 1b. Under the indicated conditions the acceptors in the space charge region (I in Fig. 1b) are for the most part neutralized as a result of electrons hopping from negatively charged acceptors to neutral centers. It is also assumed that for a given V_b in the active layer there exists an electrically neutral region (II in Fig. 1b), in which the concentration of negatively charged acceptors is equal to the concentration of compensating donors, which are completely ionized at liquid-helium temperatures. When acted upon by the exciting radiation, free holes and negatively charged acceptors arise in the space charge region. The latter ''migrate'' via the impurity band toward the back contact, ensuring constancy of the space charge region layer upon photoexcitation. Free holes move in the opposite direction, defining the main contribution to the photocurrent. Because of the hole heating effect, which lead to impact ionization of neutral acceptors in the space charge region, the photoresponse of the BIB structure can grow considerably in strong electric fields.

In our study of the current–voltage characteristics $I(V_b)$ (Fig. 2) we noted that under the conditions of impurity impact ionization which is responsible for the abrupt rise in the curves, the dark conductivity gives a noticeable contribution to the total current, especially at temperatures $T > 7$ K. To separate out the optical component of the current, current–voltage characteristics were recorded in digital form in darkness and under illumination, and then differenced. In addition, the current was measured at each experimental point relative to the ''zero'' current corresponding to zero bias voltage $V_b = 0$. This ensured compensation of parasitic current components due to the presence of a different kind of voltage, in particular, a photovoltage which arise as a result of the abrupt change in the impurity concentration at the boundary of the blocking and active layers.

The field dependence of the photocurrent, obtained at different temperatures and illumination intensities, is shown in Figs. 3 and 4. At temperatures below 6 K (Fig. 3a) and low bias voltages ($|V_b| < 0.5$ V) the current–voltage curves have a threshold character. In other words, as the tempera-

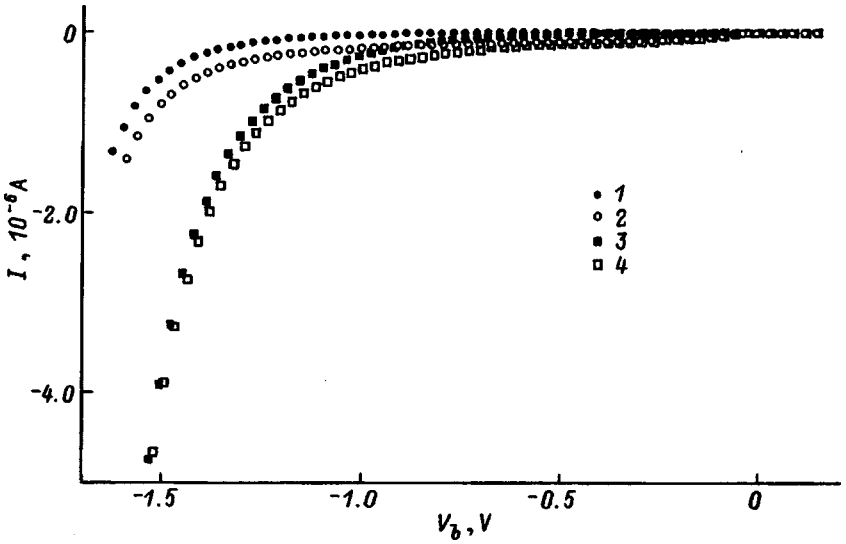

FIG. 2. Current–voltage characteristics of a Si:B based BIB-structure at temperatures $T=7.5$ K (*1*—in darkness, *2*—illuminated); 8.5 K (*3*—in darkness, *4*—illuminated). Radiation intensity $\Phi=2.8\times10^{13}$ photons/cm$^2\cdot$s.

ture is lowered, the region of maximum (linear) variation of the photocurrent is shifted along the voltage axis by some value $V_t\neq0$ (Fig. 3a). Note that the voltage shift V_t increases with decreasing temperature. The threshold voltage also grows as the illumination intensity is increased (Fig. 4). We see that at large voltages $V_b\simeq1$ V the values of the photo-

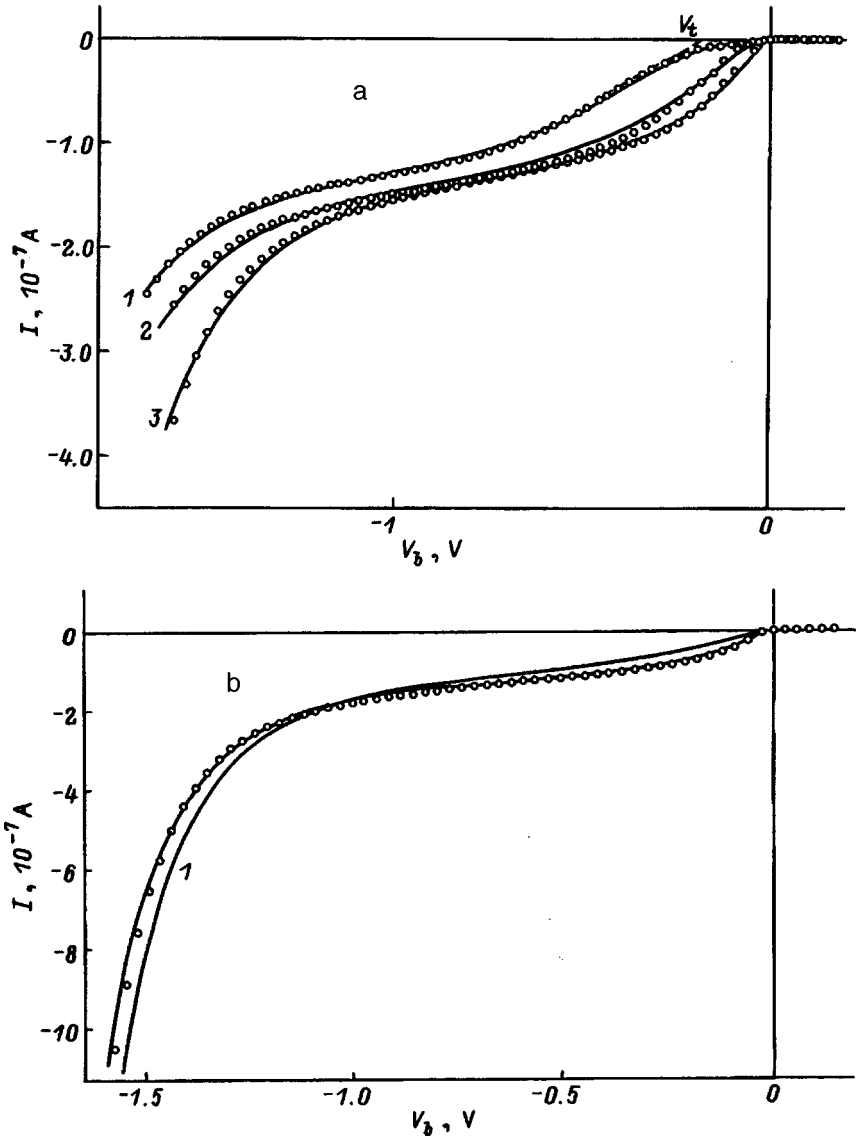

FIG. 3. Current–voltage characteristics of a Si:B based BIB-structure. a: $T=5.2$ (*1*), 6.5 (*2*), 7.5 K (*3*); radiation intensity $\Phi=2.8\times10^{13}$ photons/cm$^2\cdot$s; points—experiment, solid curves—calculation; V_t—threshold voltage. b: $T=8.5$ K, radiation intensity $\Phi=2.8\times10^{13}$ photons/cm$^2\cdot$s; points—experiment, solid curves—calculations; *1*—obtained in the uniform absorption approximation.

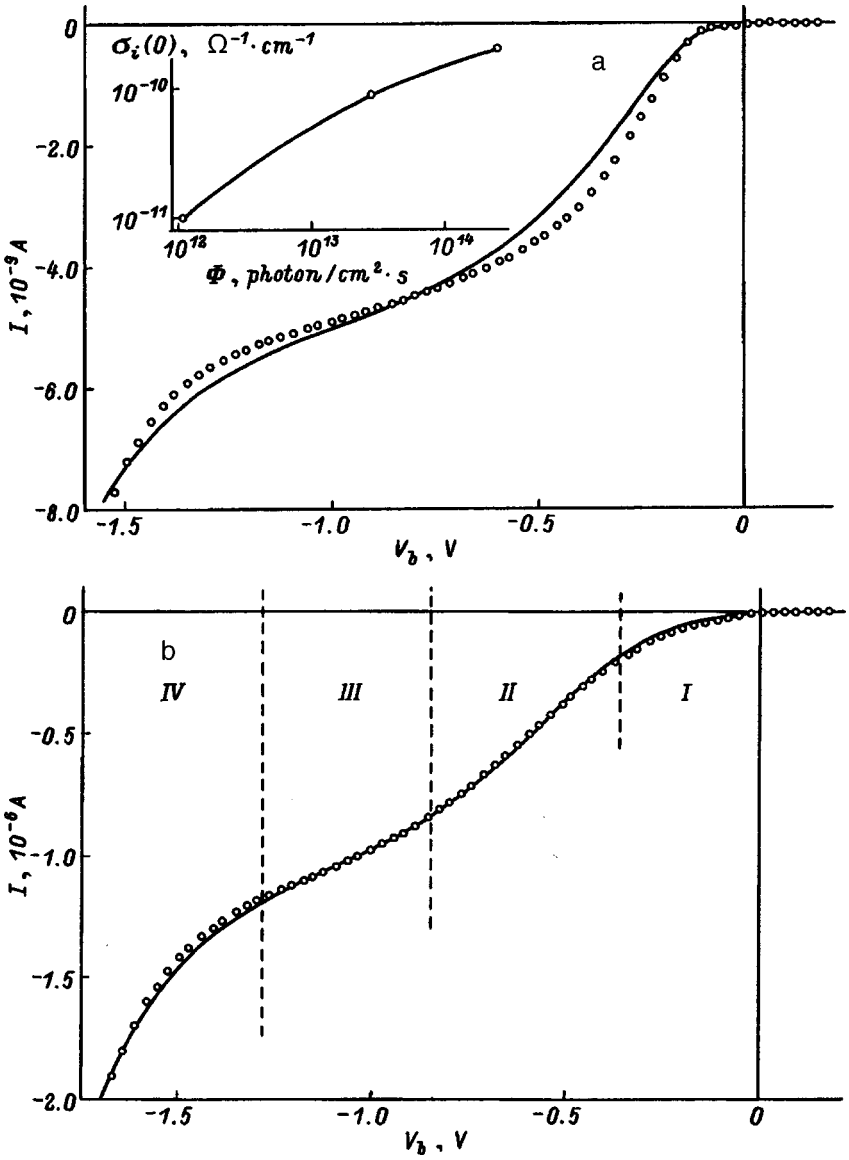

FIG. 4. Current–voltage characteristics of a Si:B based BIB-structure. a: $T=5.2$ K, radiation intensity $\Phi=1.1\times10^{12}$ photons/cm$^2\cdot$s; points—experiment, solid curves—calculation. b: $T=5.2$ K, radiation intensity $\Phi=2.5\times10^{14}$ photons/cm$^2\cdot$s; the vertical dashed lines separate the regions of exponential (I), linear (II), and sublinear (III) variation of the photocurrent with the bias voltage; region IV corresponds to impact ionization of the impurities. The inset plots the dependence of the conductivity in a weak field $\sigma_i(0)$ on the intensity of the exciting radiation Φ.

current at different temperatures nearly coincides. In this voltage region a saturation region is observed on all the curves, where this saturation is noticeably stronger than follows from calculations of the field dependences of the photosensitivity of BIB structures obtained in Ref. 3 (cf., e.g., Fig. 6 in Ref. 3).

It follows from an analysis of the data in Figs. 3 and 4 that the current–voltage characteristics acquire a threshold character as the temperature is lowered and the conductivity in the impurity band σ_i is small. The growth of the threshold voltage with increasing illumination intensity indicates that the photoresponse of the structure under these conditions is limited by the impurity-band conductivity. At the same time, the coincidence of the values of the photocurrent at different temperatures and large bias voltages V_b indicates that σ_i varies appreciably with increasing electric field.

3. DISCUSSION AND CONCLUSIONS

Let us first show in the case of a simplified model of the BIB structure that the above-noted peculiarities of the current–voltage characteristics can indeed take place under conditions of hopping-conductivity-limited photoresponse. We will accordingly use expressions from Ref. 3 for the photocurrent density in the structure

$$J=M(W)J_p(W)+e\int_0^W g(x)M(x)dx, \tag{1}$$

where J_p is the hole current density in the electrically neutral region at the boundary with the space charge region, W is the width of the space charge region, $g(x)$ is the rate of optical generation, and M is the hole multiplication coefficient, defined by the cross section σ_I and the critical field E_c of impact ionization of the neutral acceptors

$$M(x)=\exp\left[\int_0^x \xi(x')dx'\right], \tag{2}$$

$$\xi(x)=\sigma_I N_a \exp[-E_c/E(x)]. \tag{3}$$

We find the width of the space charge region from the Poisson equation, allowing for voltage drop across the electrically neutral region:

$$W=\sqrt{b^2+(\chi/2\pi eN_d)[V_b-E_0(b+d)]}-b. \quad (4)$$

Here χ is the dielectric constant, E_0 is the electric field in the electrically neutral region, which is related to the total current density by the equation of continuity

$$E_0=J/(\sigma_p+\sigma_i), \quad (5)$$

where $\sigma_p=J_p/E_0=e\mu_p\tau g(W)$ is the p-type conductivity in the electrically neutral region, and μ_p and τ are the hole mobility and lifetime, respectively.

Equations (1)–(5) can be solved analytically for J in the absence of impurity impact-ionization effects under conditions of homogeneous absorption satisfying the inequality $b^2\gg(\chi/2\pi eN_d)/[V_b-E_0(b+d)]$. Expanding the right-hand side of Eq. (4) in a series and then employing Eqs. (1) and (5), we obtain

$$J\simeq(\sigma_i+\sigma_p)[V_b/(b+d)]\left[1+\frac{4\pi\sigma_iN_db}{\chi g(b+d)}\right]^{-1}. \quad (6)$$

We assume that the conductivity σ_i for low bias voltages V_b is small enough that the second term inside the brackets in Eq. (6) satisfies the inequality $4\pi\sigma_iN_db/\chi g(b+d)\ll 1$. In this case

$$J\simeq(\sigma_i+\sigma_p)[V_b/(b+d)] \quad (7)$$

and we can expect that the dependence $J(V_b)$ will be entirely determined by the behavior of σ_i as a function of the electric field. Indeed, for a high enough doping level in p-Si ($\geqslant 10^{16}$ cm^{-3}) the product $\mu_p\tau$ and, consequently, the hole conductivity σ_p are essentially independent of the electric field E up to $\sim$100 V/cm (Ref. 10). Additionally, for small compensation the hole lifetime, by virtue of their indirect trapping at neutral acceptors, can reach record-small values, less than the energy relaxation time $\tau_\varepsilon\sim 10^{-10}$ s (Ref. 11). Estimate shows that under these conditions for the measured fluxes of incident radiation $\Phi\sim 10^{13}$ photon/cm$^2\cdot$s, the hole photoconductivity $\sigma_p\leqslant 10^{-11}\ \Omega^{-1}\cdot\text{cm}^{-1}$ and can be markedly less than σ_i if we start from data on hopping conductivity.[7] On the other hand, in the region of activation conductivity σ_i varies with E according to an exponential law[7]

$$\sigma_i=\sigma_{i0}\ \exp\left(-\frac{\varepsilon_3}{kT}\right)\exp\left(\frac{0.69}{kT}\ \sqrt{\frac{4e^3E}{\chi}}\right), \quad (8)$$

where ε_0 is the activation energy of hopping conductivity. Obviously, in the situation under consideration the photocurrent $J\sim\sigma_i$ varies in an analogous way with variation of V_b. Such behavior, however, will take place until the quantity $4\pi\sigma_iN_db/\chi g(b+d)$ is equal to 1—see Eq. (6). With further increase of V_b, the hopping conductivity ceases to limit the photoresponse; correspondingly, the derivative dJ/dV_b reaches a maximum and the dependence $J(V_b)$ becomes linear:

$$J=V_bg\chi/4\pi N_db. \quad (9)$$

Finally, we note that in structures with high enough doping level and small enough concentration of compensating impurities transition from a linear dependence $J(V_b)$ of the type (9) to sublinear is possible. This stems from to the fact that in this case for some values of the bias voltage V_b the width of the space charge region begins to noticeably exceed the width of the blocking layer and the absorption depth $l=(\sigma_{\text{ph}}N_a)^{-1}$, where σ_{ph} is the photoionization cross section of the acceptors. However, fields in which this happens are still too small for impact ionization of impurities. Disregarding reflection from the back contact of the BIB structure, we have for the generation rate

$$g(x)=\sigma_{\text{ph}}N_a\Phi\ \exp(-x\sigma_{\text{ph}}N_a). \quad (10)$$

In this case, as follows from (1),

$$J\simeq e\Phi[1-\exp(-W/l)]\simeq e\Phi \times\left[1-\exp\left(-\sigma_{\text{ph}}N_a\sqrt{\frac{\chi V_b}{2\pi eN_d}}\right)\right]. \quad (11)$$

In other words, for $W\geqslant(\sigma_{\text{ph}}N_a)^{-1}$ the photocurrent is essentially independent of V_b.

Thus, according to Eqs. (6)–(9) and (11) regions of exponential, linear, and sublinear variation of J with increasing V_b can be manifested in the dependence of $J(V_b)$. The last of these regions, when the critical field of impact ionization of the impurities is reached, should obviously give way to a region of abrupt growth of the photocurrent. Exactly such behavior is observed experimentally (in Fig. 4b the indicated regions are separated by dashed lines). This served as the basis for a numerical algorithm for calculating the current–voltage characteristics of BIB structures using relations (1)–(5), (8), and (10).

The calculated current–voltage characteristics are shown in Figs. 3 and 4 by solid lines. The calculation was done for the following fixed parameter values: $N_d=6\times10^{12}$ cm^{-3}, $b=3$ μm, $d=17$ μm, $\mu_p\tau=10^{-7}$ cm^2/V, and $\varepsilon_3=8$ meV [the values (estimates) of $\mu_p\tau$ and ε_3 are based on lifetime,[10,11] on hopping conductivity,[7] and on charge carrier mobility[12] data in doped and weakly compensated silicon]. The remaining parameters were found by fitting the calculated dependences $J(V_b)$ to the experimental values. The fit was carried out in several steps by the method of least squares. In the first step, the $J(V_b)$ curves at high temperatures (Fig. 3b), where the photoresponse of the BIB structures is not hopping-conductivity-limited, were analyzed. To start with, the incident photon flux Φ and the radiation absorption depth l were determined in the region of small bias voltages $0\leqslant V_b\leqslant 0.8$ V. For all curves l was ~ 8 μm to within 5% accuracy. Since the photoionization cross section of boron in silicon Si $\sigma_{\text{ph}}\simeq 10^{-15}$ cm^2 (at photon energies $\sim$200 meV),[13] we found the doping level of the active layer: $N_a\simeq 1.3\times10^{18}$ cm^{-3}, which turned out to be close to the specified value $N_a=10^{18}$ cm^{-3}. Figure 3b also plots the dependence calculated in the homogeneous absorption approximation (curve *1*). It can be seen that the experimental dependence is described rather poorly by this curve.

Next, on the growing segment of the curve $J(V_b)$ ($V_b\geqslant 1$ V), using the obtained values of Φ and l, we found the critical field of impact ionization $E_c=9\times10^3$ V/cm and the product $\sigma_IN_a=6\times10^6$ cm^{-1}, which corresponds to the impurity impact ionization cross section $\sigma_I=4.6\times10^{-12}$ cm^2. Note that the values of σ_I and E_c in

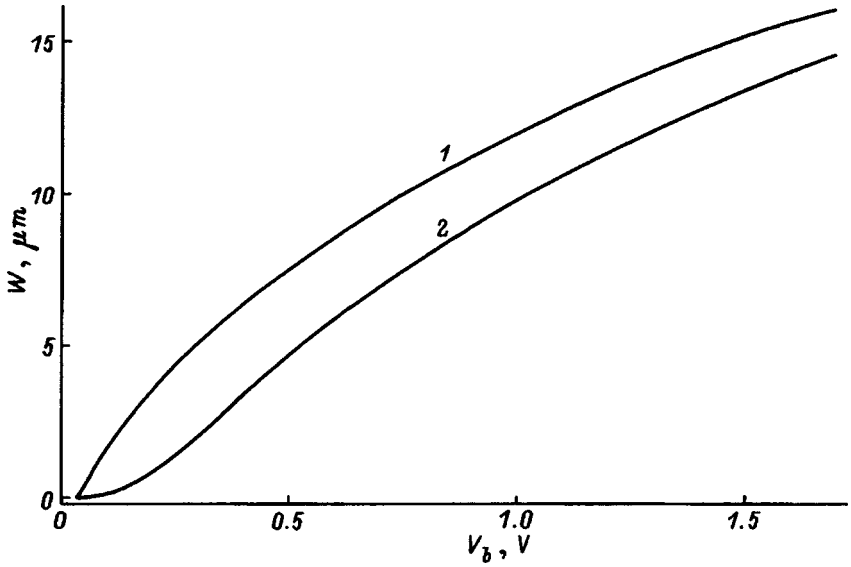

FIG. 5. Width of the space charge region W as a function of the bias voltage V_b at temperatures $T=8.5$ *1*) and 5.2 K (*2*). Radiation intensity $\Phi=2.8\times10^{13}$ photons/cm$^2\cdot$s.

our case are too high in comparison with the known values (cf., e.g., the data values given in Ref. 3: $E_c=7\times10^3$ V/cm and $\sigma_I=1.6\times10^{-13}$ cm^2). First, this can be due to the higher level of doping of the investigated BIB structures and correspondingly lower values of the carrier mobility. Second, for $V_b\simeq1.5$ V the width of the space charge region is comparable to the thickness of the active layer. This is illustrated by Fig. 5, which plots the calculated dependence $W(V_b)$ at two different temperatures. For $V_b=1.5$ V and $T=8.5$ K W reaches 15 μm. Under these conditions hole injection from the back contact can be substantial, amplifying the effects of impurity impact ionization, which in turn should lead to an increase in σ_I.

After finding the parameters Φ, l, E_c, and $\sigma_I N_a$ we analyzed the low-temperature curves $J(V_b)$ (Figs. 3a and 4). For their description it was, in fact, necessary to determine only one parameter $\sigma_i(0)$—the weak-field conductivity. An insignificant correction of E_c (increase) was also needed to describe the growing segment of the $J(V_b)$ curve. At $T=5$ K the value of E_c is 1.07×10^4 V/cm; the parameter $\sigma_I N_a$ was not varied. As can be seen from Fig. 3a, impurity impact ionization effects weaken as the temperature is lowered. This is explained by hopping-conductivity limitation of the photoresponse and a decrease under these conditions of the width of the space charge region (see Fig. 5, curve *2*).

The dependence of $\sigma_i(0)$ on the excitation intensity Φ (see the inset in Fig. 4) is of interest. The data plotted in Fig. 4 indicate that under conditions of illumination the hopping conductivity grows monotonically, saturating at $\Phi>10^{13}$ photons/cm$^2\cdot$s. It would be natural to link this behavior with the destruction of the spatial correlation of the ionized donors and acceptors (in the terminology of Ref. 14 ''1-complexes'') accompanying photoionization.[15] Indeed, according to Ref. 14, almost all the ionized acceptors (capture centers for holes) are frozen into ''1-complexes,'' i.e., they are found near (at the mean interimpurity distance from) positively charged donors. In this scenario the photoholes are trapped mainly at recombination centers bound into complexes. Correspondingly, the number of negatively charged, isolated acceptors grows (this follows from the condition of electrical neutrality),[15] thereby providing an additional increase in the hopping conductivity. On the other hand, ideas about the Frenkel'–Poole effect in the impurity band[7] also assume an increase in the hopping conductivity under equilibrium conditions due to a destruction of ''1-complexes'' due to a lowering of their binding energy in an electric field. It would seem that the higher the level of illumination, the worse the theory[7] should describe the current–voltage characteristics of BIB structures. In actual fact, however, the accuracy of fitting the calculated $J(V_b)$ curves to the experimental data is substantially better at higher levels of illumination (compare the curves in Figs. 4a and 4b). This suggests the existence of an additional mechanism for the appearance of spatial correlation of charges at impurities under nonequilibrium conditions. It is known, in particular, that under photoexcitation (A^+-A^-) complexes,[16] similar to ''1-complexes,'' can arise as a result of the establishment of spatial correlation between the holes captured into localized states of the Mott–Hubbard gap[17] and the negatively charged acceptors. Apparently, the strong variation of the hopping conductivity in an electric field, as well as its growth upon illumination, are also tied up with the formation of such complexes.

The results of this work thus demonstrate that BIB structures are suitable model objects for study of strong-field effects in the hopping conductivity of weakly compensated semiconductors with high doping level under conditions of impurity photoexcitation. In contrast to ordinary bulk samples, where conductivity in the $D^-(A^+)$ band (the upper Hubbard band) plays the dominating role under nonequilibrium conditions,[11] in BIB structures the above-noted peculiarities of the current–voltage characteristics are primarily configured by hopping transport via the impurity ground states, i.e., via the lower Hubbard band.

We are grateful to A. S. Vedeneev and N. K. Chumakov for valuable remarks.

This work was carried out with the support of the Rus-

sian Fund for Fundamental Research (Grant No. 96-02-18429-a) and the international association INTAS (Grant No. 93-1403).

Fax: (095) 1941994 (Ryl'kov); e-mail: rylkov@imp.kiae.ru

[1] M. D. Petroff and M. G. Stapelbroek, *Blocked Impurity Band Detectors* (United States Patent No. 4 568 960, February 4, 1986).
[2] N. Sclar, Quantum Electron. **9**, 149 (1984).
[3] F. Szmulowicz and F. L. Madarsz, J. Appl. Phys. **62**, 2533 (1987).
[4] Sh. M. Kogan, Zh. Eksp. Teor. Fiz. **81**, 2268 (1981) [Sov. Phys. JETP **54**, 1203 (1981)].
[5] S. Pasquier, G. Sirmain, C. Meny, A. Murray, M. Criffin, P. Ade, L. Essaleh, J. Galibert, and J. Leotin, in *Proceedings of the Eighth International Conference on Millimeter and Submillimeter Waves and Applications* (San Diego, 1994), p. 35.
[6] V. D. Shadrin, V. T. Coon, and I. K. Blokhin, Appl. Phys. Lett. **63**, 75 (1993).
[7] D. I. Aladashvili, Z. A. Adamiya, K. G. Lavdovskiĭ, E. I. Levin, and B. I. Shklovskiĭ, Fiz. Tekh. Poluprovodn. **23**, 213 (1989) [Sov. Phys. Semicond. **23**, 132 (1989)].
[8] A. G. Zhdan, A. M. Kozlov, S. N. Kostinskaya, V. F. Kocherov, and V. V. Ryl'kov, Fiz. Tekh. Poluprovodn. **26**, 2024 (1992) [Sov. Phys. Semicond. **26**, 1139 (1992)].
[9] A. G. Zhdan, A. M. Kozlov, S. N. Klëmin, and V. V. Ryl'kov, Prib. Tekh. Éksp., No. 2, 189 (1994).
[10] É. É. Godik, Yu. A. Kuritsyn, and V. P. Sinis, Fiz. Tekh. Poluprovodn. **12**, 351 (1978) [Sov. Phys. Semicond. **12**, 203 (1978)].
[11] L. A. Vorozhtsova, E. M. Gershenzon, Yu. A. Gurvich, F. M. Ismagilova, and A. P. Mel'nikov, Zh. Eksp. Teor. Fiz. **94**, 350 (1988) [*sic*].
[12] V. F. Bannaya, L. I. Veselova, and E. M. Gershenzon, Fiz. Tekh. Poluprovodn. **23**, 338 (1989) [Sov. Phys. Semicond. **23**, 208 (1989)].
[13] E. Burstein, G. S. Picus, B. W. Henvis, and M. Lax, Bull. Am. Phys. Soc. **30**, 13 (1955).
[14] B. I. Shklovskiĭ and A. L. Efros, *Electronic Properties of Doped Semiconductors* (Springer-Verlag, New York, 1984).
[15] V. N. Abakumov, V. I. Perel', and I. N. Yassievich, Fiz. Tekh. Poluprovodn. **12**, 3 (1978) [Sov. Phys. Semicond. **12**, 1 (1978)].
[16] E. M. Gershenzon, A. P. Mel'nikov, R. I. Rabinovich, and N. A. Serebryakova, Usp. Fiz. Nauk **132**, 353 (1980) [Sov. Phys. Semicond. **23**, 684 (1980)].
[17] N. F. Mott and E. A. Davis, *Electronic Processes in Non-Crystalline Materials* (Clarendon Press, Oxford, 1971). 1982).

Translated by Paul F. Schippnick

Ohmic contact formation during continuous heating of GaAs and GaP Shottky diodes

Yu. A. Goldberg and E. A. Posse

A. F. Ioffe Physicotechnical Institute, Russian Academy of Sciences, 194021 St. Petersburg, Russia
(Submitted July 28, 1997; accepted for publication July 31, 1997)
Fiz. Tekh. Poluprovodn. **32**, 200–202 (February 1998)

Changes in the current–voltage and capacitance–voltage characteristics of semiconductor–solid metal structures (GaAs–Ni and GaP–Au Schottky diodes) during continuous heating have been studied. It is shown that the rectifying contacts are transmuted into ohmic contacts at some temperature T_{ohm}. This transition precedes the possible formation of a recrystallized layer that is peculiar to conventional ohmic contacts. The transition temperature T_{ohm} is substantially lower than the melting point of the metal. The current–voltage characteristics of structures annealed at different temperatures T_{ann} and cooled to room temperature have been studied. It is shown that at some temperature T_{ann} lower than some critical temperature T_0 the structural properties remain virtually constant, that at $T_{ohm}>T_{ann}>T_0$ the structures remain rectifying but excess currents appear, and that at $T_{ann}>T_{ohm}$ the structures become irreversibly ohmic. It is assumed that after chemical interaction between the metal and the surface layer of the semiconductor, the newly formed surface acquires properties that account for the ohmic characteristics of the metal–semiconductor contact.
[S1063-7826(98)01602-0]

1. As is well known, a direct semiconductor–metal contact is a rectifying contact (Schottky diode) if a tunnel-impervious potential barrier exists between the metal and the semiconductor, and ohmic if a potential barrier is absent or it is transparent to tunneling (see, e.g., Refs. 1 and 2). The barrier can be formed as a result of a difference in the work functions of the semiconductor and metal (the Schottky model) or due to a large concentration of surface states in the band gap of the semiconductor (the Bardeen model). For most III–V semiconductors the Bardeen model applies.

In two of our papers[3,4] using semiconductor–liquid metal structures (GaP–Ga, GaP–In, and GaAs–Ga), we established that the rectifying contact transforms into an ohmic contact during continuous heating after the semiconductor surface layer dissolves in the metal. The temperature of the transition of a semiconductor–liquid metal contact from a rectifying to an ohmic contact depends substantially on the crystallographic orientation of the semiconductor surface and does not depend on the electron concentration in it.

In this paper we present results of a study of the transition of rectifying semiconductor–solid metal contacts (GaAs–Ni and GaP–Au Schottky diodes) into ohmic contacts at heating temperatures substantially lower than the melting point of the metal.

2. To create these structures we used n-type GaAs epitaxial layers (with carrier concentration $n=10^{15}$ cm^{-3}) grown on substrates of n-type GaAs ($n=10^{18}$ cm^{-3}), and n-type GaP wafers ($n=10^{17}$ cm^{-3}). All the crystals were oriented in the (100) plane. First, we prepared the ohmic contact by melting indium pellets into the GaAs substrate and GaP wafer. The opposite surface (epitaxial layer in the case of GaAs) was processed in the usual manner for preparing rectifying surface-barrier structures: mechanical polishing, chemical etching, washing. Next, a layer of nickel (on the GaAs substrate) or gold (on the GaP wafer) was chemically deposited onto the processed surface.[5,6] The initial structures were rectifying.

To study the changes in the properties of the Schottky diodes, some of the structures were continuously heated at a low heating rate (less than 5 deg/min) in a neutral medium (helium) from room temperature to 600 °C. The current–voltage ($I-U$) and capacitance–voltage ($C-U$) characteristics were measured during this heating process.

The rest of the structures were subjected to stepped heating, i.e., they were annealed at different temperatures and after each anneal were cooled to room temperature, after

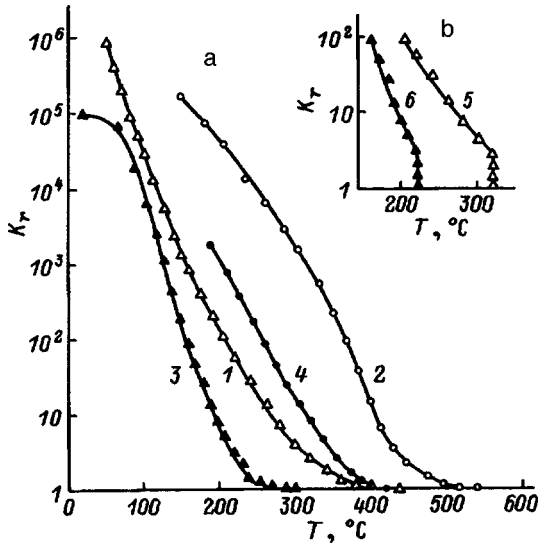

FIG. 1. Temperature dependence of the rectification coefficient K_r. a—GaAs–Ni (*1*) and GaP–Au (*2*) structures, measurements for continuous heating to the ohmic contact transition temperature T_{ohm}; for comparison, the analogous dependence is shown for the semiconductor–liquid metal structures GaAs–Ga (*3*) and GaP–In (*4*). b—GaAs–Ni (*5*) and GaAs–Ga (*6*) structures, measurements for holding at a temperature $T<T_{ohm}$.

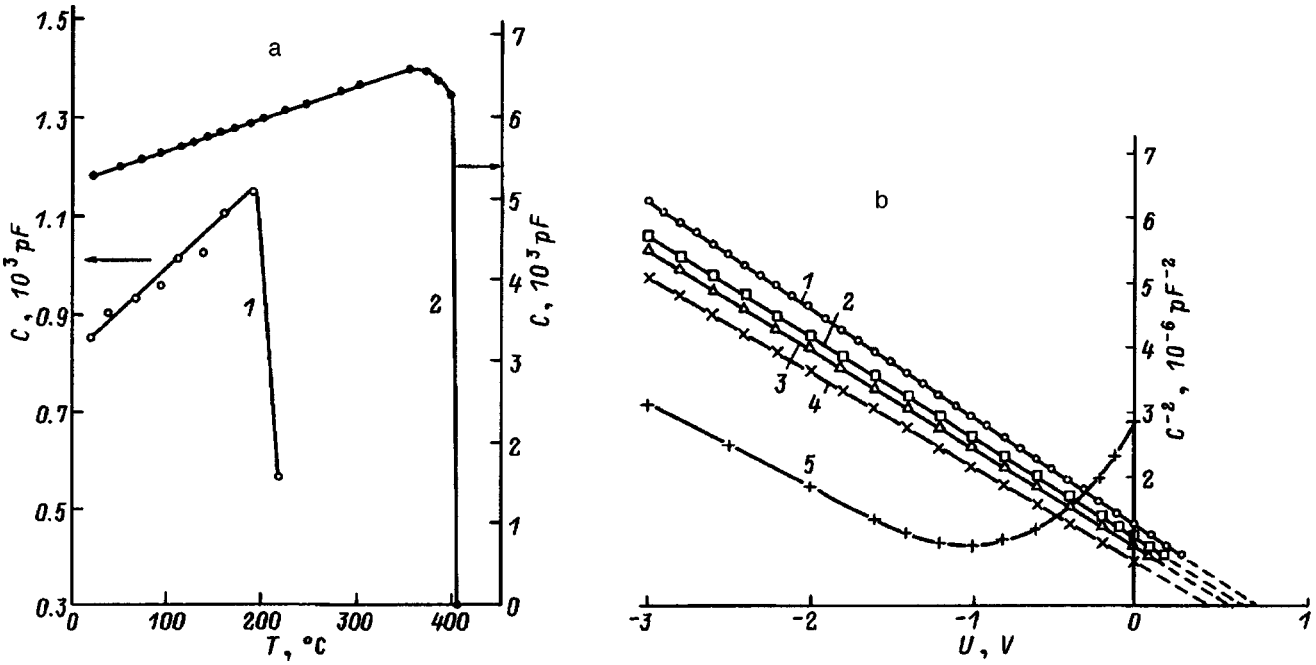

FIG. 2. a—Temperature dependence of the capacitance C, measured by the bridge method, of GaAs–Ni (*1*) and GaP–Au (*2*) structures for continuous heating. b—the $C^{-2}-U$ dependence for the structure GaAs–Ni at different temperatures T, °C: *1*—20, *2*—95, *3*—140, *4*—195, *5*—220.

which the $I-U$ and $C-U$ characteristics were measured.

As a parameter characterizing the asymmetry of the $I-U$ characteristics we chose the rectifying coefficient $K_r=I_d/I_r$ (the ratio of the direct and reverse currents) at $U=\pm 0.5$ *V*.

3. The results of the evolution of the $I-U$ and $C-U$ characteristics of the GaAs–Ni and GaP–Au Schottky diodes for continuous heating in the temperature interval 20–600 °C reduce to the following.

a) During continuous heating, Schottky diodes, like semiconductor–liquid metal contacts, transform from rectifying to ohmic at some temperature (Fig. 1a). This transition occurs before the possible formation of a highly doped or variband recrystallized semiconductor layer characteristics of a conventional ohmic contact.

b) The temperature of the transition of GaAs–Ni rectifying contacts to ohmic contacts (T_{ohm}) is ~400 °C, while for GaP–Au contacts it is ~500 °C, which is ~100 °C higher than the transition temperature for the corresponding semiconductor–liquid metal contacts. At such temperatures melting of the contact metal does not take place (the melting point is $T_m=1453$ °C for Ni and 1063 °C for Au) and therefore melting of the semiconductor in the liquid metal cannot take place. We believe that at these temperatures a chemical interaction between the semiconductor and the metal takes place. As a result, the thin semiconductor surface layer, which contains a large density of surface states responsible for the rectifying properties of the contact, disappears. Note that interaction of Au and GaP was observed in Ref. 7, where the eutectic point of the materials was 450 °C.

c) The capacitance of the GaAs–Ni and GaP–Au Schottky diodes, measured by the bridge method (Fig. 2a), at first grows as the temperature T is increased, due to a decrease in the height of the potential barrier (Fig. 2b), reaches a maximum, begins to decrease, and then abruptly falls. The rapid decrease in the capacitance is evidence of a rapid decrease in the differential resistance of the structure, i.e., the onset of the transition to an ohmic contact (in this case the capacitance, measured by the bridge method at frequencies in the range 0.1–1 MHz, differs significantly from its true value[8]).

4. In the case of stepped heating of GaAs–Ni Schottky diodes the results of the evolution of the $I-U$ characteristics measured at room temperature reduce to the following (Fig. 3).

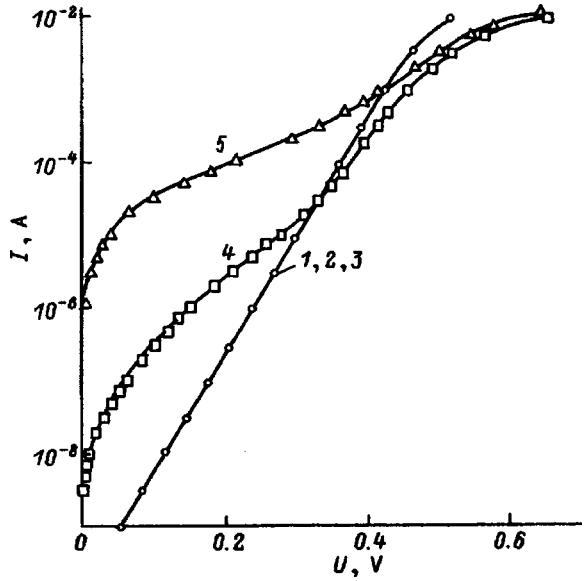

FIG. 3. The direct current I plotted as a function of the voltage U for the structure GaAs–Ni at $T=300$ K immediately after preparation (*1*) and after annealing at various temperatures T_{ann}, °C: *2*—210, *3*—280, *4*—285, *5*—290.

a) After annealing at temperatures T_{ann} less than some temperature $T_0 = 280$ °C, the $I-U$ characteristics remain essentially unchanged.

b) After annealing at a temperature $T_{ohm} > T_{ann} > T_0$ excess currents appear in the $I-U$ characteristics, although the structures remain rectifying. Note, however, that holding the structures at this annealing temperature for a long enough time leads to a transition to the ohmic state (Fig. 1b).

c) After annealing at a temperature $T_{ann} > T_{ohm}$ the contact remains ohmic after cooling (in this case the resistance of the ohmic contact was high).

5. Finally, a semiconductor–metal contact, initially a rectifying contact, is converted into an ohmic contact during heating already before the formation of a recrystallized layer. In this case, either a chemical interaction takes place between the metal and the surface region of the semiconductor (in the case of GaAs–Ni and GaP–Au Schottky diodes) or this region dissolves in the liquid metal as in the case of heating GaAs–Ga or GaP–Ga(In) contacts.[3,4]

It thus follows that the reformed surface of the semiconductor acquires properties different from those of the original surface. It may be assumed that on this surface, which is in contact with the metal, states which differ from the initial states and which pin the surface Fermi level either in the conduction band or near its bottom arise. Therefore, a potential barrier for electrons no longer can form, and the contact becomes ohmic.

We wish to thank R. V. Khasieva for assistance with this work. We also thank O. V. Konstantinov, O. I. Obolenskiĭ, and B. V. Tsarenkov for a discussion of the results.

[1] E. H. Rhoderick, IEEE Proc. **129**, Pt. 1, 1 (1982).
[2] A. Y. C. Yu, Solid-State Electron. **13**, 239 (1970).
[3] Yu. A. Gol'dberg, E. A. Posse, and B. V. Tsarenkov, Fiz. Tekh. Poluprovodn. **20**, 1510 (1986) [Sov. Phys. Semicond. **20**, 947 (1986)].
[4] Yu. A. Gol'dberg, M. V. Il'ina, E. A. Posse, and B. V. Tsarenkov, Fiz. Tekh. Poluprovodn. **22**, 555 (1988) [Sov. Phys. Semicond. **22**, 342 (1988)].
[5] Yu. A. Goldberg, E. A. Posse, and B. V. Tsarenkov, Electron. Lett. **7**, 601 (1971).
[6] Yu. A. Gol'dberg, E. A. Posse, B. V. Tsarenkov, and M. I. Shul'ga, Fiz. Tekh. Poluprovodn. **25**, 439 (1991) [Sov. Phys. Semicond. **25**, 266 (1991)].
[7] L. Bernstein, J. Electrochem. Soc. **109**, 270 (1962).
[8] Yu. A. Gol'dberg, O. V. Ivanova, T. V. L'vova, and B. V. Tsarenkov, Fiz. Tekh. Poluprovodn. **17**, 1068 (1983) [Sov. Phys. Semicond. **17**, 672 (1983)].

Translated by Paul F. Schippnick

Relaxation of the electric field in high-resistivity, strongly biased MISIM structures with deep impurity levels

B. I. Reznikov

A. F. Ioffe Physicotechnical Institute, Russian Academy of Sciences, 194021 St. Petersburg, Russia
(Submitted June 10, 1997; accepted for publication June 25, 1997)
Fiz. Tekh. Poluprovodn. **32**, 203–208 (February 1998)

The relaxation of the field and current in a high-resistivity metal-insulator-semiconductor (MISIM) structure containing a considerable concentration of deep impurity levels after the removal of strongly absorbed light is investigated numerically. It is established that the time dependence of the field distribution is determined by the relation between the times for the thermal generation of electrons (τ_n) and holes (τ_p) by an impurity. In the case of $\tau_n \gg \tau_p$ the temporal variation of the field in the bulk of the semiconductor is nonmonotonic. The drift of the photogenerated carriers after removal of light leads to the formation of a negative space charge layer of increased density and a significant increase in the field near the anode. Its maximum value can be as high as $5-6$ times the mean field $E_e = V/d$. Consideration of the additional injection of holes from the anode leads to an increase in the current, restriction of the maximum field at the anode, and appreciable acceleration of the relaxation of the field to the dark distribution. [S1063-7826(98)01901-2]

Processes which screen electric fields in metal-insulator-semiconductor structures underlie the operation of numerous optoelectronic devices[1] and are widely utilized to determine the parameters of deep centers.[2] The experiments in Refs. 3–6 and the simulations in Refs. 7 and 8, which were performed for diverse conditions, revealed different types of relaxational responses of the field and the current as functions of time. Kasherininov *et al.*[6] presented the photoelectric characteristics of high-resistivity MISIM structures based on CdTe ($\varrho = 10^7 - 10^9\ \Omega \cdot \mathrm{cm}$) with a considerable concentration of deep-level impurities ($N_t > 10^{15}\ \mathrm{cm}^{-3}$). The experiment describes:

— the stationary dark distributions of the electric field following application of a voltage;

— the temporal variation of the field and the current distribution after illumination of the biased structure is switched on;

— the temporal variation of the field after the illumination is switched off.

The main results of the experiment are as follows.

1. The electric field profile in an unilluminated structure (the dark field) decreases from the anode toward the cathode, has a minimum in the cathodic part of the structure, and increases slightly near the cathode.

2. When light is applied on the anode side (as in the case of structures with a small impurity content[5]), the field decreases at the anode and increases near the cathode. The field profile, which is nearly stationary, increases from the anode to the cathode with a positive curvature. If the light intensity and the voltage exceed certain critical values, the decrease in current after reaching a maximum gives way to an increase with gradual saturation. The effect intensifies as the voltage is increased.

3. The maximum field strengths near the electrode are significantly greater than the values measured for ''pure'' crystals.[5]

4. The temporal dependence of the field following removal of the light is nonmonotonic, in contrast to the case of crystals with a small impurity concentration.[5] Relaxation of the field occurs in two stages. In the first stage the field ''surges'' to an intermediate profile, which lies above the stationary values at the anode and below the stationary values at the cathode. The characteristic time of this process is of the order of 0.1 s. In the second stage, more prolonged stage (0.5 s), the field relaxes from the intermediate profile to the stationary dark distribution.

The increase in the field strength near the electrodes (see point 3) was associated in Ref. 6 with additional charges in the purity levels, and the nonmonotonicity of the time dependence of the current after the light is turned on (point 2) was attributed to an increase in the injection of carriers from the cathode at strong electric fields on the basis of a mechanism for lowering the barriers to injection.[9] Thus, the experiment raises several questions regarding the reasons for the nonmonotonic temporal variation of the field and the current, the characteristic fields of the relaxation processes, and the possible influence of additional carrier injection on the time dependence of the field and the current.

The purpose of the present work is to disclose the detailed physical mechanisms underlying the relaxation of the field and the current and to establish a systematic temporal picture of these processes using numerical simulation. The present work continues the investigation of the stationary photoeffect and the dark field distribution,[10–12] as well as the relaxation processes in pure, high-resistivity crystals[13] and in crystals with deep impurity levels.[14]

FORMULATION OF THE PROBLEM

Let us consider the one-dimensional distribution of the field and the carrier concentration in a high-resistivity, strongly biased metal-insulator-semiconductor structure occupying the region $0 \leqslant x \leqslant d$ with a bulk concentration of equilibrium holes p_*, to which a voltage V, which is much

greater than the contact potential between the semiconductor and the metal, is applied. It is assumed that a high-resistivity semiconductor contains not only shallow donors and acceptors, but also local impurity centers with a concentration N_t and an energy $\varepsilon_t = E_t - E_c$, which obey the Shockley-Read recombination model. The mathematical formulation of the problem nearly coincides with the one considered in Refs. 13 and 14. The electron (n) and hole (p) concentrations and the field profile $E(x)$ are found from the solution of the system of continuity equations, the Poisson equation, and an equation which describes the kinetics of the filling of the impurity levels. The carrier fluxes $q_{n,p}$ are written in the diffusion-drift approximation. The expressions for the rates of thermal generation and recombination of electrons and holes R_n and R_p take into account their trapping on a deep impurity level and emission into the corresponding band of the semiconductor.[15] The emission and surface recombination of carriers are taken into account on the semiconductor-metal interfaces at $x=0$ and $x=d$. The recombination fluxes $(q_s)_{n,p}$ are calculated on the basis of the model of a single surface level:

$$q_n(0) = -V_{n0}^T[n_0 - n_0^{\rm eq}\exp(-eV_i^0/kT)] - q_{sn}(0), \quad (1)$$

$$q_p(0) = -V_{p0}^T[p_0 - p_0^{\rm eq}\exp(eV_i^0/kT)] - q_{sp}(0), \quad (2)$$

$$q_n(d) = V_{nd}^T[n_d - n_d^{\rm eq}\exp(eV_i^d/kT)] + q_{sn}(d), \quad (3)$$

$$q_p(d) = V_{pd}^T[p_d - p_d^{\rm eq}\exp(-eV_i^d/kT)] + q_{sp}(d). \quad (4)$$

Here $n^{\rm eq}$ and $p^{\rm eq}$ are the equilibrium electron and hole concentrations at the interfaces, which depend on the height of the Schottky barrier φ_{B_n}; and $V_{n,p}^T = V_{n,p}T_{n,p}$ denotes the rates of carrier exchange through an interface, which are proportional to the rates of thermal emission into the metal $V_{n,p} = (1/4)v_{n,p}$ and to the tunneling transmission coefficients (tunneling probabilities) of the interfaces $T_{n,p}$. The latter take into account the decrease in the rates of carrier exchange through an interface due to the presence of the insulating layers and depend exponentially on a function containing the thickness of each insulating layer δ, the height of the barrier to tunneling, the potential drop across the layer, and other parameters. Due to a lack of reliable information on these quantities, the dependence of $T_{n,p}$ on the film characteristics is not specified in detail, and the tunneling transmission coefficient is assigned as an input parameter. The exponential terms appearing in (1)–(4) take into account the variation of the equilibrium carrier concentrations at the interfaces in response to the variation of the barrier height due to the potential drop at the insulator $V_i^{0,d} = E_i(0,d)\delta$, where E_i is the electric field in the insulator. Inclusion of this effect is the only difference from the model considered in Refs. 13 and 14. The details of the numerical method were described in Ref. 14. We only note that the choice of the spatial and temporal steps ensured the absence of a dependence of the total current density j on the coordinate to a high accuracy and the closeness of the numerical values of

$$j = (\varepsilon/4\pi)\partial E/\partial t + e(q_p - q_n),$$

which were calculated using difference formulas and obtained by integration over the width of the structure.

CALCULATION RESULTS

2.1. Let us study the dynamics of the establishment of the field and the current following the instantaneous removal of the light illuminating a high-resistivity CdTe structure of width $d = 0.22$ cm under a voltage $V = 400$ V. We take the same parameters for CdTe at $T = 300$ K as in Ref. 10. We set the equilibrium hole concentration in the bulk equal to $p_* = 6\times10^9$ cm^{-3}, the tunneling transmission coefficient of the interfaces equal to $T_{n,p} = 3\times10^{-3}$, and the height of the Schottky barrier equal to $\varphi_{B_n} = 0.98$ eV. In this case $p_{0,d}^{\rm eq} = 9\times10^9$ cm^{-3}, and the inequalities $p_{0,d}^{\rm eq} \gg n_{0,d}^{\rm eq}$ and $p_0 < p_*$ are satisfied. According to Ref. 12, the latter inequality ensures that the dark field decreases near the anode. The surface recombination rates are $s_n = s_p = 10^6$ cm/s. We assumed that $N_t = 10^{14}$ cm^{-3} and $\varepsilon_t = 0.78$ eV, and that the trapping cross sections at the deep level are equal to $\sigma_n = 10^{-13}$ cm^2 and $\sigma_p = 10^{-15}$ cm^2 for electrons and holes, respectively. The choice of the numerical values of φ_{B_n}, $T_{n,p}$, and N_t enables us to obtain a theoretical dark distribution of the electric field that is close to the experimentally measured profile with respect to the values of E_0 and $(dE/dx)_0$.[6] However, the variation of any of them over a fairly broad range is not critical for reproducing the ''field surge'' investigated in the present work (see point 4).

As the initial condition for the field, the electron and hole concentrations, and the occupancy of the impurity level, we use the steady-state distributions of $E(x)$, $n(x)$, and $p(x)$ obtained by integrating the original system of equations with application of a voltage and then with illumination at an intensity $I_i = 10^{16}$ cm$^{-2}\cdot$s^{-1}.

2.2. The values of the characteristic times that specify the qualitative picture of the process for the parameters assigned are as follows: the hole drift time of flight $t_{\rm dr}^p = d/\mu_p E_e = 2.4$ μs, where $E_e = V/d$; the Maxwell relaxation time $t_M = \varepsilon/4\pi e\mu_p p_* = 20$ μs; the electron and hole lifetimes at an impurity in the bulk of the structure $\tau_n = [\alpha_n(n_1 + n_*)]^{-1} = 4.4$ s and $\tau_p = [\alpha_p(p_1 + p_*)]^{-1} = 6.9$ ms, where $\alpha_{n,p} = \sigma_{n,p}v_{n,p}$; the impurity ionization time $\tau_t = (\tau_n^{-1} + \tau_p^{-1})^{-1} \approx \tau_p$; and the trapping time of holes on an impurity at equilibrium occupancy of the impurity $t_c = [\alpha_p N_t f_*]^{-1} = 6.5$ ms. The considerable difference is between the characteristic time scales calls for division of the relaxation process into several stages. The first stage includes a fast part, which takes place on the scale of the drift time $t_{\rm dr}^p$, during which the photogenerated carriers present in the structure at the time of removal of the illumination are separated by the field and accumulate at the electrodes of opposite sign. The slow part of the first stage is specified by the trapping and release of holes from the deep level. The separation of the free carriers is illustrated by Figs. 1 and 2, which show the evolution of the electron and hole profiles near the anode. After a small delay lasting about $0.2t_{\rm dr}^p$ to $0.5t_{\rm dr}^p$, which is associated with the presence of a large portion of the photogenerated holes in a region of weak negative fields, the maximum of the hole distribution begins to shift toward the cathode and decreases rapidly. After the time $2t_{\rm dr}^p$ has elapsed, the hole concentration in the semiconductor becomes much smaller than the equilibrium value in the bulk

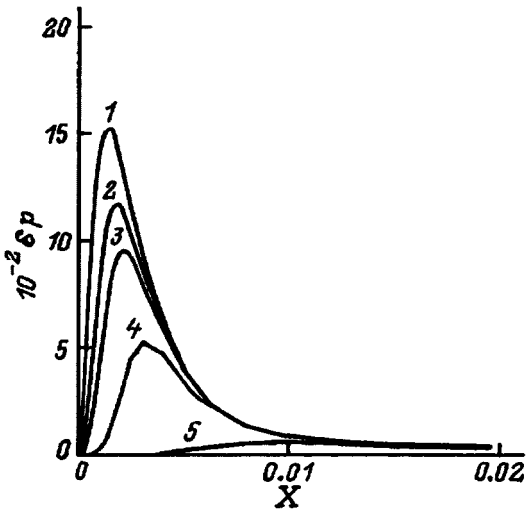

FIG. 1. Distributions of the hole concentration $\delta_p(X)=p/p_*-1$ near the anode ($X=x/d$) in the stage of carrier separation calculated at various times after the illumination is switched off $t/t_{\rm dr}^p$: *1* — 0, 2 — 0.1, *3* — 0.2, *4* — 0.5, *5* — 1.

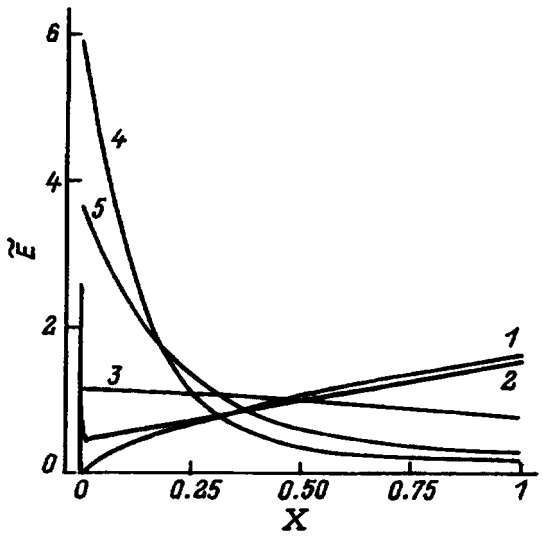

FIG. 3. Distribution of the electric field $\tilde{E}(X)=E(X)/E_e$ ($X=x/d$) in the structure at various times after the illumination is switched off $t/t_{\rm dr}^p$: *1* — 0, *2* — 2; $t\tau_t$: *3* — 1, *4* — 50, *5* — 150. Values of the field at the anode $\tilde{E}_0$: *1* — 0.96, *2* — 1.96.

p_*. The number of holes in the diffusion layer at the cathode also decreases appreciably. The photoelectrons, which are found in a layer of the order of the absorption length $\alpha^{-1}\approx 10^{-4}$ cm at the moment the illumination is switched off, are pressed against the anode by the field. The limiting concentration n_0 is established after a time $t\ll t_{\rm dr}^p$ and increases very gently at $t\leqslant 2t_{\rm dr}^p$. The escape of holes and the drift of photoelectrons causes the accumulation of negative space charge of increased density at the anode and in a layer with a thickness of order $\delta_+\approx 2kT/eE_e$. As a result, the field at the anode E_0 and the field on the outer boundary of this layer $E(\delta_+)$ at once begin to increase rapidly. These processes can be seen in Fig. 3, which presents the variation of the distribution of $\tilde{E}(x)=E(x)/E_e$ with time.

The subsequent evolution of the field profile is completely determined by the thermal generation of holes throughout the structure and by the variation of the charge of the impurity. The occupancy f of the deep level, which was much smaller than the equilibrium value in the bulk $f_*=p_1/(p_1+p_*)=6.6\times 10^{-4}$ after completion of the drift stage, begins to gradually increase (Fig. 4), at first approaching f_* and then surpassing it (at $t>0.7\tau_p$). As a result, the distribution of the field in the bulk of the structure at $t\approx\tau_p$ becomes nearly homogeneous. Then the derivative dE/dx in the bulk changes sign (Fig. 3), and $E(x)$ acquires the characteristic features of the dark profile, viz., a decrease near the anode and slow variation in the cathodic part of the structure. At $t>2\tau_p$ thermal generation results in an increase in the

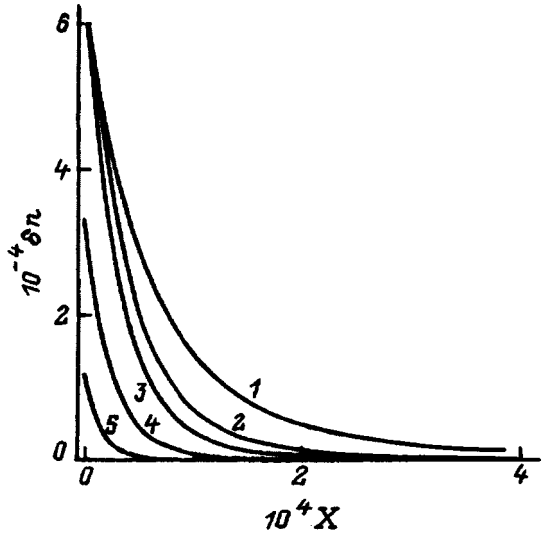

FIG. 2. Distributions of the electron concentration $\delta n(X)=n/n_*-1$ near the anode ($X=x/d$) calculated at various times after the illumination is switched off $t/t_{\rm dr}^p$: *1* — 0.1, *2* — 1, *3* — 2; $T=t/\tau_t$: *4* — 1, *5* — 5.

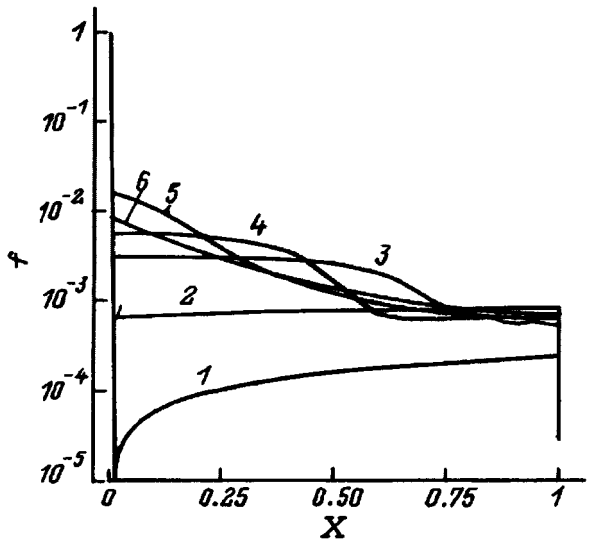

FIG. 4. Distribution of the occupancy of a deep impurity $f(X=x/d)$ at various times after the illumination is switched off t/τ_t: *1* — 0, *2* — 1, *3* — 5, *4* — 10, *5* — 50, *6* — 150.

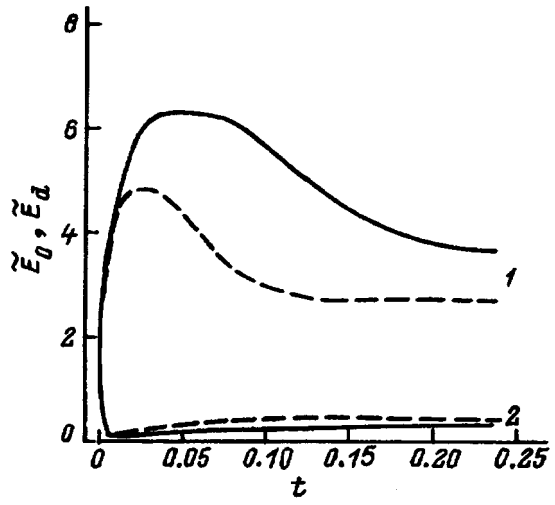

FIG. 5. Time dependence of the limiting values of the electric field: *1* — $\widetilde{E}_0$, *2* — $\widetilde{E}_d$. Dashed lines — calculation with consideration of the lowering of the barriers ($\delta=40$ Å). The time t is in units of τ_n.

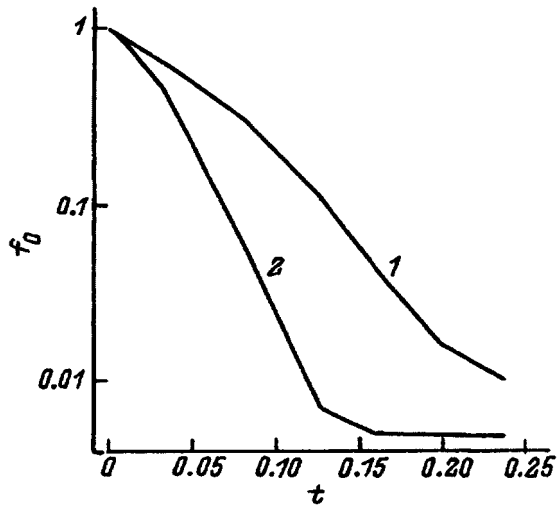

FIG. 7. Time dependence of the occupancy of the deep impurity at the anode f_0: *1* — without consideration of the lowering of the barriers, *2* — with consideration of the lowering of the barriers at $\delta=40$ Å. The time t is in units of τ_n.

hole concentration in the bulk of the structure. A region with a hole concentration close to p_*, which expands toward the anode, forms near the cathode. Two regions having the values $f=f_{0-}\approx p_1/(p_0+p_1)$ and $f=f_c\approx f_*$, which are separated by a transition layer, where f decreases from f_0 to f_c form in the structure (curves *3* and *4* in Fig. 4). Then, when electrons begin to be released, the transition layer is obliterated, and $f(x)$ decreases monotonically from the anode to the cathode (curve *5*). In the final stage of the relaxation process ($t\gg\tau_p$) the impurity is freed of electrons, so that the negative space charge of the impurity in the anodic part of the structure diminishes in absolute value, and the distribution of $\widetilde{E}(x)$ monotonically approaches the dark profile from above.

The diversity of scales for the different stages of the evolution of $\widetilde{E}(x)$ is clearly seen in Figs. 5 and 6, which presents the time dependences of $\widetilde{E}_0=E_0/E_e$ and $\widetilde{E}_d=E_d/E_e$ and of the current density j. It follows from Fig. 5 that the stage of the decrease in $\widetilde{E}_0$ is the longest and is comparable to the largest time scale τ_n. A comparison of Figs. 5 and 7, which show the time dependence of the occupancy of the deep impurity near the anode f_0, shows that an appreciable decrease in the field at the anode occurs when f_0 decreases by two orders of magnitude. Thus, the sluggishness of the release of the photoelectrons from the impurity is responsible for the nonmonotonic variation of the field distribution with time and determines the time scale of the field relaxation process.

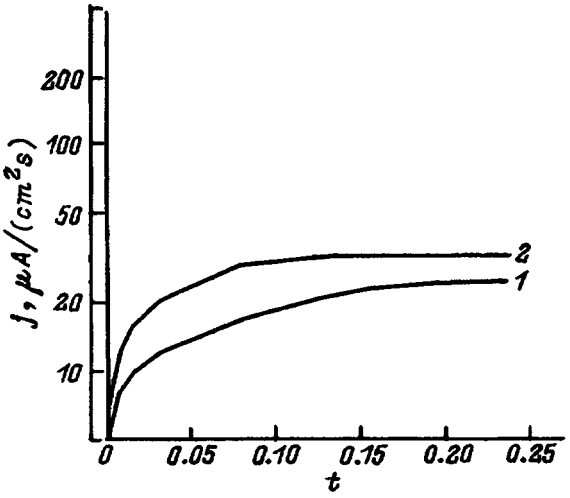

FIG. 6. Time dependence of the current density j: *1* — without consideration of the lowering of the barriers, *2* — with consideration of the lowering of the barriers at $\delta=40$ Å. The time t is in units of τ_n.

It is also seen from Fig. 5 that the value of E_0 in the ''field surge'' stage greatly exceeds the mean field E_e. When the mean field is sufficiently strong, some fundamentally new effects are introduced into the discussion. In particular, as was shown in Refs. 9 and 16, the alteration of tunneling conditions by the space and surface charge fields near an insulator-semiconductor interface is equivalent to alteration of the height of the Schottky barriers for electrons and holes, an increase in the tunneling transmission coefficient of the insulator layer, and additional carrier injection at the interface. It follows from the calculations performed that the nonmonotonic dependence of the field distribution can be simulated without postulating additional injection. Consideration of this effect gives the additional flow of holes from the anode $\Delta q_p=V_{p0}^T p_0^{\rm eq}\exp(eV_i^0/kT)$ [see Eq. (2)], which accelerates the release of electrons from the impurity level (Fig. 7, curve *2*) and, as can be seen from Figs. 5 and 6 (see the dashed lines and curve *2*), increases the current appreciably, restricts the increase in the field at the anode, and markedly shortens the relaxation time of the field and the current.

2.3. To conclusively test the conclusion that the nonmonotonicity of the variation of the field is associated with the longer time for freeing the traps of electrons than for freeing them of holes, we calculated the relaxation of the field in a structure with the opposite relationship between the lifetimes $\tau_p\gg\tau_n$ (the remaining parameters were retained). The dark field profile was found (as in the preceding case) as

a result of calculations, beginning from the equilibrium state after the supply of a voltage, and the stationary profiles observed after completion of the relaxation under illumination with an intensity $I_i = 10^{16}$ cm$^{-3}\cdot$s^{-1} were taken as the initial distributions of $E(x)$, $n(x)$, $p(x)$, and $f(x)$. Neither the dark nor the initial profile at the moment the light was switched off exhibited any differences from the preceding case. A calculation of the relaxation of the field after removal of the illumination showed that the profile of the field in the bulk relaxes monotonically from the initial to the dark profile when $\tau_p \gg \tau_n$. The remaining qualitative features of the behavior of the distributions of the physical quantities shown in Figs. 1–4 are repeated. This occurs because the main process influencing the space charge in the bulk is the thermal generation of holes. Nevertheless, the reversed relationship between the characteristic times and some particular features of the initial field distribution produce several special features in the relaxation process, particularly near the anode. The earlier release of electrons from the impurity level causes the time dependences of the field at the anode E_0, the occupancy of the deep level at the anode f_0, and the current density j to have a complex nonmonotonic character. In particular, the thermal generation of electrons from the impurity leads to a decrease in the occupancy of the deep level and of the field at the anode, as well as to the appearance of an additional minimum on the plots of $f_0(t)$ and $E_0(t)$, after which these quantities increase to the dark values. The negative space charge layer of increased density at the anode exists up to $t \lesssim \tau_p$ and then disappears. Because of the nonmonotonic variation of the field and the hole concentration at the anode p_0, the current maintains a stationary value after passing through a minimum and a maximum.

The present calculation revealed one more curious feature of the relaxation of the field, which is associated with the presence of a region of weak negative fields in the initial field distribution.[17,18,12] The presence of an inversion region for the field, which coincides with the hole-generation zone, causes confinement of the holes in this region after the light is switched off until the field in the vicinity of the anode changes sign. In the first case with $\tau_p \ll \tau_n$ the minimum on the initial field profile was at $\tilde{E}_{\min} \approx -0.02$ (this segment is not noticeable in Figs. 3 and 5), and the delay of the spreading of the pulse of photogenerated holes amounted to a fraction of $t_{\rm dr}^p$. In the second case with $\tau_p \gg \tau_n$ the minimum is at $\tilde{E}_{\min} \approx -0.1$, and because of the larger negative value of the field at the minimum, the current and the field in the bulk remained unchanged for almost 20 μs. On this basis it can be assumed that the increase in the depth of the potential well for holes as the illumination intensity is increased leads to an increase in the delay of the holes in the inversion region and greater asymmetry of the field relaxation processes when the light is switched on and when it is switched off.

Let us give an estimate of the characteristic time of the relaxation process τ. As we know, the lifetimes τ_n and τ_p, derived from the statistics of Shockley-Read recombination, characterize the real time scales of the process only at a low excitation level. In the present problem they can serve as time scales only when the characteristic concentrations in the bulk are correctly chosen because of the strong variation of the carrier concentrations in the bulk and the boundary layers. The characteristic value of the hole concentration is the value of p_0, for which the following estimate[12] is valid without the consideration of surface recombination:

$$p_0 = p_0^{\rm eq} \frac{V_p^T}{V_p^T + v_{\rm dr}^p}, \quad v_{\rm dr}^p = \mu_p E_0 . \tag{5}$$

As follows from Eq. (5), the value of p_0 can be calculated if the field at the anode E_0 is known. When $V_p = 6\times 10^6$ cm/s, $T_p = 3\times 10^{-3}$, and $\tilde{E}_0 = 5$, we obtain $p_0/p_* = 0.04$, and for $\sigma_p = 10^{-17}$ cm^2 the value of the lifetime of a hole on an impurity is $\tau = [\alpha_p(p_1 + p_0)]^{-1} \approx 15$ s, which is fairly close to the value obtained from a numerical solution.

Thus, the form of the relaxational dependence of the electric field profile is fundamentally related to the relationship between the characteristic times τ_n and τ_p, and when $\tau_n \ll \tau_p$, the variation of the field is monotonic with time, as in crystals with a small concentration of impurity levels.

We thank P. G. Kasherininov for discussing the problem.

[1] M. P. Petrov, S. I. Stepanov, and A. V. Khomenko, *Photosensitive Electro-optic Media in Holography and Optical Information Processing* [in Russian], Nauka, Leningrad (1983).
[2] L. S. Berman and A. A. Lebedev, *Capacitance Spectroscopy of Deep Centers in Semiconductors* [in Russian], Nauka, Leningrad (1981).
[3] I. T. Ovchinnikov and É. V. Yanshin, Pis'ma Zh. Tekh. Fiz. **8**, 355 (1982) [Sov. Tech. Phys. Lett. **8**, 153 (1982)].
[4] V. N. Astratov and A. V. Il'inskiĭ, Preprint No. 1091, A. F. Ioffe Physicotechnical Institute, Leningrad (1986).
[5] P. G. Kasherininov, A. V. Kichaev, and A. A. Tomasov, Fiz. Teckh. Poluprovodn. **29**, 2092 (1995) [Semiconductors **29**, 1092 (1995)].
[6] P. G. Kasherininov, A. V. Kichaev, and I. D. Yaroshetskiĭ, Zh. Tekh. Fiz. **65** (9), 193 (1995) [Tech. Phys. **40**, 970 (1995)].
[7] V. N. Klimova, Mikroélektronika **10**, 457 (1981).
[8] A. E. Iverson and D. L. Smith, IEEE Trans. Electron Devices **ED-34**, 2098 (1987).
[9] M. A. Green and J. Shewchun, Solid-State Electron. **17**, 349 (1974).
[10] P. G. Kasherininov, B. I. Reznikov, and G. V. Tsarenkov, Fiz. Tekh. Poluprovodn. **26**, 1480 (1992) [Sov. Phys. Semicond. **26**, 832 (1992)].
[11] B. I. Reznikov and G. V. Tsarenkov, Fiz. Tekh. Poluprovodn. **31**, 23 (1997) [Semiconductors **31**, 19 (1997)].
[12] B. I. Reznikov and G. V. Tsarenkov, Fiz. Tekh. Poluprovodn. **29**, 2199 (1995) [Semiconductors **29**, 1147 (1995)].
[13] B. I. Reznikov, Fiz. Tekh. Poluprovodn. **31**, 1003 (1997) [Semiconductors **31**, 857 (1997)].
[14] B. I. Reznikov, Fiz. Tverd. Tela (St. Petersberg) **39**, 1775 (1997) [Phys. Solid State **39**, 1582 (1997)].
[15] V. L. Bonch-Bruevich and S. G. Kalashnikov, *The Physics of Semiconductors* [in Russian], Nauka, Moscow (1977), p. 306.
[16] A. V. Sachenko and O. V. Snitko, *Photoeffects in the Near-Surface Layers of Semiconductors* [in Russian], Naukova Dumka, Kiev (1984).
[17] A. S. Furman, Fiz. Tverd. Tela (Leningrad) **28**, 2083 (1986) [Sov. Phys. Solid State **28**, 1164 (1986)].
[18] B. I. Reznikov and G. V. Tsarenkov, Fiz. Tekh. Poluprovodn. **27**, 1262 (1993) [Semiconductors **27**, 699 (1993)].

Translated by P. Shelnitz

Photoelectrical memory in GaAs/AlGaAs multilayer quantum-well structures

V. N. Ovsyuk*

Technological Institute of Applied Microelectronics, Siberian Branch of the Russian Academy of Sciences, 630090 Novosibirsk, Russia

M. A. Dem'yanenko, V. V. Shashkin, and A. I. Toropov

Institute of Semiconductor Physics, Siberian Branch of the Russian Academy of Sciences, 630090 Novosibirsk, Russia

(Submitted April 1, 1997; accepted for publication May 31, 1997)
Fiz. Tekh. Poluprovodn. **32**, 209–214 (February 1998)

An increase in the dark current (by 2–3 orders of magnitude) in GaAs/$Al_xGa_{1-x}As$ multilayer quantum-well structures with $x \simeq 0.4$ is observed after illumination of the structures with optical light ($\lambda < 1.3$ μm). This increase is sustained for an extended time (more than 10^3 s) at low temperatures. It then decreases to its initial value upon heating of the sample. A model of the barrier with local sag of the conduction band facilitating tunneling is proposed. The conduction band sag and the magnitude of the current grow due to optical ionization of uncontrolled deep level clusters present in the barrier and decrease due to subsequent capture of electrons from the conduction band by the deep levels upon heating. [S1063-7826(98)01802-X]

INTRODUCTION

GaAs/AlGaAs-based, multilayer, quantum-well structures have recently been studied extensively, first of all in connection with their potential use in multielement infrared photodetectors. As a rule, good agreement is observed between the experimental and theoretical values of the dark current and photocurrent for such structures assuming rectangular AlGaAs potential barriers.[1–3] At the same time, a number of studies have noted an asymmetry in the dark current and photocurrent, depending on the polarity of the applied bias voltage,[1,4–6] and also an excess tunneling current,[7] which points to a deviation from an ideal rectangular barrier. The reason for this behavior may be the well-known difference of the two boundaries between the well and the barriers,[8] the asymmetric impurity distribution in the wells,[9] and the presence of defects in the barriers.[7]

In the present work we have detected a growth of the dark current by 2–3 orders of magnitude after exposure to light in the wavelength range $\lambda < 1.3$ μm of the GaAs/$Al_xGa_{1-x}As$ multilayer quantum-well structures with $x \simeq 0.4$, grown by molecular-beam epitaxy, which persists for an extended time at reduced temperatures and which fall back to its original value after heating. This effect is explained in the framework of the model of a barrier with local conduction band sag that facilitates electron tunneling. The degree of sag and the magnitude of the current grow upon photoionization of the local clusters of uncontrolled deep levels present in the barrier and decrease as conduction band electrons are captured at these levels upon heating.

1. EXPERIMENT

As samples we used GaAs/$Al_xGa_{1-x}As$ multilayer quantum-well structures with Al content x in the range 0.26–0.43, grown by molecular-beam epitaxy on the setups ''Katun'-S'' and ''RIBER 32 P.'' The samples GaAs/AlGaAs were grown at substrate temperature in the range $T_s = 580–600$ °C, with a growth rate of ~ 1 μm/h and with a flux ratio ensuring the existence of surface structures: (2×4) As on GaAs, and (3×2) on AlGaAs. In addition, growth was interrupted at the stage of completion of growth of the GaAs well to smooth the surface. The width of the well L_w varied from 43 to 48 Å, and the barrier thickness L_b—from 300 to 500 Å. The number of periods N was 25 or 50. The quantum dots were silicon-doped both uniformly and in the δ pattern about their centers with sheet concentration $\Gamma_{Si} \simeq 10^{12}$ cm^{-2}. The n^+-GaAs layers of thickness ~ 0.5 μm with silicon doping concentration 2×10^{18} cm^{-3} served as the upper and the lower contact layers of the structure. Mesa-structures, square in shape with side length 300 μm were prepared by etching the multilayer quantum-well structures down to the lower n^+-layer. Ohmic contacts were attached to the n^+-layers by brazing in the sputtered-on layers of Ni–Au–Ge. The Al content x and the layer thicknesses L_w and L_b were determined by x-ray diffraction and *in situ* from intensity oscillations of the fast-electron-diffraction reflection pattern. The Hall mobility of the electrons in the plane of the quantum wells, measured in the multilayer quantum-well structures grown without n^+ contact layers, was ~ 2000 cm^2/(V·s) at 77 K.

Measurements of the dark current temperature dependence were made at a bias voltage $V_b = 0.2$ V in the temperature range $T = 77–300$ K. The rate of heating or cooling was 0.5 deg/s with the possibility of stopping the heating or cooling process at a preset temperature. Illumination of the samples was provided by a GaAs light-emitting diode (maximum emission at $\lambda \simeq 1$ μm) from the side of the substrate

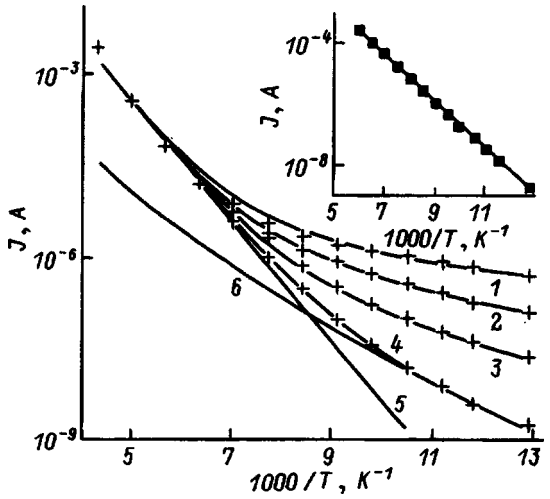

FIG. 1. Experimental (points) and theoretical (solid curves) temperature dependence of the dark current in the multilayer quantum-well structure $GaAs/Al_xGa_{1-x}As$ with $x=0.385$: *1*—after illumination; *2*,*3*,*4*—after warming to 110, 130, and above 170 K, respectively. The theoretical curves *5* and *6* correspond to the current components in the regions without and with conduction band sag. The inset plots the temperature dependence of the dark current in the multilayer quantum-well structure $GaAs/Al_xGa_{1-x}As$ with $x=0.29$. For all curves $V_b=0.2$ V.

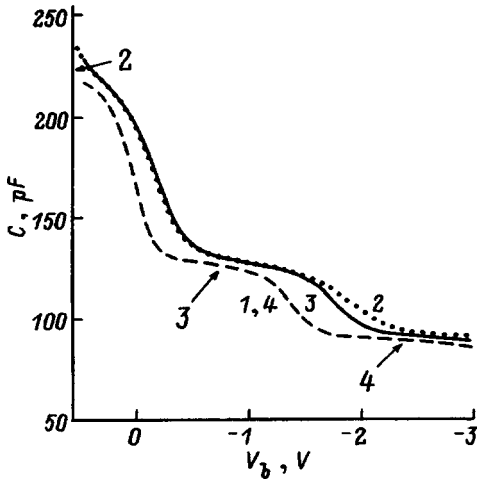

FIG. 2. Capacitance–voltage characteristics of the Schottky barrier in the multilayer quantum-well structure $GaAs/Al_xGa_{1-x}As$ with $x=0.385$, measured at 3 kHz at $T=77$ K, successively: *1*—before illumination, *2*—after illumination, *3*—after heating the previously illuminated sample to 170 K at $V_b=-1.5$ V; *4* (coincides with *1*)—after heating to 170 K at $V_b=0.35$ V.

with an intensity of $\simeq 10^{17}$ photons/cm$^2\cdot$s for 10–20 s. Measurements of the spectral dependence showed that the photoelectric memory effect discussed in this paper is observed at wavelengths $\lambda<1.3$ μm.

For samples with $x<0.3$ the dark current J corresponds to the rectangular barrier model:[1] its temperature dependence corresponds to an activation energy equal to the barrier height reckoned from the Fermi level, and the dark current does not vary after illumination in the indicated regime. To illustrate this point, the inset in Fig. 1 plots the temperature dependence for one of our samples with $x=0.29$, $L_w=43$ Å, $L_b=500$ Å, $\Gamma_{Si}=8.6\times10^{11}$ cm^{-2}, and $N=50$.

As x is increased above 0.3, the temperature dependence of the dark current and its reaction to illumination are radically altered. Figure 1 plots experimental data obtained for a multilayer quantum-well structure with $x=0.385$, $L_w=43$ Å, $L_b=400$ Å, $\Gamma_{Si}=10^{12}$ cm^{-2} (δ-doped about the center of the well), and $N=25$. Curve *4*, which is the reference curve, corresponds to the sample cooled in darkness from room temperature. In contrast to the sample with $x=0.29$, the dark-current activation energy is not constant, but decreases from roughly 0.2 eV at temperatures $T>170$ K to roughly 0.08 eV at temperatures $T<100$ K.

When the sample is illuminated at temperatures below 170 K, the current flowing through the samples increases and then remains essentially constant after the illumination is switched off. Thus, at 80 K the current grows almost threefold when the sample is illuminated and relaxes after the illumination is switched off, by roughly 10% after 1000 s. The corresponding curve *1* in Fig. 1 was obtained by measuring the current immediately after switching off the illumination at each temperature. Essentially the same dependence was obtained when the sample was heated in darkness after being illuminated at 77 K. The dark-current activation energy corresponding to dependence *1* in Fig. 1 is ~0.024 eV near 77 K, which is roughly three times less than for the reference dependence *4*, and grows as the temperature is raised. When the sample is heated above 170 K, the current follows the reference curve *4*. Subsequent cooling in darkness again gives the reference curve *4*.

If after illumination at 77 K the sample is heated to some intermediate temperature $T_0<170$ K (e.g., to 110 or 130 K) and then, after cooling it down to 77 K, the temperature dependence of the current is measured as the sample is heated again (at a rate of ~0.5 deg/s), we obtain dependences lying between curves *1* and *4* (correspondingly, curves *2* and *3* in Fig. 1). In this case, for temperatures $T<T_0$ the dependences $J(T)$ remain essentially unchanged over the course of several minutes and are independent of the direction of temperature change of the sample.

Measurements of the current in square-shaped samples with side length between 75 and 1200 μm showed that within some scatter the mean current density does not depend on the area of the sample. This allows us to assert that the noted peculiarities are inherent to the bulk of the sample, and not to its surface about the perimeter of the *a*-structure.

In order to obtain additional information about the influence of illumination on multilayer quantum-well structures, we measured the capacitance–voltage characteristics of the Schottky barriers in these samples. Accordingly, on part of the as-grown wafer, after stripping away the upper n^+-GaAs layer electrolytically a gold/titanium Schottky barrier of circular shape with an area of 1.26×10^{-3}cm^2 was sputtered on without etching out the mesa-structures. An ohmic contact to all the quantum wells and the lower n^+-layer was prepared by melting in a layer of indium about the perimeter of a sample with dimensions $\sim5\times5$ mm^2 cut from the wafer.

Figure 2 shows typical capacitance–voltage characteristics for a multilayer quantum-well structure with $x=0.385$, measured in darkness before illumination (the sample was cooled from room temperature in darkness with the bias volt-

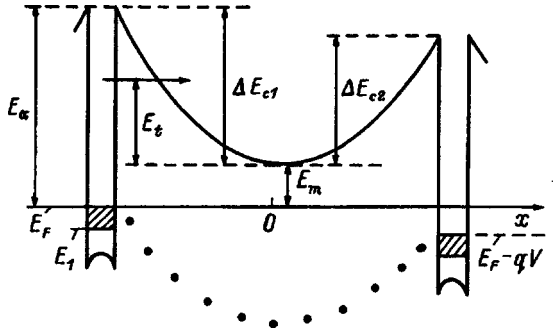

FIG. 3. Energy-level diagram of one period of a multilayer quantum-well structure for positively charged centers present in the barrier layer. E_1—first quantum level, E_F—Fermi level of the left quantum well. Points—deep levels, shallow donors, not shown. The remaining notation is explained in the text.

age on the Schottky barrier $V_b = 0.35$ V) and after (curves *1* and *2*), and also after heating to 170 K at two different bias voltages (curves *3* and *4*). During the recording of the capacitance–voltage characteristics no relaxation of the capacitance was noted. Segments with flat slope (plateaus), arising on the capacitance–voltage curves relative to the Schottky barrier voltage V_b, correspond to depletion of the next quantum well. The ordinal numbers of the quantum wells, counted from the surface of the sample, are indicated by the numbers with arrows along the corresponding plateaus of curve *1* in Fig. 2. The segments with steeper slope correspond to transitions from one completely depleted quantum well to the next.[10,11]

2. MODEL OF PHOTOELECTRIC MEMORY

The observed effect (Fig. 1) is reminiscent of the well-known phenomenon of persistent photoconductivity in doped $Al_xGa_{1-x}As$ with $x > 0.22$ (Ref. 12), which is associated with the existence of *DX* centers in this material, arising when it is doped with silicon and also some other impurities.

We assume, therefore, that in the multilayer quantum-well structures that we have investigated there are local regions that run through the entire structure, and within the limits of these regions the barrier layers contain uncontrolled donor levels—in general, both shallow, with concentration N_d, and deep, with concentration N_t. In addition, we will let the latter, similarly to the *DX* centers, be characterized by a relatively high capture barrier for free electrons from the Γ valley of the conduction band.

Under equilibrium conditions (before illumination) at least the shallow levels are ionized. This leads to the formation of an internal electric field and to ''sagging'' of the conduction band (Fig. 3). As a result, thermally assisted electron tunneling from the quantum wells into the conduction band of the barrier layers through the relatively narrow potential barriers leads to an increased dark current and a lower value of its effective activation energy (see curve *4* in Fig. 1). Ionization of deep levels upon illumination of the sample increases the sag of the conduction band, which leads to a further increase of the dark current. The presence of a high capture barrier for electrons to the deep levels ensures storage of the new state after the illumination is switched off at low temperatures. Upon subsequent heating to some temperature T_0 the electrons overcome the energy barrier and return to the deep levels, neutralizing their positive charge. The sag of the conduction band decreases and the dependence $J(T)$ approaches its original values.

Let us discuss in more detail the assumptions we have made about locality of the regions which contain the uncontrolled deep levels and about the mechanism of neutralization of the ionized deep levels via capture of free electrons from the conduction band.

2.1. Locality of regions of conduction band sag

As will become clear from the calculation in Sec. 3, the required change in the concentration of positive charge ΔN^+ in the barrier layer of the multilayer quantum-well structure after illumination should be equal to 1.2×10^{17} cm^{-3} if they are uniformly distributed over the thickness of the barrier layer. Thus, as follows from the condition of charge balance of the sample, the equilibrium free electron concentration in the quantum wells Γ_n for uniform distribution of the deep levels in the barriers over the area of the structure should increase by the amount $\Delta N^+ L_b = 4.8\times10^{11}$ cm^{-2}, which is roughly half the initial doping concentration of the quantum wells, $\Gamma_{Si} \simeq 10^{12}$ cm^{-2}. Consequently, illumination of the sample should lead to an increase by $\sim 50\%$ of the width of the plateaus on the capacitance–voltage curves shown in Fig. 2. This, however, does not happen. The actual illumination-induced increase in the equilibrium electron concentration in the quantum wells Γ_n did not exceed 10^{11} cm^{-2} (i.e., 10%), as was determined by integrating the capacitance–voltage curves between the inflection points of neighboring transitional segments. This fact allows us to assert that the deep levels responsible for the indicated change in the positive charge concentration ΔN^+ in the barrier layers upon illumination are concentrated in local regions occupying a small fraction (not more than 20%) of the entire area of the structure.

2.2. Interaction of deep levels with allowed bands

The transitional segment of the capacitance–voltage curves between the jth and $(j+1)$-th plateaus corresponds to the exponential tail of the capacitance of the depleted jth quantum well.[10,11] Its width for an ideal multilayer quantum-well structure can be estimated as $\Delta V_{j,j+1} \simeq 4(kT/q)C_p/C_{j+1}$, where k is the Boltzmann constant, q is the absolute value of the electron charge, C_p is the capacitance of one period of the multilayer quantum-well structure, and C_j is the capacitance in the center of the jth plateau on the capacitance–voltage curve. For the sample shown in Fig. 2, the quantity $\Delta V_{3,4}$ should be ~ 80 mV, but its experimental value is equal to ~ 500 mV. We associate this increase of $\Delta V_{j,j+1}$ with nonuniformity over the area of the structure of the electron concentration Γ_n in the jth quantum well, and this nonuniformity grows somewhat after illumination of the nonuniformly distributed deep levels.

Next, curve *3* in Fig. 2 was obtained after heating the pre-illuminated sample to 170 K for the bias voltage $V_b = -1.5$ V. At this bias voltage the second and third quantum wells (and the adjacent barriers) are elevated relative to

their equilibrium positions by ~600 and ~30 mV, respectively. It can be seen that after the indicated heating the slope of the transitional segment (*3,4*) grows while its width $\Delta V_{3,4}$ decreases and essentially coincides with its value for the initial curve *1*. At the same time, the indicated heating has no effect on $\Delta V_{2,3}$ (Fig. 2, curve *3*).

In the corresponding case for the bias voltage $V_b = 0.35$ V, when the positions of all the quantum wells are near their equilibrium values, the measured capacitance–voltage curve (Fig. 2, curve *4*) essentially coincides with its initial dependence. Thus we may conclude that neutralization of photoionized deep levels takes place near the quantum wells not elevated above the Fermi level and does not take place near quantum wells elevated far above it. This supports the assumption that the neutralization of photoionized deep levels is due to capture of conduction band electrons and not to dumping of holes to the valence band. In the latter case the wells elevated ~600 mV above the Fermi level would not influence the recharging of the deep levels upon heating.

3. CALCULATION OF THE TEMPERATURE DEPENDENCE OF THE CURRENT IN MULTILAYER QUANTUM-WELL STRUCTURES

The current density in the regions of a multilayer quantum-well structure without conduction band sag at low bias voltages is determined primarily by electrons thermally emitted above the conduction band edge of the barrier and is given by the standard expression[1,13]

$$j_0 = q\mu_n F(N_{2D}/L_p)kT \exp(-E_{a0}/kT). \quad (1)$$

Here μ_n is the electron mobility in AlGaAs, F is the electric field intensity, $N_{2D} = m_w^* \pi/\hbar^2$ is the two-dimensional density of states, m_w^* is the effective mass of the electron in the quantum well, $\hbar$ is Planck's constant, L_p is the period of the structure, $E_{a0} = E_{bw} - E_1 - E_F$ is the current activation energy, E_{bw} is the discontinuity in the conduction band between GaAs and AlGaAs, E_1 is the energy of the first level in the quantum well, and E_F is the Fermi energy reckoned from E_1. The theoretical dependence $J(T)$ for a sample with $x = 0.29$ (see the inset in Fig. 1) was calculated according to Eq. (1) for $E_a = 0.14$ eV and $\mu_n = 500$ cm^2/(V·s).

The current in the regions with conduction band sag is determined primarily by successive tunneling of electrons between the quantum wells and the conduction band of the barrier layers through relatively narrow potential barriers. To calculate it, we consider one period of the structure in the region of conduction band sag, to which the voltage $V \lesssim kT/q$ has been applied (see Fig. 3). Let the lowest point of the conduction band of the barrier layer in the sag region be located above the equilibrium Fermi level (for $V = 0$). The charge of the free electrons in the barrier is therefore small and does not influence the course of the potential in the barrier layers. For simplicity, we assume that the shallow and deep levels are uniformly distributed over local regions, whose dimensions exceed the barrier thickness so that the spatial dependence of the potential can be assumed uniform and the same for all the local regions. In the case of completely filled or completely ionized deep levels the charge is also uniformly distributed over the thickness of the barrier and the energy of the edge of the conduction band, reckoned from its lowest point, is given by

$$\Delta E_c(x) = qV_s\left(\frac{x-\Delta x}{L_b/2}\right)^2. \quad (2)$$

Here $V_s = (kT/q)(L_b/2)^2/(2L_d)^2$ is the magnitude of the conduction band sag for $V = 0$, $\Delta x = L_b(V/8V_s)$ is the position of the minimum of the conduction band, $L_d = (kT\varepsilon_b/2q^2N^+)^{1/2}$ is the Debye screening length, ε_b is the dielectric constant of the barrier, and N^+ is the total concentration of positively charged shallow and deep levels. Since $L_w \ll L_b$, we have disregarded the voltage drop across the quantum well.

In intermediate cases, the deep levels are partly filled as a result of heating the sample to some temperature T_0 (see Sec. 1), the charge on the deep levels will be distributed nonuniformly since the electrons will be captured in first order by deep levels, which are located near the middle of the barrier layer and which have the lowest energy barrier for electron capture. However, for simplicity we assume that, as before, the conduction band sag is described by the parabolic dependence (2).

The energy of the lowest point of the conduction band of the barrier layer E_m, reckoned from the Fermi level in the left quantum well, is given by $E_m = E_a - \Delta E_{c1}$, where $E_a = E_{a0} - \Delta E_F - \Delta E_1$, ΔE_F and ΔE_1 are the changes in E_F and E_1 in the local regions with $V_s > 0$ caused by the appearance of additional free electrons in the quantum well and ''warping'' of the potential in the quantum well (see Fig. 3), and $\Delta E_{c1} = \Delta E_c(-L_b/2)$. To first order we set ΔE_F equal to N^+L_b/N_{2D} and neglect ΔE_1. In addition, we introduce the quantities $\Delta E_{c2} = \Delta E_c(L_b/2)$, $w_1 = L_b/2 + \Delta x$, and $w_2 = L_b/2 - \Delta x$.

Let us consider tunneling of electrons with energies above E_m. The probabilities of tunneling from the left quantum well (D_1) and from the right (D_2) quantum well into the allowed region of the barrier, calculated in the quasiclassical approximation,[14] are given by

$$D_{1,2}(E_t) = \exp[-S_{1,2}\phi(E_t/\Delta E_{c1,2})], \quad (3)$$

where E_t is the electron energy reckoned from the lowest point of the conduction band of the barrier, $S_{1,2} = \sqrt{2m_b\Delta E_{c1,2}}w_{1,2}/\hbar$, m_b is the effective mass of the electron in the barrier, and $\phi(z) = \sqrt{1-z} - z\ \ln[(1+\sqrt{1-z})/\sqrt{z}]$.

Noting that $V \lesssim kT/q$ and that the barriers ΔE_{c1} and ΔE_{c2} are thick and have low tunneling transparency, we may assume that the electrons in the conduction band of the barrier layer between the barriers ΔE_{c1} and ΔE_{c2} are completely thermalized, and that their energy distribution is described by the single Fermi quasilevel E_{Fb}, which is located, in general, between the Fermi levels of the left and right quantum wells. Allowing for the principle of detailed balance, we calculate the current density in the barrier ΔE_{c1},

$$j_1 = j_{10} \exp(-E_m/kt)[1 - \exp(E_{Fb}/kt)], \quad (4)$$

where

$$j_{10}=qN_{2D}\nu_t\int_0^\infty \exp(-E_t/kT)D_1(E_t)dE_t, \qquad (5)$$

and the Fermi level of the electrons in the left quantum well E_F is taken to be equal to zero. The quantity ν_t denotes the effective frequency of collisions of an electron in the quantum well with defects (polar optical phonons, ionized impurities, and roughness of the quantum well) leading to complete conversion of the energy of motion of the electron along the quantum well into transverse energy, with which the electron tunnels into the allowed band of the barrier.[15] Integration to infinity in Eq. (5) takes into account the electrons with energy E_t above ΔE_{c1}, for which $D_1(E_t)\simeq 1$. The current j_2 through the barrier ΔE_{c2} is given by an expression such as (4). Equating the currents j_1 and j_2, we find the position of the Fermi quasilevel E_{Fb}, and for the total current j_l through the local regions of conduction band sag we obtain the expression

$$j_l=\exp\left(-\frac{E_m}{kt}\right)\frac{j_{10}j_{20}}{j_{10}+j_{20}}\left[1-\exp\left(-\frac{qV}{kt}\right)\right], \qquad (6)$$

where j_{20} is given by Eq. (5) with D_1 replaced by D_2.

Tunneling of electrons with energies less than E_m can be ignored since it proceeds directly from one quantum well to another with small probability $D<D_1(0)D_2(0)$.

The total current J through the sample is calculated assuming identicity of all the barriers. In this case

$$J=A(1-\delta)j_0+A\delta j_l \qquad (7)$$

for $V=V_b/(N+1)$. Here A is the area of the sample, δ is the fraction of the area of the structure occupied by local regions with the indicated conduction band sag, and N is the number of periods of the structure.

Curves of the theoretical temperature dependence of the dark current (7) are shown in Fig. 1 by solid lines. We chose the quantities μ_n, V_s, and product $\delta\nu_t$ in such a way as to get the theoretical curves to coincide with the experimental curves *1–4* [in the first term of expression (7) we have ignored the parameter δ since it was shown in Sec. 2.1 that $\delta\ll 1$]. At increased temperatures the current j_0 predominates. The activation energy of the current j_0, given by E_{a0} [see Eq. (1)], was found, by an independent calculation from known parameters of multilayer quantum-well structures,[16,17] to be equal to 0.194 eV. The electron mobility in the barrier μ_n was taken to be equal to 1000 $\mathrm{cm^2/(V\cdot s)}$.

At reduced temperatures the current of the local regions predominates. The magnitude of the conduction band sag V_s determines the activation energy of the local current j_l, and the product $\delta\nu_t$ determines its magnitude. Taking advantage of the coincidence of their temperature dependence in form and magnitude, we determined the values of the quantities V_s and $\delta\nu_t$. Good agreement with experiment is obtained for $\delta\mu_t=3\times 10^8$ Hz and V_s equal to 0.131, 0.122, 0.112, 0.097 V, respectively, for curves *1–4*. Here N^+ (in units of 10^{17} $\mathrm{cm^{-3}}$) and E_m (in meV) are equal to 4.7 (1.4), 4.4 (14.6), 4.0 (29.3), and 3.5 (51.4). Curves *5* and *6* in Fig. 1 correspond to the components of the current without sag Aj_0 and with sag of the conduction band $A\delta j_l$. It can be seen that the experimental temperature dependence of the current cannot be explained by either one of these components alone. Noting that the agreement of theory with the reference experimental dependence *4* in Fig. 1 requires the initial value $V_s=0.097$ eV, it must be admitted that the barriers in the above-mentioned local regions contain constantly ionized levels with concentration 3.5×10^{17} $\mathrm{cm^{-3}}$ (e.g., shallow donors). Illumination of the sample (Fig. 1, curve *1*) increases N^+ to 4.7×10^{17} $\mathrm{cm^{-3}}$ and, consequently, the concentration of recharging deep levels in the local regions is 1.2×10^{17} $\mathrm{cm^{-3}}$.

Note that during the recording of the dark current temperature dependences at temperatures greater than the preheating temperature T_0, for example, $T_0=110$ K for dependence *2* in Fig. 1, V_s decreases, resulting in a decrease in the local current. However, this decrease brings the structure into the region of significant contribution of the uniform current to the total current and is therefore unimportant.

Looking at the total picture, we may conclude that the proposed phenomenological model, despite its simplicity, provides an adequate description of the observed phenomenon of photoelectric memory in multilayer quantum-well structures.

We have not identified the nature and origin of the local clusters of donor levels in the barrier layers. However, noting that the photoelectric memory effect is observed only in $\mathrm{GaAs/Al_xGa_{1-x}As}$ multilayer quantum-well structures with $x>0.3$, we may assume that it is due to the enhanced defect content of such structures in comparison with multilayer quantum-well structures, where $x<0.3$. In this case the local clusters of shallow and deep donor levels can be either intrinsic defects of the barrier layers or *DX* centers formed as a result of thermally favored silicon diffusion out of the quantum wells via defects of the structure during its growth.

CONCLUSIONS

Growth of the dark current by 2–3 orders of magnitude in $\mathrm{GaAs/Al_xGa_{1-x}As}$ multilayer quantum-well structures with $x\simeq 0.4$ has been observed after exposing them to light ($\lambda<1.3$ μm). The increased current persists for an extended time at reduced temperatures and falls back to its initial value upon heating. The observed effect is explained in the framework of a barrier model with local conduction band sag that facilitates electron tunneling. The degree of sag and the magnitude of the current grow upon photoionization of local clusters of uncontrolled deep levels present in the barrier and decrease as conduction band electrons are captured by them upon heating.

*E-mail: vnovsyuk@ispht.nsk.su; Fax: (383-2) 35-17-71

[1] B. F. Levine, J. Appl. Phys. **74**, R1 (1993).
[2] K. K. Choi, B. F. Levine, C. G. Bethea, J. Walker, and R. J. Malik, Appl. Phys. Lett. **50**, 1814 (1987).
[3] B. F. Levine, C. G. Bethea, G. Hasnain, V. O. Shen, E. Pelve, R. R. Abbott, and S. J. Hsieh, Appl. Phys. Lett. **56**, 851 (1990).
[4] E. Pelve, F. Beltram, C. G. Bethea, B. F. Levine, V. O. Shen, S. J. Hsieh, J. Appl. Phys. **66**, 5656 (1989).
[5] B. F. Levine, A. Zussman, J. M. Kuo, and J. de Jong, J. Appl. Phys. **71**, 5130 (1992).
[6] A. Zussman, B. F. Levine, J. M. Kuo, J. de Jong, J. Appl. Phys. **70**, 5101 (1991).

[7] G. M. Williams, R. E. DeWames, C. W. Farley, and R. J. Anderson, Appl. Phys. Lett. **60**, 1324 (1992).
[8] L. Pfeiffer, E. F. Schubert, K. W. West, and C. W. Magee, Appl. Phys. Lett. **58**, 2258 (1991).
[9] H. C. Liu, Z. R. Wasilewski, M. Buchanan, and H. Chu, Appl. Phys. Lett. **63**, 761 (1993).
[10] P. N. Brounkov, S. G. Konnikov, T. Benyattou, and G. Guillot, Phys. Low-Dimens. Semicond. Struct. **10/11**, 197 (1995).
[11] V. Ya. Aleshkin, B. N. Zvonkov, E. R. Lin'kova, A. V. Murel', and Yu. A. Romanov, Fiz. Tekh. Poluprovodn. **27**, 931 (1993) [Semiconductors **27**, 504 (1993)].
[12] P. M. Mooney, J. Appl. Phys. **67**, R1 (1990).
[13] H. C. Liu, A. G. Steele, M. Buchanan, and Z. R. Wasilewski, J. Appl. Phys. **73**, 2029 (1993).
[14] L. D. Landau and E. M. Lifshitz, *Quantum Mechanics* [in Russian], Ch. 7, Sec. 50 (Nauka, Moscow, 1989) [English translation of earlier edition: *Quantum Mechanics*, (Pergamon Press, Oxford, 1974)].
[15] S. V. Meshkov, Zh. Éksp. Teor. Fiz. **91**, 2252 (1986) [Sov. Phys. JETP **64**, 1337 (1986)].
[16] S. Adachi, J. Appl. Phys. **58**, R1 (1985).
[17] B. R. Nag and S. Mukhopadhyay, Phys. Status Solidi B **175**, 103 (1993).

Translated by Paul F. Schippnick

Depletion of the inverse electron channel at the type-II heterojunction in the system *p*-GaInAsSb/*p*-InAs

T. I. Voronina, T. S. Lagunova, M. P. Mikhaĭlova, K. D. Moiseev, A. E. Rosov, and Yu. P. Yakovlev

A. F. Ioffe Physicotechnical Institute, Russian Academy of Sciences, 194021 St. Petersburg, Russia
(Submitted July 1, 1997; accepted for publication July 14, 1997)
Fiz. Tekh. Poluprovodn. **32**, 215–220 (February 1998)

Magnetotransport and the electron channel parameters are investigated in *p*-GaInAsSb/*p*-InAs heterojunctions as functions of the acceptor doping level of the quaternary (GaInAsSb) layer. An abrupt decrease in the carrier mobility with increased doping level in these heterojunctions is observed. This decrease can be attributed to the narrowing and depletion of the channel near the interface and strong localization of electrons in potential wells at the interface. © *1998 American Institute of Physics.* [S1063-7826(98)01902-4]

Earlier we showed[1–3] that in single *p*-GaInAsSb/*p*-InAs heterostructures with undoped layers of the quaternary solid solution with isolated type-II heterojunctions there exists at the heterojuction an electron channel with high electron mobility $\mu_H=(5-7)\times10^4$ cm^2/(V·s). The presence of such a channel in type-II heterojunctions is connected with spatial separation of the electrons and holes and their localization in self-consistent wells on both sides of the heterojunction.

In the present work we consider the effect of doping of the solid solution by acceptor impurities (Zn, Ge, Sn) over a wide concentration range on the properties of the electron channel in *p*-$Ga_{0.83}In_{0.17}As_{0.22}Sb_{0.78}$/*p*-InAs heterostructures. We investigated the Hall coefficient R_H, the electrical conductivity σ, and the mobility μ_H at temperatures from 77 to 200 K in magnetic fields from 1 to 20 kOe. We found that heavy doping of the *p*-GaInAsSb solid solution with an acceptor impurity leads to a rapid decrease of the mobility in the electron channel, which is attributable to a narrowing of the electron channel and an increasing role of scattering by the rough surface of the heterojunction.

EXPERIMENTAL RESULTS

The *p*-GaInAsSb/*p*-InAs heterostructures were prepared by liquid-phase epitaxy at $T=600$ °C. Epitaxial layers of the solid solution *p*-$Ga_{0.83}In_{0.17}As_{0.22}Sb_{0.78}$ ($E_g=0.63$ eV at $T=77$ K) with different levels of doping with acceptor impurities ($3\times10^{-3}\leqslant$Zn$\leqslant1.2\times10^{-2}$ at. %, $2.4\times10^{-3}\leqslant$Ge$\leqslant2.7\times10^{-2}$ at. %, $4.5\times10^{-2}<$Sn$<10^{-1}$ at. %) were grown on high-resistance *p*-type InAs substrates with parameters (at 77 K) $\sigma=0.2\ \Omega^{-1}$ cm^{-1}, $p=10^{16}$ cm^{-3} ($E_g=0.4$ eV). The thickness of the layers was roughly 2 μm. Six indium contacts were deposited on samples of rectangular shape on the surface of the solid solution. At currents $I\leqslant100$ μA, where Ohm's law applies, the voltage drop across potential probes V_σ and the Hall voltage V_H were measured in the temperature interval 77–200 K (above 200 K the substrate conductivity becomes noticeable) in magnetic fields $H=1-20$ kOe. From these data we calculated the electrical conductivity σ, the Hall coefficient R_H per unit area, and the Hall mobility $\mu_H=R_H\sigma$.

The parameters of the samples at $T=77$ K are listed in Table I. As can be seen from the table, the sign of the Hall voltage for $H\simeq1$ kOe in all of the samples with acceptor doping (Zn, Ge, Sn) points to the electronic character of the conductivity (the only exception is the structures with maximum Zn doping level; see sample 5). This, in our opinion, has to do with the conductivity of the electron channel located at the heteroboundary in the isolated type-II heterojunction on the InAs side.[2] The magnitude of the Hall mobility $\mu_H=R_H\sigma$ for light doping of the solid solution (samples 2, 6, and 8) maintained the same high values as in the structures with undoped layers (sample 1 in Table I). For heavy doping of the solid solution (samples 4, 7, and 9) an abrupt drop in the mobility was observed along with a strong magnetic field dependence for R_H and μ_H.

Figure 1 plots the dependence of R_H on the magnetic field intensity at $T=77$ K. It can be seen that for the samples whose solid-solution layer was undoped or lightly doped with acceptors (curves *1* and *2*) $R_H<0$ and is virtually independent of H; i.e., the conductivity is determined by one type of carrier (electrons). For a high level of acceptor doping (curves *4* and *9*) R_H is observed to depend sharply on H up to change of sign of the Hall voltage. Such a dependence is characteristic of a conductivity due to two types of current carrier of different sign: In a weak field in this case the highly mobile electrons concentrated on the heteroboundary play the dominant role, while in a strong field the hole conductivity of the solid solution becomes noticeable. Of course, the conductivity of the solid-solution layer increases with growth of its acceptor doping level. In the sample with maximum Zn content (curve *5*) the sign of the Hall voltage corresponds to a *p*-type conductivity in all magnetic fields. In this sample the Hall coefficient was found to remain constant for $H>10$ kOe. It may be assumed that the Hall coefficient in this field region completely reflects the properties of the doped solid solution *p*-GaInAsSb, while the electron channel is manifested only in the decrease of the magnitude of R_H for $H<10$ kOe.

Let us consider the temperature dependence of R_H for samples with different doping levels of the solid solution shown in Figs. 2 and 3. In sample 2 (Fig. 2, curve *a*), with lightly doped solid-solution layer, the Hall coefficient R_H

TABLE I. Parameters of p-GaInAsSb/p-InAs samples at $T=77$ K.

Sample No.	Impurity in solid solution		Type of conductivity from the Hall voltage	σ, 10^3 Ω^{-1}	$\mu_H=R_H\sigma$, $cm^2/(V\cdot s)$	
	type	amount, at. %		$H=1$ kOe	$H=1$ kOe	$H=20$ kOe
1	-	-	n	9.6	−57000	−45000
2	Zn	3×10^{-3}	n	8.8	−49000	−35000
3	Zn	4×10^{-3}	n	9	−24400	−18000
4	Zn	8×10^{-3}	n	10	−3500	+180
5	Zn	1.2×10^{-2}	p	13	+20	+80
6	Ge	2.5×10^{-3}	n	10	−35000	−11000
7	Ge	2.75×10^{-2}	n	14	−2800	+100
8	Sn	4.6×10^{-2}	n	9	−55000	−42400
9	Sn	10^{-1}	n	4.8	−11700	−480

falls gradually with increasing temperature in magnetic fields in the range 1–20 kOe. In sample 4 (Fig. 2, curves *b*) with heavily doped solid-solution layer, R_H is observed to increase with increasing temperature. This increase intensifies with increasing magnetic field intensity, while in strong magnetic fields ($H=20$ kOe) the Hall voltage changes sign at $T=130$ K as the dominant current carrier changes over from holes to electrons. In sample *5* (Fig. 3), with the most heavily doped epitaxial layer, this change of sign was observed in all magnetic fields, and it took place at lower values of T with decreasing value of the magnetic field H. This indicates that the contribution of the electrons to the total conductivity of the structure increases as the temperature is raised. The temperature dependence of the Hall mobility for these samples was similar to that of the resistance $R(T)$.

Figure 4 plots the Hall mobility μ_H in a weak magnetic field $H=1$ kOe (where the Hall coefficient R_H is determined mainly by the electrons in the two-dimensional channel) as a function of the Zn concentration in the solid solution. It can be seen that the mobility in sample heterostructures with lightly doped layers of solid solution ($Zn\leqslant4\times10^{-3}$ at. %) at $T=77$ and 200 K (curves *1* and *2*) has the same high values $\mu_H=(3-5)\times10^4$ $cm^2/(V\cdot s)$ as in the samples with undoped layers. At heavy doping levels ($Zn>4\times10^{-3}$ at. %) the Hall mobility in the channel falls abruptly both at $T=77$ K (curve *1*) and $T=200$ K (curve *2*). The dependence of μ_H on the impurity concentration in p-GaInAsSb/p-InAs heterostruc-

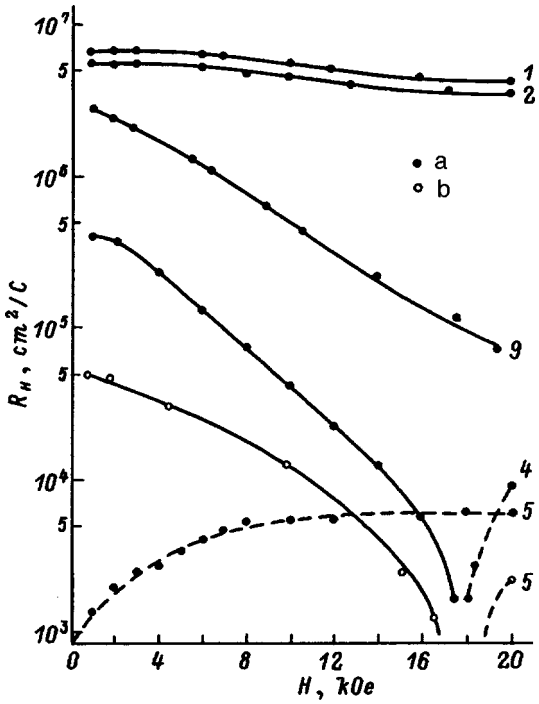

FIG. 1. The Hall coefficient R_H plotted as a function of magnetic field intensity H in p-GaInAsSb/p-InAs heterostructures at temperatures T, K: a—77, b—200. The numbers on the curves correspond to the numbers of the samples in Table I. Solid curves—$R_H<0$, dashed curves—$R_H>0$.

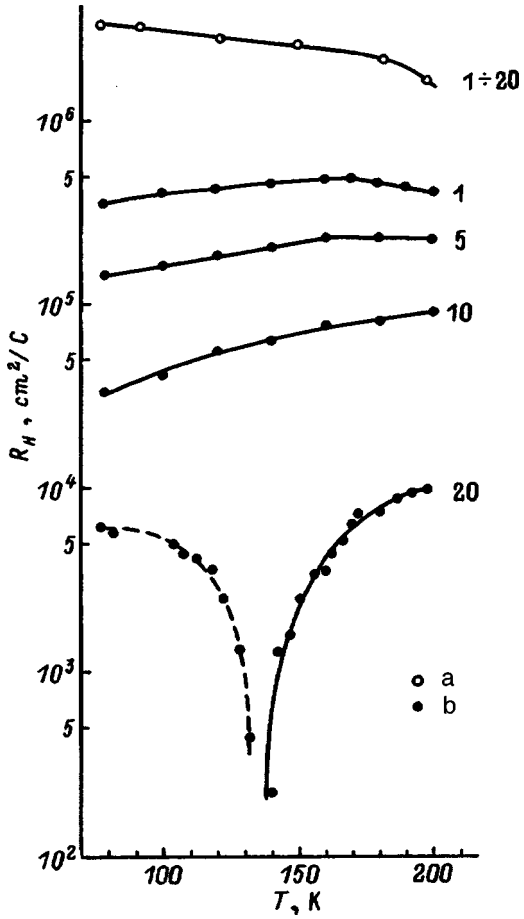

FIG. 2. The Hall coefficient R_H as a function of temperature for different magnetic field intensities for two samples from Table I: a—sample 2, b—sample 4. The solid and dashed curves have the same meaning as in Fig. 1. The numbers beside the curves are the magnetic field intensity in kOe.

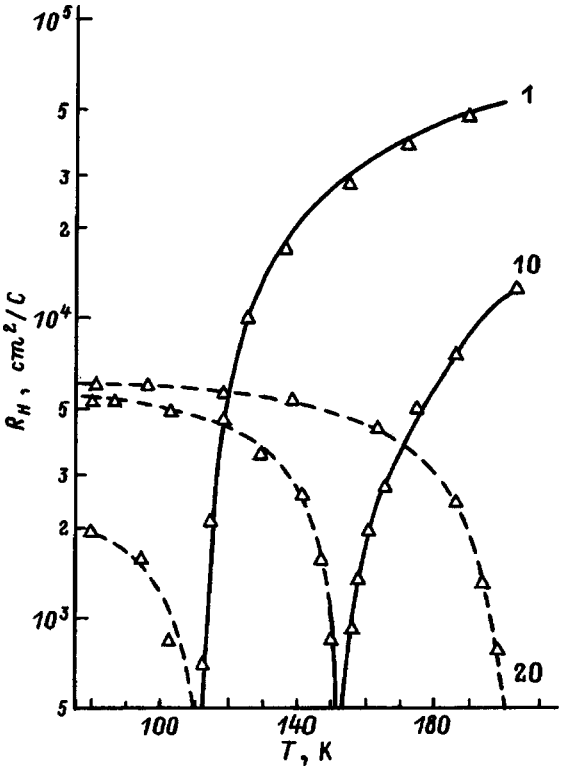

FIG. 3. The Hall coefficient R_H as a function of temperature for sample 5 for the magnetic field intensities (in kOe) indicated beside the curves. The solid and dashed curves have the same meaning as in Fig. 1.

tures obtained here differs substantially from the analogous dependence we obtained earlier[4] for an epitaxial layer of the solid solution $Ga_{1-x}In_xAs_{1-y}Sb_y$ with $x=0.1-0.2$ and $y=0.2$, grown on a GaSb substrate. The undoped layers of

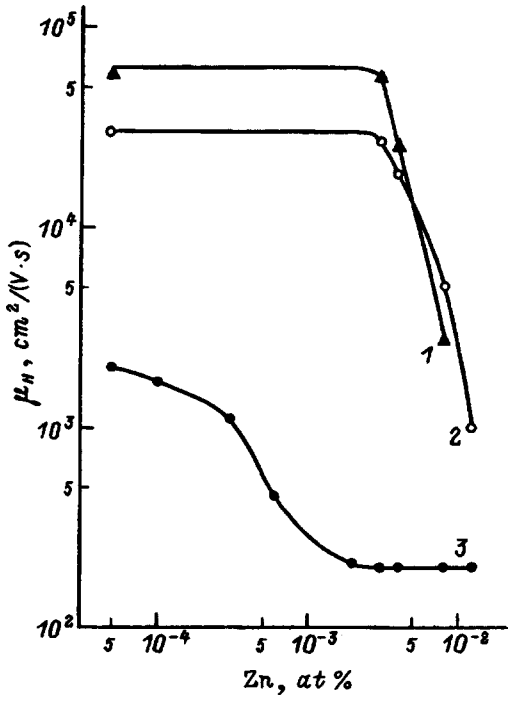

FIG. 4. The Hall mobility μ_H for $H=1$ kOe as a function of zinc doping level of the solid solution: *1,2*—for *p*-GaInAsSb/*p*-InAs heterostructures; *3*—for the solid solution *p*-GaInAsSb. Temperature *T*, K: *1,3*—77, *2*—200.

solid solution had *p*-type conductivity. The hole concentration and mobility at $T=77$ K in such layers were $p_1=10^{16}$ cm^{-3} and $\mu_1=2000$ cm^2/(V·s). When these layers were doped with acceptor impurities, the hole concentration grew, the mobility decreased smoothly and at the concentration $p>10^{18}$ cm^{-3}, at which degeneracy of the hole gas set in, the mobility became nearly constant: $\mu_1=200$ cm^2/(V·s). An important result here is that the abrupt drop of the mobility μ_H in *p*-GaInAsSb/*p*-InAs heterostructures is observed at precisely those concentrations of the Zn impurity at which degeneracy of the hole gas sets in in the *p*-GaInAsSb solid solutions and the mobility no longer depends on the doping level.

DISCUSSION

The experimental dependence of the Hall coefficient R_H and mobility μ_H on the temperature and magnetic field in *p*-GaInAsSb/*p*-InAs heterostructures shows that the properties of the electron channel at the heterojunction depends on the doping level of the solid solution, i.e., the position of the Fermi level in the solid solution.

In samples with lightly doped epitaxial layers, in which the Fermi level is located in the band gap (far from the heterointerface), the quantities R_H and μ_H, as we saw earlier, are determined by one type of charge carrier—electrons in the channel at the heterojunction. The electron mobility in the channel for light doping of the solid solution maintains high values $\mu_H=(3-6)\times10^4$ cm^2/(V·s) down to liquid-helium temperatures,[5] which is characteristic of the semimetallic state.

For high doping levels of the solid solution, for which the Fermi level is located in the valence band of the epitaxial layer (far from the heterojunction), the temperature and magnetic field dependence of R_H and μ_H indicate that both the electrons in the channel at the heterointerface and the holes in the solid solution participate in the conductivity, and also that the role of the electrons in the channel grows with increase of the temperature. The measured values of R_H and μ_H in all the samples with heavy doping of the solid solution in weak magnetic fields ($H<1-2$ kOe) are described by the formulas for the two-layer model[6] with different signs of the charge carriers in the layers:

$$R_H=(R_1\sigma_1^2b_1-R_2\sigma_2^2b_2)/\sigma^2b, \tag{1}$$

$$\mu_H=(\mu_1^2n_1b_1-\mu_2^2p_2b_2)/\sigma b, \tag{2}$$

where b is the total thickness, the subscript 2 corresponds to the epitaxial layer, and the subscript 1 corresponds to the electron channel at the heteroboundary.

The contribution of the epitaxial layer [the term $\mu_2^2p_2b_2$ in Eq. (2)] to the total measured mobility μ_H in *p*-GaInAsSb/*p*-InAs heterostructures for heavy doping of the epitaxial layer should remain practically the same as in the samples with undoped layers since, as was noted above, an increase in the hole concentration by two orders of magnitude is accompanied by a simultaneous decrease in the mobility by one order of magnitude. This gives us grounds to assert that the abrupt decrease of the measured mobility in the samples with heavily doped epitaxial layers is due not to

TABLE II. Parameters of the solid solution and electron channel.

	Solid solution				Electron channel				
			$E_v - E_F$, meV		μ_1, cm^2/(V·s)		N_s, 10^{11} cm^{-2}		d, Å
Sample No.	p_2, 10^{18} cm^{-3}	μ_2, cm^2/(V·s)	77K	200K	77K	200K	77K	200K	77K
2	0.1	2000	−14	−60	50000	40000	1	-	400
4	2	200	+16	−5	35000	5000	13	6.4	110
5	6	80	+23	+16	-	1000	-	80	-

greater influence of the epitaxial layer but to a decrease in the mobility in the electron channel, which may be due to a narrowing of the electron channel and the appearance of additional scattering mechanisms.

Estimate of the solid solution and electron channel parameters. The temperature and magnetic field dependence of the Hall coefficient and mobility allow us to estimate the parameters of the solid solution and the electron channel at the heterojunction (Table II). These estimates were made for heavily doped samples 4 and 5 (see Table II) using the two-layer model, which takes account of contributions to the conductivity of the electron channel and the quaternary solid solution.

In sample 5 with heaviest doping of the epitaxial layer the hole concentration in the solid solution can be estimated from the values of the Hall coefficient in strong magnetic fields ($H=20$ kOe) at $T=77$ K (Fig. 1). For layer thickness $b_2=2$ μm the hole concentration $p_2=6\times10^{18}$ cm^{-3}. Here the Hall mobility $\mu_H=80$ cm^2/(V·s) reflects the hole mobility in the solid solution. For the hole concentration $p_2=6\times10^{18}$ cm^{-3} the solid solution is strongly degenerate, the Fermi level is located in the valence band, and its position at $T=77$ K corresponds to $E_v-E_F=0.023$ eV. For this position of the Fermi level the electron channel at the heterojunction is hardly noticeable. Its influence shows up only in a decrease of the Hall coefficient in weak fields ($H<10$ kOe; see Fig. 1). As the temperature is increased, the Fermi level rises to the top of the valence band and the degree of degeneracy of the hole gas decreases. Under these conditions, a change in sign of the Hall voltage is observed in the temperature dependence of R_H (see Fig. 3); i.e., the electrons in the electron channel begin to play a major role, which increases with increasing temperature and decreasing magnetic field. At $T=200$ K, when the Fermi level $E_v-E_F=0.016$ eV, the dependence $R(H)$ (Fig. 1) becomes the same as in more lightly doped sample 4 at $T=77$ K. At the inversion point of the Hall coefficient $R_H=0$, according to Eqs. (1) and (2) the contributions of the electron channel and the solid solution are equal; i.e., $\mu_1^2 p_1 b_1=\mu_2^2 n_2 b_2$. From this condition, assuming that the concentration and mobility in the epitaxial layer (Table II) in the case of degeneracy remain nearly constant with increasing temperature, and that the mobility μ_H for $H=1$ kOe reflects the mobility in the electron channel ($\mu_1=1000$ cm^2/(V·s)), it is possible to estimate the two-dimensional carrier concentration in the electron channel $N_s=n_1 b_1=8\times10^{12}$ cm^{-2}. Employing concepts of the two-dimensional model,[7] it is possible to determine the width of the electron channel d from the formula

$$d=\left[\left(\frac{3}{4}\right)^2\frac{a_B}{\pi N^*}\right]^{1/3}, \tag{3}$$

where $N^*=N_{\text{depl}}+\frac{11}{32}N_s$ (N_{depl} is the residual impurity concentration in the depleted layer) and a_B is the Bohr radius. Values of d so obtained are shown in Table II.

The same calculation was performed for sample 4 with lower doping level, $p_2=2\times10^{18}$ cm^{-3}. For this hole concentration the Fermi level is $E_v-E_F=0.016$ eV at $T=77$ K. Change of sign of the Hall voltage is observed in this sample only in strong fields ($H=20$ kOe) at $T=130$ K, while in a weak field ($H=1$ kOe) the measured mobility μ_H reflected the electron mobility in the channel at all temperatures. Knowing the values of the electron mobility and assuming that p_2 and μ_2 are independent of temperature, it is possible to estimate the two-dimensional concentration N_s and the width of the electron channel at all temperatures (see Table II).

For samples with undoped and weakly doped epitaxial layers of p-GaInAsSb we estimated the parameters of the electron channel in our previous paper[5] from measurements of the Shubnikov–de Haas oscillations at low temperatures: the two-dimensional carrier concentration $N_s=1.0\times10^{11}$ cm^{-2} and width of the electron channel $d=400$ Å (sample 2 in Table II).

From the obtained data it follows that in p-GaInAsSb/p-InAs structures with heavy doping of the epitaxial layer the electron concentration in the channel grows and this growth is accompanied by a narrowing of the channel and an abrupt decrease of the mobility μ_H. The mobility in the electron channel decreases as $N_s^{-0.5}$ (see Fig. 5, solid line) and d^2 (dashed line). Analogous results were obtained in Refs. 8–10, which investigated type-II superlattices with isolated bands (broken gap) with quantum wells of different widths. Such an abrupt fall of the mobility in superlattices with thin layers was explained by the appearance of scattering by potential fluctuations and roughness of the heteroboundaries. A transition was observed here from the semimetallic to the semiconducting state.

The abrupt decrease of the mobility at high doping levels of the solid solution in the p-GaInAsSb/p-InAs heterostructures investigated by us may also be linked with a narrowing of the electron channel and the appearance of the additional

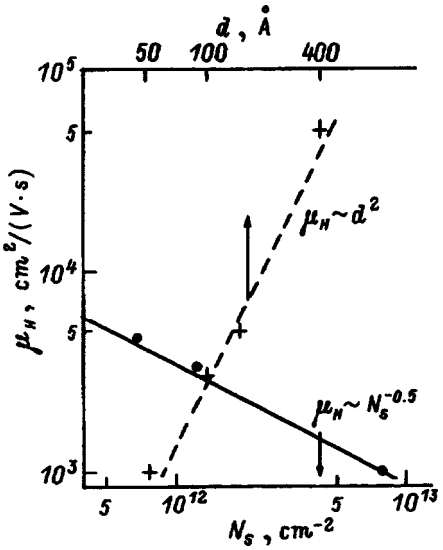

FIG. 5. The electron mobility μ_H in the channel plotted as a function of the two-dimensional electron concentration N_s. The dashed line plots the dependence of the mobility μ_H on the width of the electron channel d.

mechanisms of scattering by potential fluctuations and roughness of the heterojunction.

Comparison with the band diagram of the heterojunction. The results obtained agree with the energy diagram of an isolated type-II heterojunction, shown in Fig. 6. In p-GaInAsSb/p-InAs heterostructures the minimum of the conduction band is located lower in energy than the maximum of the valence band of the solid solution. A break is formed between the valence band of the solid solution and the InAs conduction band. This break is estimated to be $\Delta=\chi_2-\chi_1-E_{g1}=70$ meV (in the solid solution the electron affinity $\chi_1=4.2$ eV, $E_{g1}=0.63$ eV, and in InAs $\chi_2=4.9$ eV, $E_{g2}=0.41$ eV at $T=77$ K). When these two semiconductors are brought together, electrons overflow out of the valence band of the solid solution into the InAs conduction band and bends are formed in the bands at the heterojunction. Potential wells for the electrons and holes are formed in this case on both sides of the heterojunction. The Fermi level of the structure intersects the heteroboundary inside the band discontinuity and divides it in proportion to the ratio of the effective masses of the holes in the solid solution and the electrons in the InAs layer. If the solid solution is undoped or weakly doped with acceptor impurities, i.e., $p<10^{17}$ cm^{-3}, the Fermi level is located in the band gap of the solid solution. An electron channel of depth $\Delta=60$ meV and width $d=400$ Å is formed at the heterojunction (Fig. 6a) with semimetallic properties: a high electron mobility is observed in it, which is independent of the temperature.[5]

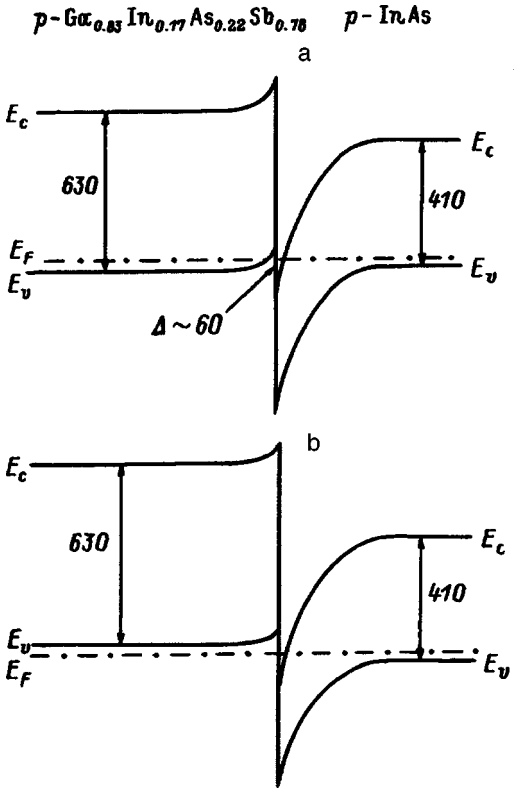

FIG. 6. Energy-level diagram of the heterojunction p-GaInAsSb/p-InAs for the epitaxial solid-solution layer: a—lightly doped, and b—heavily doped. Energy values in meV.

For heavy doping of the solid solution, when $p>10^{18}$ cm^{-3}, the Fermi level is found in the valence band of the solid solution, the magnitude of the discontinuity at the heterojunction is preserved, and the Fermi level in the electron channel falls, shadowing its shift in the solid solution (Fig. 6b). The channel narrows to a width of $d=50-150$ Å. Additional scattering mechanisms appear: from the potential fluctuations and from the roughness of the heterojunction. As the temperature is raised, the Fermi level in the solid solution rises to the top of the valence band, and following it the Fermi level rises in the electron channel. As a result, the width of the channel at the Fermi level increases as does the electron mobility in it (see Table II).

CONCLUSIONS

Thus, the properties of the electron channel in p-$Ga_{0.83}In_{0.17}As_{0.22}Sb_{0.78}$/$p$-InAs structures for different levels of doping of the solid solution with acceptor impurities depends substantially on the position in it of the Fermi level: in a lightly doped solid solution, there is an electron channel with a high electron mobility and semimetallic properties; heavy doping of the solid solution leads to an abrupt decrease of the mobility, which is associated with a narrowing of the electron channel and with the appearance of additional scattering mechanisms at the potential fluctuations and at the irregularities of the heterojunction.

We thank T. A. Polyanskaya and A. Ya. Shik for useful discussions and valuable remarks.

This work was supported in part by the Russian Fund for Fundamental Research (Grant No. 96-0217841a).

[1] T. I. Voronina, T. S. Lagunova, M. P. Mikhaĭlova, K. D. Moiseev, and Yu. P. Yakovlev, Fiz. Tekh. Poluprovodn. **30**, 985 (1996) [Semiconductors **30**, 523 (1996)].

[2] M. P. Mikhaĭlova, I. A. Andreev, T. I. Voronina, T. S. Lagunova, K. D. Moiseev, and Yu. P. Yakovlev, Fiz. Tekh. Poluprovodn. **29**, 678 (1995) [Semiconductors **29**, 353 (1995)].

[3] T. I. Voronina, T. S. Lagunova, M. P. Mikhaĭlova, K. D. Moiseev, S. A. Obukhov, A. V. Anikundinov, A. N. Titkov, and Yu. P. Yakovlev, *Abstracts of the Second Russian Conference on the Physics of Semiconductors* [in Russian] (St. Petersburg, 1996), Vol. 2, p. 158.
[4] T. I. Voronina, B. E. Dzhurtanov, T. S. Lagunova, and Yu. P. Yakovlev, Fiz. Tekh. Poluprovodn. **25**, 285 (1991) [*sic*].
[5] T. I. Voronina, T. S. Lagunova, M. P. Mikhaĭlova, K. D. Moiseev, S. A. Obukhov, A. E. Rozov, and Yu. P. Yakovlev, Pis'ma Zh. Tekh. Fiz. **23**, 1 (1997) [*sic*].
[6] R. L. Petritz, Phys. Rev. **100**, 1254 (1958).
[7] T. Ando, A. B. Fowler, and F. Stern, Rev. Mod. Phys. **54**, 437 (1982) (*Electronic Properties of Two-Dimensional Systems*).
[8] C. A. Hoffman, J. R. Meyer, E. R. Yougdale, F. J. Bartoli, R. H. Miles, and L. R. Ram-Mohan, Solid-State Electron. **37**, 1203 (1994).
[9] A. N. Silin, Usp. Fiz. Nauk **147**, 485 (1985) [Sov. Phys. Usp. **28**, 972 (1985)].
[10] L. Esaki, Lect. Notes Phys. **133**, 302 (1980).

Translated by Paul F. Schippnick

Interband absorption of long-wavelength radiation in δ-doped superlattices based on single-crystal wide-gap semiconductors

V. V. Osipov and A. Yu. Selyakov

State Science Center of the Russian Federation ''Orion,'' 111123 Moscow, Russia

M. Foygel

South Dakota School of Mines and Technology, Rapid City, South Dakota 57701–3995, USA
(Submitted July 22 1997; accepted July 25 1997)
Fiz. Tekh. Poluprovodn. **32**, 221–226 (February 1998)

A new type of superlattice formed in a single-crystal nondegenerate, wide-gap semiconductor by a sequence of pairs of closely spaced, δ-doped donor and acceptor layers is proposed. It is shown that because of the superstrong electric fields generated between these δ-doped layers, the electroabsorption of long-wavelength radiation is determined by tunneling optical transitions of electrons from the heavy-hole band (in contrast to the case of moderately strong fields when the electroabsorption is determined by light holes). The magnitude of the electroabsorption is close to the interband absorption for light and is virtually independent of the photon energy up to the far-infrared region. It was found that in the proposed InSb-based superlattice the absorption in superstrong fields can exceed 10^3 cm^{-1} up to radiation wavelengths approximately equal to 50–100 μm. It is noted that because of the spatial separation of the photogenerated electrons and holes, their lifetime and the long-wavelength sensitivity of such a superlattice have giant values. © *1998 American Institute of Physics.* [S1063-7826(98)02002-X]

1. INTRODUCTION

One of the most pressing problems of photoelectronics is the production, on the basis of wide-gap semiconductors, of photodetectors and large-format staring arrays for middle and far infrared (IR) radiation. A promising direction in the solution of this problem is the development of IR photodetectors based on different types of quantum wells and superlattice and, first and foremost, quantum-well GaAs/AlGaAs (Ref. 1) and Si/SiGe (Ref. 2) heterostructures. The progress achieved in semiconductor technology in recent years has made it possible to produce the so-called δ-doped structures,[3] which Döhler proposed and studied theoretically back in the 1970s.[4,5] During growth of such structures δ-doped regions with dopant density of the order of 10^{20} cm^{-3} and thickness of the order of one period of the crystal lattice are produced in a single-crystal semiconductor.[6,7] Until now, δ-doped p–n junctions and multilayer superlattices have been produced on the basis of different semiconductors, including Si,[7,8] GaAs,[9–13] and InSb.[14–17] In particular, sawtooth δ-doped quantum-well superlattices, in which the absorption of long-wavelength radiation is determined by transitions between minibands formed in the sawtooth potential well of such structures, have been developed on the basis of Si, GaAs, and InSb.[8,9,14] However, photodetectors based on quantum-well structures possess two substantial drawbacks — radiation incident in a direction along the normal is absorbed weakly[1,8,9,18,19] and the photocarrier lifetime and the photosensitivity are extremely small.[20,21]

Classical doped superlattices of the n–i–p–i type, which were proposed at the beginning of the 1980s and studied theoretically by Neustroev and Osipov, do not have these drawbacks.[22–25] In such superlattices, the photocarrier lifetime and the photosensitivity can reach enormous values as a result of spatial separation of the photogenerated electrons and holes. However, long-wavelength IR radiation is absorbed weakly in classical doped superlattices based on wide-gap semiconductors.[26–28] This stems from the fact that the absorption of such IR radiation is determined by the Franz–Keldysh effect[29,30] in the space-charge regions of the p–n junctions, where the maximum electric field intensity is limited by a value of the order of 10^5 V/cm. Stronger electric fields can in principle be produced in p–n junctions by increasing the dopant density, but then the tunneling current of the p–n junctions increases and therefore the effective nonequilibrium-carrier lifetime in such superlattices and the photosensitivity of IR photodetectors based on them decrease sharply.

In the present paper we examine a new type of δ-doped superlattice based on single-crystal wide-gap semiconductors, which possesses a high photosensitivity in the long-wavelength IR range and which does not have the above-noted drawbacks inherent in previously proposed different quantum and classical superlattices.

2. SUPERLATTICE STRUCTURE

The proposed superlattice consists of pairwise alternating δ-doped donor- and acceptor-type layers, grown in a nondegenerate single-crystalline semiconductor. For definiteness, we assume that a nondegenerate p-type semiconductor with acceptor density N_a is present between the δ-doped acceptor layers and a nondegenerate n-type semiconductor with donor density N_d is present in other regions of the lattice. A period L of the superlattice consists of two pairs of δ-doped acceptor- and donor-type layers (Figs. 1a), and the energy diagram of one period of the superlattice has the form shown in Fig. 1b.

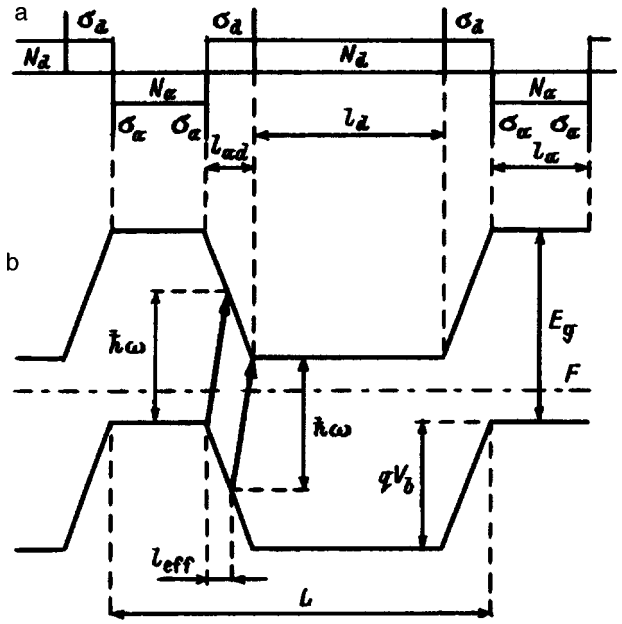

FIG. 1. Structure of a δ-doped superlattice: a — doping profile, b — band diagram. The heavy lines (b) show the indirect (in real space) interband optical transitions accompanying absorption of a photon with energy $\hbar\omega < E_g$. The notation used in the figure is explained in the text.

Let us now discuss the requirements for the parameters of such a superlattice, first and foremost the surface densities σ_d and σ_a of impurity atoms in the δ-doped donor and acceptor layers, as well as for the distances l_a, l_d, and l_{ad} between these layers (Fig. 1). For simplicity, we shall assume that $\sigma_a = \sigma_d = \sigma$ and that l_{ad} is small. Then, all electrons will move from the donor atoms in the δ-doped layers to the acceptor atoms in neighboring δ-doped layers and all donor- and acceptor-type δ-doped layers will consist of a sequence of oppositely charged planes with built-in surface charge density $+q\sigma$ and $-q\sigma$ (q is the electron charge), respectively. As a result, a constant electric field $E = 4\pi q\sigma/\varepsilon$, where ε is the permittivity of the semiconductor, arises between each pair of δ-doped donor and acceptor layers (oppositely charged planes). When $qEl_{ad} = qV_b < E_g$ (E_g is the band gap in the semiconductor, and V_b is the potential difference between the oppositely charged δ-doped layers), direct tunneling transitions between the conduction and valence bands will not occur in the superlattice under study. Let l_{ad} and the densities N_a and N_d also satisfy the condition $qEl_{ad} = qV_b = F_n - F_p < E_g$, where F_n and F_p are the Fermi levels in the n- and p-type semiconductors with donor density N_d and acceptor density N_a, respectively. When the above conditions are satisfied, there will be no space-charge regions in the n- and p-type layers and the band diagram of the superlattice will have the form shown in Fig. 1b. We note that the latter is valid for much weaker requirements for N_d and N_a, which should not be too high. These requirements essentially reduce to the conditions $l_d \leqslant L_{Dn}$ and $l_a \leqslant L_{Dp}$, where L_{Dn} and L_{Dp} are the Debye screening lengths for electrons and holes in the n- and p-type layers, respectively, since in this case the change in the potential in the n- and p-type regions is small and can be neglected. We note that these conditions hold for our InSb superlattice for $N_d < 10^{16}$ cm^{-3} and $N_a < 10^{18}$ cm^{-3} because of the smallness of the thicknesses l_a and l_d. (Estimates for l_a and l_d are presented below.)

In the present superlattice the absorption of photons with energy $\hbar\omega < E_g$ is due to the Franz–Keldysh effect in the regions of a strong electric field. We underscore that the electric field in layers of the superlattice with thickness l_{ad} (Fig. 1) is uniform and its intensity can be more than an order of magnitude higher than the maximum intensity of the field of a nondegenerate p–n junction and can reach enormous magnitudes ($E = 10^6$ V/cm with $\sigma \simeq 10^{13}$ cm^{-3} and $\varepsilon = 15$).

3. CHARACTERISTIC FEATURES OF IR ABSORPTION IN REGIONS OF A SUPERSTRONG ELECTRIC FIELD

The general expression for the IR absorption α_E in semiconductors with a parabolic dispersion law in a constant electric field has the form[29–33]

$$\alpha_E = \pi R \sqrt{\hbar\omega_E} \int_\beta^\infty \mathrm{Ai}^2(x)\,dx, \tag{1}$$

where $R = (2\mu/\hbar^2)^{3/2}(2q^2P_{cv}^2)/(m^2c\tilde{n}\omega)$, $\omega_E = (qE)^{2/3}/(2\mu\hbar)^{1/3}$, $\beta = (E_g - \hbar\omega)/(\hbar\omega_E)$, $\tilde{n}$ is the refractive index of the semiconductor, $\mathrm{Ai}(x)$ is an Airy function, P_{cv} is an interband matrix element of the momentum operator, c is the speed of light in vacuum, m is the electron mass, m_c is the effective electron mass, m_v is the effective hole mass, and $\mu^{-1} = m_c^{-1} + m_v^{-1}$ is the reduced effective mass.

We emphasize that expression (1) was derived for the case of an extended uniform semiconductor, and that it holds for relatively weak electric fields which change only slightly the energy spectra of the electrons and holes in the semiconductor. In superstrong electric fields the probability of direct tunneling transitions increases sharply. As a result, the electron and hole states mix strongly and for this reason (1) is inapplicable for extended semiconductors. A different situation materializes in our case: It is evident from Fig. 1b that in contrast to the case of an extended uniform semiconductor, direct tunneling transitions are impossible in our superlattice and therefore for such a superlattice the expression (1) can be used for arbitrarily strong electric fields provided that the thicknesses l_a and l_d are so large that the energy spectrum of the electrons and holes in the corresponding potential wells can be regarded as quasicontinuous (see below). It is also evident from Fig. 1b that the absorption of radiation with $\hbar\omega < E_g$ can occur only in a portion of the strong-field layer in the superlattice. The thickness of this absorbing region is $l_{\mathrm{eff}} = (\hbar\omega - E_g + qV_b)/qE < l_{ad}$. Hence it follows that the absorption of long-wavelength radiation in the strong-field layer of the superlattice is

$$\alpha = \alpha_E l_{\mathrm{eff}}/l_{ad} = \alpha_E(\hbar\omega - E_g + qV_b)/qV_b, \tag{2}$$

where α_E is given by Eq. (1), and $qV_b = 4\pi q^2\sigma l_{ad}/\varepsilon$.

In most direct-gap III–V semiconductors the interband matrix elements P_{cv} of the momentum operator for optical transitions from light- and heavy-hole bands are equal to one another,[34] and the light- and heavy-hole effective masses are substantially different ($m_{hh} \gg m_{lh}$). Therefore, $\mu = m_c/2$ for

optical transitions from the light-hole band and $\mu = m_c$ for optical transitions from the heavy-hole band. It is known that the absorption of a photon with $\hbar\omega < E_g$ in weak electric fields is determined by tunneling of electrons and light holes, and the corresponding absorption is exponentially small compared with the interband absorption.[29,30,33] At the same time, in the absence of an electric field the interband absorption of radiation is determined mainly by transitions of electrons from the heavy-hole band as a result of the high density of states of this band.[34] For the same reason, in our superlattice the absorption of long-wavelength photons with $\hbar\omega < E_g$ in regions of superstrong electric fields is determined not by light holes but rather by heavy holes.

To prove this point, we shall examine superstrong electric fields, for which the condition

$$E \gg (q\hbar)^{-1}(2\mu)^{1/2}(E_g - \hbar\omega)^{3/2} \tag{3}$$

holds in thin regions of thickness l_{ad} for the light and heavy holes, even for $\hbar\omega \simeq E_g/2$. As an example, we present the superlattice parameters, for which the inequality (3) can be assumed to hold for heavy holes in InSb with $E_g = 0.223$ eV, which corresponds to $T = 77$ K. It is easy to show that for $\sigma \geqslant 5\times 10^{12}$ cm^{-2} the intensity of the built-in field $E \geqslant 5\times 10^5$ V/cm, $\beta < 0.5$ for $\lambda < 10$ μm, and the condition $qV_b \leqslant E_g$ holds for $l_{ad} \leqslant 40$ Å. The condition (3) signifies that $\beta \ll 1$ and the overlap integral of the envelopes of the electron and hole wave functions in Eq. (1) is virtually identical for light and heavy holes. The overlap integral is $\int_0^\infty \mathrm{Ai}^2(x)dx = 3^{1/12}\Gamma^2(2/3)/4\pi^2$, where $\Gamma(x)$ is the gamma function. In this case we obtain the following expression from Eqs. (1) and (2):

$$\alpha = 3^{1/12}\Gamma^2(2/3)R\sqrt{\hbar\omega_E}(\hbar\omega - E_g + qV_b)/4\pi qV_b. \tag{4}$$

Since, according to Eq. (1), $\alpha_E \sim \mu^{4/3}$, it follows from Eq. (4) that the absorption is indeed more than two times greater than that for light holes. It is also evident from Eqs. (2) and (4) that in contrast to the case of weak electric fields, α in the regions of superstrong electric fields in our superlattice, where the condition (3) holds, is close to the interband absorption and is virtually independent of the photon energy up to $\hbar\omega = E_g - qV_b$, where it vanishes.

Radiation with $\hbar\omega < E_g - qV_b$ is not observed, and the quantity $E_g - qV_b$ plays the role of an effective optical band gap in our superlattice. We emphasize that $E_g - qV_b$ can be made as small as desired by varying the superlattice parameters. In another words, far-IR radiation can be absorbed in the superlattice sufficiently strongly up to wavelengths of approximately 50–100 μm.

These results are confirmed by numerical calculations which we performed using the general formula (2) for InSb with $E_g = 0.223$ eV (Figs. 2 and 3). Figure 2 shows the spectral dependence of the absorption in the strong-field region (with thickness l_{ad}) for optical transitions from the heavy- and light-hole bands in superlattices with the same effective band gap but different built-in charge densities in the δ-doped layers. Figure 3 shows the spectral dependence of the absorption for far-IR radiation determined by optical transitions from the heavy-hole band for superlattices with the same built-in charge density in the δ-doped layers but

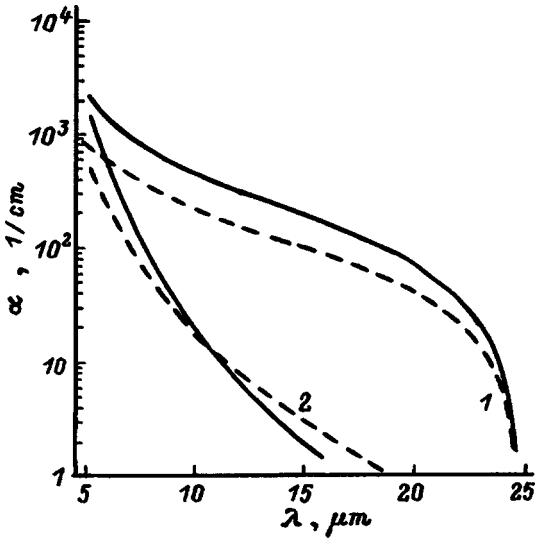

FIG. 2. Spectral dependence of the IR absorption in regions of a superstrong electric field in a δ-doped InSb superlattice: Solid curves — optical transitions of electrons from a heavy-hole band; dashed curves — from a light-hole band. *1* — $\sigma = 5\times 10^{12}$ cm^{-2}, $l_{ad} = 33$ Å; *2* — $\sigma = 10^{12}$ cm^{-2}, $l_{ad} = 165$ Å.

different effective band gap. The calculations show that the absorption is indeed determined by optical transitions of electrons from the heavy-hole band into the conduction band, and that it remains large enough right up to $\lambda = 25$ μm and even up to $\lambda = 100$ μm, depending on the superlattice parameters. It is also seen from Fig. 3 that changing the thickness l_{ad} by 7 Å, i.e., by an amount of the order of the lattice constant in InSb, shifts the long-wavelength absorption edge (λ_{co}) from 25 to 100 μm. At the same time, for such a

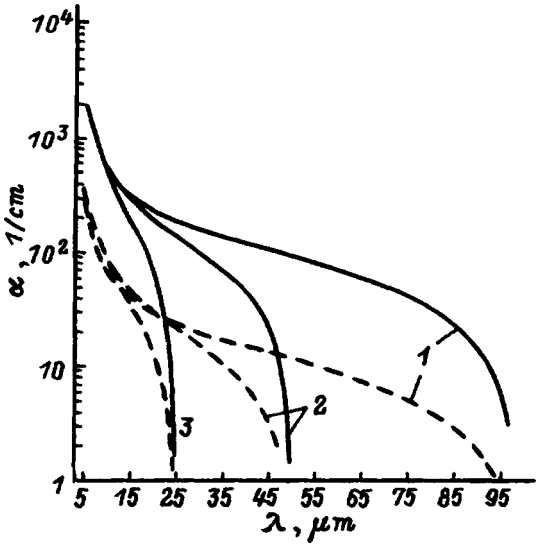

FIG. 3. Spectral dependence of the IR absorption of optical transitions of electrons from a heavy-hole band in δ-doped InSb superlattices: The solid curves determine the absorption in the regions of a superstrong electric field, i.e., α calculated according to Eq. (2); the dashed curves determine the absorption α_{eff} (7) averaged over a period of the superlattice. *1*: $l_a = 84$ Å, $l_d = 467$ Å, $l_{ad} = 40$ Å, $\lambda_{co} = 100$ μm; *2*: $l_a = 60$ Å, $l_d = 330$ Å, $l_{ad} = 38$ Å, $\lambda_{co} = 50$ μm; *3* — $l_a = 42$ Å, $l_d = 233$ Å, $l_{ad} = 33$ Å, $\lambda_{co} = 25$ μm. $\sigma = 5\times 10^{12}$ cm^{-2}.

change in the thickness l_{ad} the absorption coefficient for IR radiation in the wavelength range $\lambda < 15$ μm remains practically unchanged.

As we have already mentioned, the derivation of Eq. (1) assumed that the dispersion law was parabolic for both electrons and holes. However, in InSb-type semiconductors the dispersion law for electrons and light holes is substantially different from a parabolic law. Specifically, in semiconductors with a Kane dispersion law the effective electron and light-hole masses depend on the energy $\mathscr{E}$ of the electrons and holes and doubles at $\mathscr{E}=E_g/2$ (Ref. 33). However, this fact cannot change the basic results, since by assumption in superstrong electric fields the condition (3) holds even for heavy holes, whose mass $m_{hh} \geqslant m_{lh}$, m_c for $\mathscr{E} \leqslant E_g$.

4. EFFECTIVE IR ABSORPTION IN THE SUPERLATTICE

We shall now formulate the requirements for the thicknesses l_d and l_a of the quasineutral layers. These requirements follow from the condition that the energy spectrum of electrons and heavy holes in the potential wells corresponding to these layers be quasicontinuous. As l_d and l_a decrease, the electron and hole energy levels are displaced from the corresponding wells and the red absorption limit of the superlattice shifts into a shorter-wavelength region. The energy spectrum of the electrons and holes in the potential wells can be regarded as quasicontinuous when the energy gap $\delta\mathscr{E}$ between the lowest energy level and the bottom of the corresponding potential well does not exceed $E_g - qV_b$ (the effective optical band gap in the superlattice). Since l_a, $l_d \geqslant l_{ad}$, we can assume that to a first approximation the potential wells of the superlattice are square wells. Then, assuming $\delta\mathscr{E} \leqslant E_g - qV_b$, we find that l_a and l_d must satisfy approximately the inequalities

$$l_d \geqslant \pi\hbar/\sqrt{2m_c(E_g - qV_b)}, \tag{5}$$

$$l_a \geqslant \pi\hbar/\sqrt{2m_{hh}(E_g - qV_b)}. \tag{6}$$

It is easy to show that for $\sigma = 5\times10^{12}$ cm^{-2} and $l_{ad} = 33$ Å in InSb with $E_g = 0.223$ eV these inequalities can be assumed to hold for $l_a \geqslant 42$ Å and $l_d \geqslant 233$ Å.

It is evident from Fig. 1 that in our structure the layers absorbing the long-wavelength radiation alternate with nonabsorbing *n*- and *p*-type layers. Therefore, the absorption averaged over a period of the superlattice is

$$\alpha_{\text{eff}} = 2\alpha l_{ad}/(l_a + l_d + 2l_{ad}), \tag{7}$$

where α is given by Eq. (2).

We showed above that in the superlattice considered by us the long-wavelength IR absorption is determined mainly by optical transitions from the heavy-hole band. This circumstance makes it possible to decrease substantially the thickness of the *p* region, which does not absorb long-wavelength radiation. This is why the inequality (6) is a quasicontinuity condition for the energy spectrum of heavy holes, while the energy spectrum of light holes in such a potential well may be quantized. Moreover, it follows from the inequalities (5) and (6) and the condition $m_{hh} \geqslant m_c$ that $l_d \geqslant l_a$; i.e., the thickness of the region that does not absorb long-wavelength radiation essentially equals l_d. Accordingly, we find from Eqs. (4) and (7) that the long-wavelength absorption coefficient averaged over a period of the superlattice is approximately

$$\alpha_{\text{eff}} = 3^{1/12}\Gamma^2(2/3)R\sqrt{\hbar\omega_E}(\hbar\omega - E_g + qV_b)/2\pi qEl_d. \tag{8}$$

We see from Eq. (8) that the effective IR absorption coefficient in the superlattice is much smaller than α. However, its value remains high in a wide range of wavelengths up to 50–100 μm (Fig. 3). This property is clearly an advantage of the above-proposed superlattice for use in photodetectors for IR spectrophotometers.

5. CONCLUSIONS

We note that the superlattice studied above will have long photocarrier lifetimes and superhigh photosensitivity up to the far-IR range. The photoelectrons and photoholes produced when IR radiation is absorbed in the regions between oppositely charged δ-doped layers will be pulled apart by the field into the potential wells of the *n*- and *p*-type layers, respectively, in a manner similar to the way this process occurs in classical doped superlattices.[22–25] As a result of their spatial separation, the lifetime of the photocarriers can be several orders of magnitude longer than the volume lifetime in *n*- and *p*-type semiconductors. Estimates show that the effective lifetime in the InSb-based superlattice can be of the order of 100 μs. The superlattice which we have studied therefore has a promising future for use as a photosensitive element in a focal IR array.

This superlattice also holds promise as a source of long-wavelength IR radiation, which is generated in it as a result of indirect (in real space) interband optical transitions, in which all δ-doped $p-n$ junctions forming the superlattice are biased in the forward direction.

The research described in this publication was made possible, in part, by Award No. RE1-287 of the US Civilian Research and Development Foundation for the Independent States of the former Soviet Union (CRDF).

[1] B. F. Levin, J. Appl. Phys. **74**, R1 (1993).
[2] R. People, J. C. Bean, C. G. Bathea, S. K. Sputz, and L. J. Peticolas, Appl. Phys. Lett. **61**, 1122 (1992).
[3] E. F. Schubert [Ed.], *Delta-Doping of Semiconductors*, Cambrige University Press, N. Y., 1996.
[4] G. H. Döhler, Phys. Status Solidi B **52**, 79 (1972).
[5] G. H. Döhler, Phys. Status Solidi B **52**, 553 (1972).
[6] D. G. Liu, J. C. Fan, C. P. Lee, K. H. Chang, and D. C. Liou, J. Appl. Phys. **73**, 608 (1993).
[7] A. I. Nikiforov, B. Z. Kanter, S. I. Stenin, and S. V. Rubanov, Poverkhnost': Fizika, Khimiya i Mekhanika, No. 10–11, 95 (1992).
[8] J. S. Park, R. P. G. Karunasiri, Y. J. Mii, and K. L. Wang, Appl. Phys. Lett. **58**, 1083 (1991).
[9] H. L. Vaghjiani, E. A. Johnson, M. E. Kane, R. Grey, and C. C. Phillips, J. Appl. Phys. **76**, 4407 (1994).
[10] E. F. Shubert, A. Fisher, and K. Ploog, Appl. Phys. Lett. **47**, 219 (1985).
[11] A. M. Glass, E. F. Shubert, B. A. Wilson, C. E. Bonner, J. E. Cunningham, D. H. Olson, and W. Jan, Appl. Phys. Lett. **54**, 2247 (1989).
[12] M. Toivonen, A. Salokatve, M. Hovinen, and M. Pessa, Electron. Lett. **28**, 32 (1992).
[13] Yang Wang and K. F. Brennan, SPIE **1982**, 133 (1993).
[14] C. C. Phillips, Appl. Phys. Lett. **56**, 151 (1990).
[15] J. Heremans, D. L. Partin, D. T. Morelly, C. M. Thrush, G. Karczewski, and J. K. Furdyna, J. Appl. Phys. **74**, 1793 (1993).
[16] M.-J. Yang, W. J. Moore, R. J. Wagner, J. R. Waterman, C. H. Yang, P.

E. Thompson, and J. L. Davis, J. Appl. Phys. **72**, 671 (1992).
[17] P. E. Thompson, J. L. Davis, M.-J. Yang, D. S. Simons, and P. H. Chi, J. Appl. Phys. **74**, 6686 (1993).
[18] V. V. Osipov, F. L. Serzhenko, and V. D. Shadrin, Fiz. Tekh. Poluprovodn. **23**, 809 (1989) [Sov. Phys. Semicond. **23**, 509 (1989)].
[19] K. C. Hass and D. J. Kirill, J. Appl. Phys. **68**, 1923 (1990).
[20] F. L. Serzhenko and V. D. Shadrin, Fiz. Tekh. Poluprovodn. **25**, 1579 (1991) [Sov. Phys. Semicond. **25**, 953 (1991)].
[21] F. L. Serzhenko and V. D. Shadrin, Fiz. Tekh. Poluprovodn. **26**, 491 (1992) [Sov. Phys. Semicond. **26**, 277 (1992)].
[22] L. N. Neustroev, V. V. Osipov, and V. A. Kholodnov, Fiz. Tekh. Poluprovodn. **14**, 939 (1980) [Sov. Phys. Semicond. **14**, 553 (1980)].
[23] L. N. Neustroev and V. V. Osipov;, Fiz. Tekh. Poluprovodn. **14**, 1186 (1980) [Sov. Phys. Semicond. **14**, 701 (1980)].
[24] L. N. Neustroev and V. V. Osipov, Mikroelektronika **9**, 99 (1980).
[25] L. N. Neustroev and V. V. Osipov, Fiz. Tekh. Poluprovodn. **15**, 1068 (1981) [Sov. Phys. Semicond. **15**, 615 (1981)].
[26] C. Martijn de Sterke, J. Appl. Phys. **64**, 3187 (1988).
[27] P. P. Ruden, C. A. Marttila, T. Werner, and J. E. Carroll, J. Appl. Phys. **66**, 956 (1989).
[28] J. Maserjian, F. J. Grunthaner, and C. T. Elliott, Infrared Phys. **30**, 27 (1990).
[29] W. Franz, Zs. Naturforsch **13a**, 484 (1958).
[30] L. V. Keldysh, Zh. Éksp. Teor. Fiz. **34**, 1138 (1958) [Sov. Phys. JETP **7**, 788 (1958)].
[31] J. Callaway, Phys. Rev. **130**, 549 (1963).
[32] K. Tharmalingam, Phys. Rev. **130**, 2204 (1963).
[33] A. I. Ansel'm, *Introduction to Semiconductor Theory*, Prentice-Hall, Englewood Cliffs, N. J., 1981 [Russian original, Nauka, Moscow, 1978].
[34] R. K. Willardson and A. C. Beer [Eds.], *Optical Properties of Semiconductors* [Russian translation, Mir, Moscow, 1970].

Translated by M. E. Alferieff

Lateral traveling wave as a type of transient process in a resonant-tunneling structure

D. V. Mel'nikov*) and A. I. Podlivaev

Moscow State Engineering–Physics Institute (Technical University)
(Submitted July 15, 1996; accepted for publication July 30, 1997)
Fiz. Tekh. Poluprovodn. **32**, 227–234 (February 1998)

The temporal evolution of an initially laterally nonuniform state of resonant-tunneling structure is investigated. It is shown that a transition of the electronic system from one stable state into another is possible in the region of vertical voltages at which a hysteresis loop is observed in the current-voltage characteristic of the structure. In this case the transient process is realized in the form of a traveling wave, where one stable phase is absorbed by another. The velocity of this wave is determined. It is shown that there exists a voltage at which the velocity equals zero and stable coexistence of two phases is possible. © *1998 American Institute of Physics.* [S1063-7826(98)02102-4]

1. INTRODUCTION

Since resonant-tunneling structures (RTSs) were first proposed[1] and obtained experimentally[2,3] they have been under constant investigation by theorists and experimentalists, first, because of their wide potential technical applications and, second, because of the physical effects that appear. In connection with the possible application of RTSs as logic elements in digital computers, the question of the internal bistability in such devices is of great interest.[4–6] This effect, which is associated with electron accumulation in the region between the potential barriers, leads to a current-voltage characteristic (IVC) with a hysteresis loop. The general form of such an IVC is shown in Fig. 1, where the high values of the current in the state A are due to the high electron density in the interbarrier region of the RTS. In the other stable state of the system — state B, there are no electrons in the region between the barriers.

In the present paper the dynamical characteristics of RTSs with a transition from state A into state B (or the opposite transition) are determined in the case where the RTS is initially in a nonuniform state in the lateral direction: Part of the structure is in the state A and part is in the state B. The vertical voltage U in this case is assumed to be constant in the entire device and remains constant in time.

In principle, such a state can be realized, for example, as follows. The voltage on the heterostructure is usually determined by the potential difference between the substrate and the clamping contact.[7] Let us assume that two clamping contacts, instead one over, is present on the structure (Fig. 2). If a potential difference is briefly produced on the contacts so that the vertical voltage in the region of the first contact is less than the voltage U_1 at which the hysteresis region starts (see Fig. 1) and the voltage in the region of the second contact is higher than U_2 of the right-hand limit of hysteresis, then the heterostructure in the region of the first contact will be in the state A and the heterostructure in the region of the second contact will be in the state B. If the voltage on both contacts then changes to a certain value U ($U_1<U<U_2$), then we obtain a situation where the two phases, A and B, coexist in the presence of a constant vertical voltage U on the structure. Such a state can be regarded as an initial, laterally nonuniform state of the system. A more detailed investigation of the conditions under which the two phases A and B arise simultaneously in a real structure falls outside the scope of the present paper and can be a subject of a separate investigation.

The structure of this paper is as follows. In Sec. 2 a description of the model is given and the approximations under which the problem is solved are indicated. An equation describing the propagation of a lateral wave of electron density in the region between the barriers is presented. In Sec. 3 a solution of the problem is presented in the high-temperature limit and in Sec. 4 the problem is solved in the low-temperature limit. Because of their complexity, some of the terms in the basic equation are determined in the Appendix.

2. DESCRIPTION OF THE MODEL

At present, the electron density in two-dimensional systems (including also in a lateral direction in quantum wells) is now often determined on the basis of classical models.[8,9] In Ref. 8, collective excitations of a two-dimensional electronic system with quantum antidots were investigated on the basis of classical electrodynamics neglecting nonlocal effects and retardation. In Ref. 9 the flow of electrons between two adjacent quantum wells and the associated change in the lateral current in each well were likewise investigated in a classical theory. In the present paper the lateral flux density will likewise be described in a classical (diffusion-drift) approximation, and the electron flow in the vertical direction will be determined from the Schrödinger equation.

The resonant-tunneling structure consists of five layers: an emitter, an emitter barrier, a quantum well, a collector barrier, and a collector (Fig. 3). We assume that the electron distribution does not depend on the spatial variable Z. The variables X and Y are denoted below as the vertical and lateral coordinates, respectively.

To determine the structural parameters that most strongly influence the transient process in a RTS and to simplify the solution of the problem, we replace the real potential well of the conduction-band bottom by the model well shown in Fig. 4. In so doing, the following approximations are made.

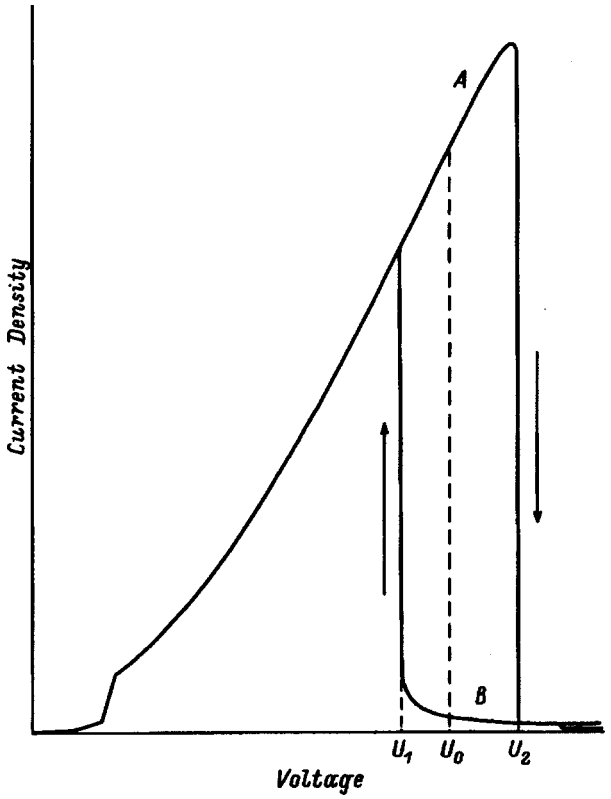

FIG. 1. Current-voltage characteristic of a resonant-tunneling structure. U_0 — voltage of stationary coexistence of phases A and B; U_1, U_2 — limits of the hysteresis region.

1. The real potential barriers, which have a finite width a and height U_b, in the RTS are replaced by barriers in the form of δ-functions. The integral of the barriers over the vertical variable X is $S=U_b a$, which adequately describes the case of high and narrow barriers.[10] A similar substitution is valid in the case where the energy E and wave number k of the electrons satisfy the conditions $E \ll U_b$ and $ka \gg 1$.

2. The potential is assumed to be constant in the region of the contacts I and III (see Fig. 3).

3. It is assumed that the potential in the region II between the barriers does not depend on the coordinate X and is determined by the external applied voltage U and the self-consistent Coulomb potential of the electrons in this region.

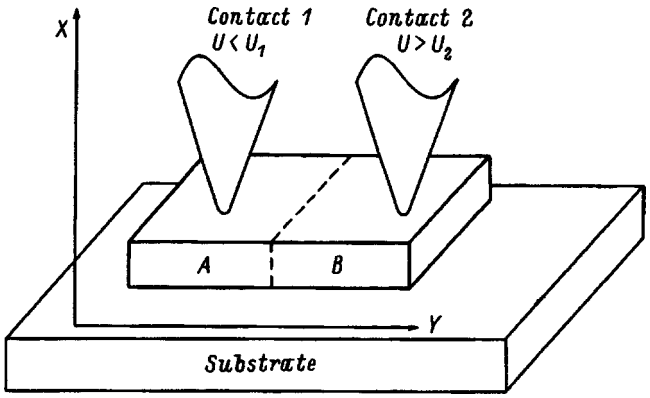

FIG. 2. Fragment of the substrate with the resonant-tunneling structure.

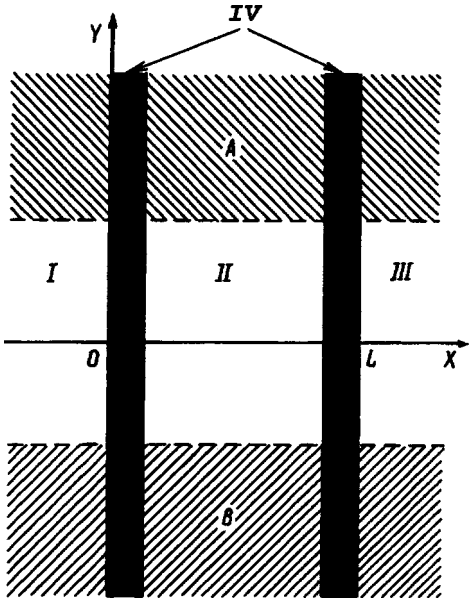

FIG. 3. Resonant-tunneling structure: I — emitter, II — interbarrier region, III — collector, IV — potential barriers. The regions in which the electron distribution is uniform in the Y direction are hatched; the region with no hatching is the transitional region.

4. The area S of the barriers is large enough so that the electron flow in X direction passes only through a narrow quasiresonance level. For this reason the characteristic lengths of the front of the transient process in the lateral

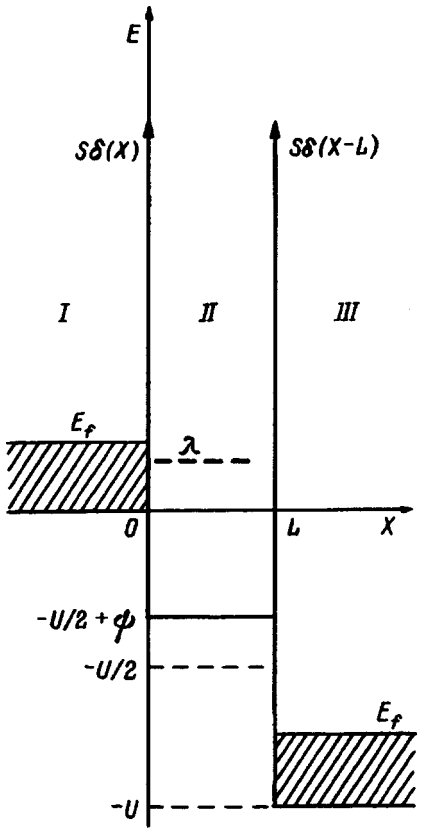

FIG. 4. Potential well of the conduction band bottom of the RTS: λ — position of the quasiresonance level, E_f — electron Fermi level in the emitter, U — applied voltage, L — width of the interbarrier region.

direction Y between regions with phases A and B (see Fig. 3) are much larger than the electron mean free path in this direction.

If the length of the front of the transient process in the Y direction is sufficiently long, the electron density can be described in the diffusion approximation

$$D\frac{\partial^2 P}{\partial Y^2}+\frac{D}{T}\frac{\partial}{\partial Y}\left(P\frac{\partial \phi}{\partial Y}\right)+F(P)=\frac{\partial P}{\partial t}, \tag{1}$$

where $P(Y,t)$ is the electron density in the well, D is the diffusion in the Y direction, t is the time, T is the temperature, $F(P)$ is the intensity of the electron flow through the barrier into the well in the X direction, and $\phi(Y)$ is the potential well of the conduction band bottom in the region of the well.

The possibility of describing the change in the electron density in the lateral direction by the diffusion equation (1) arises in the case where the electron mean free path is much shorter than the characteristic distance over which the electron density varies in this direction. The characteristic value of the electron mean free path in GaAs can be estimated from the characteristic electron velocity and relaxation time ($\tau \simeq 10^{-13}$ s; see Ref. 11) and is of the order of 100 nm for the structural parameters chosen in this paper.

In the case where the interbarrier distance L is much greater than the electron mean free path, the function F will have the form of a second derivative with respect to the variable X (transition from ballistic to diffusion regime, described, for example, in Ref. 11) and Eq. (1) will take the form of the classical two-dimensional diffusion equation. In the case at hand we have the opposite situation, and the electron flux through the barrier is described by a quantum problem if the variation of the electron density in the lateral direction is slow enough. The electron density dependence of F and ϕ in the interbarrier region is determined in the Appendix.

We seek the solution $P(Y,t)$ in the form of a traveling wave $P(Y,t)=p(\xi)$, $\xi=Y/D^{1/2}-Vt$. Using Eq. (A4) (see Appendix), we can then write Eq. (1) in the form

$$\frac{\partial^2 p}{\partial \xi^2}+\frac{\alpha}{T}\frac{\partial}{\partial \xi}\left(p\frac{\partial p}{\partial \xi}\right)-V\frac{\partial p}{\partial \xi}+F(p)=0. \tag{2}$$

We supplement Eq. (2) with the boundary conditions

$$p|_{\xi=-\infty}=p_1, \quad p|_{\xi=+\infty}=p_2, \tag{3}$$

where p_1 and p_2 are stable, stationary, homogeneous solutions of Eq. (2) [$F(p_1)$, $F(p_2)=0$]. We note that according to Eq. (A5) $p_1=0$.

Nonlinear problems of the type (2) and (3) are well known in physics. They describe the propagation of nonequilibrium superconducting phases, growth of magnetic domains, combustion waves, and so on (see, for example, Refs. 12–15). The system (2) and (3) determines the translation-invariant solution $p(\xi)$ and the velocity V.

We chose for study a heterostructure with the following parameters: Fermi energy $E_f=0.1$ eV, width of the interbarrier region $L=10$ nm, barrier area $S=2$ nm·eV, barrier height $U_b=0.4$ eV, and effective mass $m^*=0.07m_e$. Such parameters can be realized with a $GaAs/Al_xGa_{1-x}As$ structure.

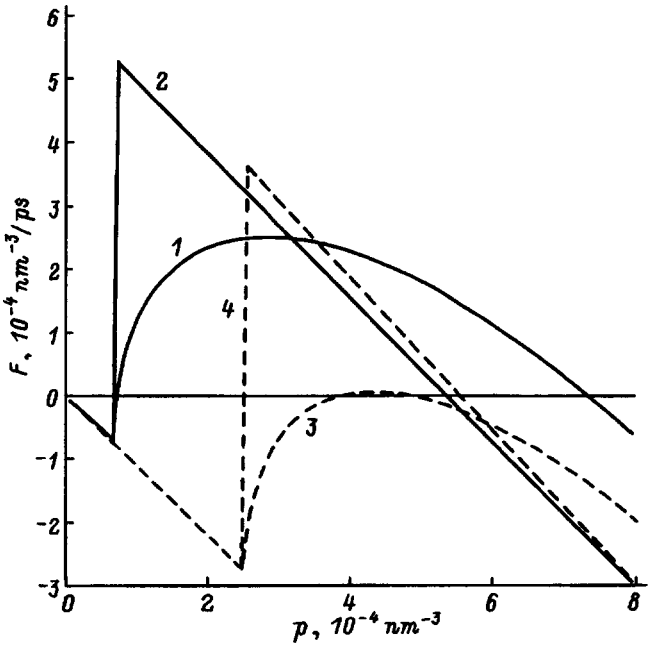

FIG. 5. F versus electron density in region II: *1* — Exact function F with voltage $U=0.11$ eV; *2* — piecewise-linear approximation of the function F with voltage $U=0.11$ eV; *3* — exact function F with voltage $U=0.1167$ eV; *4* — piecewise-linear approximation of the function with voltage $U=0.1167$ eV.

3. HIGH-TEMPERATURE LIMIT

Let us consider a temperature T such that $\alpha p_2/T \ll 1$, where α is determined in the Appendix. In this case the second term in Eq. (2) can be neglected. The equation transformed in this manner can be solved analytically for a special form of the function $F(p)$. We replace the function $F(p)$, determined by the expression (A5), by a piecewise-linear form (see Appendix)

$$F(p)=\begin{cases} -ap, & 0\leqslant p<(U/2-E_r)/\alpha, \\ a[b(E_f-E_r+U/2 & \\ -\alpha p)-p], & (U/2-E_r)/\alpha<p, \end{cases} \tag{4}$$

where

$$a=\frac{\Gamma(p=0)}{\hbar}, \quad b=\frac{\sqrt{E_r}}{\pi^2}\Xi\left(\frac{2m^*}{\hbar^2}\right)^{3/2}.$$

Such a substitution is often used to describe nonlinear waves (see, for example, Ref. 13). We shall now assess the admissability of this approximation in our case. The function $F(p)$, which corresponds to the expression (A5), and the corresponding quantity, which is determined by the expression (4) for two values of the voltage U, are shown in Fig. 5.

The expression (4) makes it possible to solve analytically the problem (2) and (3) in the high-temperature limit. This solution is

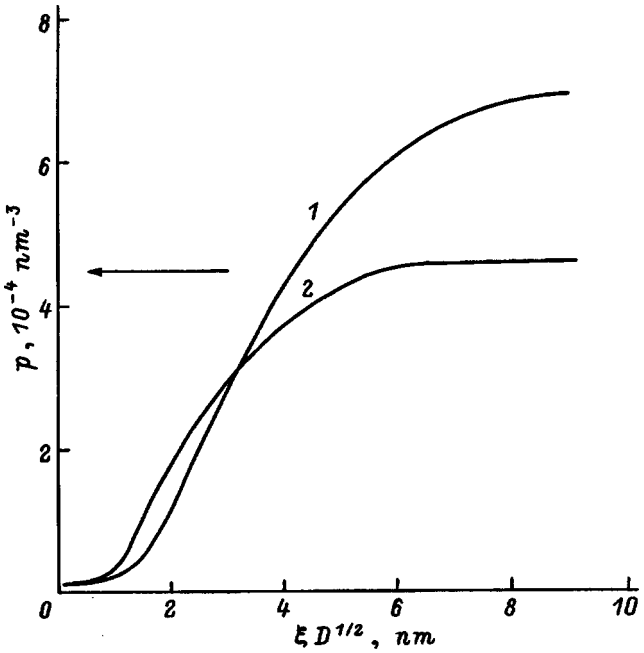

FIG. 6. Structure of the wave front with voltage $U=0.11$ eV: *1* — corresponds to the structure of the wave front with the exact function F; *2* — piecewise-linear approximation of the function F. The arrow indicates the direction of wave propagation.

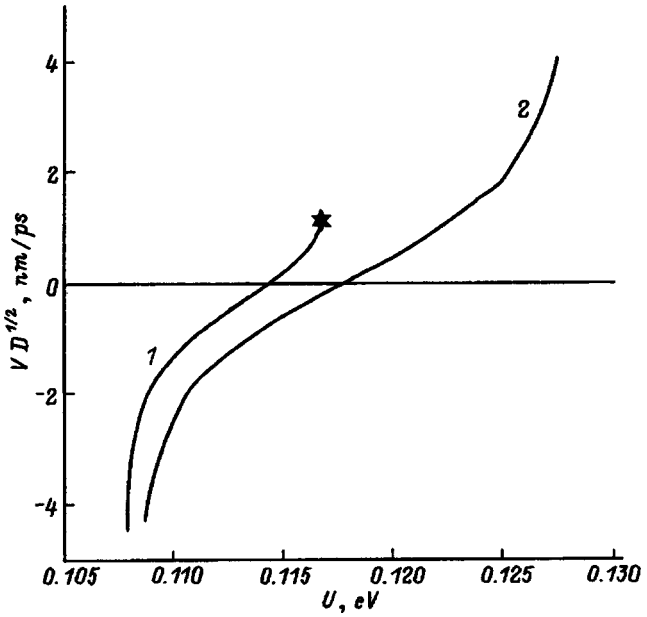

FIG. 7. Wave velocity versus voltage U: *1* — corresponds to the exact function F, *2* — piecewise-linear approximation of the function F.

$$p=\begin{cases}\chi\ \exp\left[\dfrac{-V+\sqrt{V^2+4a}}{2}\xi\right], & \xi\leqslant 0,\\ \zeta+(\chi-\zeta)\exp\left[\dfrac{-V-\sqrt{V^2+4a(1+\alpha b)}}{2}\xi\right], & \xi>0,\end{cases} \tag{5}$$

where

$$\chi=\frac{U/2-E_r}{\alpha},\quad \zeta=\frac{b(E_f-E_r+U/2)}{1+\alpha b}.$$

The velocity V is determined from the condition that the function $p(\xi)$ be continuous at the matching point $\xi=0$:

$$\chi\left[\frac{-V+\sqrt{V^2+4a}}{2}\right]=(\chi-\zeta)\left[\frac{-V-\sqrt{V^2+4a(1+\alpha b)}}{2}\right]. \tag{6}$$

Since the solution (5) and (6) is monotonic and bounded, it can be proved that it is stable against small perturbations. Figure 6 shows the structure obtained for the wave front from the Eq. (5) with $U=0.115$ eV, and the analogous dependence corresponding to the expression (A5) (curve *2*). We see that these curves are qualitatively the same.

The limits of the voltage range where hysteresis of the I–V characteristic occurs [the three zeros of the function $F(p)$] are as follows: $U_1<U<U_2$, $U_1=2E_r$, $U_2=2E_r+2\alpha bE_f$ (see Fig. 1). We shall investigate the behavior of the velocity V as a function of U in this interval. It is easy to show from the expression (6) that inside this interval there exists a voltage U_0 at which the propagation velocity of the wave equals zero. The quantity U_0 is determined by the expression

$$\frac{U_0}{2}=E_r+\frac{\alpha bE_f}{\sqrt{1+\alpha b}+1}.$$

In this case the RTS is in a position of neutral equilibrium and there is no transient process. With a departure from the value U_0, the velocity V becomes zero. For $U>U_0$ the velocity is positive and the state with a small number of electrons in the well propagates through the entire sample. For $U<U_0$ the velocity is negative and the sample switches into a state characterized by the point A in Fig. 1 (the electron density in the well equals p_2). The voltage dependence of the velocity of the wave is given in Fig. 7: The curve *1* is determined by solving Eq. (6) and the curve *2* is obtained by solving numerically the problem (*2*) and (*3*) with the function $F(p)$ determined by Eq. (A5).

It is easy to see from the expression (*6*) that the velocity of the wave becomes infinite at the limits of the voltage range where hysteresis exists ($U=U_1$ and $U=U_2$). It follows from Eq. (5) that the length of the front also diverges, but the transit time of the wave front, equal to the ratio of these quantities, remains constant and is of the order of the escape time of excess electrons from the well (the reciprocal of the width of a quasiresonance level). The divergence of the velocity at the limits of the hysteresis region is due to a singularity of the function $F(p)$. Indeed, in the case where the function $F(p)$ is continuous [see Ref. 16 , where the function $F(p)$ is given by a cubic polynomial[1)]], the velocity of the wave is bounded inside the entire region of hysteresis.

At voltages near the left-hand limit of hysteresis $U\simeq U_1$ the square-root singularity of the exact function $F(p)$ is described well by the discontinuity of the approximate function (lines *1* and *2* in Fig. 5). Conversely, at voltages near the upper limit of hysteresis $U\simeq U_2$ a qualitatively different character of the convergence of the zeros p_2 and p_3 of the exact and approximate function $F(p)$ toward one another is

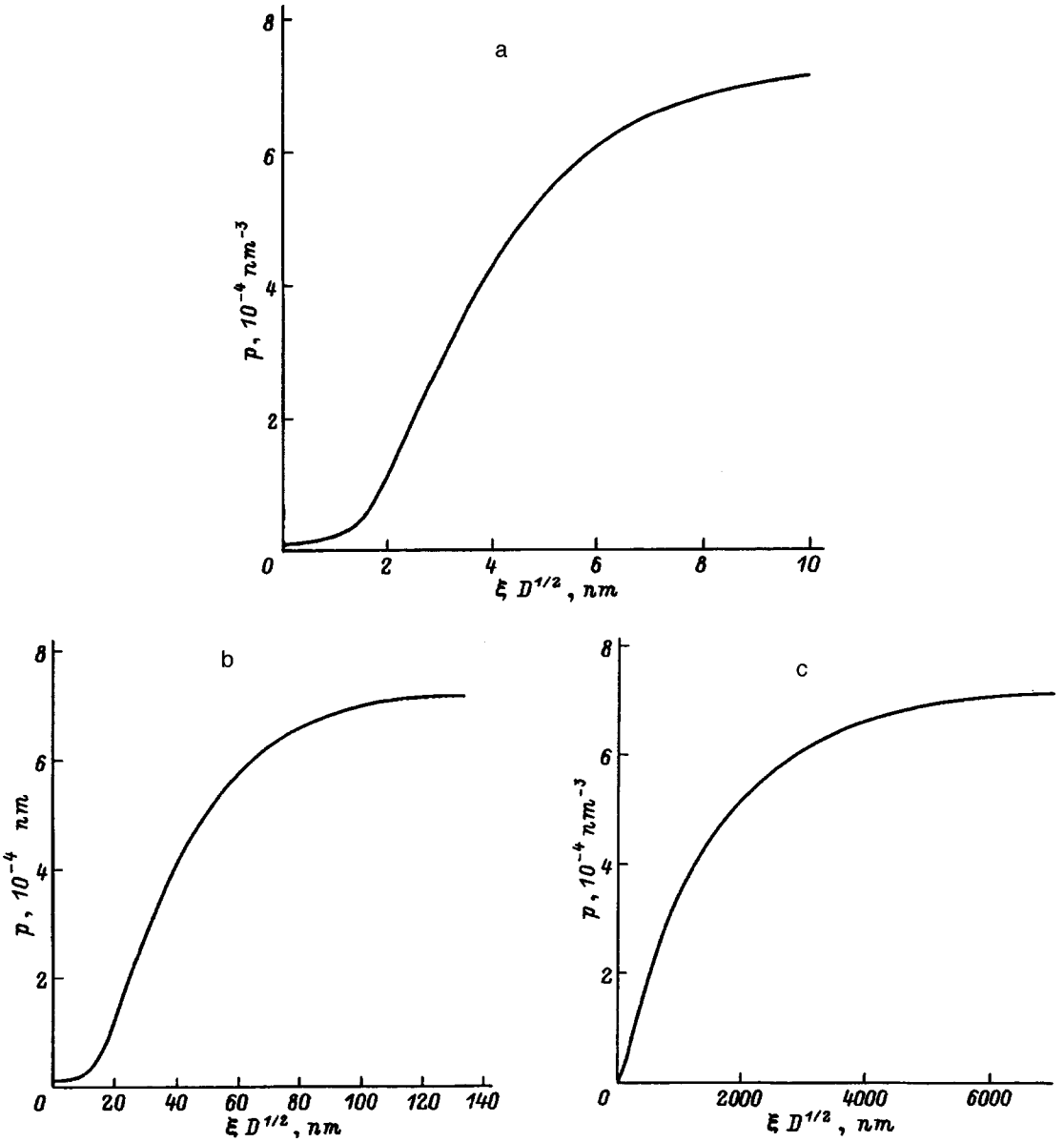

FIG. 8. Structure of the wave front with external voltage $U=0.11$ eV and various temperatures. T, K: a — 10 000, b — 100, c — 1.

observed (lines *3* and *4* in Fig. 5). The velocity of the wave as a function of voltage U behaves correspondingly. Near the lower limit of hysteresis the velocity determined according to both the exact and approximate functions $F(p)$diverges (see Fig. 8). Near the upper limit of hysteresis the behavior of the exactly and approximately determined velocity is fundamentally different — the exactly determined velocity is bounded and the approximate velocity diverges.

It can be concluded from these results that the piecewise-linear approximation, which is convenient for analytical investigation, of the function $F(p)$ adequately describes this process only in the region of negative velocities.

4. LOW-TEMPERATURE LIMIT

For $\alpha p_2/T \gg 1$ Eq. (2) becomes

$$\frac{\alpha}{T}\frac{\partial}{\partial\xi}\left(p\frac{\partial p}{\partial\xi}\right)-V\frac{\partial p}{\partial\xi}+F(p)=0. \tag{7}$$

An equation with a similar structure describes a wave of combustion in a material with a nonlinear thermal conductivity.[14]

The numerical solution of the problem (7) and (3) is shown in Fig. 8a. A fundamental distinguishing feature of this solution is the kink on the leading edge of the wave front and the absence of even a small perturbation of the electronic system in front of the wave front of the traveling wave. The formation of a kink on the wave front upon transition to the low-temperature limit is shown in Figs. 8b and 8c by curves obtained by solving the general problem (2) and (3) numerically. It is evident from the curves presented that, as a result of the decrease in the electron mobility, the perturbation of the electronic system ahead of the wave front becomes vanishingly small as the temperature decreases.

It should also be noted that such a kink is observed for both positive and negative velocities: In the first case the system passes into a nonstationary state from an unperturbed

state and in the second case it goes in a finite time to an equilibrium state without the characteristic exponential (in time) relaxation observed with an electron distribution that is uniform in the Y direction.[17]

We thank V. F. Elesin for critical remarks made during a discussion of this work.

This work was performed as part of the program ''Physics of solid-state nanostructures'' of the Ministry of Science and Technology Policy of the Russian Federation, project N 1-092/4, as well as with the support of Russian Fund for Fundamental Research (N 96-02-17363-a) and the State Committee on Institutions of Higher Education in the Russian Federation in the direction ''Molecular electronics and nanoelectronics'' (Project 3-43).

5. APPENDIX

A stationary electron density distribution P, which is uniform in the Y direction, in the potential well shown in Fig. 4 is determined from the electron wave functions $\psi(X)$, which are described by the Schrödinger equation

$$\left[-\frac{\hbar^2}{2m^*}\frac{d^2}{dX^2}+V_0(X)\right]\psi_k(X)=E\psi_k(X) \tag{A1}$$

and the corresponding boundary conditions[17]

$$\left[\psi_k+\frac{1}{ik}\frac{d\psi_k}{dX}\right]\Bigg|_{X=-0}=2A, \quad \left[\psi_k-\frac{1}{ik}\frac{d\psi_k}{dX}\right]_{X=L+0}=0,$$

where

$$k=\sqrt{\frac{2m^*E}{\hbar^2}}, \quad k_0=\sqrt{\frac{2m^*E(E+U)}{\hbar^2}},$$

$$A=\sqrt{\frac{m^*T}{\pi\hbar^2}\ln\left[1+\exp\left(\frac{E_f-E}{T}\right)\right]}$$

is the amplitude of the electron flux from the emitter, m^* is the electron effective mass (assumed to be constant over the structure), E is the electron energy, and $V_0(X)$ is the potential well of the conduction band bottom, altered by an external applied voltage U and the self-consistent Coulomb potential ϕ (see Fig. 4),

$$V_0(X)=\begin{cases} S\delta(X), & X\leqslant 0,\\ -U/2+\phi, & 0<X<L,\\ -U+S_1\delta(X-L), & L\leqslant X,\end{cases}$$

where $S_1=S(1-U/U_b)$. The term in parentheses determines the effective change produced in the collector barrier by the applied electric field.[18]

The electron density $P(X)$ in the structure is determined from the electron wave functions by the expression

$$P(X)=\int_{-\infty}^{+\infty}|\psi_k(X)|^2dk. \tag{A2}$$

After the electron wave function ψ_k is determined from the Schrödinger equation (A1) and substituted into the expression (A2) in the limit of high barriers and at a temperature much lower than the Fermi energy E_f the electron density at the center of the well can be determined according to the formula

$$P_s=P(L/2)=\frac{\sqrt{E_r}}{\pi^2}\left(\frac{2m^*}{\hbar^2}\right)^{3/2}\frac{\Gamma_l}{\Gamma}(E_f-\lambda)\Theta(\lambda)\Theta(E_f-\lambda),$$

where $E_r=\hbar^2\pi^2/2m^*L^2$ is the position of the quasiresonance level relative to the conduction band bottom in region II, $\Gamma(p)=\Gamma_l+\Gamma_r$ is the width of the quasiresonance level

$$\Gamma_l=E_r^{3/2}\frac{\hbar^2}{\pi m^*S^2}\sqrt{\lambda}\Theta(\lambda),$$

$$\Gamma_r=E_r^{3/2}\frac{\hbar^2\sqrt{\lambda+U}}{\pi m^*S^2(1-U/U_b)^2}\Theta(\lambda+U),$$

the quantity S is the product of the height U_b and width of the barrier, $\lambda=E_r-U/2+\phi$, and $\Theta(\lambda)$ is the Heaviside unit step function. In calculating this quantity it was assumed that the barriers are quite high (see approximation 1 in Sec. 2), the quantity $|\psi_k(L/2)|^2$ as a function of energy near E_r has one Lorentzian peak, and the vertical voltage U is high enough so that the quasiresonance level lies above the electron Fermi energy in the collector, and the fact that the electron density in the interbarrier region is produced only by the particles incident on the structure from the emitter (see Fig. 3) was also taken into account.

The relation between the self-consistent electron potential ϕ and the electron density in the interbarrier region is determined by the Poisson equation

$$\frac{\partial^2\phi}{\partial X^2}+\frac{\partial^2\phi}{\partial Y^2}=-\frac{4\pi e^2p}{\varepsilon}, \tag{A3}$$

where e is the electron charge, and ε is the permittivity of the medium. The second term on the left-hand side of this formula can be ignored, since the characteristic distance over which the potential changes in the lateral direction is much greater than the vertical size of the system — the interbarrier distance (see approximation 4 in Sec. 2).

As a result of the strong screening effects (see approximation 2), outside the region II the potential ϕ of the uncompensated charge is assumed to be zero, which determines the form of the boundary conditions:

$$\phi|_{X=0}=\phi|_{X=L}=0.$$

The quantity ϕ determined by Eq. (A3) depends on the variable X, but in the approximations used in the model (see approximation 3) we replace it by the following effective constant quantity:

$$\phi=\alpha p, \quad \alpha=\frac{4\pi e^2}{\varepsilon}\frac{\hbar^2}{2m^*E_r}. \tag{A4}$$

By analogy with Ref. 4 , we assume that the flux $F(p)$ of excess electrons out of the region of the well is proportional

to the width Γ of the quasiresonance level and the deviation of the density of these particles from the equilibrium value P_s:

$$F(p)=-\frac{\Gamma(p)}{\hbar}[p-P_s(p)]. \tag{A5}$$

Just as in Ref. 4, the function $F(p)$ has one zero outside the region of hysteresis and three zeros inside the region of hysteresis. The small difference between the expression (A5) and the similar expression in Ref. 4 stems from the fact that we have taken into account the dependence of the transmittance on the energy of the incident particles.

To study the behavior of the electron density analytically it is convenient to replace the continuous function $F(p)$ by a piecewise-linear approximation, assuming that the width of the quasiresonance level does not depend on the energy E of the incident electrons [the function $F(p)$ acquires then a form similar to that in Ref. 5]:

$$\begin{aligned} F(p)&=-\frac{\Gamma(p=0)}{\hbar}[p-P_{1s}(p)],\\ P_{1s}&=\frac{\sqrt{E_r}}{\pi^2}\left(\frac{2m^*}{\hbar^2}\right)^{3/2}(E_f-\lambda)\Xi\Theta(\lambda)\Theta(E_f-\lambda), \end{aligned} \tag{A6}$$

where $\Xi=\Gamma_l/\Gamma$. We assumed that $\Xi=0.1$ (this value gives the best agreement between the exact and approximate solutions of the problem).

We note, however, the large discrepancy between the results of Ref. 5 and our work in the part that determines the temporal stability of the homogeneous stationary solutions described by the condition $F(p)=0$. In our work, just as in Ref. 12, two of the three solutions are stable and the third (intermediate) solution is unstable. This follows from the nonstationary equation (1), which is homogeneous in the lateral direction. In contrast to this result, in Ref. 5 it is asserted that two of the three solutions are unstable. The discrepancy stems from the fact that in Ref. 5 the temporal evolution of the system is simulated by an iteration process, which gives results which are different from Eq. (1).

*)E-mail: mel@supercon.mephi.ru

1)In Ref. 16 the function $F(p)$ is defined so that its norm diverges near the limits of hysteresis. To compare the velocities the equation in Ref. 16 that is analogous to Eq. (2) must first be renormalized.

[1] R. Tsu and L. Esaki, Appl. Phys. Lett. **22**, 562 (1973).
[2] L. L. Chang, L. Esaki, and R. Tsu, Appl. Phys. Lett. **24**, 593 (1974).
[3] T. C. L. G. Sollner, W. D. Goodhue, R. E. Tannerwald, C. D. Parker, and D. D. Peck, Appl. Phys. Lett. **43**, 588 (1983).
[4] F. W. Sheard and G. A. Toombs, Appl. Phys. Lett. **52**, 1228 (1988).
[5] Jun Zang and J. L. Birman, Phys. Rev. B **46**, 5020 (1992).
[6] K. L. Jensen and F. A. Buot, Phys. Rev. Lett. **66**, 1078 (1991).
[7] H. C. Liu and T. C. L. G. Sollner, in *Semiconductors and Semimetals*, 1994, Vol. 41, p. 359.
[8] S. A. Mikhailov and V. A. Volkov, Phys. Rev. B **52**, 17260 (1995).
[9] V. F. Elesin, O. A. Vinokurov, V. E. Kondrashov, A. I. Podlivaev, and B. N. Shamraev, Fiz. Tekh. Poluprovodn. **29**, 83 (1995) [*sic*].
[10] V. M. Galitskiĭ, B. M. Karnakov, and V. I. Kogan, *Problems in Quantum Mechanics* [in Russian], Nauka, Moscow, 1981.
[11] A. Haque and A. N. Khondker, Phys. Rev. B **52**, 11193 (1995).
[12] V. F. Elesin and Yu. V. Kopaev, Usp. Fiz. Nauk **133**, 259 (1981) [Sov. Phys. Usp. **24**, 116 (1981).
[13] A. Vl. Gurevich and R. G. Mints, Usp. Fiz. Nauk **142**, 61 (1984) Sov. Phys. Usp. **27**, 19 (1984).
[14] Ya. B. Zel'dovich, V. B. Librovich, G. I. Barenblatt, and G. M. Makhviladze, *Mathematical Theory of Combustion and Explosions* [in Russian], Nauka, Moscow, 1974.
[15] M. C. Gross and P. C. Hohenberg, Rev. Mod. Phys. **65**, 851 (1993).
[16] E. Ben-Jacob *et al.*, Physica D **14**, 398 (1985).
[17] W. R. Frensley, Rev. Mod. Phys. **62**, 745 (1990).
[18] E. I. Golant and A. B. Pashkovskiĭ, Fiz. Tekh. Poluprovodn. **28**, 954 (1994) [Semicond. **28**, 553 (1994)].

Translated by M. E. Alferieff

The structure of porous gallium phosphide

T. N. Zavaritskaya, A. V. Kvit, and N. N. Mel'nik

P. N. Lebedev Physical Institute, Russian Academy of Sciences, 117924 Moscow, Russia

V. A. Karavanskiĭ

Institute of General Physics, Russian Academy of Sciences, 117924 Moscow, Russia
(Submitted September 24 1996; accepted for publication January 22, 1997)
Fiz. Tekh. Poluprovodn. **32**, 235–240 (February 1998)

Free films of porous GaP have been obtained for the first time and their microstructure has been investigated by transmission electron microscopy (TEM) and Raman scattering (RS). The TEM results showed that the microstructure of the porous-GaP films has a complicated spatial structure, but the local crystallographic orientation is preserved and corresponds to the initial substrate. Narrowing of the half-width and a simultaneous low-frequency shift of the *LO*-phonon peak were observed in the RS spectrum. This behavior can be satisfactorily explained in terms of the change in the plasmon–phonon interaction as a result of a decrease in the carrier density. A shift in the frequency of surface phonons of porous GaP as a function of the local void formation conditions was also observed. It is shown that in principle porous layers can be obtained without the void surfaces being covered appreciably with oxides or other products of an electrochemical reaction.
[S1063-7826(98)02202-9]

In addition to porous Si, investigators have been attracted in the last few years to other porous semiconductors.[1] The possibility of using single-crystal substrates with known properties, the relative simplicity of the fabrication technology, and the unusual (for the initial material) properties of porous layers have sparked numerous investigations, especially of porous Si. However, the example of porous silicon also showed that an unambiguous interpretation of the properties of nanodispersed semiconductors requires a detailed investigation of the structure of the frame which remains after etching, of the initial bulk material, and the state of the surface, including the composition and structure of the adsorbates.[1–3] The properties of porous GaP are interesting in that the initial material, just as in the case of Si, is an indirect-gap material and the band structure is similar to that in Si, which makes it possible to use a general approach in the interpretation of the intense photoluminescence (PL) characteristic of porous semiconductors. At the same time, GaP is an inert material, oxidizes in air only slightly, and virtually does not interact with acids. Therefore, it should be expected that the porous layers based on it will be more stable and less subject to the action of the surrounding medium than porous Si. Porous GaP and the processes leading to its formation are likewise of interest in themselves from the standpoint of materials engineering and electrochemical processes occurring on the surfaces of III–V compounds.

It was shown in previous studies[4,5] that the application of the electrolyte HF(49%):C_2H_5OH in a 1:1 proportion (which is used for producing porous Si) for GaP gives a positive result in the sense of the possibility of obtaining a porous layer, whose luminescence properties differ substantially from the properties of the initial substrate. However, additional study of the electrochemical processes on III–V compounds showed[6] that a HF-based electrolyte is suboptimal, since it is possible that insoluble reaction products (metal fluorides), which likewise could contribute to the photoluminescence, will form on the void surfaces.

In the present paper we report the results of transmission electron microscopy (TEM) and Raman scattering (RS) studies of the structure of layers of porous GaP, which was obtained by electrochemical etching in an orthophosphoric-acid-based electrolyte. It is shown that free films of porous GaP can be obtained when orthophosphoric acid is used. Narrowing of the *LO*-phonon peak, together with a simultaneous low-frequency shift of this peak, was observed in the Raman scattering spectra from porous GaP. This behavior is satisfactorily explained by the change in the plasmon–phonon interaction and agrees with the proposed mechanism of electrochemical etching. A shift of the vibrational frequency of the surface mode as a function of the local conditions of void formation was also observed.

1. SAMPLE PREPARATION AND EXPERIMENTAL TECHNIQUE

We chose orthophosphoric acid as the basis for the electrolyte. In Ref. 7 it is pointed out that orthophosphoric acid can be used as a chemical etchant for revealing the structure of defects without the formation of insoluble deposits. Although initiation of a reaction requires temperatures above 450 °C, we assumed that application of an electric field will lower this temperature to room temperature. To improve the solubility of the reaction products, acetic acid was added (as a complexing agent). A solution of orthophosphic acid, acetic acid, and ethyl alcohol in the volume ratio 1:1:2 and a

fixed current density regime were used. The process was conducted in a two-chamber electrochemical fluoroplastic cell with a working anodization surface area of 1 cm^2 and platinum electrodes. The current density 2–10 mA/cm^2 was chosen. Mirror-smooth porous layers of GaP were obtained on *n*-GaP crystalline substrates (doped with Te to density of the order of 3×10^{17} cm^{-3}) with (100) and (111) orientation, both in the form of the layers on the substrate surface and in the form of free films. To separate the films from the substrate, just as in the case of porous Si,[8] the anodization current density was increased in steps. The free films ranged in thickness from 8 to 15 μm. After etching the samples were first washed in ethyl alcohol and then dried in a stream of air. Prior to the measurements, the samples were allowed to age under natural conditions (in air at room temperature) from several days to one month in order to stabilize the properties.

The Raman scattering spectra were recorded on a microscope-equipped U-1000 Jobin-Yvon spectrometer in a microsample investigation mode. This made it possible to choose uniform sections of the sample surface under study and to check for the absence of any effects due to a thermal action of the laser beam on the sample. Argon laser radiation with a wavelength of 488 nm was used for excitation. The radiation was focused into a spot with diameter $d\simeq40$ μm. The resolution of the apparatus in the investigations of the RS spectra was equal to 0.5 cm^{-1}. To increase the accuracy of the measurements of the positions of the peaks, the lines of a neon lamp, which were located next to the *TO* and *LO* peaks which were investigated, were recorded at the same time. This made it possible to introduce a correction for the thermal drift of the apparatus in the process of each subsequent measurement and to determine the position of the *LO* and *TO* phonon peaks with an accuracy no worse than 0.3 cm^{-1}.

In addition to the RS spectroscopy, transmission microscopy (Philips CM30TEM/STEM microscope, 300 keV, equipped with an energy-dispersion x-ray microanalyzer) was used to investigate the structure. Small pieces of free porous-GaP films were used in a region which was pretoned with an Ar ion beam (5.5 keV) and in sections without ion etching (in sections along the fracture edges of the samples).

Raman scattering was used to investigate samples of two types — free porous-GaP films secured on diaphragms for electron-diffraction measurements and plates, where sections of the initial single crystal were present together with a porous layer. This made it possible in the first case to compare the RS and TEM results and in the second case to record systematically the RS spectrum of porous GaP and the initial crystal in a single geometry and under virtually identical conditions.

2. EXPERIMENTAL RESULTS

Figures 1–3 show TEM photomicrographs of free porous-GaP films. We see that the object investigated possesses a multilevel structure: The film consists of elements in the form of ''inflorescences'' consisting of spherical globules formed by radially directed ''petals.'' In addition, despite the large variance in the angles of orientation of the ''petals'' of the globules, they are distinct crystalline formations (without an amorphous impurity phase), in which the crystallographic orientation characteristic of the initial substrate is preserved (the microscopic diffraction pattern in the imaged region is shown in the inset in Fig. 2). The ''petals'' in turn also consist of smaller, 50–200 Å, objects (Fig. 3).

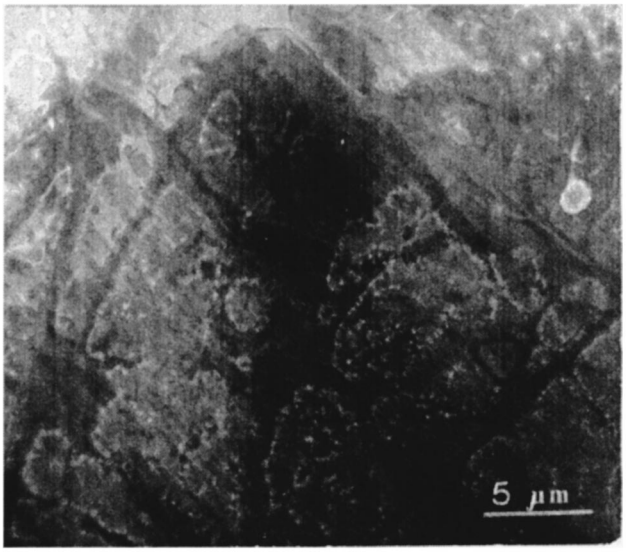

FIG. 1. Photomicrograph of a free porous-GaP film. The image was obtained in a Philips CM30TEM/STEM microscope (magnification 4.8×10^4).

The RS spectra of different porous-GaP samples and, for comparison, the RS spectra of the initial single-crystal GaP are shown in Figs. 4–6. The well-known spectra for the initial GaP single crystal[9] contain one or two peaks (367 and 403 cm^{-1}), depending on the orientation of the surface and the corresponding to transverse (*TO*) and longitudinal (*LO*) phonons. The RS spectra of porous GaP have a number of characteristic features.

1. Irrespective of the initial orientation of the substrate and the scattering geometry (for example, when the selection rules permit only *LO* or *TO* phonons), both *LO* and *TO* phonons are always present simultaneously in the porous-GaP spectra (Fig. 4).

2. A band corresponding to surface vibrations at the boundary of single-crystal GaP is clearly seen in the RS spectra of porous GaP. In addition, the position of this band is not strictly fixed and was found to depend on the local conditions of formation. A narrow strip of a transitional layer from single crystal to porous section was present along the perimeter of the porous section. This strip corresponds to the region where the edges are clamped to the substrate, where the contact with the electrolyte and therefore the local conditions of anodization most likely differ from the average over the remaining surface of the porous layer. Figure 5 shows the RS spectra of different points of porous GaP with the excitation spot moving from the single-crystal substrate to a uniform section of porous GaP through the above-indicated transitional layer.

3. The longitudional phonon band becomes narrower and shifts into the low-frequency region of the spectrum (Fig. 6).

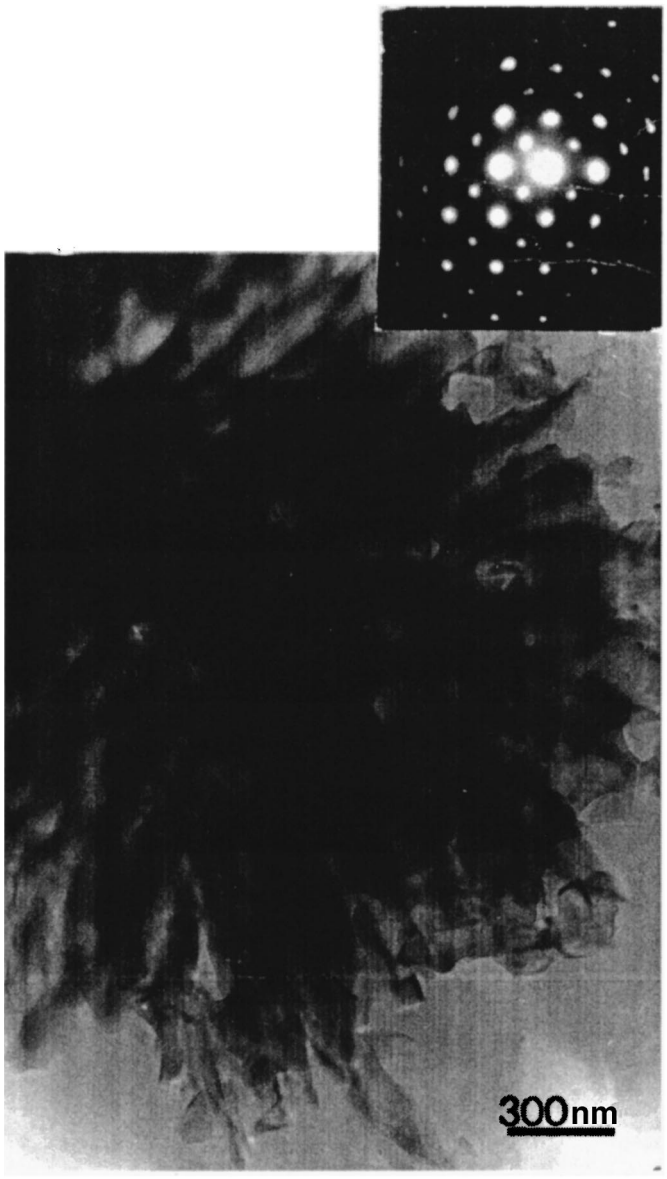

FIG. 2. Image of a ''globule'' with ''petals'' (magnification 6.6×10^5). Inset: Microdiffraction pattern in this region.

FIG. 3. Photomicrograph in the region of one of the petals (magnification 5.7×10^6).

3. DISCUSSION

The volume and surface vibrations of crystalline GaP are well known.[9] It is also known that the selection rules break down in microstructures, where neither phonons nor light are described by plane waves, which results in the appearance of selection-rule-forbidden vibrations in the spectra. The spectrum of the surface oscillations in GaP was first obtained on a thin GaP plate (20 μm).[10] Earlier, it was shown in a study of the effect of roughness on the RS spectra[11] that a ''shoulder'' due to surface vibrations of a GaP single crystal appears on the low-frequency side of the longitudinal phonon band in the RS spectra from a ''rough'' surface (rough spots on the order of 0.3 mm). The frequency of this band did not depend explicitly on the size of the rough spots.

The maximum frequency of a surface vibration for a polar semiconductor is described well by the expression

$$\omega_s=[(\varepsilon_0+\varepsilon_c)/(\varepsilon_\infty+\varepsilon_c)]^{1/2}\omega_{TO}, \qquad (1)$$

where ω_{TO} is the transverse phonon frequency, ε_∞ and ε_0 are the high-frequency and static dielectric constants of the semiconductor, and ε_m is the dielectric constant of the medium adjacent to the semiconductor. Using Eq. (1), we can estimate the value of ε_0 for the bordering medium on the void surfaces in the transitional layer (Fig. 5). The arrows in the figure indicate the computed positions of the frequencies of the surface vibrations for two types of interfaces: GaP–air (1) and GaP–medium (2) with $\varepsilon_c\simeq2.25$ ($n\simeq1.5$). On the basis of the result obtained in Ref. 11 — that the frequency ω_s is independent of the size of the rough spots, it can be concluded that in the first case we have a porous film, in which the surface of the voids consists of a clean air—⟨crystalline GaP⟩ interface. In the second case the RS spectra correspond to a crystalline-GaP surface with a transitional layer or insulating coating with refractive index $n\simeq1.5$. The results obtained do not answer the question of whether or not these results are attributable to additional roughness of the void surfaces or to adsorption or oxidation (the surface vibrations in principle make it possible to observe fractions of a monolayer coating[11]). However, microanalysis of the elemental composition in electron-diffraction analysis does not show the presence of compounds other than GaP. In any case, it can be concluded that an orthophosphoric-acid-based electrolyte can in principle be used to obtain porous layers without an appreciable coating of oxides or other products of an electrochemical reaction.

We devoted more attention than was done in Ref. 4 to the position and shifts of the *TO* and *LO* phonon bands be-

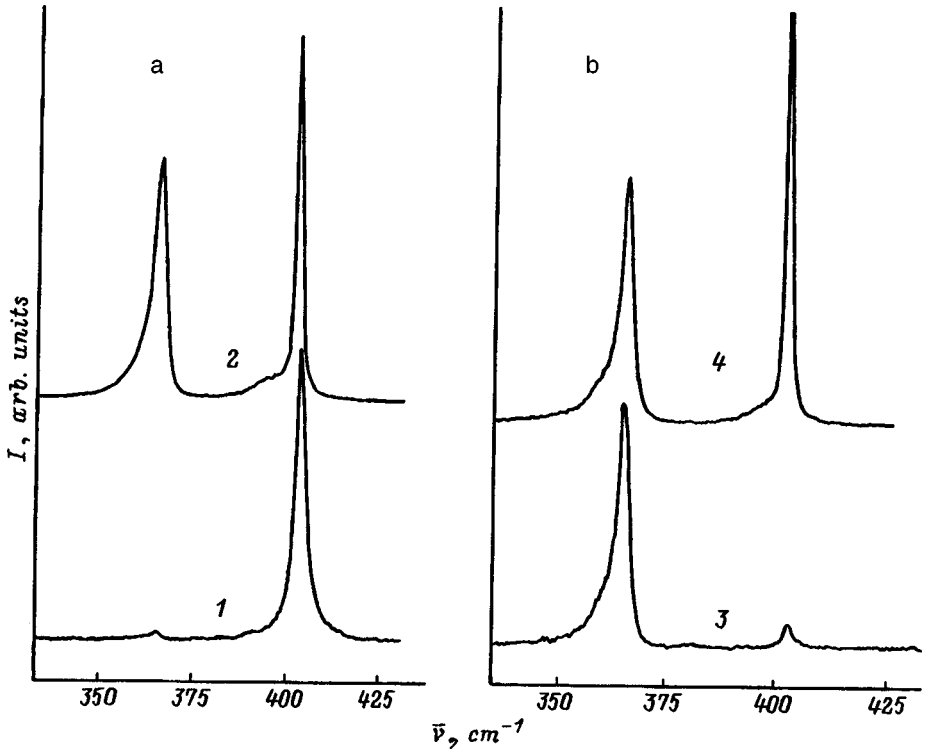

FIG. 4. Comparative Raman scattering spectra of the initial GaP substrate (*1*, *3*) and porous GaP (*2*, *4*) in different scattering geometries and with different orientations of the substrate: a — $x(yz)\bar{x}$, [100]–*LO*, b — $y'(z'z')\bar{y}'$, [110]–*TO*.

cause of the possibility of calibrating each measured spectrum. We found that to within the accuracy of the measurements there was no shift in the position of the *TO* lines, while for the *LO* peaks a shift into the low-frequency region and narrowing were observed. The latter cannot be explained by disordering or breakdown of the wave-vector selection rules in nanocrystals.

It seems to us that this effect can be explained by the fact

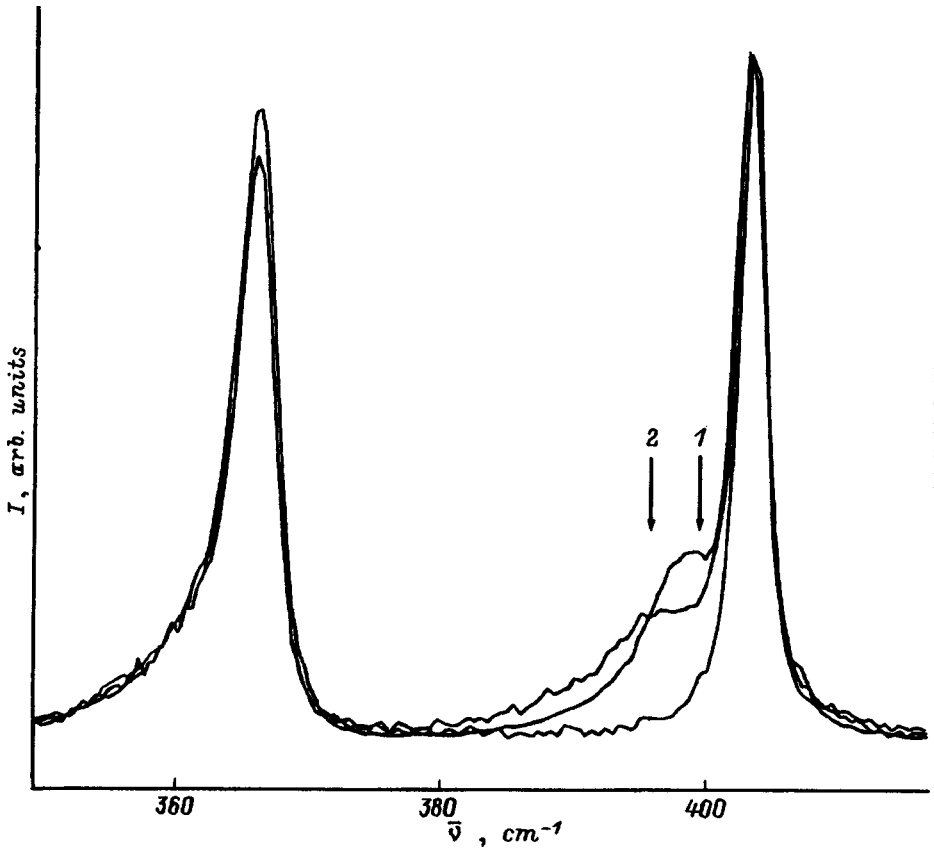

FIG. 5. Raman scattering spectra obtained from different sections of the transitional layer of porous GaP (*1*, *2*) and the GaP substrate with a transition from the substrate to a uniform region of the porous layer.

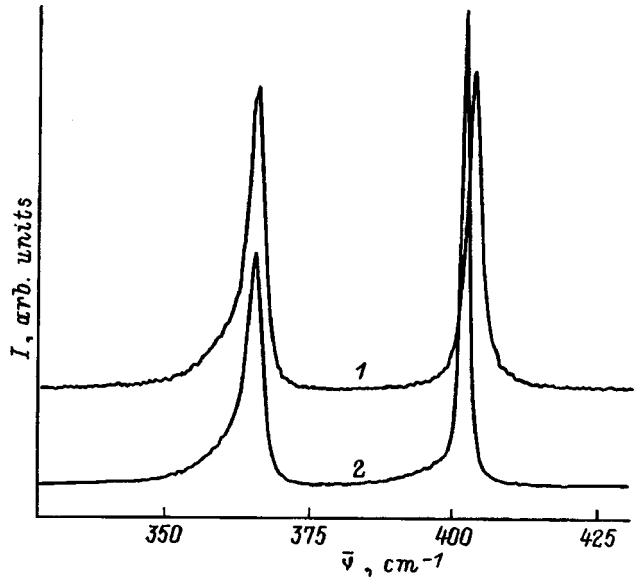

FIG. 6. Narrowing and low-frequency shift of the *LO*-phonon. Raman scattering spectra: *1* — GaP single crystal, *2* — porous GaP.

that the carrier density in the initial single crystal is different from that in the porous material. Indeed, when carriers are present in the semiconductor, plasma-phonons are formed with frequencies determined by the expression

$$\omega_{\pm}^2 = \{(\omega_p^2 + \omega_{LO}^2) \pm [(\omega_p^2 - \omega_{LO}^2)^2 + 4\omega_p^2(\omega_{LO}^2 - \omega_{TO}^2)]^{1/2}\}/2, \quad (2)$$

where ω_p is the plasma frequency for carriers with density N and effective mass m^*. For comparatively low carrier densities the frequency ω_+ is somewhat higher than ω_{LO}. If defects and impurity centers are removed from the single crystal during the etch process, then the remaining crystalline frame will have a lower carrier density than the initial single crystal and ω_+ will decrease. At the same time, the smaller number of defects and the fact that the plasmon lifetime does not contribute to the broadening of the longitudinal phonon band apparently explain the narrowing of the *LO*-phonon peak. An estimate of the carrier density in the initial and porous layers [using Eq. (2) and the value of ω_{LO} for the initial single crystal 403.3 cm^{-1} and the porous film 401.8 cm^{-1}] gives 3×10^{17} cm^{-3} and 9.2×10^{16} cm^{-3}, respectively. According to the specifications, the carrier density for GaP substrate was equal to 2.75×10^{17} cm^{-3}. Comparing it with earlier results obtained for porous-GaP layers using a HF-based electrolyte (narrowing of the *LO*-phonon peak was not observed in them), it can be concluded that the crystallographic quality of the films is higher in the case of the electrolyte with orthophosphoric acid.

In summary, it has been shown that an electrolyte based on orthophosphoric acid (instead of HF) is optimal for obtaining porous-GaP layers. Free porous-GaP films were obtained for the first time and their microstructure was investigated. Narrowing of the *LO*-phonon peak, together with a simultaneous low-frequency shift of the peak, was observed in the Raman scattering spectra from porous GaP. A shift in the frequency of the surface mode, depending on the state of the surface of the pores, was also observed. It was shown that the proposed electrolyte in principle can be used to obtain porous layers without an appreciable coating of the surface of the voids with oxides or other products of an electrochemical reaction. Analysis of the Raman scattering spectra and the results of transmission electron microscopy shows that the observed effects can be satisfactorily explained in terms of the change in the plasmon–phonon interaction as a result of a decrease in the carrier density. This explanation agrees with the mechanism of electrochemical etching, which presumes that the defects are removed from the single crystal during the etching process. The microstructure of the porous-GaP films has a complex spatial structure, but the local crystallographic orientation characteristic of the initial substrate remains.

This work was supported in part by the Interdisciplinary Program ''Physics of solid-state nanostructures'' (Projects 1-010 and 1-042), the Russian Fund for Fundamental Research (Grants 95-02-04510 and 95-02-04450), and the State Science and Technology Program ''Fundamental spectroscopy.''

[1] Y. Kanemitsu, Phys. Rep. **263**, 1 (1995).
[2] F. Koch and V. Petrova-Koch in *Porous Silicon*, edited by Z. C. Zeng and R. Tsu, World Scientific, Singapore, 1994, p. 133.
[3] K. N. El'tsov, V. A. Karavanskiĭ, and V. V. Martynov, JETP Lett. **63**, 119 (1996).
[4] A. I. Belogorokhov, V. A. Karavanskiĭ, A. N. Obraztsov, and V. Yu. Timoshenko, JETP Lett. **60**, 274 (1994).
[5] A. Anneda, A. Sepri, V. A. Karavanskii, I. M. Tiginyanu, and V. M. Ichizli, Appl. Phys. Lett. **67**, 3316 (1995).
[6] *Etching of Semiconductors: Collection of Articles* [Russian translation], Mir, Moscow, 1965.
[7] B. D. Luft, V. A. Perevoshchikov, L. N. Vozmilova, I. A. Sverdlin, and K. G. Marin, *Physicochemical Methods of Treatment of Semiconductor Surfaces* [in Russian], Radio i svyaz', Moscow, 1982.
[8] V. S. Dneprovskiĭ, V. A. Karavanskiĭ, V. I. Klimov, and A. P. Maslov, JETP Lett. **57**, 406 (1993).
[9] A. Mooradian and G. B. Wright, Solid State Commun. **4**, 431 (1966).
[10] J. B. Valdez and S. Ushioda, Phys. Rev. Lett. **38**, 1089 (1977).
[11] V. M. Agranovich and L. Milns, *Surface Polaritons* [in Russian], Nauka, Moscow, 1985.

Translated by M. E. Alferieff

InAsSbP double-heterostructure lasers for the spectral range 2.7–3.0 μm ($T=77$ K)

T. N. Danilova, A. P. Danilova, O. G. Ershov, A. N. Imenkov, M. V. Stepanov, V. V. Sherstnev, and Yu. P. Yakovlev[a)]

A. F. Ioffe Physicotechnical Institute, Russian Academy of Sciences, 194021 St. Petersburg, Russia
(Submitted June 5 1997; accepted June 10 1997)
Fiz. Tekh. Poluprovodn. **32**, 241–244 (February 1998)

We have produced, by using liquid-phase epitaxy, 2.7 to 3.0-μm lasers based on InAsSbP double-heterostructures with different phosphorus contents in the active and wide-gap regions. The lasers possess threshold current density ~ 0.8 kA/cm^2 at 77 K and operate in the pulsed mode up to ~ 124 K with maximum threshold current density 10–12 kA/cm^2. The lasers have a low series resistance $\sim 0.45\ \Omega$. © *1998 American Institute of Physics.* [S1063-7826(98)02302-3]

1. Sources of radiation in the spectral region 2.7–3.0 μm are promising for hygrometry and gas analysis, since strong absorption lines of molecules such as H_2O, CO_2, H_2S and others lie in this spectral region.

The fabrication of lasers for the wavelength range 2.7–3.0 μm encounters definite technological difficulties. Pulsed, room-temperature, 2.5-μm lasers based on GaInAsSb/AlGaAsSb double heterostructures (DHSs) with a $Ga_{0.745}In_{0.255}As_{0.230}Sb_{0.770}$ active region have been fabricated by liquid-phase epitaxy (LPE).[1] Longer-wavelength radiation could not be obtained because of proximity to the limit of immiscibility of the solid solutions GaSb–InAs.[2] However, room-temperature 2.78-μm lasers have been fabricated by molecular beam epitaxy (MBE).[3] The active region of the lasers contains four quantum wells with the composition $In_{0.24}Ga_{0.76}As_{0.16}Sb_{0.84}$, the interwell barriers with the composition $A_{0.25}Ga_{0.75}As_{0.02}Sb_{0.98}$, and confinement regions with the composition $Al_{0.9}Ga_{0.1}As_{0.08}Sb_{0.92}$, and the lasers operate in a pulse mode up to temperature 60 °C. The lasers do not operate in the continuous-wave regime at room temperature. A substantial drawback of these lasers is that their supply voltage is high because of the high residual resistance. With a direct current of 0.1 A, the bias voltage in the forward direction equals 4.8 V at 78 K and 2.2 V at 300 K.

Attempts have been made to produce diode lasers by LPE on the basis of the solid solution $InAsSbP_x$, which is isoperiodic to the substrate InAs, with different phosphorus content in the active and confinement regions.[4,5] However, because of the low phosphorus content in the confinement regions — $x=0.1$ obtained in Ref. 4 and $x=0.2$ obtained in Ref. 5, the lasers emitting at 3 μm (Ref. 4) operated only in the pulsed mode at 77 K with threshold current density 3 kA/cm^2 and a maximum working temperature of 145 K. Lasers emitting at 2.5–2.7 μm (Ref. 5) operated only in the pulsed mode up to a temperature of 55 K with threshold current density ~ 29 kA/cm^2.

In a previous work[6] we reported the fabrication of diode lasers by the LPE method on the basis of the solid solution $InAsSbP_x$, isoperiodic to the substrate InAs, with different phosphorus content in the wide-gap and active regions. In the wide-gap regions $x=0.35$, and in the narrow-gap region x varied from 0.02 to 0.10. The thickness of the active region in them was equal to 0.5 μm. Lasers lasing at wavelength 2.7–3 μm in a pulsed mode at 77 K with threshold current 400 mA and threshold current density ~ 5.7 kA/cm^2 were obtained.

In the present study we report the results of an ongoing experimental study of the development of 2.7 to 3-μm lasers and also the development of lasers with low threshold currents.

2. The lasers, fabricated by the LPE method, consist of a double heterostructure based on the solid solution $InAsSbP_x$ in the active and wide-gap regions. The phosphorus content is $x \simeq 0.08-0.12$ in the active region and $x \simeq 0.25-0.28$ in the confinement regions. According to the calculations, the band gap E_g ranges in the interval 0.42–0.47 eV in the active region and 0.55–0.58 eV in the wide-gap regions at 77 K. The structures possess a type-II heterojunction at the boundaries of the narrow- and wide-gap regions with conduction- and valence-band offsets of ~ 100 meV and ~ 15 meV, respectively.

The active region, without any special doping, was of n-type with electron density $\sim 10^{16}$ cm^{-3}. The confinement P-type region was doped with Zn and had hole density $\sim(1-2)\times 10^{18}$ cm^{-3}. The confinement N-type region was doped with Sn and had electron density $\sim(5-7)\times 10^{18}$ cm^{-3}.

The active and confinement regions were each ~ 1.5 μm thick. The computed refractive-index difference between the active and confinement regions was equal to 0.03–0.04 (at $T=300$ K).

Mesastripe structures with ~ 25 μm stripe width were fabricated from epitaxial laser structures by photolithography. Lasers with a 225 to 300-μm-long cavity were fabricated by cleaving.

The emission spectra, directional patterns, and integral intensity of the laser radiation were investigated. The lasers operated at liquid-nitrogen temperature in a quasi-cw regime and were powered by a train of alternating (meander-type) square-shaped current pulses with a repetition frequency of 80 Hz. The temperature dependence of the threshold current density was determined with the lasers powered by 100-ns current pulses with a repetition frequency of 10^5 Hz.

3. The lasers possessed threshold currents $I_{th}=70-80$ mA at liquid-nitrogen temperature. This corresponded to threshold current density ~ 0.8 kA/cm^2. The lasers have a low supply voltage. With a direct current $I=0.1$ A flowing

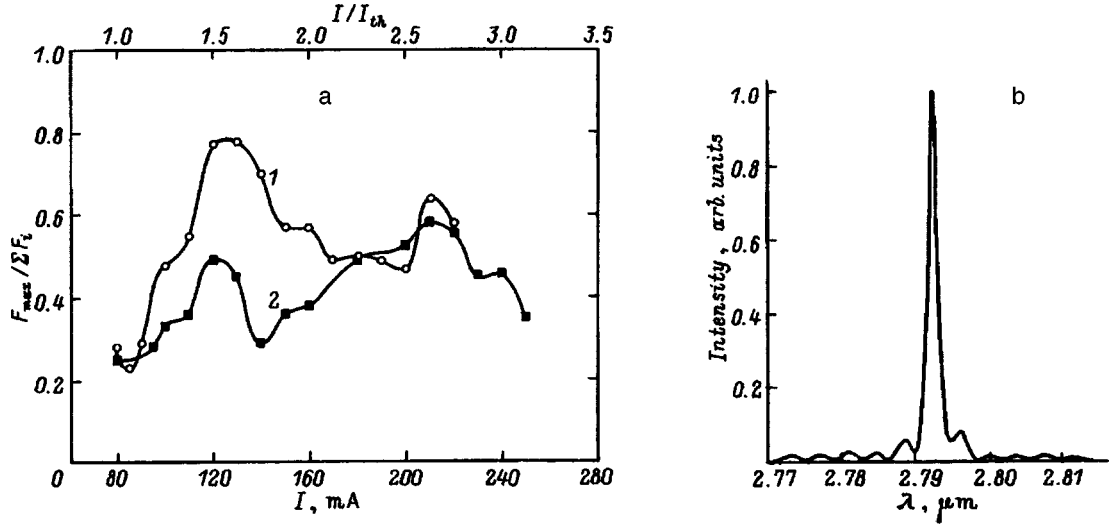

FIG. 1. Spectral characteristics of the lasers. The ratio $F_{\max}/\Sigma F_i$ of the intensity of the maximum mode to the sum of the intensities of all modes versus current I (a) for laser S-197 No. 2 (1) and for laser S-197 No. 1 (2). The spectrum of coherent radiation (laser S-197 No. 2) in the maximum unimodal regime (b).

through the laser diode the voltage drop is $U=0.67$ V and the residual resistance is 0.45 Ω.

The lasers emitted in the spectral region 2.7–3 μm, and the wavelength of the radiation depended on the composition of the active region. The laser radiation had good coherence properties. The mode composition and spatial distribution of the radiation were investigated. The mode composition of the radiation spectrum depended on the pump current. The intermode spacing was equal to 35–40 Å. A single-mode lasing regime was observed in a definite current interval. A numerical estimate of the radiation intensity in the predominant mode as a fraction $F_{\max}$ of the total radiation intensity ΣF_i for all modes in the spectrum is shown in Fig. 1a for two lasers as a function of current. As one can see, for both lasers this dependence has two maxima at currents $\sim 1.5I_{th}$ and $\sim 2.6I_{th}$. The maximum corresponding to lower currents for one of the lasers (S-197 No. 2) is higher (curve *1*) and the maximum corresponding to the lower currents for the other laser (S-197 No. 1) is lower (curve *2*). The largest value is $F_{\max}/\Sigma F_i \simeq 0.8$. For the laser corresponding to curve *1* both maxima of the function $F_{\max}/\Sigma F_i(I)$ correspond to the same predominant mode, and at the currents between the maxima of the curves the neighboring mode with a longer wavelength became the dominant mode. For the laser with $F_{\max}/\Sigma F_i(I)$, represented by curve *2*, different maxima correspond to different predominant modes, which are separated from one another by two intermode intervals. The intermediate modes have a small advantage at near-threshold currents. Figure 1b shows the coherent radiation spectrum (laser S-197 No. 2) in the maximum unimodal regime with the wavelength of the predominant mode $\lambda \approx 2.792$ μm.

Investigation of the spatial distribution of the radiation of the lasers showed that it corresponds to a single longitudinal mode. The current dependence of the spatial distribution and intensity of the integrated radiation are presented in Fig. 2 (laser S-197 No. 1). The spatial distribution is characterized by the half-width $\Delta\Theta$ of the directivity pattern. This width corresponds to the width of the pattern at half-maximum. As one can see, for the spatial mode (Fig. 2a) in the plane of the $p-n$ junction (curve *1*) $\Delta\Theta$ has a minimum value $\sim 11°$ at near-threshold currents. At currents above $1.25I_{th}$ $\Delta\Theta$ increases with current and reaches 19.5° for $I \simeq 2I_{th}$. In a plane perpendicular to the plane of the $p-n$

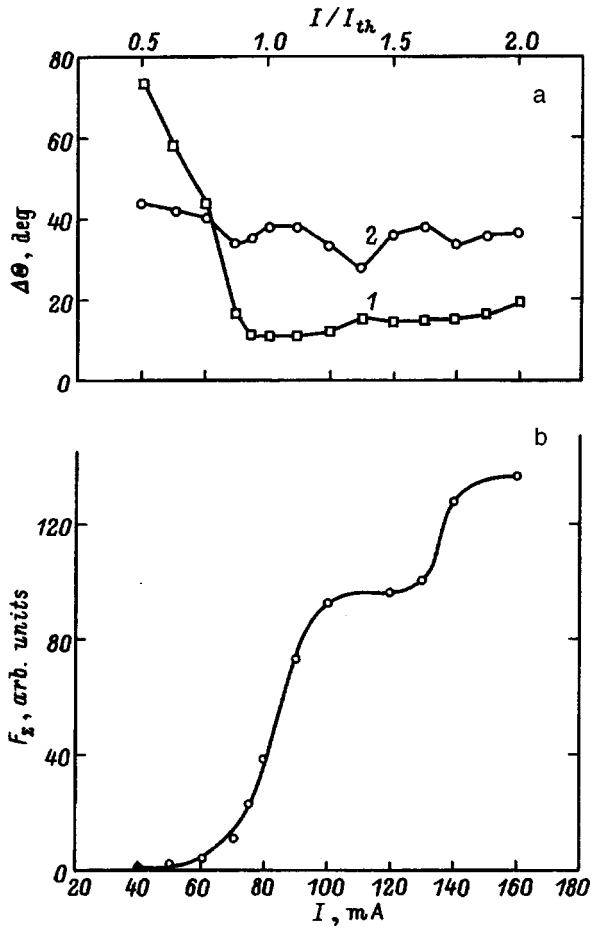

FIG. 2. Width $\Delta\Theta$ (a) of the directivity pattern at half-maximum in the plane of the $p-n$ junction (1) and in the plane perpendicular to the plane of the $p-n$ junction (2) versus the bias current I (a) and intensity of the integrated radiation F_Σ versus the bias current I (b) for laser S-197 No. 1.

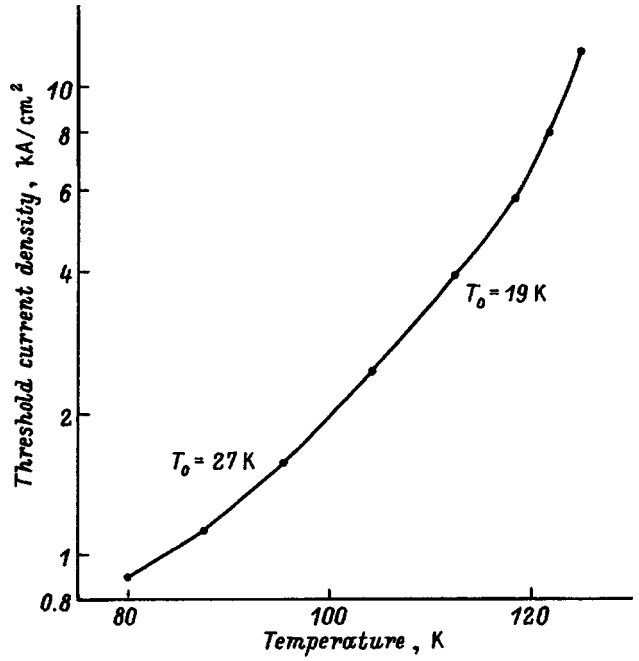

FIG. 3. Threshold current density versus temperature.

junction (Fig. 2a, curve *2*) $\Delta\Theta \simeq 40°$ on the average. For some currents, corresponding to mode hops to a different predominant mode in the radiation spectrum, small minima are present in the curves $\Delta\Theta(I)$. These minima correspond to inflections in the curve of the integral radiation F_Σ versus current (Fig. 2b). The mismatch between the currents at the indicated characteristic points of the curves is about 10% of the current, which is good enough for independent measurements.

The threshold current density increases rapidly with temperature (Fig. 3); the characteristic temperature is $T_0 \sim 27$ K in the range 80–100 K and $T_0 \sim 19$ K in the range 100–120 K. Then the threshold current density increases even more rapidly, and lasing stops at a temperature of ~ 124 K and current densities in the range 10–12 kA/cm^2.

4. Let us discuss the results which we obtained. The threshold currents and threshold current densities of the lasers presented in this paper are approximately five times lower than reported in our previous work for the similar lasers.[6] The threshold current densities at 77 K for the lasers developed correspond to the average threshold currents of our InAsSb/InAsSbP based lasers emitting in the spectral region 3.2–3.9 μm but their temperature dependence is sharper. The coherence properties reported by us for the radiation of the lasers, which were investigated at 77 K, also correspond to the coherence properties of our mid-range lasers emitting in the spectral region 3.2–3.9 μm. Thus, one of two or three neighboring modes predominates in the spectra of the lasers developed by us and investigated in the entire current interval from I_{th} up to $3I_{th}$; here the ratio $F_{\max}/\Sigma F_i$ reaches a maximum value of 0.8 (Fig. 1). The spatial distribution of the radiation in the plane of the $p-n$ junction is in one longitudinal mode.

Our lasers do not attain parameters better than those of the lasers emitting in the spectral region 3.2–3.9 μm at 77 K, reported in Ref. 7. One reason for this could be that in them the refractive-index difference Δn between the narrow- and wide-gap regions, which determines optical confinement, is approximately half as large. The small value of Δn can be explained by the fact that when the dominant mode hops into a different position, a small spatial broadening of the radiation flux occurs in a plane perpendicular to the plane of the $p-n$ junction. The broadening of the radiation flux results in narrowing of the directivity pattern as a result of a decrease in the diffraction losses. The penetration of the radiation flux into the wide-gap regions is accompanied by a decrease in the integral intensity of the radiation (Fig. 2b) as a result of an increase in the absorption by free carriers.

Raising the temperature sharply increases the threshold current density of the lasers investigated and disrupts lasing at the low maximum working temperature and at comparatively low current densities (Fig. 3). We shall examine the possible reasons for such a temperature dependence of the threshold current density.

The lasers investigated by us are based on type-II heterostructures. According to the theory of recombination of nonequilibrium carriers in a type-II heterostructure,[8] Auger recombination processes in such structures are effectively suppressed. As a result, the threshold current density should show a weak temperature dependence. According to this theory, the Auger recombination rate has a minimum for definite values of the parameters of the heterostructure (the ratio $\Delta E_v/\Delta E_c \approx 3$). For the lasers produced in our work $\Delta E_v = 15$ meV, $\Delta E_c = 100$ meV, and $\Delta E_v/\Delta E_c = 0.15$. Therefore, the energy diagram of these lasers does not permit using the advantages of the type-II heterostructure in the sense of suppressing Auger recombination processes. Moreover, the very small valence-band offset (15 meV), which is comparable to kT, can serve as the reason why even at low temperatures and low current densities disruption of lasing occurs as a result of vanishing of the electronic confinement for holes.

Another reason for the low maximum working temperature at quite low maximum threshold currents could be disruption of lasing as a result of vanishing of the optical confinement with increasing temperature. Rapid growth of the threshold current density with temperature results in a higher free-carrier density N in the active region. As a result, the index of refraction there decreases[9] and, consequently, optical confinement decreases. Despite the fact that the refractive index itself increases with temperature and for III–V semiconductors the change in the refractive index with carrier density depends inversely on the temperature $\delta \sim dn/dN \sim -1/T$,[10] the estimates show that for an $InAsSbP_x$-based heterostructure with different phosphorus contents $-dn/dN$ can cause the optical confinement to vanish at sufficiently low temperatures.

We also note that the thicker the active region, the less radiation penetrates into the confinement layers and the substrate and the less radiation is absorbed by free carriers. The lasers which we investigated have much better parameters than those reported in Ref. 6. This is apparently attributable to the more than three times larger thickness of the active layer.

As a result, it has been shown that lasers emitting in the region 2.7–3.0 μm and having threshold current densities $\sim$0.8 kA/cm^2 at 77 K and $\sim$10–12 kA/cm^2 at the maximum working temperature $\sim$124 K have been produced by the LPE method on the basis of InAsSbP$_x$ heterostructures with different phosphorus contents in the active and wide-gap regions. In some range of currents the lasers operate in a one-mode regime and have a spatial distribution in the form of one longitudinal mode. A positive quality of the lasers is their low series resistance $\sim$0.45 Ω. It should be noted that the construction of the lasers can be optimized for specific applications. The lasers investigated by us have a stripe width $\sim$25 μm. To improve the coherence properties of the lasers, the stripe width must be decreased.[7] To obtain lower current densities the stripe width and length must be increased. A slightly higher maximum temperature can therefore be obtained.[11]

However, to significantly increase the maximum working temperature, solid solutions with a larger band gap must be used in the wide-gap regions and the heterojunctions providing electronic confinement must be of type-II with the largest possible valence-band offset.

This work was supported by a grant from the European Society INCO-Capurnicus.

[a)]Telephone: (812) 247-9956; Fax: (812) 247-0006; e-mail: yak@iroptl.ioffe.rssi.ru

[1] A. N. Baranov, E. A. Grebenshchikova, B. E. Dzhurtanov, T. N. Danilova, A. N. Imenkov, and Yu. P. Yakovlev, Pis'ma Zh. Tekh. Fiz. **14**, 1839 (1988) [Sov. Tech. Phys. Lett. **14**, 798 (1988)].
[2] A. N. Baranov, A. A. Guseĭnov, A. M. Litvak, A. A. Popov, N. A. Charykov, V. V. Sherstnev, and Yu. P. Yakovlev, Pis'ma Zh. Tekh. Fiz. **16**, 33 (1990) [Sov. Tech. Phys. Lett. **16**, 177 (1990)].
[3] H. Lee, P. K. York, R. J. Monna, R. U. Martinelli, D. Z. Garbuzov, S. Y. Narayan, and J. C. Connoly, Appl. Phys. Lett. **66**, 1942 (1995).
[4] N. Kobayashi and Y. Horikoshi, Jpn. J. Appl. Phys. **19**, 4641 (1990).
[5] S. Akiba, Y. Matsushima, T. Iketani, and M. Usami, Electron. Lett. **24**, 1069 (1988).
[6] T. N. Danilova, O. G. Ershov, A. N. Imenkov, I. N. Timchenko, V. V. Sherstnev, and Yu. P. Yakovlev, Pis'ma Zh. Tekh. Fiz. **20**, 87 (1994) [Tech. Phys. Lett. **20**, 172 (1994)].
[7] T. N. Danilova, A. P. Danilova, O. G. Ershov, A. N. Imenkov, M. V. Stepanov, V. V. Sherstnev, and Yu. P. Yakovlev, Fiz. Tekh. Poluprovodn. **31**, 1392 (1997) [Semiconductors **31**, 1200 (1997)].
[8] G. G. Zegrya and A. D. Andreev, Zh. Éksp. Teor. Fiz. **109**, 615 (1996) [J. Exp. Theor. Phys. **82**, 328 (1996)].
[9] P. P. Paskov, Solid State Commun. **82**, 739 (1992).
[10] P. G. Eliseev and A. P. Bogatov, Tr. FIAN **166**, 15 (1986).
[11] T. N. Danilova, O. G. Ershov, A. N. Imenkov, M. V. Stepanov, V. V. Sherstnev, and Yu. P. Yakovlev, Fiz. Tekh. Poluprovodn. **30**, 1265 (1996) [Semiconductors **30**, 667 (1996)].

Translated by M. E. Alferieff

Gamma-induced metastable states of doped, amorphous, hydrated silicon

M. S. Ablova, G. S. Kulikov, and S. K. Persheev

A. F. Ioffe Physicotechnical Institute, Russian Academy of Sciences, 194021 St. Petersburg, Russia
(Submitted June 6 1997; accepted June 10 1997)
Fiz. Tekh. Poluprovodn. **32**, 245–248 (February 1998)

The temperature dependence of the electrical conductivity of B- and P-doped *a*-Si:H films before and after irradiation with γ rays from a ^{60}Co source has been investigated. The irradiation dose was $10^{17}-10^{18}$ photons/cm^2. The behavior of the *n*-type films was observed to be substantially different from that of the *p*-type films. The electrical conductivity of the *p*-type films increases slightly (by a factor of 2–3) and that of the *n*-type films decreased sharply (by 2–3 orders of magnitude). The observed difference is explained by the different character of the γ-irradiation-induced charge redistribution on the broken silicon bonds D^+ and D^-. Comparing the results with the published data shows that the γ rays induce metastable states of *a*-Si:H which are due to the motion of bound hydrogen. © *1998 American Institute of Physics.* [S1063-7826(98)02402-8]

1. INTRODUCTION

The study of the effect of γ-irradiation on the properties of amorphous hydrated silicon (*a*-Si:H) yields valuable information about defects in material saturated with broken bonds. Thus, O. Imagawa *et al.*[1] used γ-irradiation to study the main defects in intrinsic *a*-Si:H: broken silicon bonds in three electronic states — D^+, D^0, and D^-. It was established that, passing through the *a*-Si:H film, the γ rays do not produce new broken bonds D^0 (as happens, for example, under irradiation with visible light), but rather they give rise to a redistribution of charges on the broken bonds with unoccupied states D^+ predominating. Since only undoped material was investigated in Ref. 1, we investigated the effect of γ-irradiation on the electric properties of P- and B-doped *a*-Si:H.

2. INVESTIGATION METHOD AND EXPERIMENTAL RESULTS

The films for the investigations were prepared by decomposing a mixture of monosilane (SiH_4) and phosphine (PH_3) or diborane (B_2H_6) gases in a high-frequency glow discharge with a quartz substrate temperature of 290 °C. The ratio of the gaseous components during film deposition was $[B_2H_6]/[SiH_4]=2\times10^{-2}$ and $[PH_3]/[SiH_4]=3\times10^{-2}$. According to IR spectroscopy data, the hydrogen content in the films was 10–12%. The thickness of the films was equal to 0.2–0.5 μm.

Irradiation was conducted in room-temperature air with a γ-ray flux 7.7×10^{11} photons/(cm$^2\times$s) from the ^{60}Co source. The irradiation doses were equal to 7.3×10^{17} and 1.6×10^{18} photons/cm^2. Since the penetration depth of γ-rays was greater than the film thickness, it could be assumed that the defects are produced uniformly over the entire film volume. The temperature dependence of the dark conductivity was determined before and after γ-irradiation. The room-temperature thermoelectric power was also measured to determine the sign of the carriers.

The main results of the measurements are presented in Figs. 1a and 1b: the typical curves $\log\sigma=f(1/T)$ for *n*- and *p*-type samples before and after irradiation. As follows from the results which we obtained, the irradiated *n*- and *p*-type films exhibit substantially different behavior. While the electric conductivity of the *p*-type films in the temperature range 20–100 °C increases only slightly (approximately by a factor of 2–3), the electric conductivity of the *n*-type films in the same temperature interval and with the same irradiation doses drops sharply (approximately by three orders of magnitude). After irradiation the films retain the starting type of conductivity. As the irradiation dose increases, the conduction activation energy decreases from 0.22 to 0.14 eV in *p*-type films and increases from 0.2 to 0.36 eV *n*-type films. We note that activation energies $E_A>1$ eV are observed for *n*-type films in the temperature interval 72–127 °C. These activation energies are, in general, atypical for doped *a*-Si:H.

The changes observed in the electric conductivity after γ-irradiation are reversible, since the electric conductivity of the films was restored to its initial values by heating the irradiated *n*- and *p*-type films to 200 °C (in the course of the measurements of the electric conductivity) and also by storing the films at room temperature for 40–60 days.

We note that similar differences in the dark conductivity of *n*- and *p*-type doped *a*-Si:H were observed by Kurova *et al.*,[2] with prolonged irradiation with intense white light. They showed that the dark conductivity of *p*-type films increases, and that of *n*-type films decreases. In other words, the sign of the Stabler–Wronski effect is different for samples doped with B and P.

3. DISCUSSION

The effect of γ-irradiation on an amorphous semiconductor can be divided into two parts: electronic excitations and structural damage, leading to the formation of multicomponent complexes.

As we have already mentioned, the main type of electronic charged defects in *a*-Si:H, which determine its electrical conductivity, are broken silicon bonds in three states: D^+, D^0, and D^-. Neutral broken bonds D^0 give rise to deep

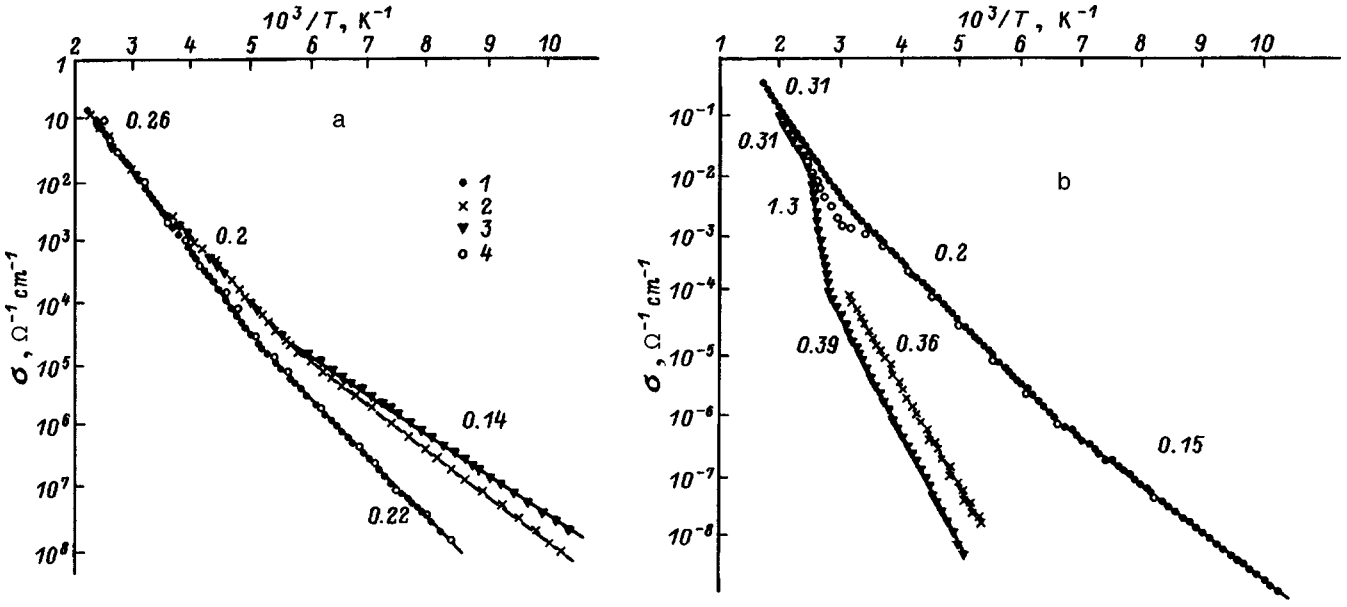

FIG. 1. Effect of γ-irradiation on the temperature dependence of the electrical conductivity σ of doped amorphous hydrated silicon samples: a — a-Si:H⟨B⟩, b — a-Si:H⟨P⟩. Measurements were performed *1* — before irradiation, *2* — after irradiation with a dose of 7.3×10^{17} photons/cm^2, and *3* — after irradiation with a dose of 1.6×10^{18} photons/cm^2. The open circles show the results of the measurements: a — 40 days after irradiation, b — after heating to 200 °C in the course of measurements of the electrical conductivity. The numbers on the curves are the activation energies (in eV).

traps (near the center of the band gap) for electrons and holes via the reactions

$$D^0+e\rightarrow D^-, \tag{1}$$

$$D^0+h\rightarrow D^+. \tag{2}$$

When a dopant is introduced, a peak of the density of D^- states for n-type films and a D^+ peak for p-type films appear in the band gap instead of D^0 states.[3] In this connection, the basic reactions (1) and (2) also change. According to the data in Ref. 4 , double trapping of D^- states via the reaction

$$D^-+2h\rightarrow D^+, \tag{3}$$

which determines deep traps for holes, predominates in n-type films, while double trapping of D^+ states via the reaction

$$D^++2e\rightarrow D^-, \tag{4}$$

which determines deep traps for electrons, is characteristic of p-type films.

Assuming that the results of Ref. 1 are valid for doped a-Si:H films, we assume that γ-rays do not produce new D^0 broken bonds in our films, but rather they give rise to a redistribution of charge over existing broken bonds, where unoccupied D^+ states are formed predominately. Then the processes described by the reaction (3) are directed in the same direction as the action of γ-rays, and the processes occurring via the reaction (4) compensate for the effect of the γ-rays. Therefore, it can be expected that irradiation will have a substantially different effect in n- and p-type films.

Let us now examine on this basis our results for n-type a-Si:H films. The irradiated n-type film (Fig. 1b) had a phosphorus atom density $N_P=8\times10^{20}$ cm^{-3}, which corresponds to donor density $N_D=6.34\times10^{18}$ cm^{-3}, and negatively charged broken bond density $D^-=6.30\times10^{18}$ cm^{-3}.[5] To convert the conductivity in a film into p-type the irradiation-induced D^+ bond density must be at least 6.3×10^{18} cm^{-3}. However, according to the data of Ref. 1, the total number of defects in undoped a-Si:H after irradiation with a γ-ray dose of 10^{17} photons/cm^2 is $2[D^0]+[D^+]+[D^-]=4\times10^{16}$ cm^{-3}. A comparison shows that even the total number of defects is two orders of magnitude smaller than required to change the sign of the conductivity in our irradiated film. Therefore, γ-irradiation could not have changed the sign of the conductivity in the n-type film which we studied.

As noted above, for n-type samples an unusually large activation energy $E_A>1$ eV for doped a-Si:H was observed on the curve $\log\sigma=f(1/T)$ in the temperature range 72 −127 °C (Fig. 1b). At higher temperatures (127–200 °C) the curves $\sigma(T)$ for irradiated and nonirradiated samples are identical just as in the case of cooling from 200 °C to room temperature and below. Therefore, annealing eliminates high values of the activation energy.

The character of the curves $\log\sigma=f(1/T)$, which is similar to that of the curve *3* in Fig. 1b, has been noted repeatedly and investigated in the literature.[6–10] It has been determined that this character of the curves corresponds to different metastable states of a-Si:H. It is now thought that the electronic properties of doped a-Si:H are described well on the basis of a model of metastable thermodynamic equilibrium. Figure 2, where our results are compared with the data from Ref. 6, shows the spectrum of possible metastable states of a-Si:H which are obtained with different external actions. The temperature T_E corresponding to the kink in the curves 1–4 can be viewed as the temperature at which thermodynamic equilibrium is established. Metastable states due to the motion of bound hydrogen along defects, in accordance with the ''hydrogen glass'' model proposed by Street,[7] are present at temperatures below T_E. At temperatures above

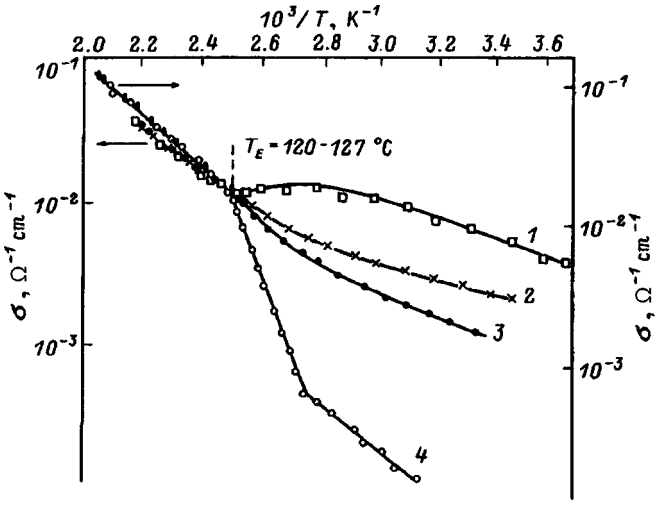

FIG. 2. Temperature dependence of the electrical conductivity σ in n-type a-Si:H samples: *1* — rapidly cooled sample (400 K/min); *2* — slowly cooled sample (1 K/min); *3* — after exposure to white light; *4* — after γ-irradiation with a dose of 1.6×10^{18} photons/cm^2. Curves: *1–3* — from Ref. 6, *4* — our data. For convenience in making comparisons, the data of Ref. 6 are slightly shifted along the ordinate.

T_E hydrogen is ''freed'' to a large degree and its motion no longer influences the chemical bonds in the silicon matrix. Accordingly, the curves *1* and *2* in Fig. 2 are determined by the motion of hydrogen along weak Si–Si bonds, which are broken on heating; curve *3* is determined by the motion of hydrogen along the same bonds broken by light. Curve *4* constructed according to our data apparently characterizes one of the possible γ-irradiation-induced metastable states of a-Si:H. In view of the similarity in the form of the curves *1–4* and the closeness of the temperatures T_E ($T_E=120$ °C for curves *1–3* and $T_E=127$ °C for curve *4*), we have grounds for believing that the processes determining the character of these curves apparently can be explained from the standpoint of a single physical model of hydrogen glass.

However, it is difficult for us to imagine that the high activation energy (>1 eV) which we observed can be produced only by a redistribution of charge on the broken bonds. At high irradiation doses, most likely, the formation of complexes of the type Si–P–H, which is stimulated by the motion of bound hydrogen, starts to play a role in the γ-induced metastable state of a-Si:H. The decomposition of these complexes in the temperature range 72–127 °C could be an additional factor determining the high values of the conduction activation energy which were observed in the experiment.

Structural formations in a Si-matrix can also be expected to appear in p-films under γ-irradiation. The B atoms doping the film are strong acceptors. Having an energetically unstable electronic configuration ($2s^22p^1$), such an atom in an amorphous matrix can hold a large number of binding electrons around itself. It will strive to undergo a transition to a more stable sp^3-hybridization state ($2s^12p^2$) or it can even assume the configuration $2s^2p^6$. As shown in Refs. 11 and 12, boron manifests great versatility in bond formation, changing ''when necessary'' the coordination number from 3 to 4–6 and even up to 9. Boron atoms can form bridge bonds with one another or with Si via hydrogen. On this basis it can be expected that a-Si:H⟨B⟩ films are heterogeneous from the moment they are prepared (on account of complexes based on B, Si, and H atoms). As a-Si:H passes into a different metastable state in the process of irradiation, the B atoms can then rapidly bring about structural adaptation and heal a portion of the defects that are formed. This process returns the system into a metastable state close to the initial state, which accounts for the weak effect of γ-irradiation on the electrical conductivity of p-type films, as we observed.

[1] O. Imagawa, K. Yasuda, and A. Yoshida, J. Appl. Phys. **60**, 4719 (1989).
[2] I. A. Kurova, V. N. Meleshko, D. A. Machalova, and N. N. Ormont, in *Abstracts of the All-Union Conference on Photoelectric Phenomena in Semiconductors* [in Russian], FAN, Tashkent, 1989.
[3] R. A. Street, J. Non-Cryst. Solids **77/78**, 1 (1985).
[4] R. A. Street, J. Zesch, and M. J. Thompson, Appl. Phys. Lett. **43**, 672 (1983).
[5] M. S. Ablova, U. Zh. Abdumanapov, K. P. Abdurakhmanov, G. S. Kulikov, D. P. Utkin-Édin, and K. Kh. Khodzhaev, Fiz. Tekh. Poluprovodn. **22**, 20 (1988) [Sov. Phys. Semicond. **22**, 12 (1988)].
[6] S. C. Agarwal, Bull. Mater. Sci. **18**, 669 (1995).
[7] R. A. Street, J. Kalalios, C. C. Tsai, and T. M. Hayes, Phys. Rev. B **35**, 1316 (1987).
[8] A. A. Andreev, M. S. Ablova, T. A. Sidorova, E. A. Kazakova, A. G. Pilatov, and T. Turgunov, Neorg. Mater. **25**, 900 (1989).
[9] S. B. Aldabergenova, S. B. Feoktistov, V. C. Karpov, K. V. Koughia, A. V. Pevtsov, and V. N. Solovyov, in *Transport, Correlation and Structural Defects*, edited by H. Fritzsche, N. Y., 1990.
[10] H. Fritzsche [Ed.], *Amorphous Silicon and Related Materials*, World Scientific Pub., 1989 [Russian translation, Mir, Moscow, 1991].
[11] O. A. Golikova, I. A. Drabkin, V. N. Zaĭtsev, M. M. Kazanin, D. N. Mirlin, I. V. Nelson, E. N. Tkalenko, and T. Khamidov, in *Boron: Production, Structure, and Properties* [in Russian], Mitsniereba, Tbilisi, 1974.
[12] P. V. Samsonov, T. I. Serebryakova, and V. A. Neronov, in *Borides* [in Russian], Atomizdat, Moscow, 1975.

Translated by M. E. Alferieff

Subthreshold characteristics of electrostatically controlled transistors and thyristors. 1. Shallow planar gate

A. S. Kyuregyan* and S. N. Yurkov

V. I. Lenin All-Russia Electrical Engineering Institute, 111250 Moscow, Russia
(Submitted February 20, 1997; accepted for publication April 15, 1997)
Fiz. Tekh. Poluprovodn. **32**, 249–254 (February 1998)

A rigorous analytic theory of the blocking state of electrostatically contolled thyristors and transistors and a shallow planar gate of arbitrary width is constructed in the model with a completely depleted base. Formulas are obtained for the subthreshold currents and blocking factor g as functions of the electrode potentials and device parameters: source and gate widths and thickness and doping of the base. It is shown that sufficiently heavy doping not only influences the parameters of the current-voltage characteristics and the factor g but it also changes the qualitative form of the current-voltage characteristic near threshold.
 [S1063-7826(98)03101-9]

1. INTRODUCTION

Electrostatically controlled transistors and thyristors (ECTs) are the most promising devices for switching high powers in the frequency range 10 kHz–1 MHz.[1] The operating principles of such devices are described in detail in Ref. 2 at the qualitative level, but the analytic theory required for a clear understanding of the physics of the devices and for calculating the parameters is still in a state of infancy. This is also true of the theory of the blocking state of ECTs, which is described completely by the dependences of the drain current I_d, gate current I_g, and source current I_s on the drain voltage U_d and gate voltage U_g. A simple analysis of current balance in ECTs shows that I_d, I_g, and I_s are related as

$$\begin{cases} I_d = I_g + I_s, \\ I_g = S j_{dg} + 2\Lambda J_{sg}^S + I_{dg}^S, \\ I_s = \Lambda J_s - 2\Lambda J_{sg}^S, \end{cases} \tag{1}$$

where S is the device area, and Λ is the total source length. The drain-gate surface leakage current I_{dg}^S and the linear source-gate leakage current density J_{sg} depend mainly on the quality of the treatment and the shielding of the electrode-free surface of the device, so that their analysis is not part of our problem. The current density j_{dg} is determined by thermal generation in the space-charge region (SCR). In thyristors it also depends on hole injection from the drain

$$j_{dg} = \frac{j_T \overline{M}_T + (\overline{M}_n + \beta_p \overline{M}_p - 1)\Lambda J_s / S}{1 - \beta_p \overline{M}_p}, \tag{2}$$

where j_T is the thermal generation current density in the SCR, and β_p is the current gain of the composite transistor. Obviously, $\beta_p = 0$ if the ECT is a transistor. The avalanche multiplication coefficients $\overline{M}_n$, $\overline{M}_p$, and $\overline{M}_T$, averaged over the area of the device and introduced in Eq. (2) to complete the picture, must be calculated on the basis of a non-one-dimensional problem, which cannot be solved analytically. Ordinarily, however, there is no need for this procedure, since the blocking capability of most ECTs is determined not by impact ionization in the SCR but rather by the law governing the increase in the electron injection current density J_s through the barrier at the saddle point of the two-dimensional potential well $\varphi(x,y)$ produced by the interaction of the fields generated by the gate, sink, and volume charge of the impurities.[1,2] As shown rigorously in Ref. 3, in the diffusion approximation

$$J_s = q N_s D_n \xi \exp\left(- \frac{|q\tilde{\varphi}|}{kT} \right), \tag{3}$$

where q is the electron charge, N_s is the electron density at the source-SCR boundary, D_n is the electron diffusion coefficient, k is Boltzmann's constant, and T is the temperature. The remaining two quantities in Eq. (3) completely describe the barrier near the saddle point: $|q\tilde{\varphi}|$ is the minimum height of the barrier and $\xi = \left(-\frac{\partial^2 \varphi}{\partial y^2} / \frac{\partial^2 \varphi}{\partial x^2} \right)^{1/2}$ is the relative ''slope'' in the directions y (along the channel) and x (across the channel). Therefore, to determine the subthreshold characteristics of ECTs it is sufficient (on the basis of the stipulations made above) to find the dependence of these two quantities on U_d, U_g, and the device parameters. In turn, this requires knowing the function $\varphi(x,y)$, to calculate which analytically great efforts have been made. However, the authors of nearly all studies known to us either used ''original'' approximate methods, whose error is impossible to estimate,[4–8] or they actually solved the problem by approximate numerical methods while claiming that they have developed an analytical theory.[9,10] As far as we know, the only exception is Ref. 11, where a mathematically correct solution for $\varphi(x,y)$ was obtained for a very simple model of ECTs with a shallow, closely spaced, planar gate and source of the same width, but the solution was used only for calculating the blocking factor. One cell of this device is shown in Fig. 1.

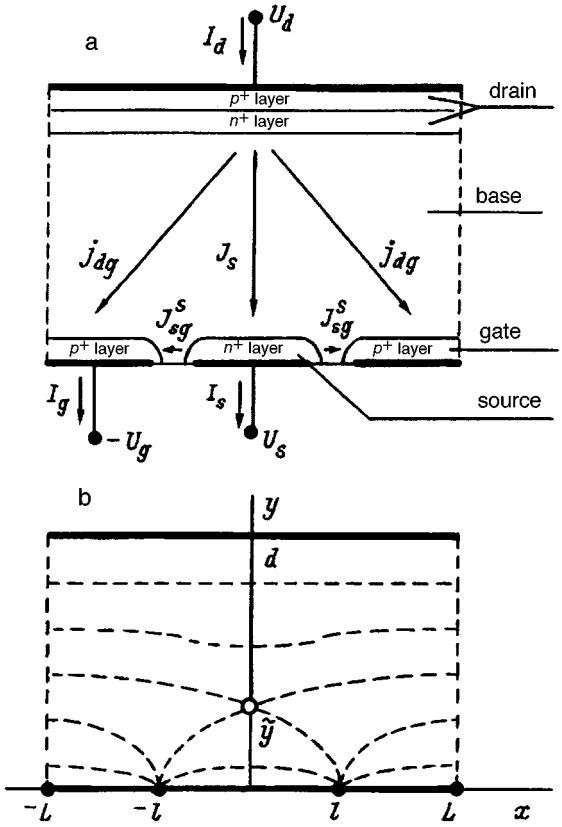

FIG. 1. Electrostatically controlled thyristor: a—Schematic diagram of a cross section of a thyristor with a shallow planar gate and source; in a transistor there is no p^+ layer at the drain. b—Model of a thyristor cell with flat adjoining source and gate, used for calculating the potential distribution; the dashed lines represent equipotential lines.

In the present paper we extend the results of Ref. 11 to the case of an arbitrary gate-to-source width ratio and the parameters in the relation (3) are calculated taking into account the base doping, whose role is analyzed more accurately than in Ref. 11.

2. POTENTIAL DISTRIBUTION

To calculate the potential distribution $\varphi(x,y)$ in the SCR, following Ref. 11 we shall employ two basic assumptions.

1. Assuming that the current density in the blocking state is low, we shall ignore, as is ordinarily done,[2–11] the volume charge of electrons and holes in the SCR. This assumption can even be regarded as valid by definition of the subthreshold operating regime.

2. We shall assume that the distance δ between the n^+ source and the p^+ gate and their thicknesses are sufficiently small, and that the doping is sufficiently heavy so that they can be regarded as flat equipotential adjoining electrodes (see Fig. 1b). Since for our problem it is necessary to know $\varphi(x,y)$ only in a narrow strip along the axis of the channel, δ can be disregarded, if it is much less than the width $2l$ of the source and the gate width $2(L-l)$.

For this model $\varphi(x,y)$ is a solution of the Poisson equation

$$\Delta\varphi(x,y)=-\frac{q}{\varepsilon\varepsilon_0}N(y) \tag{4}$$

in a strip with translationally symmetric boundary conditions

$$\varphi(x,0)=\begin{cases}0 & \text{for } 2mL-l<x<2mL+l,\\ -U_g & \text{for } 2mL+l<x<2(m+l)L-1,\end{cases} \tag{5}$$

$$\varphi(x,w)=U_d, \tag{6}$$

where $\varepsilon\varepsilon_0$ is the permittivity of the semiconductor, $N(y)$ is the total density of donors and acceptors in the SCR, $m=0,\pm1,\pm2,\ldots$, and w is the width of the SCR.

For high drain potentials, when the SCR fills the entire base of thickness d and is bounded on the drain side by a heavily doped n^+ layer, the equality $w=d$ is satisfied. In the opposite case (when $w<d$), as is well known, the additional condition

$$\text{grad }\varphi(x,y)|_{y=w}=0 \tag{7}$$

must be used to determine the position of the boundary of the SCR; in addition, strictly speaking, $w=w(x)$ because of the multidimensional nature of the problem. If $w=d$, then $\varphi(x,y)$ can be represented as

$$\varphi(x,y)=\varphi_N(y)+\varphi_0(x,y), \tag{8}$$

where $\varphi_N(y)$ is the solution of the one-dimensional Poisson equation (4) with zero boundary conditions, and $\varphi_0(x,y)$ is the solution of the classical Dirichlet problem for a strip[12] with the boundary conditions (5) and (6). It can be shown that taking into account the possible dependence $N(y)$ does not give a solution which is qualitatively different from the typical case $N=\text{const}$. Therefore, we shall restrict the discussion here to describing the results for ECTs with a uniformly doped base. In this case

$$\varphi_N(y)=V_d\frac{y}{d}\left(1-\frac{y}{d}\right), \tag{9}$$

where $V_d=qNd^2/2\varepsilon\varepsilon_0$. The potential $\varphi_0(x,y)$ can be obtained by using, for example, the Schwarz integral for a strip.[12] In our case, using the relation (6), this integral can be put into the form

$$\varphi_0(x,y)=U_d\frac{y}{d}+\frac{\sin(\pi y/d)}{2d}\int_{-\infty}^{+\infty}\frac{\varphi(x',0)dx'}{\cosh[\pi(x-x')/d]-\cos(\pi y/d)}. \tag{10}$$

Substituting the expression (5) into (10), we obtain an expression for $\varphi_0(x,y)$ in the form of a slowly converging series. It is more convenient to use a Fourier series expansion of $\varphi(x,0)$. Substituting this expansion into Eq. (10) gives, after integrating and combining it with Eq. (9),

$$\varphi(x,y)=U_g\left[M\frac{y}{d}-1+\frac{l}{L}+G_\varphi\left(\frac{l}{L},\frac{d}{L},\frac{x}{L},\frac{y}{L}\right)\right]-V_d\frac{y^2}{d^2}, \tag{11}$$

where $M=\dfrac{U_d+V_d+U_g}{U_g}-\dfrac{l}{L}$,

$$G_\varphi(\nu,\eta,z,t) = \frac{2}{\pi}\sum_{m=1}^{\infty}\frac{\sinh[\pi m\eta(1-t)]}{m\,\sinh(\pi m\eta)}\sin(\pi m\nu)\cos(\pi mz). \tag{12}$$

The field intensity E_y along the y axis is obtained from Eq. (11) by differentiating:

$$E_y(x,y) = \frac{U_g}{d}\left[-M + G_E\left(\frac{l}{L},\frac{d}{L},\frac{x}{L},\frac{y}{d}\right)\right] + 2V_d\frac{y}{d^2}, \tag{13}$$

$$G_E(\nu,\eta,z,t) = 2\eta\sum_{m=1}^{\infty}\frac{\cosh[\pi m\eta(1-t)]}{\sinh(\pi m\eta)}\sin(\pi m\nu)\cos(\pi mz). \tag{14}$$

As expected, the field intensity in the $y=d$ plane assumes its minimum value on the channel axis. Therefore, the minimum value of the drain potential $V_{d\,\min}$, for which $w=d$ and the formulas derived above are still valid, is determined by the equality $E_y(0,d)=0$. We thus obtain

$$V_{d\,\min} = V_d + U_g\left[\frac{l}{L} - 1 + G_E\left(\frac{l}{L},\frac{d}{L},0,1\right)\right]. \tag{15}$$

However, even for $U_d < V_{d\,\min}$ there is no need to take into account the ''non-one-dimensionality'' of the additional boundary condition (7). Indeed, $E_y(0,d)$ depends on x only because of the presence of the term $G_E(l/L\,,d/L\,,x/L,1)$, which, as one can see from Eq. (14), is exponentially small when $d \geqslant 2L$. This inequality holds in all cases of practical interest. For this reason, to within the order of $4\,d/L\exp(-\pi d/L)$, the SCR boundary can be assumed flat even when $U_d < V_{d\,\min}$, and the quantity w can be found from the equation $E_y(0,w)=0$, which is equivalent to the condition (7), to the same degree of accuracy—after all d's in the expression for E_y are replaced by w. Therefore, disregarding in Eq. (13) the term G_E, we obtain

$$V_d = U_d + U_g(1-l/L). \tag{16}$$

It thus follows (since now $V_d = qN_Dw^2/2\varepsilon\varepsilon_0$) that

$$w = \left\{\frac{2\varepsilon\varepsilon_0}{qN_D}\left[U_d + U_g\left(1-\frac{l}{L}\right)\right]\right\}^{1/2}. \tag{17}$$

The quantity G_E can be regarded as small and the SCR boundary can be regarded as flat, if $w \geqslant 2L$, or

$$U_d \geqslant V_{w\,\min} \equiv 4V_L - U_g\left(1-\frac{l}{L}\right), \tag{18}$$

where $V_L = qNL^2/2\varepsilon\varepsilon_0$.

Estimates show that $|G_E(l/L\,,d/L\,,x/L,1)| \leqslant 0.02$ when $U_d = V_{w\,\min}$, and the deviation of the real SCR boundary from the flat plane $y=w$ is of the order of $0.02w$. For consistency, we assume below that the thickness of the SCR equals d, but if $V_{w\,\min} < U_d < V_{d\,\min}$, then in all formulas d must be replaced by w from Eq. (17).

We employed in Eqs. (16)–(18) the symbol N_D instead of N to underscore that everything said above concerning the case $w<d$ is meaningful only for devices in which the base is doped with donors (i.e., $N=N_D>0$) and the SCR is adjoining to the source. If the base is doped with acceptors (this variant of a thyristor is discussed in, for example, Ref. 11), then only the case $w=d$ is relevant to our problem, because in such devices the ''main'' SCR is adjoining to the central p-n junction and for $w<d$ the source and gate are located outside the SCR.[11]

3. PARAMETERS OF THE SADDLE POINT

The parameters of the saddle point, which lie on the channel axis near the source, can be easily found after the expressions (12) and (14) are put into the form[1]

$$G_\varphi(\nu,\eta,0,t) = \frac{2}{\pi}\sum_{m=-\infty}^{\infty}\arctan\left[\frac{\sin\,\pi\nu}{\exp(\pi|2m+t|\,\eta)-\cos\,\pi\nu}\right] \times \operatorname{sign}\left(m+\frac{1}{2}\right), \tag{19}$$

$$G_E(\nu,\eta,0,t) = \eta\sum_{m=-\infty}^{\infty}\frac{\sin\,\pi\nu}{\cosh[\pi(2m+t)\,\eta]-\cos\,\pi\nu}, \tag{20}$$

where for $\eta \geqslant 2$ the terms with $m=0$ are sufficient. Substituting them into Eqs. (11) and (13) yields the following formulas, which are correct to within $2\exp(-2\pi d/L)$, for $\varphi(0,y)$ and $E_y(0,y)$:

$$\varphi(0,y) = U_g\left\{M\frac{y}{L} - \frac{2}{\pi}\arctan\left[M_0\,\tanh\left(\frac{\pi y}{2L}\right)\right]\right\} - V_d\frac{y^2}{d^2}, \tag{21}$$

$$E_y(0,y) = \frac{U_g}{L}\left[\frac{\sin(\pi l/L)}{\cosh(\pi y/L)-\cos(\pi l/L)} - M\right] + 2V_d\frac{y}{d^2}, \tag{22}$$

where $M_0 = \cot(\pi l/2L)$. The coordinate $\tilde{y}$ of the saddle point is a root of the equation $E_y(0,y)=0$. If in Eqs. (21) and (22) the last terms are neglected, then

$$\tilde{y} = \frac{2}{\pi}L\,\tanh^{-1}\sqrt{\frac{1-M/M_0}{1+MM_0}}, \tag{23}$$

$$\tilde{\varphi} = \varphi(0,\tilde{y}) = \frac{2}{\pi}U_g\left[M\,\tanh^{-1}\sqrt{\frac{1-M/M_0}{1+MM_0}} - \arctan\left(M_0\sqrt{\frac{1-M/M_0}{1+MM_0}}\right)\right]. \tag{24}$$

For $N=0$ these formulas hold (with the stipulations made at the beginning of Sec. 2) right up to vanishing of the barrier at $M=M_0$. Near the threshold, where

$$\sqrt{1-\frac{M}{M_0}} \ll \sqrt{1+M_0^{-2}}, \tag{25}$$

Eq. (24) can be simplified by expanding the arctangent in a series with respect to the small argument:

$$\tilde{\varphi}=-\frac{4U_g}{3\pi}\frac{M_0}{\sqrt{M_0^2+1}}\left(1-\frac{M}{M_0}\right)^{3/2}. \tag{26}$$

If $N\neq 0$, then, as is easily verified, the last terms in Eqs. (21) and (22) can be disregarded only if

$$M_0\sqrt{(M_0^2+1)\left(1-\frac{M}{M_0}\right)}\gg\frac{|V_L|}{U_g}. \tag{27}$$

Now, in order that a region of applicability of Eq. (26) exist, the inequalities (25) and (27) must hold simultaneously, and hence. The following condition must be satisfied:

$$U_g(M_0^2+1)\gg|V_L|. \tag{28}$$

Of course, for sufficiently small $M-M_0$ the inequality (27) is not satisfied, but $\tilde{y}$ becomes so small that the right side of Eq. (21) can be expanded in a series in the small parameter yM_0/d and the potential distribution near the source can be obtained in the form

$$\varphi(0,y)=V_L\frac{y}{L}\left[\frac{2}{3}\frac{y^2}{y_0L}-\frac{y}{L}+(M-M_0)\frac{U_g}{V_l}\right], \tag{29}$$

where $y_0=\frac{8}{\pi^2}\frac{V_L}{U_g}\frac{L}{M_0(M_0^2+1)}$. The coordinate of the saddle point is now determined by the equation

$$\tilde{y}^2-\tilde{y}y_0+y_0L\frac{U_g}{V_L}\frac{(M-M_0)}{2}=0. \tag{30}$$

Substituting this equation into Eq. (29), we obtain

$$\tilde{\varphi}=-V_L\frac{\tilde{y}^2}{L^2}\left(\frac{4}{3}\frac{\tilde{y}}{y_0}-1\right). \tag{31}$$

For $M<M_0$ Eq. (30) has only one positive root:

$$\tilde{y}=\frac{1}{2}\left[y_0+\sqrt{y_0^2+2y_0L\frac{U_g}{V_L}(M_0-M)}\right]. \tag{32}$$

It can be shown that the expansion employed in the derivation of Eqs. (29)–(32) is justified near threshold if the inequality (28) holds. Relations (26) and (31) therefore are valid only for sufficiently high gate voltages. Here expression (26) transforms into expression (31) as U_d increases.

As one can see from Eqs. (31) and (32), $\tilde{y}$ and $\tilde{\varphi}$ simultaneously approach zero as $M\to M_0$ only when $y_0\propto N\leqslant 0$. However, if $N>0$, then as $M\to M_0$, the barrier does not vanish, since $\tilde{y}\to y_0$ and the potential at the saddle point approaches $\tilde{\varphi}_0=-V_dy_0^2/3d^2$ (Fig. 2, curve *2*). The second root in Eq. (32) with $M>M_0$ becomes positive, and a local maximum appears on the curve $\varphi(0,y)$. This means that there arises in the region between the source and the saddle point a potential well (Fig. 2, curve *3*) that must be filled with electrons from the source until the positive donor charge is completely compensated, and the position of the SCR boundary in direct proximity to the saddle point changes. For this reason, our initial model becomes inapplicable for $M>M_0$, even if the barrier $|q\tilde{\varphi}_0|$ is still high and if the volume charge of the electrons injected into the SCR can be ignored.

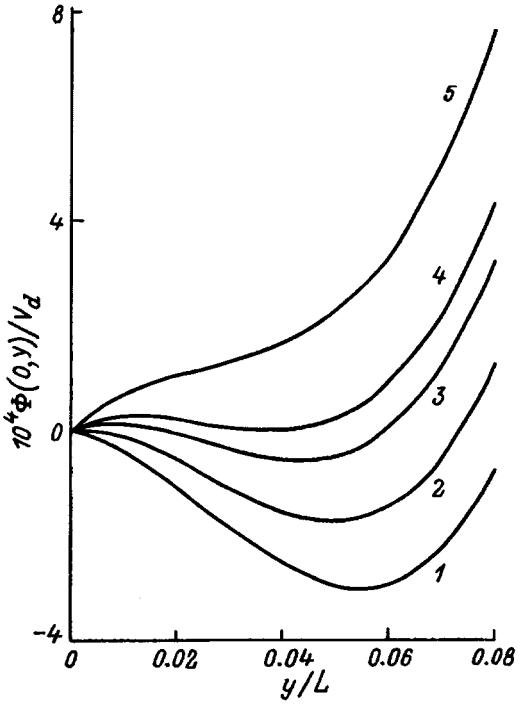

FIG. 2. Potential distribution along the channel axis of an electrostatically controlled thyristor—with a donor-doped base, $d=2L$, $L=2l$, $U_g=2U_d$, and drain voltages U_d/U_0: *1*—0.9987, *2*—1.0000, *3*—1.0012, *4*—1.0017, *5*—1.0025.

In devices with a nondoped base the parameter $\xi=1$, because $\varphi_N=0$, and φ_0 is a harmonic function.[3] If $N\neq 0$, then

$$\frac{\partial^2\varphi}{\partial x^2}=\frac{\partial^2\varphi_0}{\partial x^2}=-\frac{\partial^2\varphi_0}{\partial y^2}\quad\text{and}\quad\frac{\partial^2\varphi}{\partial y^2}=\frac{\partial^2\varphi_0}{\partial y^2}=-2\frac{V_d}{d^2},$$

so that

$$\xi=\sqrt{1-2\frac{V_L}{L^2}\left[\frac{\partial^2\varphi_0(0,\tilde{y})}{\partial y^2}\right]^{-1}}. \tag{33}$$

Far from threshold, when the inequality (27) holds, the second term in Eq. (33) is small and, again, $\xi=1$. In the opposite case, the expansion of $\varphi_0(0,y)$ employed in the derivation of Eq. (29) can be used. We thus obtain

$$\xi=\sqrt{1-\frac{y_0}{2\tilde{y}}}. \tag{34}$$

Thus, in the region of applicability of our model (i.e., for $M<M_0$) the parameter ξ varies from 1 for small M up to $1/\sqrt{2}$ at $M=M_0$.

4. BLOCKING FACTOR

The blocking factor g, equal to the ratio of the threshold drain voltage U_{d0} and gate voltage U_{g0}, is one of the main parameters of an ECT.[2] But there are still no generally accepted values of U_{d0} and U_{g0}. In engineering practice it is customary to use the condition that the drain current equals a prescribed small value I_t:

$$I_d(U_{d0},U_{g0})=I_t.$$

In application to an ECT, it is virtually equivalent [see Eqs. (1)–(3)] to the equality $|\tilde{\varphi}(U_{d0},U_{g0})|=\tilde{\varphi}_t$, which has been used by many authors but with different values of the ''threshold'' potential φ_t in the range from 0 (Ref. 11) to 0.8 V (Ref. 14). However, because of the strong dependence $I_d(U_d,U_g)$ in the subthreshold region, these definitions should all give threshold voltages which are identical with accuracy sufficient for practical purposes. For this reason, in the model of a completely depleted SCR we believe it is best to use the simplest and physically clearest threshold onset condition

$$\tilde{\varphi}(U_{d0},U_{g0})=0. \tag{35}$$

If $N\leqslant 0$, then, as follows from the results of the preceding section, the relation (35) holds simultaneously with the equation $\tilde{y}=0$ and hence $E_y(0,0)=0$. This makes it possible to determine g for devices with nondoped and acceptor-doped bases of arbitrary thickness. Indeed, in such devices $w=d$ always. Therefore, setting in Eq. (13) $x=y=0$ and $E_y=0$, we obtain

$$g=g_0-\frac{V_d}{U_g}, \tag{36}$$

where the blocking factor of an ECT with a nondoped base is

$$g_0=G_E\left(\frac{l}{L},\frac{d}{L},0,0\right)-1+\frac{l}{L}\approx\frac{d}{L}\cot\left(\frac{\pi l}{2L}\right)-1+\frac{l}{L}. \tag{37}$$

The latter equality in Eq. (37) holds to a high degree of accuracy for $d\geqslant L$.

For $N=N_D>0$ our model of an ECT becomes unsuitable until the barrier vanishes, so that, strictly speaking, the threshold onset condition (35) cannot be used. However, for the following reasons this is of no practical value for calculating g. First, the difference between the drain voltages $U_d=U_0$ (for which $M=M_0$) and $U_d=U_1=U_0+3V_dy_0/8d$ [for which the barrier vanishes in accordance with Eqs. (31) and (32)],

$$\frac{U_1-U_0}{U_0}=\frac{3V_dy_0}{8U_0d}\geqslant\frac{3y_0}{8d}\ll\frac{L}{dM_0},$$

is very small (see curve *4* in Fig. 2), especially for ECTs with a large blocking factor, $g\approx M_0d/L\gg 1$. Secondly, the donor-neutralization effect in the near-cathode region, as described in Sec. 3, should evidently result in the barrier decreasing more rapidly than implied by Eqs. (31) and (32). Thus, in all cases of practical interest it can be assumed that the threshold onset conditions (35) and $E_y(0,0)=0$ are equivalent, to a high degree of accuracy, and Eq. (36) can be used to calculate the blocking factor.

It follows from Eq. (36) that when the base is doped, the blocking factor becomes dependent on not only the device parameters, but also the gate voltage. This dependence changes when $U_d<V_{d\,\min}$: Substituting in Eq. (36) w for d and using Eqs. (17), we obtain

$$g=\frac{U_g}{4V_L}\cot^2\left(\frac{\pi l}{2L}\right)-1+\frac{l}{L}. \tag{38}$$

Donor doping of the base decreases g and acceptor doping increases g. This effect was noted and explained in Ref. 11. In the particular case $L=2l$ Eqs. (36)–(38) are identical to the results obtained by us for the case of a uniformly doped base.

We wish to thank A. V. Gorbatyuk and T. T. Mnatsakanov for many helpful discussions of the questions considered in this paper.

Financial support of this work was provided by the Russian Fund for Fundamental Research (Project 95-02-05767) and INTAS (Project 94-0417).

*Fax: (095)362 5617; e-mail: kyureg@semlab.vei.msk.ru

[1)]This requires expanding cosech($\pi m\eta$) in Eqs. (12) and (14) in a series for large arguments, changing the order of summation, and using the standard[13] formulas for sums of series with exponential and trigonometric functions.

[1] J. I. Nishizava, Power conv. and intel. motion., **13**, 15 (1987).
[2] B. J. Baliga, *Modern Power Devices*, Singapore, 1987, p. 132.
[3] A. V. Gorbatyuk and A. S. Kyuregyan, Mikroelektronika **20**, 254 (1991).
[4] T. Ohmi, IEEE Trans. Electron Devices **ED-27**, 536 (1980).
[5] R. K. Gupta, J. Appl. Phys. **53**, 1754 (1982).
[6] K. C. Kun, IEE Proc., pt. 1 **131**, 87 (1984).
[7] C. Bulucea and A. Rusu, Solid-State Electron. **30**, 1227 (1987).
[8] V. A. Makarov, S. M. Agafonov, Yu. N. Maksimenko, M. B. Pal'nikhin, and O. I. Bonomorskiĭ, Mater. Elementy Elektron. Tekhniki Elektrotekhniki, No. 15, 131 (1987).
[9] A. Timotin and C. Zaharescu, Rev. Roum. Sci. Techn., Ser. Electrotechn. et. Energ. **33**, 3 (1988).
[10] A. G. M. Strollo and P. Spirito, IEEE Trans. Electron Devices **ED-38**, 1943 (1991).
[11] A. V. Gorbatyuk and I. V. Grekhov, Fiz. Tekh. Poluprovodn. **15**, 1353 (1981) [Sov. Phys. Semicond. **15**, 781 (1981)].
[12] M. A. Lavrent'ev and B. V. Shabat, *Methods of the Theory of Functions of a Complex Variable* [in Russian], Nauka, Moscow, 1987.
[13] A. P. Prudnikov, Yu. A. Brychkov, and O. I. Marychev, *Integrals and Series* [in Russian], Nauka, Moscow, 1987.
[14] M. S. Adler and B. J. Baliga, Solid-State Electron. **23**, 735 (1980).

Translated by M. E. Alferieff